Ghent University
Faculty of Sciences
Department of Solid State Sciences

In situ Electron Paramagnetic Resonance Study of Breathing Phenomena and Related Framework Transformations in Paramagnetically Doped Metal-Organic Frameworks

by

Irena Nevjestić

Promoters:
prof. dr. ir. Henk Vrielinck
prof. dr. Freddy Callens
prof. dr. Pascal Van Der Voort

Thesis submitted for the degree of
Doctor in Sciences: Physics

Academic year 2017-2018

Contents

Nederlandstalige samenvatting

Deze thesis kadert in een gemeenschappelijk FWO-project tussen de EMR en COMOC-onderzoeksgroepen van de UGent. De focus van dit project rond metaal-organische netwerken (Eng: metal-organic framework, MOFs) lag zowel op de studie van hun fundamentele eigenschappen zoals structurele transformaties ('breathing') als op toepassingen, in dit geval katalyse. Het doel van deze EMR-thesis was een gedetailleerde studie van de elektronische en structurele veranderingen in MOFs gebruikmakend van elektronen paramagnetische resonantie (EPR) als voornaamste spectroscopische techniek. EPR kan informatie leveren i.v.m. de valentietoestand, de coördinatiegeometrie en de verdere omgeving van transitiemetaaldopanten in MOFs. Alhoewel EPR dergelijke belangrijke structurele informatie kan aanleveren aan een relatief lage kost, werd deze techniek tot nog toe maar zelden gebruikt in structurele en katalytische studies van MOFs.

MOFs vormen een nieuwe klasse van kristallijne, poreuze materialen die opgebouwd zijn uit metaalionen, verbonden door organische groepen, zogenaamde linkers. O. Yaghi introduceerde de term 'metal-organic framework' in 1995 en sindsdien heeft deze klasse van materialen de aandacht van veel wetenschappers getrokken. Deze materialen worden gekenmerkt door verscheidene bijzondere eigenschappen, gaande van een heel hoge specifieke oppervlakte (tot 6000 m^2/g) en porositeit (tot 90% van het volume), tot een welomlijnde poriegrootte en vorm. De structuur van MOFs kan eenvoudig worden afgestemd om bepaalde eigenschappen te verkrijgen door verschillende metaalcentra en organische linkers te combineren. Dankzij hun opbouw uit zowel organische als anorganische 'ingrediënten', bieden deze materialen meer flexibiliteit in ontwerp en mogelijkheden in vergelijking met bijvoorbeeld zeolieten wat ze zeer interessant maakt voor een breed bereik aan toepassingen, gaande van katalyse en sensoren tot de opslag, het inbrengen, transporteren en op de juiste plaats afleveren van medicijnen.

In Hoofdstuk 2 wordt het enorme potentieel van MOFs geïllustreerd aan de hand van een aantal veel-bestudeerde structuren zoals ZIF-8, MIL-101, MOF-5, UiO-66, HKUST-1 en MIL-53. Zoals voorzien in het originele plan van het project waarin dit onderzoek kadert, werden de MOFs MIL-47(V) en MIL-53(Al), en in mindere mate de structuren COMOC-2(V) en DUT-5(Al), diepgaand bestudeerd. Na hun synthese zijn de poriën van MIL-47(V) en MIL-53(Al) geblokkeerd door

restproducten van de synthese zoals niet-gereageerde linkers en oplosmiddelen (AS toestand). Deze kunnen worden verwijderd door calcinatie, d.w.z. door de MOF te verwarmen tot op hoge temperatuur, of door solventextractie (activatie van de MOF).

De geactiveerde vormen van MIL-53(Al) en COMOC-2(V) vertonen een structurele flexibiliteit die ademen (Eng: breathing) wordt genoemd, terwijl MIL-47(V) en DUT-5(Al) rigide structuren vormen. Dit ademen bestaat algemeen genomen uit een (reversibele) transitie tussen toestanden met (varianten van) nauwe/gesloten poriën en toestanden met (varianten van) grote/open poriën, gestuurd door temperatuur, druk of de aanwezigheid van gastmoleculen. Een belangrijk doel van dit doctoraatswerk was om meer inzicht te krijgen in het mechanisme achter dit ademen door verschillende experimentele technieken te combineren, voornamelijk EPR, elektronen-nucleaire dubbele resonantie (ENDOR) en X-straal diffractie (XRD), veelal toegepast *in situ*. Gezien de aanwezigheid van V^{IV} ($3d^1$ configuratie) in het vanadyl ion in de bestudeerde stalen, zijn de hierboven vernoemde magnetische-resonantie-technieken inderdaad een krachtig hulpmiddel voor dit project. Een tweede doel was om de katalytische activiteit van V-gedoteerde stabiele MOFs te bestuderen als alternatief voor het wel katalytisch actieve, maar in contact met water onstabiele MIL-47.

In Hoofdstuk 3 worden de relevante theoretische en praktische aspecten van EPR en ENDOR toegelicht. Spectra worden geanalyseerd met het spin-Hamiltoniaan formalisme. In het geval van het vanadylion moeten in de eerste plaats de elektronische en nucleaire Zeemaninteractie en de hyperfijninteractie (HF) met de ^{51}V kern ($I = 7/2$, die leidt tot het typische 8-lijnen EPR spectrum) worden beschouwd. Informatie over de elektronische en geometrische structuur is vervat in de hoofdwaarden en assen van de g en A tensoren. Het bekomen van deze informatie bracht een moeilijke en tijdsintensieve fitprocedure met veel parameters met zich mee. De parameterruimte kon evenwel beperkt worden dankzij de beschikbaarheid van spectra in verschillende frequentiebanden in het microgolfgebied (L, X, Q, W en J-band, 4-275 GHz), wat essentieel is gebleken om de spectra ondubbelzinnig te interpreteren en inderdaad heeft geleid tot verbeteringen van bestaande resultaten in de literatuur. De zwakkere HF interacties met naburige ^{1}H en ^{27}Al kernen werden bestudeerd met ENDOR en lieten toe om de nabije omgeving van de vanadylionen in kaart te brengen, hetgeen informatie opleverde over het welslagen van de synthese en de V-dotering.

Hoofdstuk 3 vermeldt ook andere nuttige informatie die EPR oplevert. Dit omvat de bepaling van de (relatieve) spinconcentraties uit de spectrale intensiteiten en informatie over de valentietoestanden, voornamelijk bepaald uit V^{IV} intensiteitsveranderingen en lijnverbreding. Lijnverbreding werd in dit werk veroorzaakt door een te hoge concentratie aan V^{IV} ionen of door de aanwezigheid van paramagnetisch zuurstof (Hoofdstuk 8). De V-V interactie maakt het moeilijker

om informatie te halen uit spectra van hoog-geconcentreerde structuren zoals MIL-47(V) of COMOC-2(V) hoewel ook hier is gebleken dat een substructuur kon worden geresolveerd uit de spectra van MIL-47(V) door met verschillende microgolffrequenties te werken. In hetzelfde hoofdstuk werd ook een overzicht van literatuurdata over COMOC-3 en MIL-53(M) (M=Cr,V/Al) gegeven.

Om lijnverbreding tot een minimum te beperken en dus beter geresolveerde EPR spectra te bekomen, werd de meerderheid van de studies in dit werk uitgevoerd op MIL-53(Al) (en DUT-5(Al)), gedoteerd met een lage concentratie aan V.

Een andere veel gebruikte techniek in deze thesis was poeder XRD. De basisprincipes van deze techniek worden beschreven in hoofdstuk 4. Naast de infrastructuur aanwezig in de Vakgroep Vastestofwetenschappen (*in situ* XRD in functie van temperatuur, onderzoeksgroep COCOON), werden in dit project twee synchrotrons bezocht: de Diamond Light Source in Oxford, V.K. en de European Sychrotron Radiation Facility (ESRF) in Grenoble, Frankrijk. In Diamond Light Source werd *in situ* XRD uitgevoerd, onder vacuüm in functie van de temperatuur. In het ESRF werd X-ray near edge structure (XANES) spectroscopie uitgevoerd wat inzicht gaf in de oxidatietoestand van V in MIL-53(Al).

Naast de hierboven genoemde experimentele technieken werden bovendien thermogravimetrische analyse (TGA) en Fourier-transform infrarood spectroscopie toegepast om V-gedoteerd MIL-53(Al) te karakteriseren.

Vanaf Hoofdstuk 5 worden onze eigen resultaten op MOFs gepresenteerd. In de zoektocht naar een katalysator met verbeterde eigenschappen werd een reeks van laag-geconcentreerde MIL-53(Al) AS stalen (0.5-5 %) gesynthetiseerd. De goed geresolveerde EPR spectra van deze AS stalen worden gedomineerd door één vanadyl-component, die de lage symmetrie van de metaalsites in het rooster reflecteert. Het is opmerkelijk dat de dopantconcentratie noch de gebruikte V precursor (VCl_3 en $VOSO_4$) een rol blijkt te spelen voor de vorm van het EPR spectrum. Door de EPR resultaten, opgemeten voor verschillende frequentiebanden, te analyseren in termen van spin-Hamiltoniaanparameters is gebleken dat de hoofdassen van de g en $A(^{51}V)$ tensoren niet samenvallen, dit in tegenstelling tot wat in de literatuur te vinden is. Bovendien toont deze analyse aan dat de vanadylionen voorkomen in (ten minste twee) subtiel verschillende omgevingen.

Dankzij de ENDOR spectra werd bewezen dat de meerderheid van de V^{IV}=O ionen gewone Al^{III}-OH groepen vervangen in AS MIL-53(Al) en bijv. niet inbouwen in poriën. De goed geresolveerde HF structuur en relatief kleine lijnbreedte in de EPR spectra tonen aan dat de V^{IV} centra goed zijn verdeeld in de MOF. De conclusie luidde dat de gehanteerde synthesemethode (Hannes Depauw, COMOC) reproduceerbaar is en een betrouwbare basis vormt om de eigenschappen van geactiveerde stalen te bestuderen.

In Hoofdstuk 6 wordt het ademen van MIL-53(Al) bestudeerd. Een eerste EPR studie identificeerde twee verschillende toestanden uit de spectra, die NP en LP werden genoemd. Deze karakteristieke spectra lieten ons toe om het ademen in geactiveerd V-gedoteerd MIL-53(Al) te volgen in functie van de temperatuur met *in situ* EPR, zowel in lucht als in vacuüm. Parallelle (synchrotron) XRD experimenten leverden complementaire en compatibele resultaten op. Wanneer de temperatuur wordt verhoogd van 350 tot 400 K vergroot de bijdrage van de LP toestand gradueel. Als de temperatuur wordt verlaagd van 450 K tot kamertemperatuur wordt de LP toestand aangehouden in vacuüm, terwijl in lucht het staal gedeeltelijk terugkeert naar de NP toestand nabij kamertemperatuur. Dit is wellicht te wijten aan de opname van watermoleculen uit de lucht.

De XRD metingen onthulden bijkomend dat MIL-53(Al) transformeert in een metastabiele intermediaire NP toestand tussen 320 en 350 K alvorens de LP toestand te bereiken. Uit de TGA resultaten werd besloten dat het V-gedoteerde MIL-53(Al) in dit temperatuurbereik dehydrateert, wat leidde tot de toewijzing van de intermediaire NP toestand aan gedehydrateerde NP (NP-d). De transitie tussen NP-h en NP-d is niet abrupt, H_2O wordt geleidelijk vrijgemaakt uit de MOF, met een continue verandering in roosterparameters tot gevolg. De NP-d toestand wordt gekenmerkt door een kleiner eenheidscelvolume dan de NP-h toestand. Bijkomend werd een verbreding van het EPR spectrum van de LP toestand waargenomen tijdens het afkoelen tot kamertemperatuur in lucht. Dit effect wordt besproken in Hoofdstuk 8 (zie hieronder).

Verdere *in situ* XRD experimenten werden uitgevoerd teneinde de exacte omstandigheden om MIL-53(Al) in een bepaalde toestand te brengen te achterhalen. Het bleek dat de NP-h toestand kon worden gemaakt door het materiaal eenvoudigweg in contact te brengen met (vochtige) lucht bij kamertemperatuur zodat water het rooster kan binnendringen en zich in de poriën nestelen. De LP toestand kan gemaakt worden door het staal te verhitten boven 400 K in vacuüm of in lucht. Voor de NP-d toestand werden drie bijkomende XRD experimenten uitgevoerd. *In situ* opwarmen van kamertemperatuur tot 350 K en terug naar kamertemperatuur afkoelen van MIL-53(Al) toonde een reversibele fasetransitie aan van NP-h naar NP-d en terug naar NP-h. Een eerste manier om de NP-d toestand te bekomen is dus opwarmen tot 350 K. Hierbij moet omzichtig worden omgesprongen omdat de MOF zich kan openen en de LP toestand vormen kort nadat de NP-d toestand wordt bereikt. In een andere aanpak wordt NP-h gedehydrateerd door te pompen bij kamertemperatuur. Met deze procedure trad de LP toestand niet op. Een derde *in situ* XRD experiment toonde aan dat het rooster ook (gedeeltelijk) kon worden gedehydrateerd door het verminderen van de omgevingsluchtvochtigheid, wat suggereert dat het water slechts zwak gebonden is aan de MOF structuur. Door het droogproces te volgen met *in situ* geattenueerde totale reflectie (ATR) IR spectroscopie is gebleken dat de

dehydratatie niet noodzakelijk volledig is.

Gewapend met de kennis om de drie toestanden van geactiveerd V-gedoteerd MIL-53(Al) te scheiden, konden de individuele EPR spectra worden opgemeten (Figuur 1). Dit werd besproken en geanalyseerd aan de hand van het spin-Hamiltoniaanformalisme in Hoofdstuk 7. Analoog als voor de AS toestand zijn de g en $A(^{51}V)$ tensoren voor alle toestanden van geactiveerd MIL-53(Al) t.o.v. elkaar gedraaid. Voor de structuren met 'lege' poriën, LP en NP-d, worden de EPR spectra gedomineerd door slechts één V^{IV} gerelateerde component. De situatie is anders voor de NP-h toestand waarbij de aanwezigheid van H_2O in de poriën van het rooster zorgt voor (ten minste twee) licht verschillende omgevingen voor de V^{IV}=O paramagnetische centra, analoog als voor de AS toestand met BDC moleculen in de poriën. De spin-Hamiltoniaanparameters van de LP en AS toestanden zijn opvallend gelijkaardig wat verklaard kan worden door een vergelijkbare kristalstructuur met grote poriën.

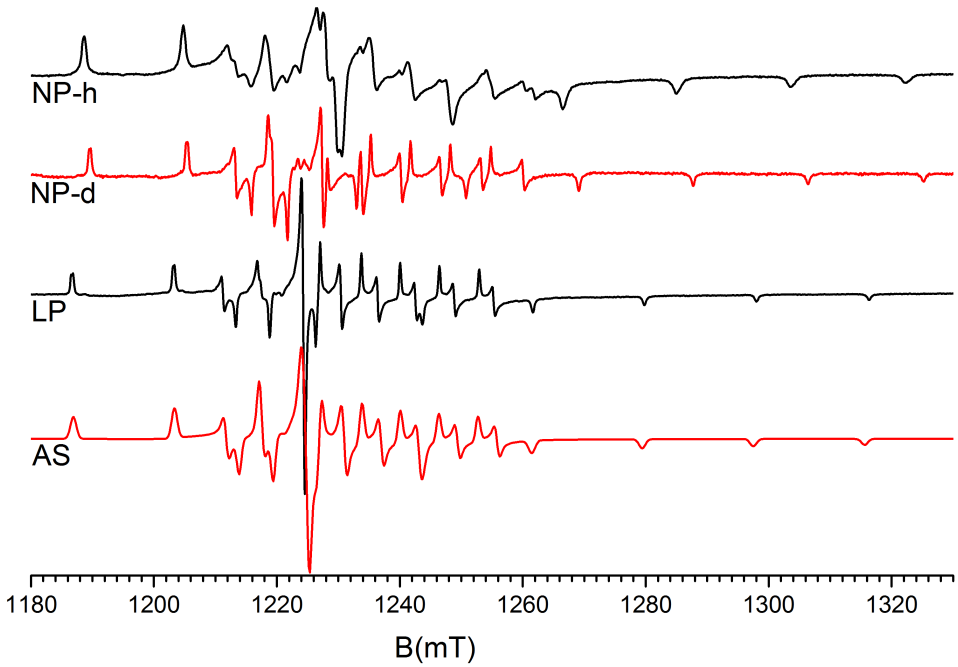

Figuur 1: EPR spectra van V^{IV}=O in vier MIL-53(Al) toestanden: NP-h, NP-d, LP en AS

Verder werd in Hoofdstuk 7 de oxidatietoestand van V in MIL-47(V) en MIL-53(Al) in de AS en geactiveerde toestanden onderzocht aan de hand van zowel XANES als EPR metingen. Het $V^{III}Cl_3$ zout werd gebruikt als V-precursor in de synthese van beide MOFs. In AS MIL-47(V) en MIL-53(Al) bevindt de meerderheid van de V ionen zich in de +III oxidatietoestand. Na calcinatie werden de V^{III} ionen geoxideerd tot V^{IV}. Er kon worden aangetoond dat activatie door zowel

solventextractie als calcinatie de hoeveelheid V^{IV} vergroot, hoewel de transitie enkel volledig is bij calcinatie. Het is belangrijk te vermelden dat EPR en XANES complementaire resultaten geven waarbij EPR de beter toegankelijke en goedkopere techniek is.

Zoals reeds hierboven vermeld, blijkt het EPR spectrum van geactiveerd V-gedoteerd MIL-53(Al) gevoelig te zijn aan zuurstof. De uitwisselingsinteractie tussen de paramagnetische V^{IV}=O centra en aanwezige O_2 moleculen veroorzaakt een verbreding van het LP EPR spectrum. Dit is noch voor de NP-h, noch voor de NP-d spectra het geval. Dit geeft aan dat enkel in de LP toestand het O_2 voldoende dicht bij het paramagnetische V^{IV}=O kan komen om een meetbare verbreding te veroorzaken. De EPR lijnbreedte in functie van de O_2 druk vertoont een bijna-lineaire afhankelijkheid met een gevoeligheid van enkele mbar. Dit opent perspectieven voor toepassingen in zuurstofdetectie (Hoofdstuk 8).

De vergaarde kennis over de MIL-47(V) en V-gedoteerde MIL-53(Al) structuren werd verder gebruikt in de studie van de V-gedoteerde DUT-5(Al) en COMOC-2(V) roosters. Het EPR spectrum van volledig geconcentreerd COMOC-2(V) is analoog aan dat van MIL-47(V), d.w.z. het vertoont een brede lijn zonder HF structuur. In de stalen met zowel V als Al neemt de intensiteit van de brede lijn af met toenemende Al concentratie, ten gunste van de geleidelijk toenemende component met HF structuur. Deze smalle-lijn component doet denken aan het EPR spectrum van V-gedoteerd MIL-53(Al) in de LP toestand. Deze component verbreedt sterk door contact met paramagnetisch O_2, wat een vergelijkbare situatie is als in V-gedoteerd MIL-53(Al). Naast het brede signaal en het 'MIL-53-achtige' signaal is er op zijn minst één bijkomende component terug te vinden in deze stalen met zowel V als Al. Deze component is niet gevoelig aan de aanwezigheid van O_2. Dit EPR spectrum vertoont wel enkele overeenkomsten met het spectrum van $VOSO_4$ (het zout dat wordt gebruikt als precursor in de synthese) in de poriën van DUT-5(Al), maar de precieze oorsprong blijft onduidelijk.

In Hoofdstuk 9 werd V-gedoteerd MIL-53(Al) getest als katalysator in de oxidatie van cyclohexaan in vloeibare fase. Het vertoonde een opmerkelijk lage katalytische activiteit in vergelijking met volledig gedoteerd MIL-47(V). De resultaten uit deze thesis laten enig licht schijnen op deze vaststelling. V-gedoteerd MIL-53(Al) wordt verwacht om samen te trekken tot de NP toestand in een vloeistof waardoor het ontoegankelijk wordt voor gastmoleculen. Deze uitleg impliceert dat enkel V ionen op de randen kunnen deelnemen aan de katalyse. Op basis van de O_2 gevoeligheidsmetingen kan zelfs worden verwacht dat de concentratie aan V lager is dan berekend op basis van de geometrie. Dit kan worden uitgelegd door het voorkomen van een zogenaamde 'eigeel' structuur, die ook werd gerapporteerd voor MIL-53(V/Cr) in de context van hetzelfde FWO project (thesis van Hannes Depauw), waarbij V preferentieel incorporeert in de MIL-53(V/Al)

kern (het eigeel) en waarbij het Al ion voornamelijk aanwezig zijn in de buitenste schil.

Er kan worden besloten dat het gepresenteerde werk aantoont dat EPR en ENDOR spectroscopie bijzonder nuttige technieken zijn om MOFs te bestuderen en complementair zijn aan XRD. Door de nabije omgeving van de paramagnetische groep in kaart te brengen met ENDOR kon de succesvolle incorporatie van de V dopanten op de Al-plaatsen van de MIL-53(Al) worden bewezen. Het ademen van V-gedoteerd MIL-53(Al) werd gedetailleerd gevolgd met *in situ* EPR en XRD. De EPR spectra van V^{IV}=O in vier toestanden van MIL-53(Al) nl. AS, NP-h, NP-d en LP, zijn duidelijk onderscheidbaar en werden nauwgezet geanalyseerd om te komen tot interessante informatie over de elektronische en geometrische structuur van deze materialen, vervat in de g en A tensoren. Van bijzonder belang, ook voor toekomstig computationeel werk, is de bevinding dat de globale structuurveranderingen konden worden gevolgd door lokale veranderingen van de vanadylomgeving. EPR spectroscopie is ook een krachtig middel gebleken om de oxidatietoestand van het geïncorporeerde V-dopant te bepalen en te volgen voor een lagere kost dan XANES. Het zuurstofgevoelige LP spectrum van V-gedoteerd MIL-53(Al) biedt perspectieven voor zuurstof- en gasdetectie in het algemeen. Er wordt verwacht dat de nieuwe inzichten die werden bekomen in deze thesis voor een selectie aan MOFs zeer nuttig kunnen zijn voor toekomstige studies zoals aangetoond voor de bimetallische COMOC-2(V)-DUT-5 reeks. De kennis over de verschillende toestanden van de MOF structuur, zoals afgeleid uit de variaties van de vanadylspectra hebben ook bijgedragen aan het uitleggen van de lage katalytische activiteit van V-gedoteerd MIL-53(Al) (niet-toegankelijke NP toestand in vloeibare omgeving en 'eigeel' structuur analoog aan degene gerapporteerd voor MIL-53(V/Cr)).

English summary

This thesis frames in a joint FWO project between the EMR and COMOC research groups of Ghent University. The focus of this project on metal-organic frameworks (MOFs) was both on the study of their fundamental properties like structural transformations (breathing) and on applications, in this case catalysis. The goal of this EMR thesis was a detailed study of the electronic and structural changes occurring in MOFs using electron paramagnetic resonance (EPR) techniques as primary spectroscopic tools. EPR can provide information on the valence state, the coordination geometry and further environment of transition metal dopants in MOFs. Although EPR can reveal important structural information at relatively low cost, it has been rarely used in structural and catalytic studies on MOFs.

MOFs represent a novel class of crystalline porous materials constructed of metal ions connected by organic linkers. O. Yaghi introduced the term 'metal-organic framework' in 1995 and from then on MOFs have attracted much interest among scientists. These materials possess many interesting features, from a very high specific surface area (up to 6000 m^2/g) and porosity (up to 90% of the volume), to a well-defined pore size and pore shape. The structure of MOFs can easily be tuned to desired properties by employing different combinations of metal centres and organic linkers. Having both organic and inorganic 'ingredients' in the same structure, these materials offer more a flexible design and possibilities in comparison with e.g. zeolites, and are thus interesting for a broad range of possible applications, from catalysis and sensing, to drug storage and delivery.

In Chapter 2, the high potential of MOFs is illustrated by discussing the properties of a few largely investigated structures like ZIF-8, MIL-101, MOF-5, UiO-66, HKUST-1 and MIL-53. As originally planned, the MOFs studied in-depth in this thesis are MIL-47(V) and MIL-53(Al) and, to a smaller extent, the structures COMOC-2(V) and DUT-5(Al). After synthesis, the pores of MIL-47(V) and MIL-53(Al) are blocked with leftovers from the synthesis, e.g. unreacted linkers and solvent (AS state). These can be removed by calcination, i.e. heating the framework to high temperature, or by solvent extraction (activation of the MOF).

The activated forms of MIL-53(Al) and COMOC-2(V) exhibit a structural flexibility called breathing, whereas MIL-47(V) and DUT-5(Al) are rigid structures. The breathing phenomenon in general involves (reversible) transitions between (variants of) narrow/closed pore and (variants of) large/open pore states, trig-

gered by temperature, pressure or guest molecules. A major goal of the PhD work reported here was to get a better insight into the mechanisms of breathing using a combination of techniques, mainly EPR, Electron Nuclear Double Resonance (ENDOR) and X-ray diffraction (XRD), often applied *in situ*. In view of the presence of V^{IV} ($3d^1$ configuration) in the vanadyl ion in studied samples, the mentioned magnetic resonance techniques indeed appeared very powerful in this project. A second goal was to investigate the catalytic activity of V-doped stable MOFs as an alternative to the catalytically active but water-unstable MIL-47.

In Chapter 3 the theoretical and practical aspects of EPR and ENDOR relevant for this thesis are explained. The spectra are analysed using the spin-*Hamiltonian* formalism. In the case of the vanadyl ion, mainly the electron and nuclear Zeeman interactions and the hyperfine (HF) interaction with the ^{51}V nucleus ($I = 7/2$, leading to the typical 8-line patterns in the EPR spectra) have to be considered. The information concerning the electronic and geometric structure is contained in the principal values and axes of the g and A tensors. Obtaining the latter information implied a great deal of difficult and time-consuming multi-parameter fitting. The parameter space was largely restricted by the availability of spectra in several microwave frequency bands (L, X, Q, W and J-band; 4-275 GHz), which appeared essential for unambiguous interpretation of the spectra and indeed led to improvement of earlier literature results. The weaker HF interactions with neighbouring ^{1}H and ^{27}Al nuclei were studied with ENDOR and allowed to map the nearest environment of the vanadyl ions, yielding information about the success of the synthesis and V-doping procedures.

Other useful information retrievable from EPR that was discussed in Chapter 3, included determination of (relative) spin concentrations from the spectrum intensity and valence state information mainly derived from V^{IV} intensity changes and line broadening. The latter phenomenon occurred in this thesis either by too high a concentration of V^{IV} ions or by the proximity of paramagnetic oxygen (Chapter 8). The former V-V interaction made the spectra of highly concentrated structures like MIL-47(V) or COMOC-2(V) less informative although also in Chapter 3 the multi-frequency approach revealed some substructure in the spectra of MIL-47(V). In the same chapter (EPR) literature data on COMOC-3 and MIL-53(M) (M=Cr,V/Al), relevant for the later chapters, were also reviewed.

To reduce line broadening and to get better resolved EPR spectra, the major part of the studies in this thesis were performed on MIL-53(Al) (and DUT-5(Al)) doped with low V concentration and thus leading to a diluted paramagnetic environment.

Another widely used experimental technique in this thesis was powder XRD, the basics of which are described in Chapter 4. Next to the in-house infrastructure (*in situ* XRD as a function of temperature, COCOON group), during this project

two synchrotron facilities were visited, the Diamond Light Source in Oxford, UK and The European Synchrotron Radiation Facility (ESRF) in Grenoble, France. In Diamond Light Source *in situ* XRD under vacuum and heating was carried out. In ESRF X-ray absorption near edge structure (XANES) spectroscopy gave insight into the oxidation state of V in the MIL-53(Al) framework.

Besides the aforementioned experimental techniques, characterization of V-doped MIL-53(Al) by means of thermal gravimetric analysis (TGA) and Fourier-transform infrared spectroscopy (FTIR) was also done.

From Chapter 5 onwards our own results on MOFs are presented. A series of lowly concentrated V-doped MIL-53(Al) AS samples (0.5-5 %) was synthesized in the search for a catalyst with improved performance. The nicely resolved EPR spectra of these AS samples are dominated by the same low-symmetry V^{IV} related component. It is remarkable that neither the dopant concentration nor the vanadium salt precursor (VCl_3 and $VOSO_4$) did influence the EPR spectra qualitatively. The multi-frequency EPR analysis required for an accurate determination of the spin-*Hamiltonian* parameters, revealed, at variance with literature results, that the g and $A(^{51}V)$ tensor principal axes do not coincide. Furthermore, the same analysis demonstrated that vanadyl occurs in (at least two) slightly different environments.

Via the ENDOR spectra it was proved that the majority V^{IV}=O ions substitute regular Al^{III}-OH in the AS MIL-53(Al) framework and not, e.g., in the pores. The well-resolved HF structure and relatively narrow linewidths in the EPR spectra indicate that the V^{IV} centres are well dispersed in the framework. It was concluded that the synthesis method used by Hannes Depauw presents a reproducible and reliable basis for studying the properties of activated samples.

In Chapter 6, breathing was studied in activated V-doped MIL-53(Al). From a first EPR study the spectra of two distinct states, labelled NP and LP, were identified. These probes allowed us to monitor the breathing effect in activated V-doped MIL-53(Al) with *in situ* EPR as a function of temperature in air and in vacuum. Using parallel (synchrotron) XRD experiments complementary and compatible results were obtained. When raising the temperature in the range from 350 to 400 K the fraction of sample in the LP state gradually increases. When lowering the temperature from 450 K to RT, the LP state is retained in vacuum, whereas in air, close to RT, part of the sample returns to the NP state, most probably by uptake of water from air.

The XRD data additionally revealed that between 320 and 350 K, MIL-53(Al) transforms into a metastable intermediate NP state before reaching the LP state. From the TGA results it was concluded that the V-doped MIL-53(Al) framework dehydrates and the intermediate NP state was assigned as the dehydrated NP (NP-d) state. The transition between hydrated NP (NP-h) and NP-d is not abrupt,

H_2O is gradually released from the framework, with a gradual change in lattice parameters. The NP-d state is characterized by a smaller unit cell volume than the NP-h state. Additionally, broadening of the EPR spectrum of the LP state was observed while cooling the sample down to RT in air. This effect is discussed in Chapter 8 (see below).

Further *in situ* XRD experiments were carried out in order to determine the exact conditions for bringing MIL-53(Al) in a particular state. It appeared that the NP-h state can be obtained simply by leaving the material in contact with ambient air at RT where water from the air enters the framework and occupies the pores. The LP state can be obtained by heating the sample above 400 K in vacuum or in air. For the NP-d state, three additional XRD experiments were done. An *in situ* heating XRD experiment from RT up to 350 K and back to RT on MIL-53(Al) showed a reversible phase transition, from NP-h to NP-d and back to the NP-h state. Thus a first way to obtain the NP-d state goes by heating the sample to about 350 K. With this approach care has to be taken since the framework opens to the LP state soon after the NP-d state is obtained. Another approach of dehydrating the NP-h MIL-53(Al) framework is by pumping at RT. Using this procedure the LP state was not observed. A third *in situ* XRD experiment demonstrated that the framework can also be (partly) dehydrated by desiccation, pointing to the fact that water is only loosely bound to the structure. Monitoring the desiccation process with *in situ* attenuated total reflection (ATR) IR spectroscopy, made indeed clear that the dehydration is not necessarily complete.

Knowing how to separate these three states of activated V-doped MIL-53(Al), in Chapter 7 the individual EPR spectra were recorded (Figure 2) and the spin-*Hamiltonian* analysis of the spectra of these states was carried out. Similar as for the AS state, in all activated MIL-53(Al) states the g and $A(^{51}V)$ tensors are tilted with respect to each other. For the 'empty' pore structures, LP and NP-d, the EPR spectra are dominated by only one V^{IV} related component. The situation is different for the NP-h state where the presence of H_2O in the framework pores produces (at least two) different environments for the V^{IV}=O paramagnetic centres, similar as in the AS state with BDC molecules in the pores. The spin-*Hamiltonian* parameters of the LP and AS states are strikingly very close which can be explained by a similar wide pore crystal structure.

In the same Chapter 7 the oxidation state of V in MIL-47(V) and MIL-53(Al) in the AS and activated states was investigated by XANES and EPR measurements. $V^{III}Cl_3$ is used as a dopant salt in the synthesis of both MOFs. In AS MIL-47(V) and MIL-53(Al) the majority of the V ions is in the +III oxidation state. After calcination the V^{III} ions are oxidized to V^{IV}. It was shown that activation by both solvent extraction and calcination increases the V^{IV} fraction, but calcination makes the transition complete. It is worth noting that EPR and XANES give complementary results, EPR being the more available and less expensive technique.

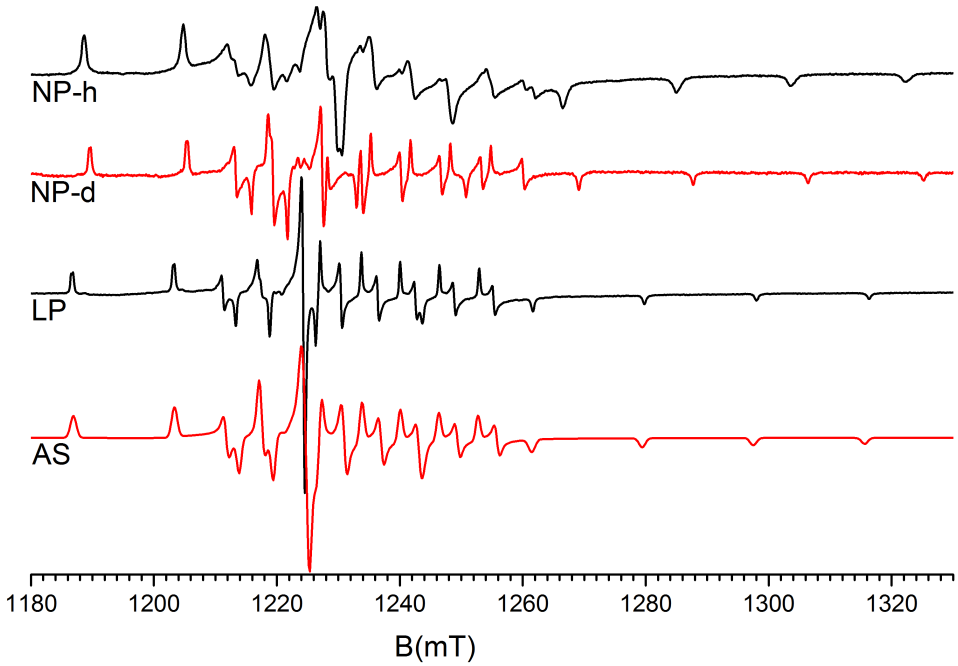

Figure 2: EPR spectra of V^{IV}=O in four MIL-53(Al) states: NP-h, NP-d, LP and AS.

As already mentioned above, the EPR spectrum of activated V-doped MIL-53(Al) in the LP state is found to be sensitive to oxygen. Exchange interaction between the paramagnetic V^{IV}=O centres and O_2 molecules causes broadening of the LP EPR spectrum. This is not the case for the NP-h nor for the NP-d spectrum. This points to the fact that only in the LP state, O_2 can come close enough to the paramagnetic V^{IV}=O to produce a measurable broadening. The EPR linewidth as a function of O_2 pressure shows a close-to-linear dependence with a sensitivity of a couple of mbar. This opens perspectives for applications in oxygen sensing (Chapter 8).

The knowledge obtained from the MIL-47(V) and V-doped MIL-53(Al) structures was further used in the study of the V-doped DUT-5(Al) and COMOC-2(V) frameworks. The EPR spectrum of fully concentrated COMOC-2(V) is similar to that of MIL-47(V), i.e., only a broad line with no HF structure is observed. In the mixed-metal samples the signal intensity of the broad line decreases and the HF structure gradually becomes resolved with increasing Al concentration. A narrow-line component very much resembles the EPR spectrum of V-doped MIL-53(Al) in the LP state. The latter component strongly broadens in contact with paramagnetic O_2 which is a comparable situation as in V-doped MIL-53(Al). Next to the broad signal and the 'MIL-53-like' signal at least one more component is present in these mixed-metal samples. This component is not sensitive to O_2

and even though it shows some resemblance with the EPR spectrum of $VOSO_4$ (dopant salt used in the synthesis) impregnated DUT-5(Al), the origin of this component remains unclear.

In Chapter 9 V-doped MIL-53(Al) was tested as catalyst in a liquid phase oxidation of cyclohexene. It showed surprisingly low catalytic activity when compared to fully doped MIL-47(V). The results obtained during this thesis can shed some light on this observation. V-doped MIL-53(Al) in liquid is expected to contract to the NP state which is not accessible to guest molecules. Under this assumption only V ions on the boundaries can be involved in catalysis. From the O_2 sensitivity experiments, one may even suspect that the concentration of V ions is lower than geometrically expected. This could be explained by the occurrence of an 'egg-yolk' structure, reported for MIL-53(V/Cr) within the framework of the same FWO project (thesis of Hannes Depauw), where V would preferentially incorporate into the MIL-53(V/Al) core and where the Al ions would be mainly present in the outer shell.

As a conclusion, the work presented in this thesis demonstrates that EPR and ENDOR spectroscopy are particularly useful techniques in the study of MOFs, complementary to XRD. By mapping the direct environment of the paramagnetic species with ENDOR, the successful incorporation of the V dopant ions on the Al-sites of the MIL-53(Al) structure was proved. The breathing effect of V-doped MIL-53(Al) was monitored in detail with *in situ* EPR and XRD. The EPR spectra of V^{IV}=O in four states of MIL-53(Al), i.e. AS, NP-h, NP-d and LP state, are clearly distinct and were carefully analysed leading to interesting electronic and geometric information contained in the g and A tensors. Particularly interesting, also for future computational work, is the finding that global structure changes could be monitored by local changes of the vanadyl ion environment. EPR spectroscopy also appeared powerful to determine and monitor the oxidation state of incorporated V dopant ions at lower cost than XANES. The oxygen sensitive LP spectrum of V-doped MIL-53(Al) offers perspectives in oxygen and gas sensing in general. The new insights gathered in this thesis on a selection of MOFs can be expected to be very useful in future MOF studies as was demonstrated for the bimetallic COMOC-2(V)-DUT-5 series. The knowledge about the different states of the MOF structure, as derived from the variations in the vanadyl spectra, also helped to understand the low catalytic activity of V-doped MIL-53(Al) (non-accessible NP state in liquid environment and 'egg-yolk' structure similar to one reported for MIL-53(V/Cr)).

List of abbreviations

AS	As-synthesized
ATR	Attenuated total reflection
BDC	Terephthalate or 1,4-benzenedicarboxylate
BET	Brunauer-Emmett-Teller theory
BPDC	4,4-biphenyl dicarboxylate
BPEE	1,2-bipyridylethene
BPY	Bipyridine
BTC	Benzene-1,3,5-tricarboxylic acid
BTE	4,4,4-[benzene-1,3,5-triyl-tris(ethyne-2,1-diyl)]tribenzoate
COMOC	Centre for ordered materials, organometallics and catalysis
CP	Closed pore
CW	Continuous wave
DMF	Dimethylformamide
DHBDC	2,5-dihydroxy-1,4-benzenedicarboxylate
DOBDC	2,5-dioxido-1,4-benzenedicarboxylate
DPE	1,2-bis(4-pyridyl)ethane
DPPH	2,2-diphenyl-1-picrylhydrazyl
DUT	Dresden University of Technology
EMR	Electron magnetic resonance
ENDOR	Electron nuclear double resonance
EPR	Electron paramagnetic resonance
F-AAS	Flame atomic absorption spectroscopy
FTIR	Fourier transform infrared spectroscopy
HF	Hyperfine
HKUST	Hong Kong University of Science and Technology
IR	Infrared spectroscopy
IRMOF	Isoreticular MOF
LP	Large pore
MIL	Materials of the Institute Lavoisier
MOF	Metal-organic framework

NDC	2,6-naphthalene dicarboxylate
NMR	Nuclear magnetic resonance
NP-d	Dehydrated narrow pore
NP-h	Hydrated narrow pore
RF	Radio frequency
RT	Room temperature
T	Temperature
TEMPO	2,2,6,6-tetramethyl-1-piperidinyloxyl
TGA	Thermogravimetric analysis
VNP	Very narrow pore
XANES	X-ray absorption near edge structure
XRD	X-ray diffraction
ZFS	Zero field splitting

Part I

Background: theory and materials

1

Introduction

The work presented in this thesis is part of a joint project of the Electron Magnetic Resonance (EMR) and Centre for Ordered Materials, Organometallics and Catalysis (COMOC) research teams of Ghent University. The main objective of this project was *in situ* observation of coordinative and structural transformations in paramagnetically doped metal-organic frameworks (MOFs) with electron paramagnetic resonance as main technique. This project was set up to gain further insight in the structural flexibility and catalytic activity of such materials. MOFs are crystalline porous materials constructed of metal centres connected by organic linkers. An important characteristic of these materials is the possibility of tuning the structure by combining different metal nodes with particular linkers. In this way desired physical and chemical properties can be obtained, like well-defined structure, pore size or shape of the channels. Another intriguing feature of certain MOFs is their particular high structural flexibility called breathing. The framework can reversibly change from an open large pore (LP) to a closed narrow pore (NP) state in the presence of external stimuli like temperature and/or pressure sometimes resulting in a dramatic change of the pore size. This effect is correlated with the gas sorption capacity of the material. Due to the large variety of resulting structures, MOFs have potential application in diverse fields from gas adsorption and separation,[1,2] storage,[3,4] catalysis,[5–8] sensing[9,10] and drug delivery.[11] The framework porosity in combination with the possibility that guest molecules reach catalytically active centres in the framework form an ideal basis for catalysis. Generally, heterogeneous catalysis involves adsorption of reactants on the active sites, surface reaction and desorption, including regeneration of the active sites. For redox catalysis this is accompanied by an oxidation or reduction of the metal centre. There is only a limited number of reports on the fundamental mechanisms of these processes on MOFs.

This part of the project has focussed on the study of electronic and structural

changes occurring in MOFs using electron paramagnetic resonance (EPR) techniques as primary spectroscopic tools. As will be explained in more detail in Chapter 3, EPR can provide information on the valence state, the coordination geometry and further environment of the metal ion EPR probe in MOFs. Since the number of MOFs reported so far is quite large, the study was restricted to the selection of V^{IV}=O and isostructural Al^{III}-OH MOFs, shown in Figure 1.1, and their combinations. The chosen subset of MOFs is particularly well suited for studying the conditions for breathing, as for three out of the six pure structures in the scheme (MIL-53, COMOC-1, COMOC-2) flexibility has been reported, which is not the case for the other three. Interestingly, this phenomenon can neither be solely attributed to the vanadium ion (the EPR probe with an $Ar(3d)^1$ electron configuration), nor solely to the linker. It can be speculated that the interplay between these building blocks determines the flexibility of the MOF. Long-range interactions may play an important role in the flexibility too.

The EPR spectra of the $(V^{IV}=O)^{2+}$, the vanadyl ion, can be detected in a wide temperature range, but in fully concentrated MOFs, they show limited resolution. Hence, the breathing behaviour of V^{IV}=O substituted Al^{III}-OH MIL-53 were studied over a wide concentration range in order to observe (abrupt or gradual) changes in the conditions for breathing. MIL-53 is among the most studied MOFs so far with numerous of articles reporting different properties and practical applications of this material by using different techniques. The results from this variety of reports are scattered and difficult to connect. An additional complication arises from the fact that the flexibility of MIL-53 strongly depends on the MOF's pretreatment. Its crystal structure is strongly influenced by the temperature, pressure or guest molecules. In this respect, comparing reported results in a wide range of experimental conditions without raw experimental spectra is nearly impossible. Furthermore, reported results are often conflicting. For this reason, the major part of the work in this thesis was focussed on V-doped MIL-53(Al) and its counterpart MIL-47(V), i.e. the first row of Figure 1.1. The investigation of these materials resulted in a systematic overview of different properties focusing mainly on breathing. It proved itself to be a fruitful field where EPR combined with (synchrotron) *in situ* X-ray diffraction (XRD), Fourier transform infrared spectroscopy (FTIR) and Thermogravimetric analysis (TGA) gave complementary new insight into the breathing of MIL-53(Al).

The development of mixed-metal MOFs like the Al/V ones mentioned above is a relatively new experimental field with good perspectives for further improvement of MOF properties towards desired applications. Even though three rows (Figure 1.1) were originally set out the be studied, only two (top and bottom) were covered.

The first part of this thesis is based on theoretical concepts necessary for understanding the experimental part. In Chapter 2 the reader can find the definition

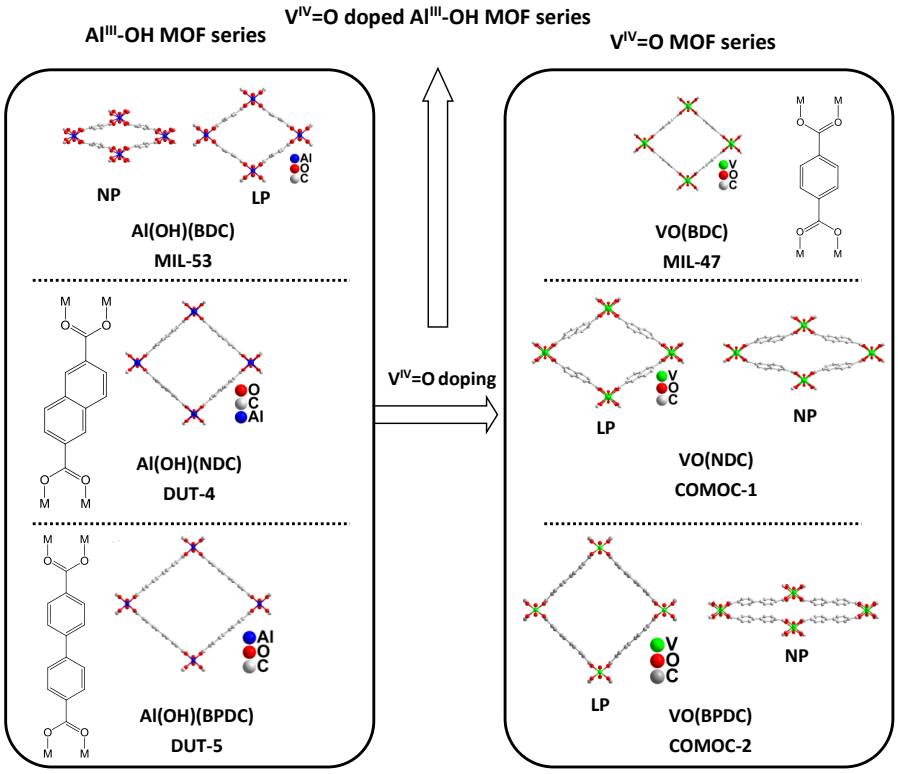

Figure 1.1: Structures of MOFs included in the project. The left column shows structures of Al^{III}-OH MOFs while the right column shows the corresponding V^{IV}=O MOFs. Top row, left, MIL-53(Al) structures in narrow pore (NP) and large pore (LP) state. Right: MIL-47(V). Middle row: structures of DUT-4 and COMOC-1. Bottom row: structures of DUT-5 and COMOC-2. COMOC-1 and 2 also exhibit breathing. For all structures, the linkers are shown.

of MOF structures with a short explanation of the different features of a selection of the most cited MOFs : ZIF-8, MIL-101, MOF-5, MIL-53, UiO-66 and HKUST-1. Furthermore, an overview of the most intriguing applications is given: catalysis, sensing, drug storage and delivery.

In Chapter 3 a description of the primary techniques used in this thesis, EPR and electron nuclear double resonance (ENDOR), is given. At the end of this chapter the available EPR results on MIL-47(V), COMOC-3 and MIL-53 can be found with a small contribution of multi-frequency EPR results of MIL-47(V) obtained during this project.

XRD was also extensively used in this thesis. Chapter 4 provides a basic explanation of the technique itself with an additional explanation of the Diamond Light Source synchrotron facility.

In the second part of this thesis the main experimental results are presented. MIL-47(V) is already known as a highly selective catalyst in the oxidation of cyclohexene. One drawback of this material is poor stability in contact with water. A solution for this problem may be doping the highly stable MIL-53(Al) structure with catalytically active V^{IV}. In order to understand the properties of such a doped framework, it is necessary to verify the actual position of the dopant in the framework. The pores of the as-synthesised (AS) MIL-53(Al) are blocked with uncoordinated linker molecules. EPR and ENDOR spectroscopy allowed to determine the local coordination environment and the site symmetry of the V^{IV} dopant ions in this AS structure. These results are presented in Chapter 5.

Molecules trapped in the pores of MIL-53(Al) AS structure can be removed by calcination or solvent extraction, which is referred to as activation of the MOF. Activated MIL-53(Al) exhibits a structural flexibility. The breathing of activated V-doped MIL-53(Al) was monitored with *in situ* EPR and XRD and these results are discussed in Chapter 6.

In Chapter 7 the conditions for isolating a particular state of the MIL-53(Al) framework have been investigated. A detailed EPR spectrum analysis for V^{IV} in the different states is also given.

In Chapter 8 sensing the guest molecules in the MIL-53(Al) framework was done using the EPR spectrum of V^{IV} dopant ions. The obtained knowledge about the V-doped MIL-53(Al) structure provided the starting point for exploring samples from the third row of Figure 1.1, DUT-5 and COMOC-2. EPR analysis on V-doped DUT-5 showed some similarities with V-doped MIL-53(Al). DUT-5(Al)-COMOC-2(V) mixed-metal MOF structures were explored in-depth by synchrotron XRD under high CO_2 pressure (up to 17.5 bars) in the framework of the PhD thesis of Hannes Depauw.

MIL-47(V) and V-doped MIL-53(Al) were tested as catalysts in the oxidation of cyclohexene. These results together with possible implications for catalysis are discussed in Chapter 9.

My main tasks were spectroscopic characterisation, where possible *in situ*, of these materials with main focus on EPR based techniques and XRD. Part of the work in this thesis has been performed in collaboration with several other researchers and laboratories:

- The samples were synthesized and provided by Hannes Depauw from COMOC, our partner in the aforementioned FWO-project.
- The S-band and J-band EPR spectra were respectively recorded at ETH Zürich by Vidmantas Kalendra and at the Huygens Laboratory of Leiden University by Peter Gast.

- The Lebail refinements of the synchrotron XRD results were done by Claire A. Murray from the Diamond Light Source synchrotron facility.
- The XANES analysis was done by Pieter Tack from Ghent University.
- The dehydration of MIL-53(Al) was studied by Alexander Hoffman using FTIR in the framework of his master thesis 'Experimental and computational vibrational spectroscopy of metal-organic frameworks' at Ghent University.
- Catalytic tests using MIL-47(V) and V-doped MIL-53(Al) were performed by Hannes Depauw.

2

Metal-Organic Frameworks

2.1 Introduction

In 1995, the research group of Omar M. Yaghi introduced the term 'metal-organic frameworks' in a publication on a Cu(BPY)(BPY=Bipyridine) framework containing large rectangular channels.[12] An other influential paper on the design and synthesis of the MOF-5, ($Zn_4O(BDC)_3$, BDC= terephthalate or 1,4-benzenedicarboxylate), framework followed in Nature in 1999 by the same research group.[13] MOF-5 was the first structure reported with permanent porosity, which did not collapse in the absence of guest molecules.[14,15] MOF-5 was considered a 'break-through' material due to its higher surface area and pore volume compared to most porous crystalline zeolites.

MOFs known also as porous coordination networks or porous coordination polymers are materials that represent a new stage of development for porous materials. These materials have attracted much interest among scientists since their first synthesis.[16,17] The interest in MOFs has arisen from their numerous possible applications ranging from the more conventional applications of porous materials, including gas storage and separation, to the potential use in sensing, catalysis, drug storage and delivery. The MOF networks are self-assembled (usually in solution) by coordination of suitable metal cations (or clusters) with organic ligands. Organic linkers act like electron donors resulting in a neutral skeleton. The MOF connectivity is driven by the coordination chemistry between the metal centre and the functional group of the organic linker. Characteristics of these self-assembling modular compounds, e.g. pore size, internal surface area or thermal stability can be modified within a wide range by employing different metal ions and/or organic linkers. By connecting them it becomes possible to tune the structure to well-defined properties. Certain MOF structures feature a very high specific surface area (up to 6000 m^2/g) and porosity (up to 90% volume),

combined with a well-defined pore size, volume and shape.[18] Depending on their size, pores can be divided in three categories: macropores (with diameters above 50 nm), mesopores (in the range 2-50 nm) and micropores (smaller than 2 nm).[19] MOFs typically cover the micro and mesopore ranges.

Which advantages do MOFs offer over other classes of porous materials, and in particular over zeolites? For the synthesis of zeolite structures (beside the components of the resulting compound and the solvent) it is mandatory to use an inorganic or organic template. It often happens that the framework (mostly cationic) collapses during the extraction of this template because of the strong host-guest interaction. In the synthesis of MOFs, the solvent acts as template and the interaction between the framework and solvent is weaker compared to zeolites. After the extraction of the solvent, the framework becomes intact with accessible porosity. Additionally, the presence of both organic and inorganic species in the same structure opens up the possibilities for different properties. For example, hydrophilic and hydrophobic parts of the framework can have different characteristics during adsorption. Another significant advantage of MOFs is the large variety of metal centres that can be incorporated, while zeolites are mostly obtained with only a few cations (Si and Al) without any organic moiety.[20] Apart from metal centres a range of linkers can also be used, in particular functionalised organic linkers. In comparison with the rigid zeolite frameworks or active carbon (carbon derived from charcoal and processed to microporous material), MOFs offer more flexible rational design, through control of the architecture and functionalisation of the pores due to the presence of both organic and inorganic moieties. In this way a broader range of potential applications and better performance can be achieved. This is especially interesting for industry where adsorptive separation and catalytic activities are very important and where the need for more efficient, selective and stable materials is omnipresent.[16]

2.2 MOFs

To date more then 10 000 articles have been published reporting on various types of MOFs, their properties or application possibilities. MOFs are usually labelled as 'MOF' or by an abbreviation of the institute where they have been developed followed by a number. MIL-53,[21] e.g., has been developed at the Institute Lavoisier (MIL = Materials of the Institute Lavoisier) or HKUST-1[22] was first synthesized at Hong Kong University of Science and Technology. The most attractive applications of MOFs are in gas adsorption, separation, storage and catalysis. There is a rapid increase of interest in MOFs in recent years due to their excellent properties and various potential applications which will be briefly discussed in the following sections.

MOF-5, reported as first stable MOF by Omar M. Yaghi with permanent porosity, is also known as IRMOF-1 (IRMOF stands for isoreticular MOF). The structure of MOF-5 is shown in Figure 2.1A. The IRMOF series is based on MOF-5 having the same framework topology and metal nodes but different organic linkers, resulting in different pore sizes. Figure 2.1A,B and C compares three IRMOFs structures. The pore sizes increase as the linkers get longer. In MOF-5 the core of the cluster consists of a single O atom bonded to four Zn atoms, forming a regular Zn_4O tetrahedron. The nodes are then connected by BDC linkers resulting in a MOF with chemical formulation $Zn_4O(BDC)_3$. Due to its high internal surface area it is mainly used for gas adsorption, gas storage, and catalysis.[23,24]

ZIFs, Zeolitic Imidazolate Frameworks, are a class of MOFs that are topologically isomorphic with zeolites and simultaneously possess the characteristics of both MOFs and zeolites. ZIF-8,[27] shown in Figure 2.1D, is made by Zn(II) ions coordinated by four imidazolate rings in the same way as Si and Al atoms are covalently joined by bridging oxygens in zeolites. ZIF-8 exhibits permanent porosity and exceptional thermal, chemical and mechanical stabilities, probably due to the strong interactions between the metal centres and the imidazolates. The effective pore size in ZIF-8 is proven to be a strong function of guest molecules. Shortly after the synthesis of powder ZIFs it is recognised that the formation of ZIF films or membranes are very useful in many applications. Membranes combine ZIFs intrinsic properties especially the molecule-sized porosity and easy handling. The ZIF-8 membrane has the advantage in gas separation, in particular H_2 from other large gas molecules.[28] The adsorption of methanol, ethanol, 1-propanol, 2-propanol, and 1-butanol from water vapour revealed that ZIF-8 has the potential for biofuel recovery. It has been reported as efficient heterogeneous catalysts in numerous reactions as reviewed by Chen *et al*.[28] ZIF-8 is also used as chemical sensor and for drug delivery.[29–32]

HKUST-1, $Cu_3(BTC)_2$(BTC=Benzene-1,3,5-tricarboxylic acid), is also known as MOF-199 or Cu-BTC. It has interconnected $Cu_2(O_2CR)_4$ units (where R is an aromatic ring), which create a three-dimensional (3D) system of large square-shaped pores and an accessible porosity of about 40% of the volume in the solid (see Figure 2.1E). It is reported to be capable of adsorbing significant amounts of hydrogen. Therefore it can be considered as an effective hydrogen storage material.[33–35] It has also been reported to be a good heterogeneous solid catalyst.[36,37] HKUST-1 is commercialised under the name Basolite® C300.

Another important MOF, MIL-101, has been reported with Cr^{III}, Fe^{III}, Al^{III} and V^{III} metal ions.[38–41] MIL-101(Cr), $Cr_3(O)(OH)(BDC)_3$, is a 3D porous material constructed of Cr(III) trimeric inorganic building blocks crosslinked by BDC. It has two types of pores with diameters of 29 and 34 Å, which have pore apertures of 12 and 16 Å, respectively, as shown in Figure 2.1 G. It is reported to be a highly efficient catalyst.[26,42–45] MIL-101(V) exhibits the highest specific surface

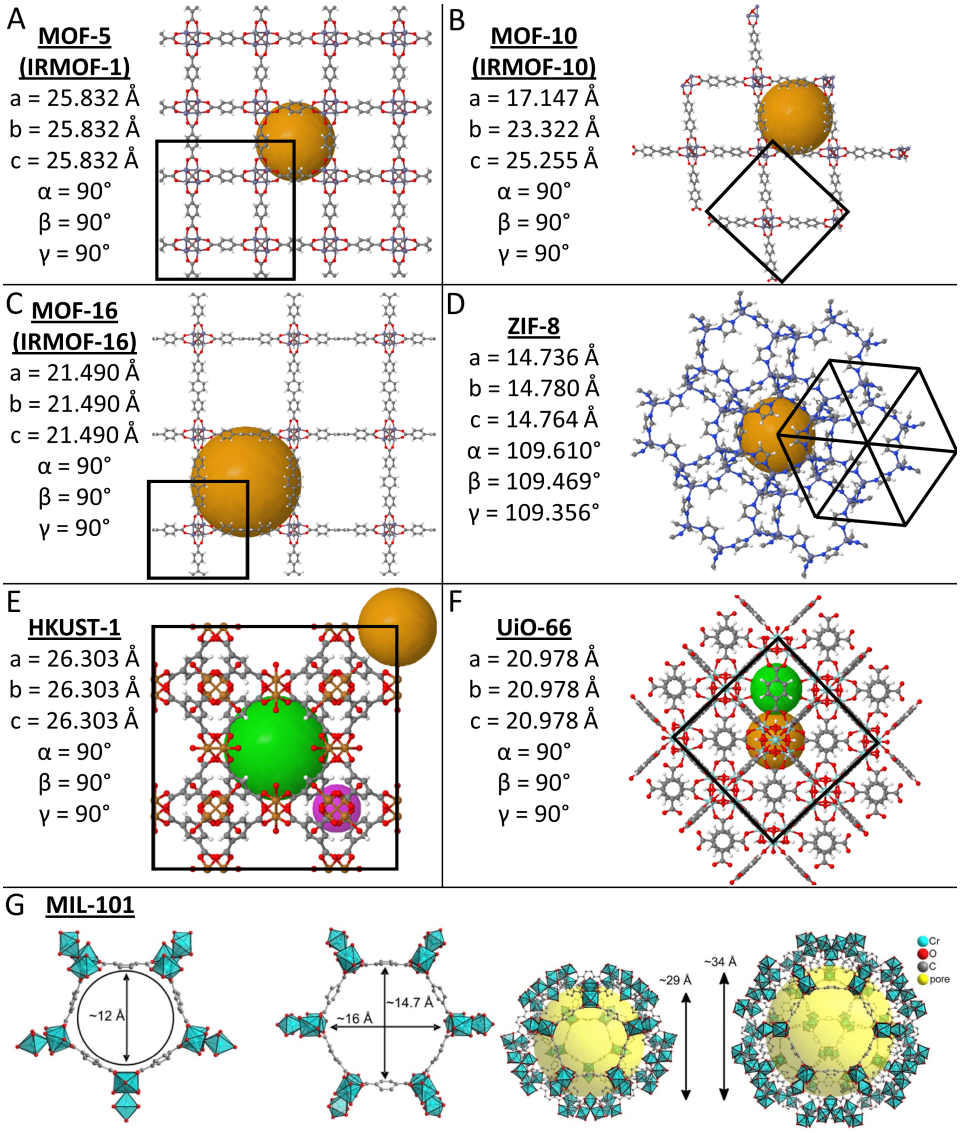

Figure 2.1: A: IRMOF-1 (also known as MOF-5) with BDC linker. B: IRMOF-10 (also known as MOF-10) with BPDC (BPDC=4,4-biphenyl dicarboxylate) linker. C: IRMOF-16 (also known as MOF-16) with p-terphenyl-4,4′-dicarboxylate linker. D: ZIF-8 structure. E: HKUST-1 structure. F: UiO-66 structure. The spheres represent the pore size that can be used for gas storage. Unit cells are represented together with lattice parameters.[25] G: MIL-101(Cr) structure. Cr_3O building blocks and bridging BDC form pentagonal and hexagonal rings which are assembled into mesopores. The yellow spheres in the mesopores take into account the Van der Waals radii of the framework walls.[26]

area among the vanadium MOFs synthesized to date.

UiO-66 developed at the University of Oslo[46] (Figure 2.1F) is constructed of

$Zr_6O_4(OH)_4$ octahedra that are 12-coordinated to adjacent octahedra through a BDC linkers. Zr-MOFs, including UiO-66, are known for their outstanding stability when compared to most of the other known MOF. They are thermally stable up to 725 K, do not suffer any significant damage in contact with many organic solvents and acidic aqueous solutions and under high pressure their crystal structure is retained. Two types of defects can be present in Zr-MOFs: missing linkers and missing clusters. Their crystal structure can contain unusually large amounts of defects while preserving remarkable stability. Defects offer the possibility for further improvements of already great features for practical applications. These applications include gas sorption/separation, heterogeneous catalysis, drug delivery and sensing.[47]

2.3 Breathing

Apart from the features mentioned in the previous section, some types of MOFs also exhibit breathing. This is a reversible phenomenon where expanding and shrinking frameworks act like sponges keeping the same topology.[48] This flexibility is characterised by a transformation between two or more states upon exposing the framework to external physical or chemical stimuli. This results in a structural change of the complete framework. Drastic volume changes may follow from strong host-guest interactions. This phenomenon was predicted by Kitagawa and Kondo 1998.[49] The prediction was illustrated by the observation of gate opening or breathing behaviour in two-dimensional (2D) layered frameworks. Shortly after this publication, a zirconium phosphate MOF was reported, where during the dehydration process a reversible shrinkage of the structure was observed.[50]

Detailed information on the breathing phenomenon has been obtained by monitoring the physical and chemical properties of MOFs with a variety of analytical techniques. *In situ* XRD has played a central role in many of the studies. X-ray thermodiffractometry and CO_2 sorption measurements were, e.g., used to study thermal behaviour and host-guest and guest-guest interactions under exposure to a variety of liquid or gas phase compounds. XRD presents a straightforward way of detecting phase transitions since it provides direct insight in the crystal structure. Neutron powder diffraction provides complementary information but at a higher cost, which makes it a less widely available technique. TGA is mostly used for determining the thermal stability of the framework but also to detect dehydration of the framework. Dehydration in some frameworks can trigger a phase transition. Still, TGA does not provide additional information about the structure therefore it is usually used in combination with other techniques. EPR can also provide detailed information on molecular structure but has so far not

been extensively used in the study of MOFs. This will be explained in further detail in Chapter 3.

2.3.1 MIL-53

In 2002, MIL-53(Cr) was the first of a series of flexible MIL-53(M) MOFs (M(OH)(BDC)) (M=Cr,[51] Al,[21] Ga,[52] Sc,[53] Fe[54]), all synthesised by Férey's group. Among the flexible MOFs, MIL-53 is one of the most widely studied and best known material because of the pronounced changes in its structure when exposed to changes in temperature or gas pressure.[55] The MIL-53(M) framework is constructed from chains of trans-corner-sharing $MO_4(OH)_2$ octahedra, in the other two dimensions connected with BDC. They form a 3D ordered network. After synthesis, the MIL-53(M) as-synthesized (AS) framework is not flexible due to the blocking of the pores by disordered, uncoordinated terephthalic acid molecules and residual solvent or water molecules. These can be removed by heating, also known as calcination, or by solvent extraction methods,[56] which are referred to as activation of the MOF. For several (M), among which (Al), activated MIL-53 exhibits strong breathing. The activated structure can reversibly change between a monoclinic hydrated narrow pore state (NP-h) and an orthorhombic large pore (LP) state as a result of heating or large uptake of certain gases, in particular CO_2.[57] NP-h is characterised by contracted pores due to water uptake in ambient conditions. The MIL-53(Cr) and (Ga) variants were reported to behave similarly with a distinct transition from a NP-h state to a LP state, with slightly different temperature required for this transition. For the MIL-53(Cr), (Al) and (Ga) lattices, completely or partially dehydrated NP (NP-d) states have been reported in literature.[58–60] By Liu *et al.*, in water-free conditions, the transition between the NP-d and LP states in MIL-53 can be induced by temperature without the aid of gas molecules. For this reason the NP state is also often referred to as the low-temperature (LT or lt) state and LP as high-temperature (HT or ht) state. The transition between these states was reported to exhibit a very large temperature hysteresis. The transition from the LP to NP-d state occurs at approx. 125-150 K while the transition from NP-d to LP state occurs around 325-375 K.[59]

A concise overview of the various (de)hydrated NP and LP states for MIL-53(M) lattices available in literature and obtained by heating and/or evacuating, starting from ambient conditions is given in Figure 2.2. For the MIL-53(Sc) and (Fe) variants different behaviour is reported from that of the other three. MIL-53(Sc) after synthesis and solvent removal is present in NP-d state. By hydration at room temperature (RT) an intermediate (INT) state is observed with two types of pores. The INT state is characterised by part of the framework being still in NP-d state while part of the framework is in the NP-h state. Complete NP-h was not reported. By heating NP-d state up to 625 K as opposed to MIL-53(Cr, Al, Ga), which

open their pores, MIL-53(Sc) contracts even more to a very-narrow pore (VNP) state. The situation is similar in MIL-53(Fe), however after synthesis and solvent removal, the framework is reported to be in NP-h state. By heating up to 325 K the INT state is observed and with further heating the VNP state is obtained. The term 'closed pore (CP) state' is used in literature, when referring to a contracted empty pore structure, not accessible to any guest molecule. Part of the work in this thesis is devoted to the elucidation of different states in MIL-53(Al). The structure was doped with ≈1% V to allow EPR investigation. More information is given in Chapter 7.

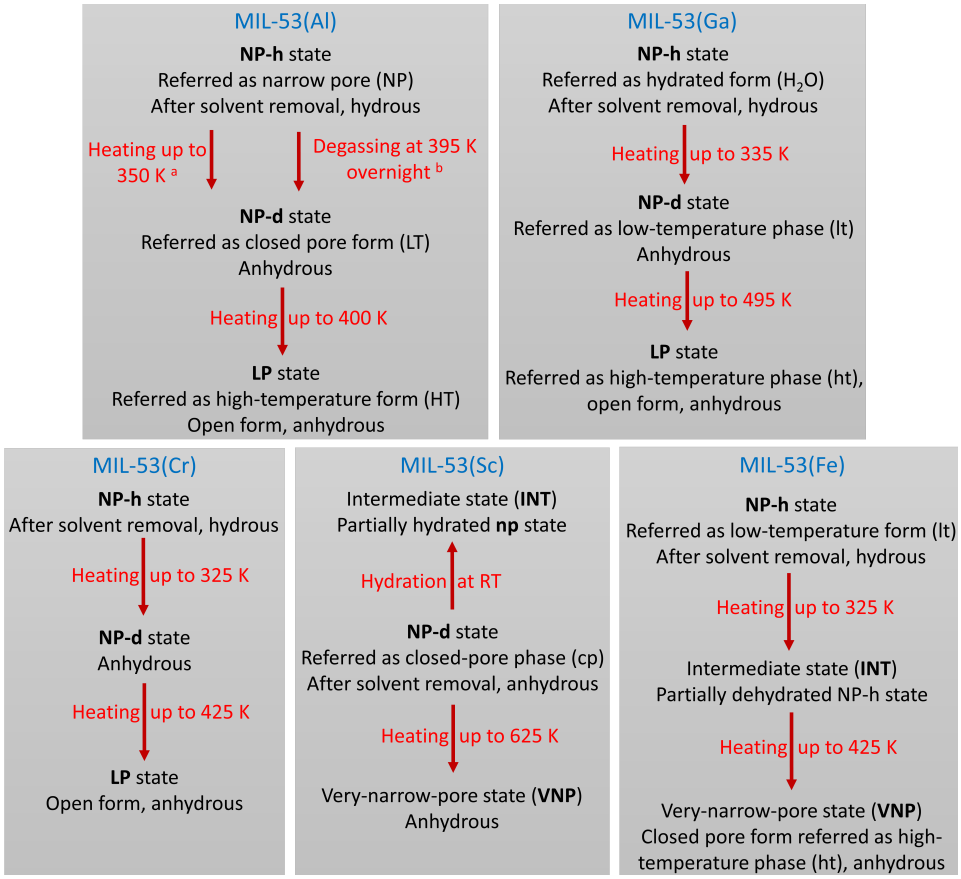

Figure 2.2: Overview of the various (de)hydrated NP and LP states for MIL-53(Cr),[51,58] MIL-53(Al) a[60] and b,[59] MIL-53(Ga),[52] MIL-53(Sc)[53] and MIL-53(Fe)[54] lattices obtained by heating and/or evacuating, starting from ambient conditions.

In MIL-53(Al), first-principles calculations by Coudert *et al.* predict that at RT, in vacuum, the LP state is most stable.[61] However, under ambient air conditions, uptake of H_2O leads to pore contraction. For this reason, very often the NP-h state (or a mixture of NP-h and LP states) is found back at RT when storing MIL-53(Al)

at ambient conditions. When heating MIL-53(Al) above 375 K water is released from the structure and the LP state is obtained.[21,51] The presently known crystal structure lattice parameters for the AS, NP-h, NP-d and LP states of MIL-53(Al) are summarised in Table 2.1. We adopt the parameters reported by Loiseau *et al.*[21] and Liu *et al.*[59]

Table 2.1: Reported lattice parameters of MIL-53(Al) in the AS, NP-h, NP-d and LP states. Bottom: MIL-53 (Al^{III}-OH(BDC)) structure in the AS (left), NP (middle) and LP (right) states. Blue: aluminium, red: oxygen, grey: carbon. In the AS structure the light grey spheres represent linker residue from the synthesis.

AS[21]	**NP-h**[21]	**NP-d**[59]	**LP**[21]
Orthorhombic *Pnam*	Monoclinic *Cc*	Monoclinic *C*2/*c*	Orthorhombic *Imcm*
a = 17.129 Å	a = 19.513 Å	a = 20.756 Å	a = 16.675 Å
b = 12.182 Å	b = 7.612 Å	b = 7.055 Å	b = 12.813 Å
c = 6.628 Å	c = 6.576 Å	c = 6.6087 Å	c = 6.608 Å
$\beta = 90°$	$\beta = 104.24°$	$\beta = 113.58°$	$\beta = 90°$
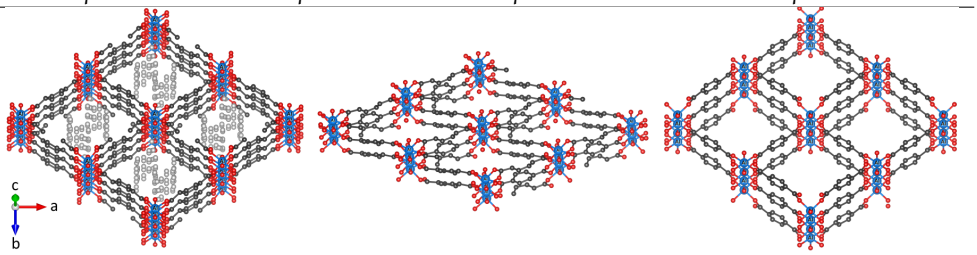			

In Table 2.1 the space groups and lattice parameters have been converted[62] in such a way that for each structure *a* corresponds to the longest lattice parameter and *c* to the shortest. This way, for all three structures the *c* axis lies along the Al-OH chains in the framework and indicates the direction of the channel-like pores. The Miller index labelling of the XRD peaks in this work follows this definition.

2.3.2 MIL-88

Another significantly breathing MOF is MIL-88.[63,64] It is built up from the connection of trimers of Fe(III) or Cr(III) octahedra that share oxygen with dicarboxylate in such a way that results in two types of cavities. Both tunnels and triangular cages can be seen in Figure 2.3. This feature induces very large flexibility which greatly depends on the linkers used. MIL-88A is reported with fumarate, MIL-88B with BDC, MIL-88C with NDC (NDC=2,6-naphthalene dicarboxylate) and MIL-88D with BPDC. The Cr version of MIL-88D has the largest variation in cell volume upon hydration/dehydration (up to 300% of the volume) so far, while preserving crystallinity of the structure.[65]

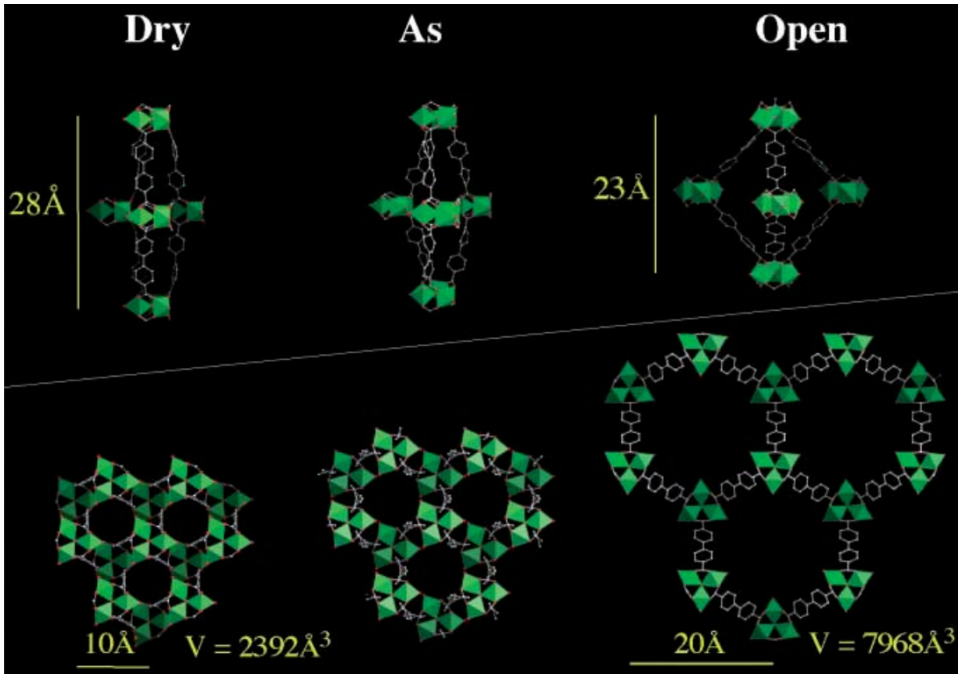

Figure 2.3: Structure of Cr MIL-88D in AS, LP (referred as 'open' state, after AS state accept solvent) and NP-d (after desolvation through heating provides the desolvated form, 'dry') states. The upper figure show differences in shape and dimension of the pores, metal clusters are represented in green. The lower figure part shows a (001) projection in different states.[65]

2.3.3 MIL-47

Another characteristic type of MOF with one-dimensional rhombically shaped porous channels, and also studied in detail in this project, is MIL-47. It was originally synthesized by Férey's group.[66] MIL-47 only exists in the vanadium form and was the first porous vanadium based MOF reported in the literature. It has a 3D framework built up of V^{IV} centres (or V^{III}, see below) coordinated to four oxygen atoms from four carboxyl groups, and two more on the O-V-O axis, thus forming a saturated octahedral coordination node. The nodes are connected by BDC linkers. This is shown in Figure 2.4. MIL-47(V) has a large surface area, it is stable up to 675 K and a catalytically active.

The synthesis involves VCl_3, a V^{III} salt. In AS form the structure has V^{III}-OH metal nodes. For activation these nodes need to transfer into V^{IV}=O. This is why MIL-47 is activated by calcination in air, rather than by the solvent extraction method, leading to the LP (sometimes called empty) pore state. No change in topology of the framework occurs during calcination. The empty pore form exhibits pores accessible for certain gases and particles. MIL-47(V^{IV}) exhibits

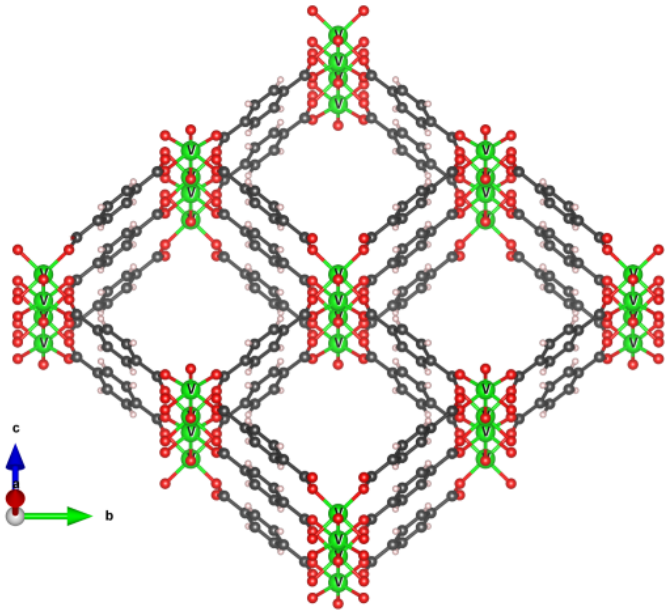

Figure 2.4: Activated MIL-47 (V^{IV}=O(BDC)) structure, green: vanadium, red: oxygen, grey: carbon, white: hydrogen.

a rigid structure. This has been attributed to the absence of hydroxyl groups. Interestingly, Leclerc *et al.*[67] reported an alternative activation procedure where vanadium stays in the V^{III} state even after activation. In that study MIL-47(V^{III}) proved to be a flexible structure where the hydroxyl groups act as preferential adsorption sites for H_2O or CO_2. They obtained a structure with mixed V^{III}/V^{IV} metal centres and demonstrated that V^{IV} is the main reason for the non-flexible character of MIL-47(V^{IV}). Further, it was reported that mechanical pressure can induce pore closure in MIL-47(V^{IV}). When a pressure of 340 MPa was applied to the MIL-47(V^{IV}) structure the unit cell contracted by 43%.[68] Available crystal structures lattice parameters for the MIL-47(V^{IV}), MIL-47(V^{III}) NP-h, MIL-47(V^{III}) LP states and MIL-47(V^{IV}) under pressure are summarized in Table 2.2.

Table 2.2: Lattice parameters of MIL-47(V) in various states.

MIL-47(V^{IV}) activated[67]	**MIL-47(V^{III}) NP-h**[67]	**MIL-47(V^{III}) LP**[67]	**MIL-47(V^{IV}) 340 MPa**[68]
a = 16.070 Å	a = 19.808 Å	a = 16.515 Å	a = 21.117 Å
b = 13.960 Å	b = 7.593 Å	b = 13.647 Å	b = 6.710 Å
c = 6.818 Å	c = 6.816 Å	c = 6.860 Å	c = 6.717 Å
β = 90°	β = 104.29°	β = 90°	β = 114.41°

As discussed above, the flexibility and mechanisms for breathing are intriguing

but still far from being completely understood. A complicating factor is that the flexibility of the frameworks strongly depends on the nature of the metal site, linker and external stimuli.

Besides the experimental observations of the breathing effect, in order to be able to apply or tune the MOF for certain requirements it is important to understand the physical aspects for this behaviour. Three parts of the structure could be involved or be influenced during structural transformations: the metal cluster, the linker or the junction between these two. When the metal cluster is in question, the number of possible bonds for the attachment of linkers or other molecules is important together with the nature and symmetry of the metal site. Free rotation and degrees of freedom within the linker are required to allow structural flexibility. This depends on the nature of the linker but also its functionalisation can play a role. Structural transformations can be influenced by introduction of guest molecules inside the framework where host-host, guest-guest or host-guest interactions will define the nature of the flexibility.[55]

2.4 Gas adsorption

Introduction

The classical use of microporous materials is for separation of gases or solutions, e.g. purification of O_2 and N_2, removal of toxic and hazardous compounds, separation of CO_2 from CH_4, H_2, etc. This is essential for a large number of industries and for a healthy environment in general. In 1997 Kondo *et al*. reported on their pioneer work in reversible adsorption of CH_4, N_2, and O_2 in the pressure range of 1-36 bar without deformation of the 2D crystal framework $M_2(BPY)_3(NO_3)_4$ (M = Co, Ni, Zn).[69]

Adsorption is the phenomenon of accumulating atoms or molecules at the surface of a liquid or solid material. The more surface available for adsorption, the greater the capacity for adsorbed gas. If the material is porous, it allows the gas molecules to access the large internal surface built up by the pores. Due to their high internal surface areas and large pore sizes, MOFs are particularly interesting for gas adsorption.

Adsorption of N_2

The internal surface area of a particular porous material is generally obtained from N_2 adsorption measurements at 77 K (temperature of liquid nitrogen). If a quantity q of a gas or vapour is adsorbed by a porous solid at constant

temperature and the steady state equilibrium relative pressure to atmospheric is p, then the function $q(p)$ is the adsorption isotherm. Isotherms can take one of six forms (types I to VI, by International Union of Pure and Applied Chemistry classification[70]) illustrated in Figure 2.5. Hereunder, only the isotherms that are relevant for this thesis are discussed in detail, i.e. types I, II and IV. More information can be found in publication by Thommes *et al*.[70]

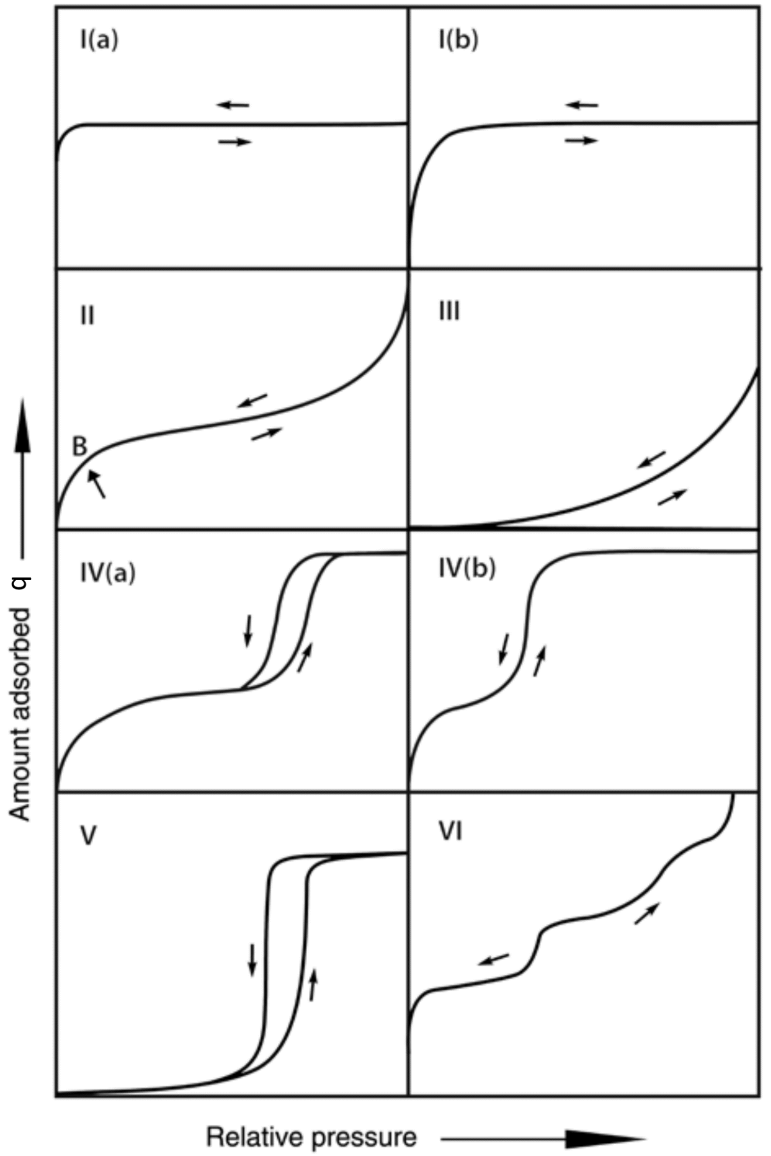

Figure 2.5: Classification of physisorption isotherms.[70]

Reversible type I isotherms are common for adsorption of gas on microporous

materials whose pore size is comparable with the diameter of the gas molecules. Complete filling of the framework pores then corresponds to the completion of a molecular monolayer. Interaction between gas molecules and framework is present while interaction between gas molecules itself does not occur. Type I(a) is characteristic for microporous materials with mostly narrow micropores. Type I(b) isotherms are found in materials having pore size distributions over a broader range including wider micropores and narrow mesopores.

A reversible type II isotherm does not exhibit saturation: after a monolayer is completed (B in Figure 2.5), adsorption occurs in successive layers. This can happen for materials with a wide distribution of pore sizes, macroporous and non-porous materials. Before reaching the plateau, interaction between gas molecules and framework is dominant. After the monolayer is formed and multilayers start forming, interactions between the gas molecules are determinant.

Reversible type IV isotherms are similar to type II isotherms at lower pressures. The formation of monolayer is followed by multilayer formation. By increasing the pressure further, after multilayer started forming, capillary condensation can occur. If the pores are big enough, gas in the pores liquefies and greater uptake is observed. This is due to smaller volume of liquid in comparison with the gas volume. The saturation pressure (P_S, first plateau) for monolayer formation is always below the saturation pressure of vapour/liquid (second plateau). This is characteristic of mesoporous materials.

A hysteresis loop is often present in type IV isotherms during adsorption and desorption. Some porous materials desorb a smaller quantity of gas at a given pressure than the amount that was adsorbed at the same pressure. In mesoporous materials this is due to capillary condensation and in microporous materials due to breathing.

MOFs, mainly microporous materials, does not exhibit capillary condensation because the pores are too small. In this case, a type IV isotherm is obtained when flexibility of the structure is present. MIL-53(Al) shows first plateau when monolayer is formed in NP-d state. By increasing gas pressure (usually CO_2) even further, NP-d opens up to LP state.

Results obtained by adsorption/desorption experiments are usually explained by the Langmuir adsorption model or the Brunauer-Emmett-Teller (BET) theory, under certain assumptions. The Langmuir model only explains type I isotherms through the formation of a monolayer in microporous materials (most MOFs). It is used for obtaining Langmuir surface areas via N_2 adsorption in MOFs. The formation of multilayer is implicit in the BET theory used for mesoporous and macroporous materials but sometimes also MOFs. By the BET theory, gas molecules physisorb on a surface in layers and gas molecules only interact with adjacent layers. Further, the Langmuir theory can be applied to each layer. This

model can fit any of the isotherm types II to VI. For small values p/P_S BET theory is reduced to the Langmuir equation. Based on these theories, one can estimate the number of molecules required to cover the porous material's internal surface. Multiplying this number by the cross section area of the adsobent gas molecule yields the sample's surface area.[19]

N_2 adsorption in most vanadium and aluminium MOFs follows a reversible type I isotherm.[71] An example of a N_2 isotherm measured on one of the V-doped MIL-53(Al) samples presented in this thesis is shown in Figure 2.6.

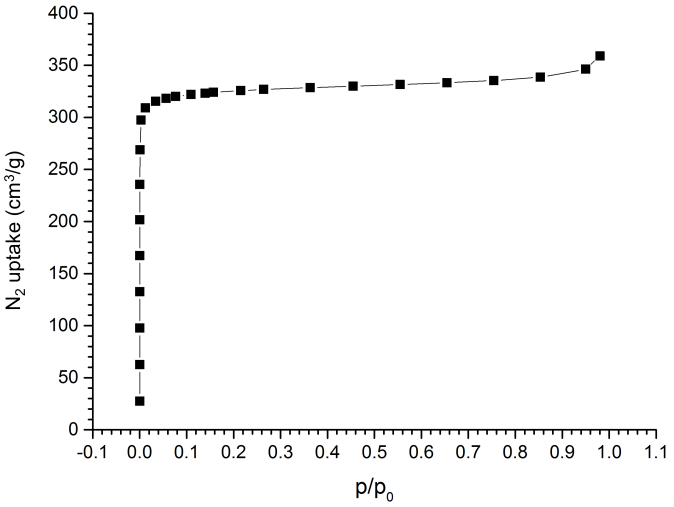

Figure 2.6: Langmuir N_2 adsorption isotherm of V-doped MIL-53(Al) at 77 K, $p_0 = 1$ bar.

It is reported that the MIL-53(M) series with M = Al, Cr and Ga show type I isotherm during N_2 adsorption indicating their porosity without hysteresis upon desorption.[21,51,52] In contrast, dehydrated MIL-53(Fe) and MIL-53(Sc) show no porosity because structures are in a CP state or a VNP state.[53,54]

Reported results on MIL-100(V), $V_3OF(BTC)_2$, MIL-101(V), ($V_3OCl(DMF)_2(BDC)_3$), and functionalised NH_2-MIL-101, ($V_3OCl(DMF)_2(BDC\text{-}NH_2)_3$), show a sub-step in their type I isotherm as it can be seen in Figure 2.7, left. This is explained as the presence of two types of pores, microporous and mesoporous, in their structures with different sizes.[39,72]

A remarkable observation is published for COMOC-2(V).[73] This framework was already introduced in Chapter 1, Figure 1.1. COMOC-2 and its Al variant DUT-5(Al)[74] are isoreticular structures of the MIL-47(V) and MIL-53(Al), respectively. COMOC-2(V) contains an infinite chain of corner-sharing VO_6 polyhedra in which the V-centres are in the V^{IV} state. The chain in DUT-5(Al) is built up by infinite Al-OH-Al interconnections, with aluminium in the Al^{III} valence state. The COMOC-2(V) and DUT-5(Al) structures are shown in Figure 2.8.

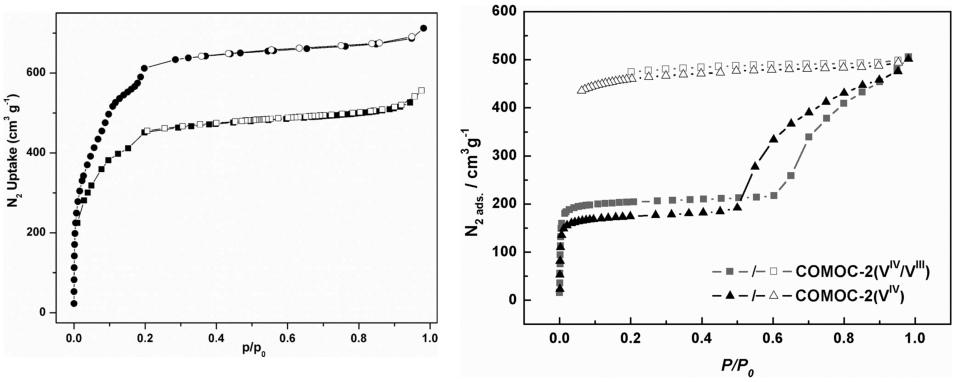

Figure 2.7: Left: Low pressure N_2 adsorption (solid symbols) and desorption (empty symbols) isotherms of activated MIL-101(V) (circles) and functionalized NH_2-MIL-101 (squares) measured at 77 K.[39] Right: N_2 adsorption (solid symbols) and desorption (empty symbols) isotherms of COMOC-2(V^{IV})(black) and COMOC-2(V^{IV}/V^{III}) (gray) at 77 K.[73]

Liu *et al.* synthesised COMOC-2(V) with combination of V^{III} and V^{IV} metal centres. Type II isotherms are reported during adsorption of N_2 in COMOC-2(V^{IV}) and COMOC-2(V^{IV}/V^{III}) as presented in Figure 2.7, right. It was shown that the presence of V^{III} ions in the framework suppresses the flexibility of the material and the opening of the structure occurs at higher pressure.[73] This phenomenon is contrary to the situation in MIL-47(V^{IV}), in which the presence of V^{IV} centres prevents the flexibility to a large extent.[67]

MIL-47(V^{IV}) and DUT-5(Al) showed a type I isotherm during N_2 adsorption.[66,74]

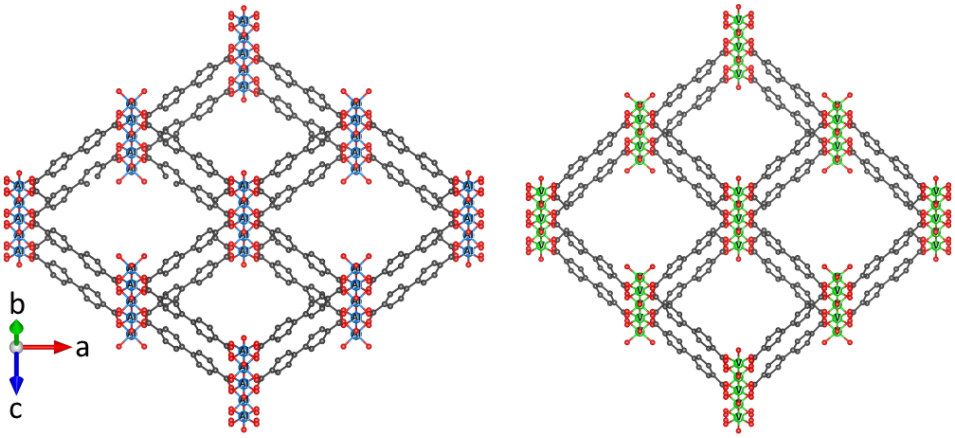

Figure 2.8: DUT-5 (Al^{III}-OH(BPDC), left) and COMOC-2 (V^{IV}=O(BPDC), right) structures. Blue: aluminium, green: vanadium, red: oxygen, grey: carbon.

Adsorption of CO_2

As a result of the increased awareness about global warming, solutions for CO_2 emission have become an important field of research and development. There are two standard techniques to measure gas uptake: the volumetric and gravimetric method. In the volumetric method, the volume of adsorbed gas on the porous material is measured. More accurate measurements are performed by weighing the porous material mass exposed to the gas atmosphere using a very sensitive microbalance. This is the gravimetric method.

MOF-210, $Zn_4O(BTE)_{4/3}(BPDC)$, currently has the highest total gravimetric CO_2 uptake among all reported MOFs.[18] Among the vanadium MOFs, the largest CO_2 uptake capacity was reported for MIL-100(V), in line with its isostructural Al, Cr and Fe variants.[75] MIL-101(V) and functionalised NH_2-MIL-101(V) show significantly lower CO_2 uptake in comparison with the Cr and Al versions.[39] This difference is assigned to solvent left in the pores, leading to a considerably smaller accessible surface area. Due to the lower thermal stability of the vanadium framework the activation is performed at lower temperatures and therefore solvent is present in the pores.

Llewellyn *et al.* reported that MIL-53(Al) and MIL-53(Cr) in the LP state at RT exhibit a type IV isotherm if CO_2 is used as adsorbate as shown in Figure 2.9a. This is due to the specific interaction of CO_2 molecules and the OH groups of the framework which shrinks to the NP-d state for pressures below 6 bar. A further increase in the adsorption pressure leads to reopening of the structure to the LP state and total pore filling. In the same study adsorption of CO_2 in the NP-h state showed a different behaviour (Figure 2.9b). MIL-53(Cr) stays in the NP-h state up to 5 bar of CO_2 pressure. Further increase of pressure forces part of the pores to open to the LP state and a coexistence of the NP-h and LP states is confirmed via XRD. Above 15 bar the framework transforms completely to the LP state.[76]

By Mowat *et al.* uptake of CO_2 at 196 K on MIL-53(Sc) occurs in two stages starting from the NP-d state without permanent porosity for CO_2. Then a transition to a more open state follows with full opening to the LP state at higher partial pressures, as shown in Figure 2.10.[53]

According to Guillou *et al.*, in MIL-53(Fe) CO_2 adsorption occurs in three steps. Starting from the NP-d state, the formation of an INT state at RT and 2 bar pressure is followed by the transition to the NP state filled with CO_2 molecules at 10 bar. The LP state is obtained also at 10 bar but by decreasing the temperature to 220 K. The INT state contains two types of pores with different sizes and only the larger ones are occupied with CO_2 molecules. In the NP+CO_2 and the LP state all pores are reported to be equally occupied.[77]

The reported CO_2 adsorption on MIL-47(V) in various oxidation states is shown

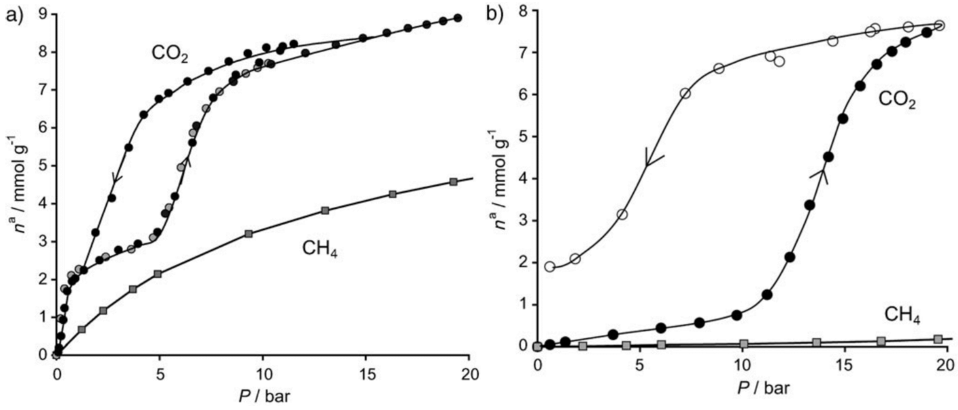

Figure 2.9: Comparison of the adsorption isotherms of CO_2 and CH_4 at 304 K on a: LP and b: NP-h state of MIL-53(Cr).[76]

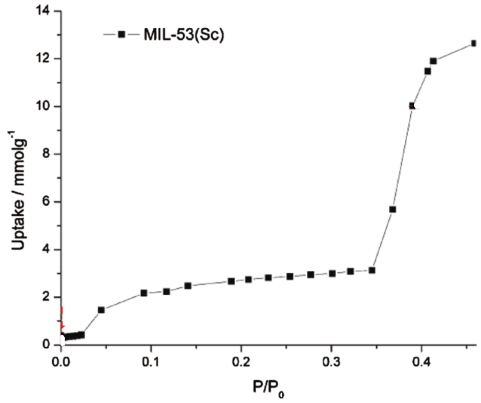

Figure 2.10: CO_2 adsorption isotherm measured at 196 K on the MIL-53(Sc).[53]

in Figure 2.11. MIL-47(V^{III}), which contains OH groups, showed a type II CO_2 adsorption isotherm. On the contrary, MIL-47(V^{IV}) does not show this behaviour because of its rigid framework and the absence of OH groups. It showed type I isotherm. No specific adsorption sites are present in the MIL-47(V^{IV}) framework for the CO_2 molecules to interact with. Nevertheless, the CO_2 uptake capacity is comparable with the one of the MIL-53(Al) and MIL-53(Cr) frameworks.[57,67]

In the study by Liu *et al.*, COMOC-2(V^{IV}) showed a hysteresis loop during adsorption/desorption of CO_2 at 265 K, similar as for N_2. This is a surprising result since COMOC-2(V^{IV}) does not contain OH groups. This behaviour was assigned to a structural transition from the NP to the LP state. The hysteresis loop was lacking during adsorption or desorption at RT.[73]

Even though numerous investigations reporting different properties and behaviour of certain MOFs exist, not much systematic knowledge about these

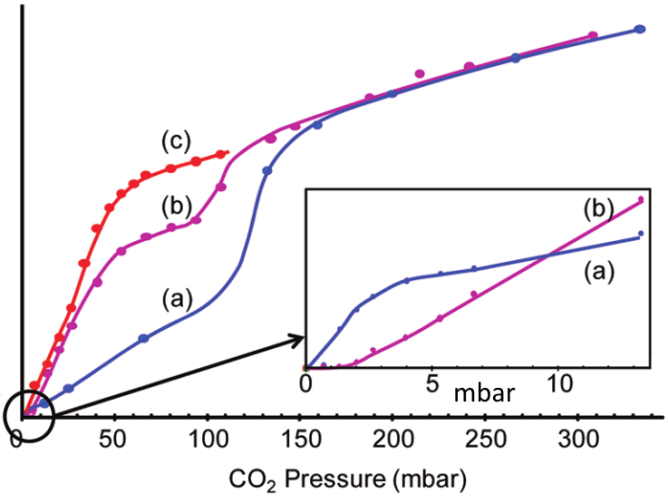

Figure 2.11: Adsorption of CO_2 at 220 K for a) MIL-47(V^{III}), b) MIL-47(V^{III}/V^{IV}), c) MIL-47(V^{IV}) The inset corresponds to the enlargement of the amount of CO_2 adsorbed in the 0-13 mbar pressure range.[67]

phenomena is available.

Adsorption of H_2

Hydrogen is one of the most promising alternatives for carbon based fuels since it has the highest energy per mass of any available fuel and does not emit CO_2 after burning. At this moment safe and effective hydrogen storage is a main problem for the advancement in this prospective field. The first MOF reported for hydrogen storage was MOF-5 (Rosi *et al.*, 2003[78]). After that publication, hundreds of MOFs were developed for this application.[3] The gravimetric H_2 storage capacity at 77 K and high pressure are proportional to the MOFs pore volume and surface area. This means that the complete interior volume of the MOF can be filled with H_2 molecules, not only the surface. MOF-210 still holds the record for H_2 gravimetric uptake of 15 wt% (wt% of the gas versus the MOF) at 80 bar and 77 K[18,79] which is higher than for carbon-based adsorbents.[80] A problem that is still not overcome is operation at higher temperatures.

Rowsell and Yaghi measured the H_2 adsorption of eight MOF (IRMOF series, HKUST-1 and MOF-74 (Zn_2(DHBDC)(DHBDC = 2,5-dihydroxy-BDC))) at 77 K up to 1 bar. All these MOFs showed a type I isotherm without hysteresis. Because of its larger pore volume, HKUST-1 achieved greater capacity and a larger gain in capacity before saturation (Figure 2.12). The gas amount adsorbed per gram by HKUST-1 is approximately double that of MOF-5 (IRMOF-1) at 77 K and 1 bar.[81]

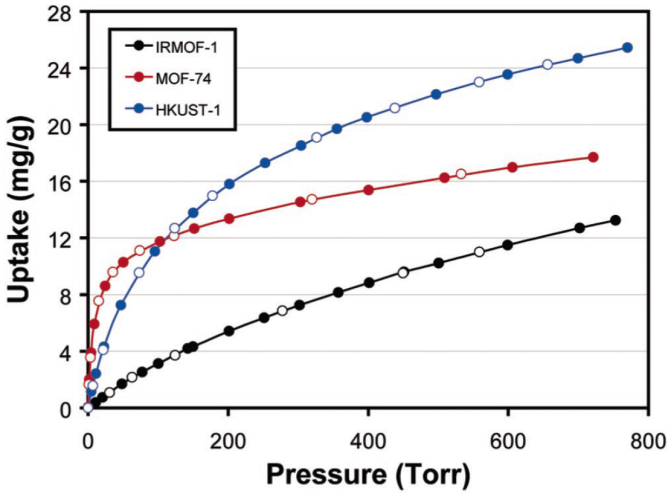

Figure 2.12: Comparison of the H_2 adsorption isotherms of HKUST-1, MOF-74 and MOF-5 (IRMOF-1) at 77 K. Adsorption is represented with closed circles and desorption with open circles.[81]

Adsorption/storage of CH_4

Another application of MOFs in the field of alternative fuels is methane storage, which is already realised at RT and at high pressures.[82,83] HKUST-1 still gives the highest volumetric methane storage at RT due to its specific structure and it is the closest to reach the requirements for commercial application.[84,85] Increasing the volumetric uptake is also possible by functionalising MOF. Besides MOFs, zeolites, active carbons and covalent organic frameworks (COFs) were also explored for methane adsorption. Zeolites have relatively small surface areas and together with extremely hydrophilic properties their capacity for methane storage is relatively low. Although great progress has been made for porous carbon materials as methane adsorbates, these materials are still less effective if compared with MOFs. COFs are promising materials due to their stability in water and gravimetric methane uptake but the material density is usually very low leading to a very low volumetric storage capacity.[84] MIL-53(Al) is commercialised by BASF under the name Basolite® A100 for mobility applications using methane as a fuel due to its easily reproducible synthesis in aqueous environment, good thermal stability and possibility to scale up at low cost.[86]

Data available in literature points to the fact that CH_4 adsorption in all vanadium MOFs show type I isotherms. The CH_4 adsorption capacities of MIL-47(V) and MIL-100(V) at RT are comparable with MIL-53(Al) and MIL-53(Cr). The adsorption isotherms are typical of those obtained with nanoporous materials like zeolites or activated carbons. Much lower values are reported for COMOC-2(V)

and functionalized NH_2-MIL-47.[87] No hysteresis was reported for the flexible MIL-47(V^{III})[67] and COMOC-2(V)[73] frameworks.

In the study by Llewellyn *et al.*, LP MIL-53(Cr) showed a gradual uptake of CH_4, as opposed to NP-h MIL-53(Cr) where adsorption of methane becomes close to zero, as shown in Figure 2.9. This was attributed to water molecules blocking the pores, to unfavourable conditions for the incorporation of the nonpolar methane molecules or to pre-treatment with CO_2.[76]

Gas separation

Separation of gases is another important application of MOFs. High purity single components are in high demand. Some MOFs showed the ability to separate one particular gas from a mixture. The preferential adsorption of one gas over the other is called selectivity. Kinetic effects can play a role in selectivity. Different gas molecules can enter the framework with different rates or can diffuse through the framework in a different way. In some cases pore openings can be too small for a certain gas to penetrate. This approach is efficiently achieved with MOF structures since pores can be easily modified in a wide range by employing a particular linker. This is called size or shape selective adsorption. During desorption, the rate at which different gases desorb from the framework can also play a role.[19]

$Cr_3(BTC)_2$, and MOF-74(Fe) (Fe_2(DOBDC)(DOBDC = 2,5-dioxido-1,4- benzenedicarboxylate)), were investigated for efficient O_2/N_2 separation in the study by Murray *et al*. At RT, the O_2 adsorption isotherm for $Cr_3(BTC)_2$ rises steeply to a capacity of 11 wt % at 2 mbar (saturation pressure for O_2). The corresponding N_2 adsorption isotherm displays very little uptake, gradually rising to a capacity of 0.58 wt % at 1 bar which can be seen in Figure 2.13. Thus this MOF displays an exceptional O_2/N_2 selectivity factor of 22.[88]

Bloch *et al.* reported for the Fe version of MOF-74 (Figure 2.14) that the framework binds O_2 preferentially over N_2. At RT, an irreversible capacity of 9.3 wt % was achieved, corresponding to the adsorption of one O_2 molecule per two iron centres. By decreasing temperature to 211 K, the O_2 uptake showed to be fully reversible and the capacity increased with a factor of two.[89]

MIL-53(Cr) is reported for selective adsorption of CO_2 from CO_2/CH_4 mixtures. In that study the selectivity toward CO_2 molecules was increased by hydration of the framework as it can be seen from Figure 2.9.[76]

MIL-47(V) and functionalised NH_2-MIL-47(V) were investigated by Leus *et al.* for CO_2/CH_2 separation (Figure 2.15). A decrease in the capacity (per gram adsorbent) was observed for the amino version of the material, corresponding to 20% for CO_2 and 10% for CH_4 at 25 bar. This can be attributed to the

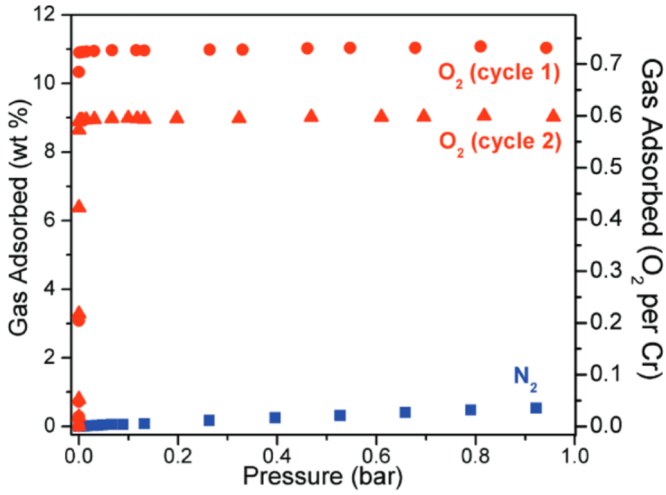

Figure 2.13: Uptake of O_2 (red symbols) and N_2 (blue squares) by $Cr_3(BTC)_2$ at RT. Upon evacuation, the O_2 isotherm for a second cycle reveals a slightly reduced capacity, while every further cycle showed similar isotherm (capacity) as for the second cycle.[88]

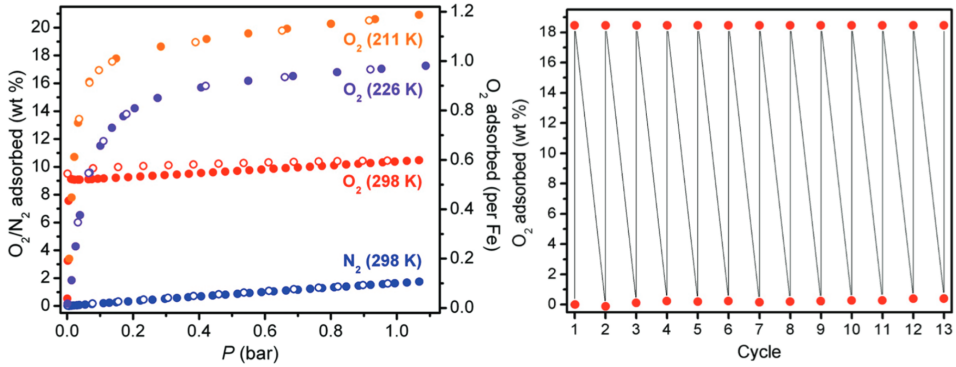

Figure 2.14: Left: O_2 adsorption isotherms for MOF-74(Fe) at 211, 226 and 298 K and N_2 adsorption at 298 K. Solid and open symbols represent adsorption and desorption, respectively. Right: Adsorption and desorption of O_2 for MIL-74(Fe) over 13 cycles at 211 K. Reversible adsorption/desorption with similar capacities per cycles is presented.[89]

presence of amino groups in the pores which decrease the available pore volume. Interestingly, in the low pressure range the adsorption isotherms of both materials coincide indicating a similar affinity for both types of guest molecules.[87] The adsorption properties of the rigid MIL-47(V) and NH_2-MIL-47(V) are similar to those of MIL-53(Al) in the low pressure region. On the contrary, Couck *et al.* reported that the amine functionalisation of MIL-53(Al) improves the separation factor by several orders of magnitude.[90]

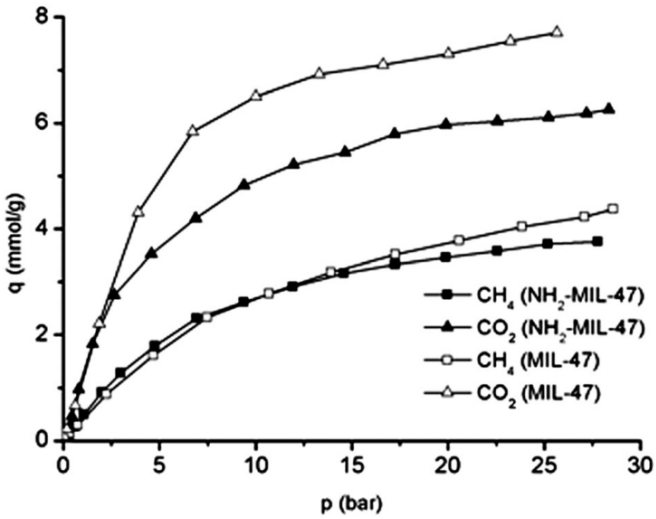

Figure 2.15: CO_2 and CH_4 adsorption isotherms of MIL-47(V) and NH_2-MIL-47(V) at RT.[87]

2.5 Applications of MOFs

As already mentioned, MOFs are a relatively new class of materials with potential application in a broad range of mostly industrial fields. The variety of reported MOFs and applications is quite extensive and a complete overview is thus beyond the scope of this thesis. In this section a brief explanation will be given for certain applications with few exciting examples.

2.5.1 Catalysis

Catalysts are important materials for large variety of industries. Approximately 85 - 90% of the products of chemical industry are made in catalytic processes. Catalysts play an important role in production because of major environmentally harmful waste reduction.[91] In fundamental scientific research, catalysis is a challenging field where there is a lot of room for further improvement and optimisation. Catalysts can be divided into three main groups: homogeneous, heterogeneous and biocatalysts. In homogeneous catalysis both the catalyst and the reactants are in the same phase, liquid or gas. During heterogeneous catalysis, solids catalyse reactions of molecules in a gas or in a liquid solution. If the solid is non-porous, the catalysis takes place at the external surface of the catalyst. Biocatalysts are enzymes which are highly specific and efficient.[92] Heterogeneous catalysis presents one of the most important applications of MOFs where easy post-reaction separation, catalyst reusability and high stability are achieved. Heterogeneous catalysis in general offers easier separation of catalyst,

reagents and products, and smaller amounts of waste. Thus it presents an eco-friendly and efficient system in comparison with its homogeneous counterparts.

The first catalysis obtained with a 'pre' MOF, a 2D square network of cadmium(II) and BPY ($Cd(BPY)_2(NO_3)_2$), was published in 1994.[93] Another example was a 2D square grid framework containing Pd(II) metal centres that catalysed a range of reactions.[94] These examples, largely obtained by trial and error, represent the introduction of MOFs in the field of catalysis. Further examples on the already mentioned HKUST-1 led to a large progress in catalytic activity.[22,95]

In MOF heterogeneous catalysis, supported vanadium oxide catalysts are an important class of catalytic materials. Vanadium oxide catalysts are widely used as selective oxidation catalysts in a variety of industrial reactions. Also in fundamental studies, these catalysts became models for catalytic systems. Vanadium oxide catalytic centres are usually incorporated in porous structures, like e.g. MOFs, which offer mechanical strength, easy recovery and recycling, in combination with high surface area.[96]

A limited number of studies is dealing with the catalytic activity of MIL-47(V^{IV}). One of the reasons could be the poor stability of the MIL-47(V^{IV}) structure in aqueous environment. Phan *et al*. reported MIL-47(V) as a highly catalytically active and chemically stable catalyst in the conversion of methane to acetic acid with 70% yield. The MOF catalysts proved to be reusable and remain catalytically active for several recycling steps without losing their crystalline structures.[97] The COMOC research group of Ghent University reported MIL-47(V^{IV}) as a catalyst in the liquid phase oxidation of cyclohexene with tert-butyl hydroperoxide (TBHP) as oxidant. MIL-47(V^{IV}) showed catalytic activity with similar conversion and selectivity towards cyclohexene oxide as the homogeneous catalyst $VO(acac)_2$ (acac = acetyl acetonate). Four catalytic runs proved that MIL-47(V^{IV}) can be recovered and reused. No leaching of metal ions was observed during additional runs.[5] MIL-47(V) was further investigated for the same reaction but with BDC linkers functionalized with OH, F, Cl, Br, CH_3 and NH_2 by Vandichel *et al*. It is reported that functionalisation of the linker leads to an increased activity in comparison with the MIL-47(V) framework.[98] Further, Leus *et al.* post-functionalised NH_2-MIL-47 with a $TiO(acac)_2$ complex in order to create a bimetallic catalyst. A significantly higher cyclohexene conversion was detected in comparison with the NH_2-MIL-47 catalyst. Additionally, the material was reused three times without any loss of activity or stability. Neither for V nor for Ti leaching was observed.[99] By the same research group, COMOC-3(V), VO(NDC), although not porous was tested for catalytic activity in the same reaction using TBHP in decane as oxidant. A similar conversion of cyclohexene and selectivity as for MIL-47(V) was obtained in the same conditions.[100]

MIL-101(Cr) is reported to be good catalyst because of its unique pore structure.

The size of the pores is large enough for solvent molecules to penetrate into framework but also for product molecules to move out. Furthermore, water molecules coordinated to chromium atoms can be easily removed by evacuation leaving coordinatively unsaturated metal centres for coordination or activation of substrates. Numerous catalytic reactions are reported for MIL-101, like Lewis acid, Lewis base, oxidation, hydrogenation, etc. More information can be found in review by Bhattacharjee *et al*.[101]

MOFs as catalysts have already improved since the first tries but still a lot of development is needed. Chemical and thermal stability, activity and selectivity are not at their best yet. Often problems occur with leaching of active metal complexes during catalytic reaction. In recent years, experimental research is progressively more complemented with theoretical/computational studies in order to obtain a complete understanding of the behaviour of MOFs in catalysis. This approach may ultimately lead to more rational MOF catalyst design. The variety of catalytically active MOFs and catalytic reactions is quite extensive and complete overview is beyond the scope of this thesis. More information can be found in reviews by Chughtai *et al*.[102] and Zhu *et al*.[103]

2.5.2 Sensing

Introduction

MOFs have also been explored in sensing. The porous character of a MOF makes it a great medium for accommodating analytes (components that have to be detected). Tuning the pore size and shape allows size-based adsorption/desorption of particular guest molecules. Functional sites in the framework can behave as specific binding sites with specific coordination or hydrogen bonding interaction.[84,104]

Fast and reliable, but still convenient and cheap detection of explosives have become important in everyday life. The highly luminescent microporous Zn based MOF, $Zn_2(BPDC_2)(BPEE)$(BPEE=1,2-bipyridylethene), was synthesized by Lan *et al.* for fast and reversible selective detection of trace explosives. 2,4-Dinitrotoluene (DNT) a byproduct in the production of 2,4,6-trinitrotoluene (TNT) has a RT vapour pressure 20 times higher than that of TNT. The detection of nitroaromatic explosives is often done by DNT detection. On the other hand, plastic explosives are often detected via 2,3-dimethyl-2,3-dinitrobutane (DMNB). Luminescence quenching is the process behind this detection. Quenching refers to any process which decreases the luminescence intensity of a given material. The aforementioned MOF exhibits bright violet luminescence when illuminated with UV light. After exposure to DNT or DMNB vapour at RT, already after 10s, 80% of

fluorescence was quenched. The luminescence was recovered simply by heating for 1 min.[105]

ZIF-8 showed good perspective in chemical sensing due to its remarkable selective adsorption properties. Thin film ZIF-8 is reported to be a selective sensor for chemical vapours and gases, by following the thin film's refractive index. It was demonstrate to be sensitive to various concentrations of chemicals with fast response (within 1 min.) and reversible refractive index changes. Due to its hydrophobic nature, the sensor is unresponsive to water vapour.[32]

Furthermore, ZIF-8 was tested in one study as electrochemical biosensor for *in vivo* measurements of glucose.[106] ZIF-8 has been studied also as a luminescence sensor for detecting metal ions and small molecules. The luminescence intensity of ZIF-8 is highly sensitive to Cu(II) and Cd(II) ions and small molecules such as acetone. The luminescence intensity increases gradually with the increased amount of acetone.[107]

H_2O detection

Due to their easy uptake of water, certain MOFs are reported as humidity detectors. For sensing water vapour levels Yu *et al.* used lanthanide based MOFs. These materials are sensitive to the chemical environment of the lanthanide ions. MOFs constructed of $Tb(NO_3)_3$ or $Eu(NO_3)_3$ upon dehydration showed a decrease in luminescence emission intensity. This process is reversible: upon rehydration the intensity of emission is restored within 9 h at relative humidity levels beyond 85%. The Tb MOF additionally showed the greatest change in luminescence intensity when the dehydrated framework was exposed to a known quantity of water vapour.[108]

Another reported example is the Zn(DPE)(BDC)(DPE=1,2-bis(4-pyridyl)ethane) MOF which showed changes in luminescence intensity when exposed to water vapour, but in this case the linker is the source of luminescence rather than the metal. Luminescence originates from interaction between DPEs. A reversible luminescence response was reported upon cycling between RT and 360 K. It was shown that the dehydration process results in dramatic luminescence changes from pale blue upon hydration to bright white light generation upon dehydration. Dehydration here leads to an increase in the emission intensity in contrast with the studies discussed above.[109]

HKUST-1 is a popular material for detection of water vapour. In one study, HKUST-1 was used as a coating for piezoresistive microcantilever sensor. This sensor was exposed to different concentrations of water in nitrogen gas at RT and 1 bar. Water was adsorbed on the HKUST-1 leading to a change of the electrical resistance of the microcantilever. The sensing mechanism was demonstrated to be

highly sensitive and reversible, both for water vapour and for methanol. In the case of water vapour, the electric response was shown to be proportional to the concentration.[110]

O_2 detection

O_2 is the main component for maintaining life. Monitoring and quantifying O_2 levels in living cells is of great importance when diagnosing various vascular, pulmonary diseases and tumours. Lower levels of O_2 in the cancer tissue is correlated with worse overall survival probabilities of the patients compared to patients with well-oxygenated tumours.[111]

O_2 molecules in some MOFs can be efficiently detected by luminescence quenching.[112] A nanoscale MOF was reported as an intracellular oxygen sensor with a Pt(II)-porphyrin ligand as O_2 sensitive probe in living cells. Pt(II)-porphyrin shows bright phosphorescence in air at RT and its intensity is highly dependent on the O_2 concentration. MOF was loaded into tumorous tissue and tissues were placed into three pressure chambers. Three different O_2 levels were examined: 0.005 (hypoxia), 0.04 (normoxia) and 0.2 bar (aerated conditions). Ratiometric luminescence imaging revealed good agreement with measurements of O_2 pressure in the chambers.[113]

An impressive example was published on a flexible ultramicroporous fluorescent Zn(II) MOF, doped with a low concentration of Ru(II). Upon exposing the MOF to increasing oxygen concentrations, the intensity of the emission decreased linearly and blue shifted with a very fast response (Figure 2.16b). High O_2 uptake was measured at RT and 1 bar. A simple colour changing oxygen sensor was produced, from a composite thin film of MOF in silicone rubber on a glass substrate (Figure 2.16a). It showed a very high and tunable oxygen quenching efficiency, good reversibility and stability. To obtain colour-changing device, the luminescent thin film of MOF was also fabricated on the outer surface of a commercially available blue-light emitting diode (LED). This presents an easy method to detect changes in the oxygen concentration. Under the UV light and the presence of a N_2 atmosphere, the LED would shine magenta as a combination of blue light from the LED and the red/orange emission from the MOF. In the presence of O_2, the LED shines blue/violet because the red/orange light from the MOF decreases significantly, as shown in Figure 2.16c and d.[114]

2.5.3 Drug storage and delivery

The possibility of tuning the chemical composition of MOFs, their surface area and pore size(s), their structural variety and biodegradability all make this class

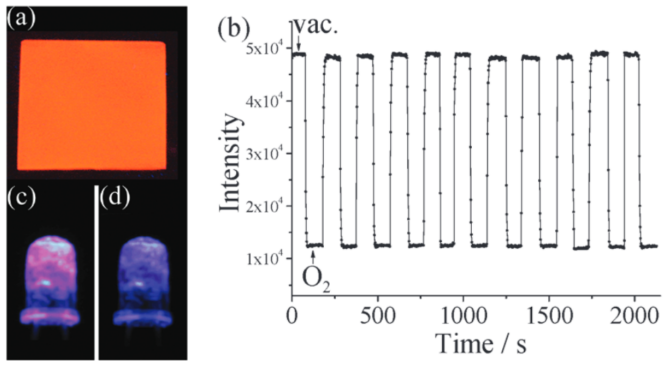

Figure 2.16: a: Photograph of a luminescent thin film of MOF under 365 nm UV light. b: Repeated luminescence response cycles in vacuum and O_2 (1 bar), and photographs of a thin film coated blue-light LED under c: N_2 flow or d: O_2 flow.[114]

of materials ideal candidates for storage, transport and targeted release of a wide range of drugs and biomolecules. For drug delivery, controlled loading and release is mandatory which became already feasible with MOFs. In literature the high porosity and mesoporous pores are exploited for very large loadings of drugs or proteins and for controlled release of these compounds.[115–118]

The potential application of MOFs for this purpose was first investigated by Férey's group on Cr based MIL-100 and MIL-101. Both frameworks showed remarkable adsorption of Ibuprofen. In both structures there are two types of pores, which can lead to selective occupation. MIL-100 has smaller pores in comparison with MIL-101 and it adsorbed 0.35 g of Ibuprofen per gram of dehydrated MIL-100. On the other hand, MIL-101 showed an impressive uptake of drug, larger than the initial MOF weight: 1.4 g of Ibuprofen per gram of dehydrated MOF. Hence, only small amount of MOF is required to deliver a high amount of drug. The smaller pores in the MIL-100 are on the size limit for accommodating Ibuprofen molecules. Thus it was concluded that Ibuprofen occupies only the larger pores in MIL-100 and both types of pores in MIL-101. Complete drug release was achieved in MIL-100 after 3 days and in MIL-101 after 6 days.[119]

MIL-53(Cr, Fe) were also studied for drug delivery of Ibuprofen by Horcajada *et al*. Both MIL-53(Cr) and MIL-53(Fe) adsorbed around 20 wt% of the drug and very slow and complete delivery was successfully reached.[120] A new MOF, a Pt-containing nanoscale coordination polymer $(Tb_2(DSCP)_3(H_2O)_{12}$ (DSCP = disuccinatocisplatin)) was developed by Rieter *et al*. Release of the DSCP moieties is reported which would presumably reduced to cytotoxic Pt(II) species for effective delivery of Pt-based anticancer drug.[121]

Yet another fascinating example is superparamagnetic magnetite particles em-

bedded in HKUST-1 framework. This approach provides easy manipulation for controlling the location of the MOF and targeted drug delivery by applying a static magnetic field. Superparamagnetic magnetite particles heats up quickly when exposed to an alternating magnetic field and this feature could be used for controlled release of the drug.[122,123]

ZIF-8 possess few significant characteristics specific for drug storage and delivery applications. It is stable in water and in sodium hydroxide aqueous solution[27] but is quickly decomposable in acid solution. Significant loading capacity for various anticancer drugs was published. Besides high loading, gradually release is also reported.[124,125] Sun *et al.* used its pH-sensitive properties for the release of the encapsulated anticancer drug. In acid environment drug is released via degradation of the ZIF-8 framework which is particularly useful for drug delivery to tumours.[124] Another intriguing feature was reported besides high loading and pH-responsive drug delivery. Carbon nanodots@ZIF-8 nanoparticles with green fluorescence intensity were synthesised for simultaneous drug delivery and fluorescence imaging of cancer cells.[126]

The concerning issues with some of these materials are the toxic compounds of the framework, metal release and biocompatibility. Hence, significant efforts have been put in the development of non-toxic MOFs with the same or even better adsorption capacity and drug delivery efficiency. A series of non-toxic porous Ir^{III} based MOFs were published. These materials were shown to be nanocarriers for efficient controlled delivery of antitumoural and retroviral drugs against cancer and AIDS.[118]

3

Electron Paramagnetic Resonance

Electron paramagnetic resonance (EPR) makes use of the magnetic moment of electrons. Two historic experiments led to the discovery of the electron magnetic moment and its quantisation. In the late 1800s, the Dutch physicist Pieter Zeeman observed that the yellow D-lines in the optical emission spectrum of sodium split into two or more components of slightly different frequency when the light source is placed in a static magnetic field. Zeeman's finding was originally explained by means of the orbital angular momentum of the electrons, but this could not explain all observations. The second experiment was conducted in the 1920s by Otto Stern and Walther Gerlach. A beam of silver atoms was sent through a non-uniform magnetic field and atoms were deflected up or down before reaching a detector, on which two distinct traces were observed. This observation can only be explained by assuming that next to their orbital angular momentum, electrons also have an intrinsic angular momentum, called spin. George E. Uhlenbeck and Samuel A. Goudsmit came to a quantitative interpretation of the Zeeman and Stern - Gerlach experiments by proposing that the gyromagnetic ratio (ratio between magnetic and angular momentum) for the spin angular momentum of electrons is twice as large as for their orbital angular momentum. When an external magnetic field is applied, the magnetic moment of the electron interacts with it and can only take on certain orientations with respect to the field. This interaction alters the atomic energy levels leading to a splitting of atomic spectral lines.[127,128] In EPR spectroscopy transitions between the quantized electron magnetic moment states are observed.

In the late 1930s Isidor Isaac Rabi discovered nuclear magnetic resonance (NMR). By then the structure of atoms was already understood: it was known that atoms consist of a nucleus surrounded by an electron cloud and that the nucleus

itself is built up of protons and neutrons. All three types of particles have spin and magnetic moment. For certain nuclei the individual magnetic moments of protons and neutrons add up to a non-zero total magnetic moment. Rabi proposed that by absorption of radiowaves the magnetic moment of the nucleus can change its direction with respect to an external magnetic field. By returning to the original orientation state it would emit the same amount of energy and it should be possible to detect this transition. Rabi used a beam of lithium chloride molecules exposed to radio waves while varying the magnetic field strength. At the matching combination of external magnetic field and the radio frequency he observed magnetic resonance adsorption. The magnetic moment of the nuclei changed direction, and since each nucleus has a characteristic pattern of resonance frequencies that are slightly modified by interaction with electrons and surrounding nuclei, it became possible to identify atom types in molecules and obtain information on molecular structure. In 1944 Rabi obtained the Nobel Prize in Physics for this discovery.[129]

Inspired by the work of Rabi, Yevgeny Konstantinovich Zavoisky in the 1940s managed to improve the detection sensitivity in the setup, and in 1944 he detected the first magnetic resonance signals for electrons (electron magnetic resonance) for samples of hydrous copper chloride, copper sulfate and manganese sulfate.[130]

In the further sections of this chapter a short description of the basics of EPR will be given. The emphasis is placed on the concepts necessary for a good understanding of the experimental part of this work. The discussion is restricted to continuous wave (CW) EPR and electron nuclear double resonance (ENDOR). EPR results available in literature on COMOC-3, MIL-47 and MIL-53 are presented at the end of the chapter.

3.1 Intrinsic magnetic properties of electrons and nuclei

Electrons have an intrinsic spin angular momentum characterized by the quantum number $S = 1/2$. The operator for the spin angular moment is $\hat{\vec{S}}$ and the magnitude of the angular momentum itself is given by the square root of the eigenvalue of $\hat{\vec{S}}^2$, which is $(S(S+1))^{1/2}$. The eigenvalues of the projection of the angular momentum on a specified direction M_S take the values S, $S-1$,..., $-S$. For an electron in free space these values are $M_S = +1/2$ and $M_S = -1/2$. The operator for the magnetic dipole moment, $\hat{\vec{\mu}}_S$ is

$$\hat{\vec{\mu}}_S = -g_e \mu_B \hat{\vec{S}} \tag{3.1}$$

where $g_e = 2.002319$ is the free-electron g factor, $e\hbar/2m_e = \mu_B = 9.27402 \times 10^{-24} J/T$ is the Bohr magneton, $\hbar = h/2\pi$, h is Planck's constant and m_e is the electron mass. The minus sign comes from the negative charge of the electron and indicates that the magnetic dipole moment and the electron spin are antiparallel.

In a similar way we can define an angular moment due to the nuclear spin, $\hat{\vec{I}}$, whose magnitude is $(I(I+1))^{1/2}$. The projection on a specified direction is M_I which runs in integral steps from $+I$ to $-I$. The associated nuclear magnetic moment $\hat{\vec{\mu}}_I$ is

$$\hat{\vec{\mu}}_I = g_n \mu_n \hat{\vec{I}} \tag{3.2}$$

where g_n is the nuclear g factor and μ_n is the nuclear magneton, $\mu_n = e\hbar/2m_p = m_e\mu_B/m_p \approx \mu_B/1836$, m_p the proton mass. g_n depends on the type of nucleus. It can be used, together with the nuclear spin, to identify nuclei.[131,132]

3.2 Spins in an external magnetic field and magnetic resonance

The quantum mechanical *Hamiltonian* operator for the magnetic dipole moment, associated with a free electron, and a static magnetic field is

$$\hat{H} = -\hat{\vec{\mu}} \cdot \vec{B} = g_e \mu_B \hat{\vec{S}} \cdot \vec{B}. \tag{3.3}$$

This interaction between the electron's spin and a magnetic field is named after Pieter Zeeman: the (electron) Zeeman interaction. If the magnetic field defines the z-direction, $\vec{B} = (0, 0, B)$, Equation 3.3 becomes

$$\hat{H} = g_e \mu_B B \hat{S}_z. \tag{3.4}$$

This *Hamiltonian* has the eigenvalues

$$E = g_e \mu_B B M_S. \tag{3.5}$$

In zero magnetic field, the two M_S states are degenerate. The separation between these states increases linearly with B, as shown in Figure 3.1 in the left panel. The lower state corresponds to $M_S = -1/2$, where the spin is antiparallel and the magnetic moment is parallel to the external magnetic field direction. In an EPR experiment magnetic dipole transitions between these two M_S states are induced by electromagnetic (EM) waves (following selection rule $\Delta M_S = \pm 1$) that satisfy the resonance condition

$$\Delta E = g_e \mu_B B = h\nu \tag{3.6}$$

where ν is the frequency of the wave.[131,132]

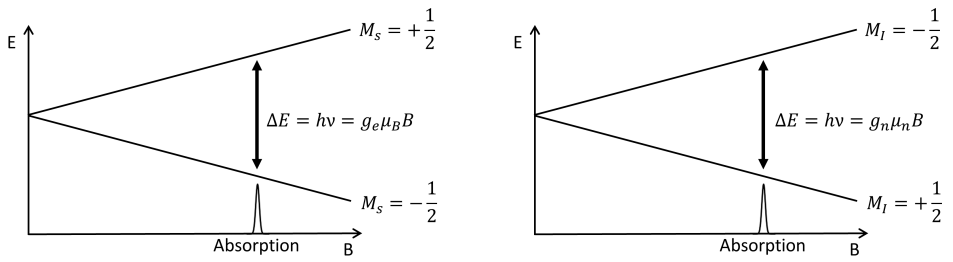

Figure 3.1: Energy levels for a system with $S = 1/2$ (left) and $I = 1/2$ (right, for positive gyromagnetic ratio $\gamma_n = g_n\mu_n$) in an applied magnetic field B. The two diagrams are not on the same scale.

For a magnetic field on laboratory scale ($0.1 - 10$ T) the resonance frequency is in the microwave range.

Equation 3.6 shows that the resonance condition can be fulfilled in two ways: by changing the frequency ν at fixed field, and by changing the magnetic field B at fixed frequency. For technical reasons (see further in section 3.5), in EPR spectroscopy most often the frequency is kept fixed while the magnetic field is swept, as shown in Figure 3.1. The microwave frequency bands used in this thesis are listed in Table 3.1.

Table 3.1: Frequencies of the EM microwaves used in this thesis. The resonance magnetic fields are also presented for the free electron, $g_e = 2.002319$.

S-band	X-band	Q-band	W-band	J-band
4 GHz	9.5 GHz	34 GHz	94 GHz	275 GHz
143 mT	339 mT	1213mT	3354 mT	9813 mT

Net resonance absorption of microwaves can only occur if the lower spin state exhibits a larger population than the excited spin state. Electron spins promoted to the excited spin state fall back to the ground state with a characteristic time constant τ_e, the electron spin relaxation time or excited state lifetime. At low microwave power, the spin level population in this two-level system is hardly affected. The amplitude of the absorption line then increases linearly with the exciting magnetic field, i.e. proportional to the square root of the power. At high microwave power the population difference between the two spin levels markedly decreases and the EPR line intensity saturates. It is worth noting that the thermal energy $k_B T$ at 300 K corresponds to 6.25 THz, much larger than the microwave frequencies listed in Table 3.1. This implies that the population differences between the energy levels involved in EPR transitions are small, even at low temperatures.

The finite lifetime of the excited state also gives EPR transitions a finite linewidth and a Lorentzian line shape through the Heisenberg uncertainty principle. This is called natural or homogeneous line broadening. For paramagnetic centres in solids at low concentration, the excited spin state lifetime is usually determined by spin-lattice relaxation. Interactions between paramagnetic centres may decrease τ_e considerably through spin-spin relaxation, as will be shown in Chapter 8 of this work. Besides lifetime, also sample inhomogeneity and unresolved interactions with other (nuclear) magnetic moments in the electron spin's environment lead to line broadening. If such inhomogeneous broadening mechanisms are dominant, the shape of the EPR line is Gaussian.

Finally, it should be noted that, in order to improve the signal-to-noise ratio, field modulation and lock-in detection are usually applied in EPR spectroscopy (see section 3.5). As a result, the spectra obtain a shape that resembles the first derivative of the absorption spectrum in Figure 3.1.

The interaction between external magnetic field and the magnetic moment of the nucleus is called nuclear Zeeman interaction. Its *Hamiltonian* takes the form

$$\hat{H}_{NZ} = -\hat{\vec{\mu}} \cdot \vec{B} = -g_n \mu_n \vec{B} \cdot \hat{\vec{I}}. \tag{3.7}$$

For a magnetic field along the z-axis, the eigenvalues of *Hamiltonian* are

$$E = -g_n \mu_n B M_I. \tag{3.8}$$

The energy levels for a nucleus with $I = 1/2$ are shown in the right panel of Figure 3.1. In the lower energy state both the magnetic moment and the spin are parallel to the external magnetic field direction (for positive γ_n). The resonance condition for NMR transitions is

$$\Delta E = g_n \mu_n B = h\nu \tag{3.9}$$

with selection rule $\Delta M_I = \pm 1$.[131,133]

3.3 The spin-*Hamiltonian*

In this thesis, EPR spectroscopy is used to obtain a detailed map of the surroundings of unpaired electrons bound to atoms (or molecular fragments) in a solid state (MOF) environment. In that case the electron is not free but rather experiencing complicated interactions with its surroundings. Finding the eigenvalues of such a *Hamiltonian* is too complicated for analysing EPR spectra. Therefore, a simplification is made, based on the fact that the energy splittings observed in EPR spectroscopy are several orders of magnitude smaller than the energy required

for a transition from the ground state to most of the electronically excited states. Because of that, the electronic ground state, which is a $2S^* + 1$ fold degenerate in zero magnetic field and is the only state with appreciable thermal population, is considered as an isolated system with effective spin S^*. The *Hamiltonian* operator of the effective spin is called the spin-*Hamiltonian*.

For the paramagnetic centres considered in this work, it is sufficient to consider the following interactions in the spin-*Hamiltonian*:

- the electronic Zeeman interaction between the effective spin S^* and an external magnetic field ($\hat{H}_{EZ}$), which also includes effects of orbital angular momentum,
- the fine structure or zero field splitting (ZFS) interaction ($\hat{H}_{ZFS}$), which occurs for paramagnetic centres with $S^* > 1/2$, and is due to indirect (second-order) effects of the crystal field potential on the electronic levels and/or interactions between electron spins,
- the nuclear Zeeman interactions ($\hat{H}_{NZ}$) between nuclear spins in the system and the external magnetic field, which was already described in the previous section,
- the hyperfine interactions ($\hat{H}_{HF}$) between the electron's effective spin S^* and the spins of neighbouring nuclei,
- nuclear quadrupole interactions ($\hat{H}_Q$) occurring between the quadrupole moment of nuclei with $I > 1/2$ and electric field gradients in the system.

Each term in the spin-*Hamiltonian* is characterized by a number of parameters. From these parameters information about the local (chemical and geometrical) environment of the unpaired electrons can be derived. The spin-*Hamiltonian* describes a system of $(2S^* + 1)\prod_j(2I_j + 1)$ levels in between which EPR and NMR transitions may take place. For simplicity, we will write effective spin S^* again as S in the following text.[134]

The various terms of the spin-*Hamiltonian* and the corresponding parameters will be briefly discussed in the following subsections.

3.3.1 Electronic Zeeman interaction and the g tensor

In general, electrons orbiting around the nucleus in an atom or molecule exhibit next to their intrinsic magnetic moment also a magnetic moment associated with their orbital angular momentum L

$$\hat{\vec{\mu}}_L = -\mu_B \hat{\vec{L}}. \tag{3.10}$$

The total electron magnetic moment is the vector sum of the orbital and the spin contribution

$$\hat{\vec{\mu}} = \hat{\vec{\mu}}_S + \hat{\vec{\mu}}_L = -\mu_B(g_e\hat{\vec{S}} + \hat{\vec{L}}). \tag{3.11}$$

Very often in the electronic ground state the orbital momentum is quenched: $< L >= 0$. One might expect that in that case the observed g value is the same as for a free electron. However, due to spin-orbit coupling this is not the case. Spin-orbit coupling is the interaction of the electron's intrinsic magnetic moment with the magnetic field produced by its orbital motion around the nucleus. It is described by the *Hamiltonian*

$$\hat{H}_{SO} = \lambda\hat{\vec{L}} \cdot \hat{\vec{S}} \tag{3.12}$$

where λ is the spin-orbit coupling constant. This interaction mixes excited states with non-zero L in the electronic ground state. As a result, the effect of the orbital momentum to the electron magnetic moment is not exactly zero, even though it often remains small. In spin-*Hamiltonian* theory this is modelled as a g-factor differing from the free-electron value. Moreover, when the unpaired electrons are at a site with symmetry lower than tetrahedral, the g-factor depends on the magnetic field orientation with respect to the molecular axes. The electronic Zeeman interaction is then characterised by a g tensor

$$\hat{H}_{EZ} = \mu_B\vec{B} \cdot \tilde{g} \cdot \hat{\vec{S}}. \tag{3.13}$$

In this thesis, the focus is placed on the vanadyl molecular ion VO^{2+}. In this molecular ion V^{IV} has a $3d^1$ electron configuration and $S = 1/2$. In an axially symmetric (tetragonal) environment, the energy level arrangement is as shown in Figure 3.2. The z direction of the molecule is defined as the V=O axis. Taking into account the effects of spin-orbit coupling via second-order perturbation, one finds for the principal values of the g tensor

$$\begin{aligned} g_x = g_y = g_\perp &= g_e - \frac{2\lambda}{\Delta_1} \\ g_z = g_\parallel &= g_e - \frac{8\lambda}{\Delta_2} \end{aligned} \tag{3.14}$$

with Δ_1 the energy separation of the d_{xy} ground state and the degenerate d_{xz}, d_{yz} level, and Δ_2 the distance to the $d_{x^2-y^2}$ level. Typical g values for vanadyl are: $g_\perp = 1.97$ and $g_\parallel = 1.94$. When the symmetry is lower, the degeneracy of the d_{xz} and d_{yz} levels is lifted and $g_x \neq g_y$.[131,133]

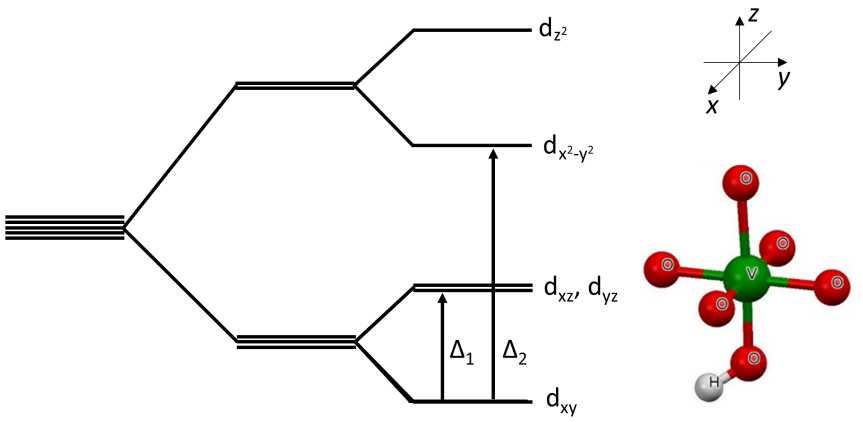

Figure 3.2: Level scheme for the *d*-orbitals in a tetragonally compressed octahedral crystal field.

3.3.1.1 Spectra of single crystals and powders

As a consequence of Equation 3.13 the resonance condition depends on the orientation of the magnetic field with respect to the principal axes of the g tensor. For $\vec{B} = B\vec{b} = B(l, m, n)$, one finds

$$h\nu = \mu_B B(\vec{b} \cdot \tilde{g} \cdot \tilde{g} \cdot \vec{b})^{1/2} \tag{3.15}$$

with

$$g = [\vec{b} \cdot \tilde{g} \cdot \tilde{g} \cdot \vec{b}]^{1/2} \tag{3.16}$$

In axial symmetry $(l^2 + m^2)^{1/2} = sin(\theta)$ and $n = cos(\theta)$. We then find

$$g = [g_{\parallel}^2 cos^2\theta + g_{\perp}^2 sin^2\theta]^{1/2} \tag{3.17}$$

where θ is angle between $\vec{B}$ and the symmetry axis.

In large single crystal samples, all molecular axes are oriented parallel (or take a limited number of symmetry related orientations) and the EPR spectrum depends on the orientation of the magnetic field with respect to the crystal axes. The MOF crystals studied in this work are typically μm-sized and powder samples, in which all single crystal orientations occur. The EPR spectrum is then the sum of all single crystal spectra.

We consider again a paramagnetic centre with spin $S = 1/2$, with an axially symmetric g tensor. The dependence of the resonance field, B_{res}, on the angle

θ between the externally applied magnetic field and the symmetry axis direction of any particular paramagnetic complexes in the system is:

$$B_{res}(\theta) = \frac{h\nu}{\mu_B}(g_{\parallel}^2 cos^2\theta + g_{\perp}^2 sin^2\theta)^{-1/2}. \tag{3.18}$$

In fine powders, it is expected that all orientations of the unique $g_{\parallel}$ axis with respect to the external magnetic field are equally probable. Therefore the resonance condition is fulfilled for a fraction of the paramagnetic centres for all fields between $h\nu/\mu_B g_{\parallel}$ and $h\nu/\mu_B g_{\perp}$. The left panel of Figure 3.3 shows an absorption spectrum and its first derivative for the case where $g_{\perp} > g_{\parallel}$. In the first derivative EPR spectrum, pronounced spectral features occur at fields corresponding to the principal values of the g tensor.

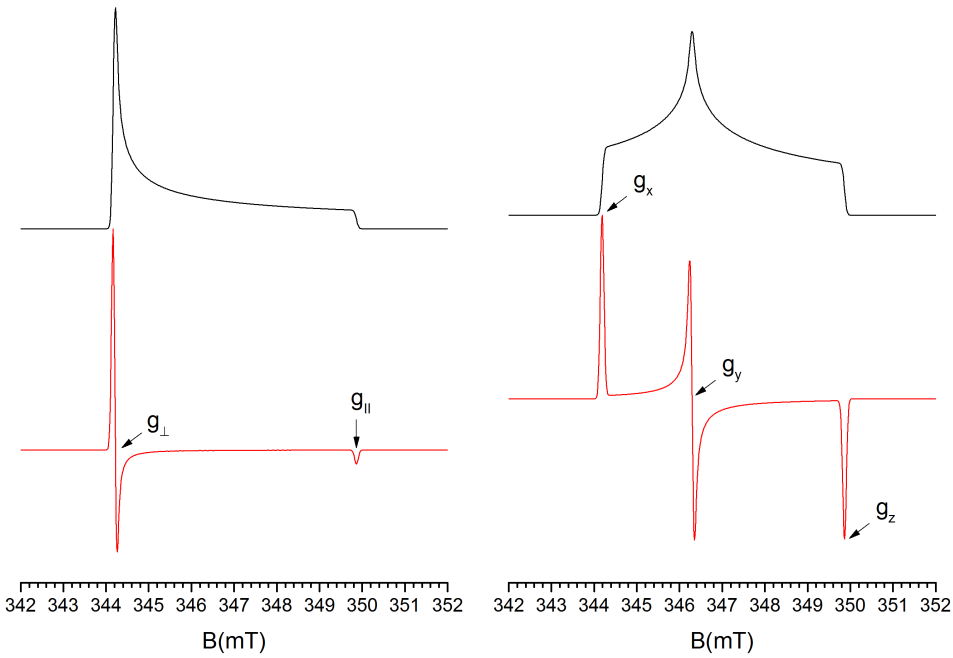

Figure 3.3: Black: absorption powder spectra, red: first derivative of absorption. Left: Simulated spectra for a axial system $g_{\perp} = 1.972$ and $g_{\parallel} = 1.940$ at $\nu_{MW} = 9.5$ GHz. Right: Simulated spectra for a rhombic system $g_x = 1.972$, $g_y = 1.960$ and $g_z = 1.940$ at $\nu_{MW} = 9.5$ GHz.

For orthorhombic g tensors, the absorption spectrum exhibits three distinct features, corresponding with the three different principal g values. The typical shape of the absorption spectrum and its derivative are given in the right panel of Figure 3.3.[131–133]

3.3.2 Zero field splitting

For centres with $S > 1/2$ the spin energy levels are already split in zero field. For high-spin transition metal centres, the origin of this ZFS is the influence of the crystal lattice potential on the total effective spin of the unpaired electrons through spin-orbit coupling. ZFS also occurs when the spins of close-by paramagnetic centres are coupled through magnetic exchange and dipole-dipole interactions. Figure 3.4 shows an example of ZFS for an $S = 1$ centre. The arrows mark the two allowed transitions, following the selection rule $\Delta M_S = \pm 1$, and the forbidden transition with $\Delta M_S = 2$.[131,134,135]

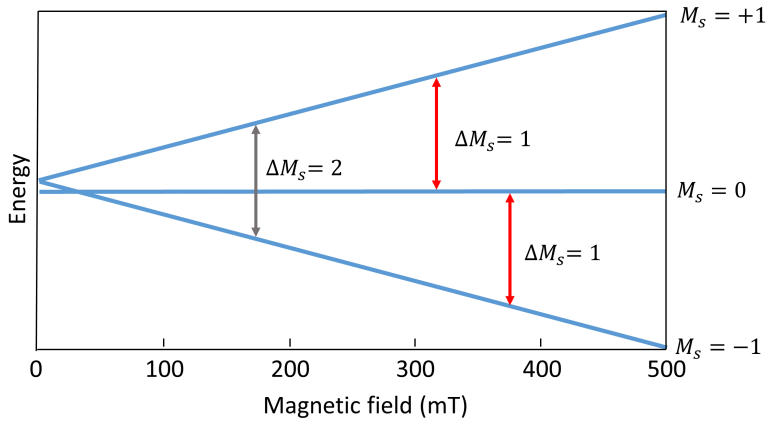

Figure 3.4: Energy levels scheme for a paramagnetic centre with $S = 1$ in an external magnetic field, $\nu_{MW} = 9.5$ GHz. In the absence of a magnetic field, the $M_S = \pm 1$ energy levels are separated from $M_S = 0$ by the zero field splitting energy E_{ZFS} (in this case $E_{ZFS} =$ 800 MHz). The grey arrow indicates the $\Delta M_S = 2$ transition while the red arrows indicate the $\Delta M_S = 1$ transitions.

The spin-*Hamiltonian* including the Zeeman and the lowest order ZFS terms is

$$\hat{H} = \mu_B \vec{B} \cdot \tilde{g} \cdot \hat{\vec{S}} + \hat{\vec{S}} \cdot \tilde{D} \cdot \hat{\vec{S}} \tag{3.19}$$

where $\tilde{D}$ is the traceless ZFS tensor with $D_x + D_y + D_z = 0$. This tensor reflects the symmetry of the paramagnetic centre: it is zero for cubic symmetry and for axial symmetry $D_x = D_y = -D_z/2$. The principal D values are often given in frequency units (MHz or GHz). In the principal axes system of $\tilde{D}$, the ZFS term H_{ZFS} can be written as:

$$\hat{H}_{ZFS} = D_x \hat{S}_x^2 + D_y \hat{S}_y^2 + D_z \hat{S}_z^2. \tag{3.20}$$

Since $S_x^2 + S_y^2 + S_z^2 = S(S+1)$, when defining $D = \frac{3}{2} D_z$ and $E = \frac{1}{2}(D_x - D_y)$, the

ZFS Hamiltonian can be rewritten as

$$\hat{H}_{ZFS} = D(\hat{S}_z^2 - \frac{1}{3}(S(S+1))) + E(\hat{S}_x^2 - \hat{S}_y^2). \tag{3.21}$$

For paramagnetic centres with axial symmetry the term $E(\hat{S}_x^2 - \hat{S}_y^2)$ is zero.[131]

3.3.2.1 Example of Cr^{III}

Framework transformations of MIL-53(Al) have been studied by Mendt *et al.* They monitored the EPR spectrum of Cr^{III} ions which substitute Al^{III} in the metal nodes.[136] Cr(III) has a $3d^3$ electron configuration, resulting in $S = 3/2$. The anisotropy of the g tensor for these centres is often very weak. When applying the magnetic field along the principal D_z direction, the energy levels for this $S = 3/2$ system are

$$\begin{aligned}
E_{+3/2} &= +\frac{1}{2}g\mu_B B + [(g\mu_B B + D)^2 + 3E^2]^{1/2} \\
E_{+1/2} &= -\frac{1}{2}g\mu_B B + [(g\mu_B B - D)^2 + 3E^2]^{1/2} \\
E_{-1/2} &= +\frac{1}{2}g\mu_B B - [(g\mu_B B + D)^2 + 3E^2]^{1/2} \\
E_{-3/2} &= -\frac{1}{2}g\mu_B B - [(g\mu_B B - D)^2 + 3E^2]^{1/2}.
\end{aligned} \tag{3.22}$$

When the magnetic field is rotated in the D tensor framework, these energy positions change. In single crystals, the principal directions of the D tensor have a fixed relation with the crystallographic axes. As a result, the EPR spectrum depends on the orientation of the magnetic field in the crystal frame. This is illustrated in Figure 3.5 with simulations for a centre with principal D orientations along the crystallographic axes and for rotation in the $D_z - D_x$ plane. The parameters are chosen to correspond with those reported in above mentioned study for Cr^{III} in LP MIL-53(Al) at RT ($g = 1.9734$, $D = 8.3$ GHz and $E = 0.0088$ GHz),[136] and the simulation is performed at $\nu = 34.0$ GHz. The simulations are limited to $B < 1600$ mT, because this corresponds with the maximum field of the Q-band spectrometer used in the published study. The angular dependence of the three $\Delta M_S = 1$ transitions can be clearly followed. They exhibit turning points (local extrema) at $\theta = 0°$ and $\theta = 90°$. The $M_S = 1/2 \rightarrow M_S = -1/2$ transition shows another extreme at $\theta \approx 42°$.

The reported RT Q-band powder EPR spectrum of Cr-doped MIL-53(Al) in the LP state is shown in Figure 3.6. Only the transitions corresponding with extremes in the single crystal angular variation are expected to be resolved. Indeed, one observes three features for the $M_S = -\frac{1}{2} \leftrightarrow +\frac{1}{2}$ at about 1220 mT for $\theta = 0°$, 1170 mT for $\theta = 90°$ and at 1320 mT for $\theta = 42°$. These three transitions are indicated in

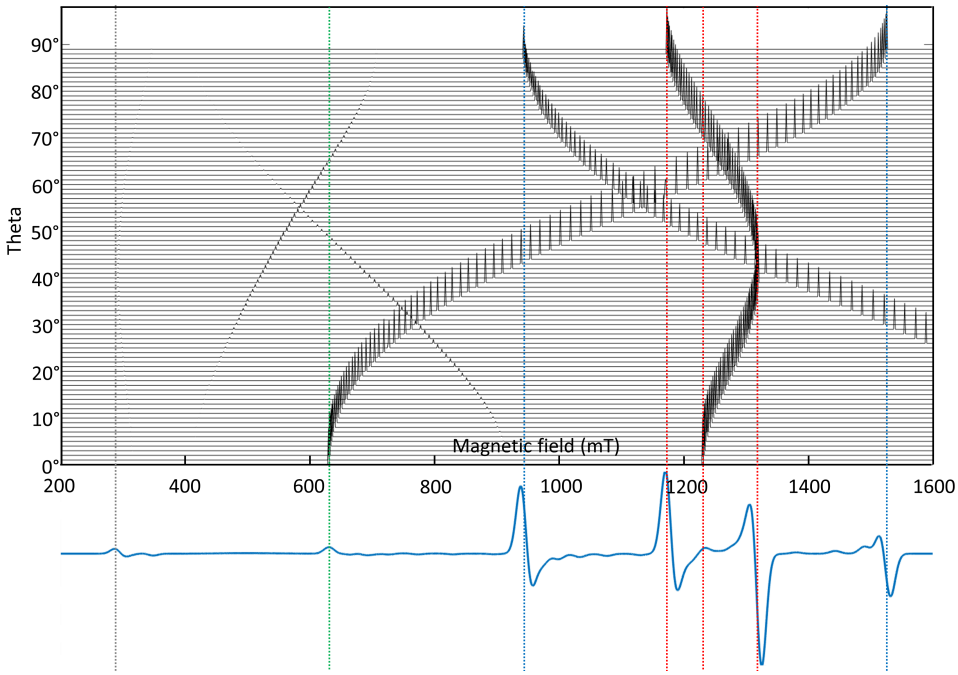

Figure 3.5: Angular dependence of the Q-band EPR spectrum (top) and powder spectrum (bottom) of Cr(III) with $g = 1.9734$, $D = 8.3$ GHz and $E = 0.0088$ GHz. Low intensity peaks in the low field range correspond to forbidden transitions, $\Delta M_S = 2$ and $\Delta M_S = 3$. Dashed lines indicate extremes in the single crystal angular variation.

red in Figures 3.5 and 3.6. The two $M_S = \pm\frac{3}{2} \leftrightarrow \pm\frac{1}{2}$ transitions at $\theta = 90°$ result in intense features at 940 mT and 1520 mT, indicated in blue. These lines show no noticeable splitting, which indicates an almost axially symmetric ZFS tensor ($E \approx 0$). The weak peak at 630 mT is assigned to the $M_S = +\frac{3}{2} \leftrightarrow +\frac{1}{2}$ transition (indicated with green dashed line) at $\theta = 0°$, the $M_S = -\frac{3}{2} \leftrightarrow -\frac{1}{2}$ transition occurs outside the measured field range. The low-field signals at 300 mT are due to forbidden transitions ($\Delta M_S = 3$).

For the MIL-53 structure the ZFS parameters D and E can be considered as a measure for the deviation of the crystal field at Cr(III) sites from octahedral symmetry. The ratio $E/D \approx 0$ indicates that the $CrO_4(OH)_2$ centres have almost perfectly axial symmetry.[136]

3.3.3 Hyperfine interaction

The magnetic interaction between the unpaired electron spin S and a nuclear spin I gives rise to an additional energy splitting and affects the EPR spectrum. This

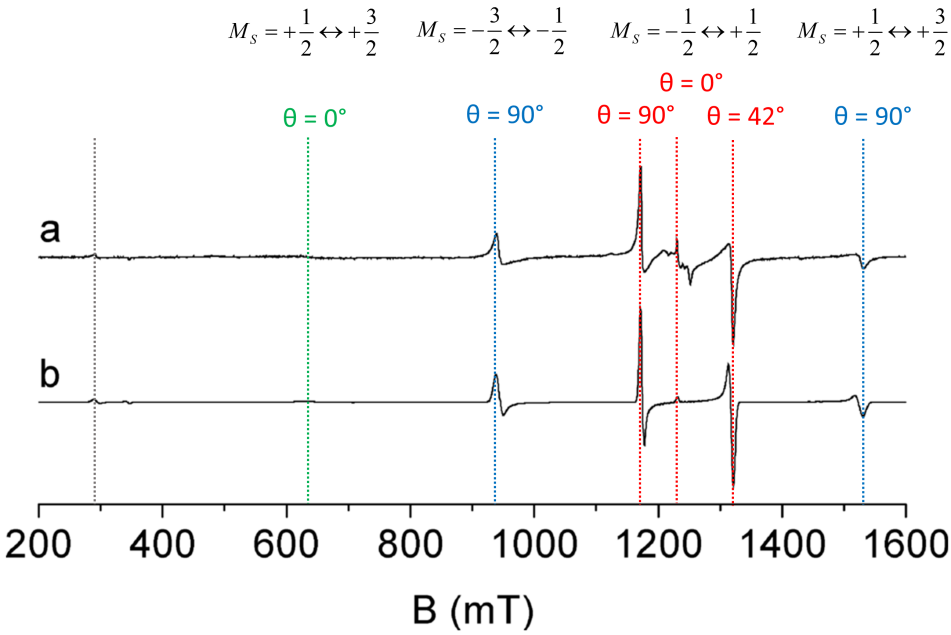

Figure 3.6: RT Q-band EPR spectrum of Cr-doped MIL-53(Al) in the LP state a) experiment and b) simulation.[136]

interaction is in general called hyperfine (HF) interaction, although sometimes the distinction between HF and superhyperfine (SHF) (ligand hyperfine) interactions is made. The term HF interaction is then preserved for the nucleus on which the unpaired electron density is for the larger part localised, while interactions with ligand and more distant nuclei are called SHF interactions. For simplicity the discussion and examples are restricted to centres with $S = 1/2$, thus without ZFS.

Like the other interactions discussed so far, HF interactions may exhibit anisotropy. In fact, the anisotropic contribution to the HF interaction is the easiest to understand, since it results from the dipolar coupling between the electron and nuclear magnetic moments, as discussed further on in section 3.4. The origin of isotropic contributions to the HF interaction is in general more difficult to explain. For transition metals, Fermi contact interaction and core polarisation are the most important. The isotropic part is interpreted as the Fermi contact interaction between an unpaired electron and the central nucleus, which is proportional to the probability of finding the electron at the nucleus. This probability is non-zero for *s* electrons.[137] A second source of isotropic HF interaction is core polarization. This is a polarization effect on the filled *s* shells through exchange interaction with the unpaired electrons in partly filled shells. In spite of the more complicated theoretical background, for introducing the effect of HF interactions to EPR spectra we first consider the isotropic interaction between one unpaired

electron ($S = 1/2$) with isotropic g and a nucleus with $I = 1/2$. The *Hamiltonian* of this HF interaction is

$$\hat{H}_{HFiso} = A\hat{\vec{S}} \cdot \hat{\vec{I}}. \tag{3.23}$$

Like the ZFS parameters, the HF constant A is often expressed in frequency units (MHz).

The complete spin-*Hamiltonian* of this system also includes the electron and the nuclear Zeeman interaction terms

$$\hat{H} = g\mu_B \vec{B} \cdot \hat{\vec{S}} - g_n \mu_n \vec{B} \cdot \hat{\vec{I}} + A\hat{\vec{S}} \cdot \hat{\vec{I}}. \tag{3.24}$$

Since the spin system is isotropic, we may choose the z-axis along the direction of the magnetic field, and Equation 3.24 can be written as:

$$\hat{H} = g\mu_B B\hat{S}_z - g_n \mu_n B\hat{I}_z + A\left(\hat{S}_z\hat{I}_z + \frac{1}{2}\left(\hat{S}_+\hat{I}_- + \hat{S}_-\hat{I}_+\right)\right). \tag{3.25}$$

The HF energy is in general much smaller than the electron Zeeman energy and one finds the eigenvalues of this *Hamiltonian* for the $|M_S, M_I\rangle$ states via second-order perturbation theory

$$\begin{aligned}
E_{(+1/2,+1/2)} &= +\frac{1}{2}g\mu_B B - \frac{1}{2}g_n\mu_n B + \frac{1}{4}A \\
E_{(+1/2,-1/2)} &= +\frac{1}{2}g\mu_B B + \frac{1}{2}g_n\mu_n B - \frac{1}{4}A + \frac{A^2}{4g\mu_B B} \\
E_{(-1/2,+1/2)} &= -\frac{1}{2}g\mu_B B - \frac{1}{2}g_n\mu_n B - \frac{1}{4}A - \frac{A^2}{4g\mu_B B} \\
E_{(-1/2,-1/2)} &= -\frac{1}{2}g\mu_B B + \frac{1}{2}g_n\mu_n B + \frac{1}{4}A
\end{aligned} \tag{3.26}$$

Very often, the second-order terms, quadratic in A may also be neglected. In Figure 3.7 the first-order energy levels of a system with $S = 1/2$ and $I = 1/2$ is presented for $A > 2g_n\mu_n B > 0$. In the left part of the figure, only the electron Zeeman interaction is taken into account. In the middle part the HF interaction is also included and the right part shows the energy levels for the complete spin-*Hamiltonian*. The dashed arrow in the middle part of the figure presents the transition corresponding to $h\nu = g\mu_B B$, thus in the absence of HF interaction. When $A \neq 0$, two allowed EPR transitions occur with $\Delta M_S = \pm 1$ and $\Delta M_I = 0$. They are represented by solid arrows. The resonant fields for these two transitions are to first-order given by

$$B = \frac{h\nu}{g\mu_B} \mp \frac{1}{2}\frac{A}{g\mu_B}. \tag{3.27}$$

These two transitions are centred around the resonance field for $A = 0$ and the

splitting between them is $\frac{A}{g\mu_B}$. The first term in Equation 3.27, which determines the centre of the HF pattern, is frequency dependent, while the second term, related to the splitting within the pattern, is not. This shows that recording and analysing spectra in several frequency bands helps in obtaining a consistent spin-*Hamiltonian* analysis. This may be particularly helpful in cases where both g and A are anisotropic. Most often, the anisotropy in the HF interaction is best determined at low microwave frequency, where the effect of g anisotropy is minimised. On the other hand, the g anisotropy is best resolved at high microwave frequency. In Chapters 5 and 7 of this thesis, microwave frequencies from 4 up to 275 GHz are used in order to obtain a consistent spin-*Hamiltonian* analysis of vanadyl centres in MIL-53(Al).

It is interesting to note that to first-order the nuclear Zeeman interaction has no influence on the transition fields. Furthermore, the sign of A, relative to g and g_n, is difficult to determine from the EPR spectrum.

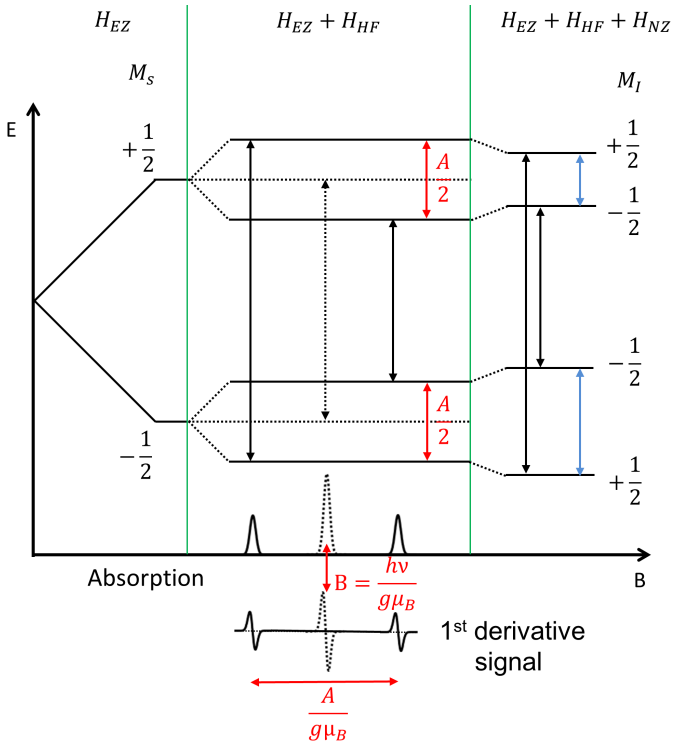

Figure 3.7: Energy levels of a paramagnetic centre with $S = 1/2$ and $I = 1/2$ ($A > 2g_n\mu_n B > 0$). The electron Zeeman, (first-order) HF and nuclear Zeeman interactions are successively taken into account. Solid black arrows represent allowed EPR transitions, blue arrows represent allowed NMR transitions. The dashed arrow represents the transition when only electron Zeeman interaction is considered. The absorption and first derivative EPR spectra are also shown.

The blue arrows in Figure 3.7 represent the allowed NMR transitions. They obey the selection rules $\Delta M_S = 0$ and $\Delta M_I = \pm 1$, and are found at the NMR resonance frequencies:

$$\Delta E_1 = |g_n \mu_n B + \frac{1}{2}A| \qquad \Delta E_2 = |g_n \mu_n B - \frac{1}{2}A|. \tag{3.28}$$

For the situation in Figure 3.7 ($A > 2g_n\mu_n B > 0$), the two transitions are centred at $A/2$ with a splitting of $2g_n\mu_n B$ between them. If $2g_n\mu_n B > A > 0$, the transitions are centred around $g_n\mu_n B$ at a distance A from one another. If the HF coupling is very small, the two transitions coincide at the Larmor frequency of the nucleus.[134,138–140]

3.3.3.1 A tensor

Now anisotropy can gradually be introduced into the spin-*Hamiltonian*. First, we only consider anisotropy in the HF interaction, which is then characterized by a HF tensor $\tilde{A}$. The spin-*Hamiltonian* becomes

$$\hat{H} = g\mu_B \vec{B} \cdot \hat{\vec{S}} + \hat{\vec{S}} \cdot \tilde{A} \cdot \hat{\vec{I}} - g_n \mu_n \vec{B} \cdot \hat{\vec{I}}. \tag{3.29}$$

In general, the electron spin is quantized along the resultant of the externally applied magnetic field and the magnetic field created by the nucleus. Both the magnitude of this resultant field and its orientation with respect to the externally applied magnetic field are orientation dependent. For small HF couplings, however, (or sufficiently high magnetic field) the HF field is much smaller than the applied field: the electron Zeeman interaction is the dominant energy term. Hence, the electron magnetic moment alignment is much less affected by the nuclear magnetic moment than by $\vec{B}$. This allows quantisation of $\hat{\vec{S}}$ along $\vec{B} = B\vec{b}$: $\hat{\vec{S}} = \vec{b}\hat{S}_z$. Furthermore, only first-order HF corrections to the electron Zeeman energy levels are considered.

Inserting all these approximations in 3.29 one obtains

$$\hat{H} = g\mu_B B\hat{S}_z + S_z \vec{b} \cdot \tilde{A} \cdot \hat{\vec{I}} - g_n \mu_n B\vec{b} \cdot \hat{\vec{I}}. \tag{3.30}$$

The first-order eigenvalues are

$$E = g\mu_B B M_S + (M_S^2 \vec{b} \cdot \tilde{A} \cdot \tilde{A} \cdot \vec{b} + (g_n\mu_n B)^2 - 2M_S g_n \mu_n B\vec{b} \cdot \tilde{A} \cdot \vec{b})^{1/2} M_I. \tag{3.31}$$

It is interesting to note that in general the nuclear Zeeman interaction may have a non-negligible effect on the EPR spectrum. However, if the nuclear Zeeman interaction is much smaller than the HF interaction, the second and third terms in

the quadratic HF correction may be neglected. We then find

$$E = g\mu_B B M_S + (\vec{b} \cdot \tilde{A} \cdot \tilde{A} \cdot \vec{b})^{1/2} M_S M_I. \tag{3.32}$$

Equation 3.32 shows that the EPR spectrum ($\Delta M_S = \pm 1$ and $\Delta M_I = 0$) contains $(2I + 1)$ equally spaced lines separated by the effective HF coupling constant $\vec{b} \cdot \tilde{A} \cdot \tilde{A} \cdot \vec{b}$.

If both the electron Zeeman and the HF interaction are anisotropic Equation 3.32 can be extended to

$$E = g\mu_B B M_S + (\vec{b} \cdot \tilde{g} \cdot \tilde{A} \cdot \tilde{A} \cdot \tilde{g} \cdot \vec{b})^{1/2} M_S M_I \tag{3.33}$$

where

$$g = (\vec{b} \cdot \tilde{g} \cdot \tilde{g} \cdot \vec{b})^{1/2} \tag{3.34}$$

and the $\Delta M_S = 1$ and $\Delta M_I = 0$ transitions are found at:

$$h\nu = g\mu_B B + (\vec{b} \cdot \tilde{g} \cdot \tilde{A} \cdot \tilde{A} \cdot \tilde{g} \cdot \vec{b})^{1/2} M_I. \tag{3.35}$$

This shows that the effective HF coupling constant also reflects the g-anisotropy. This is particularly true for paramagnetic centres with low symmetry where the principal directions of $\tilde{g}$ and $\tilde{A}$ do not coincide. Even though for powder samples the orientation of the principal $\tilde{g}$ and $\tilde{A}$ directions cannot be determined in an absolute (molecular or crystal) reference frame, the principal directions of $\tilde{A}$ can still be determined relative to those of $\tilde{g}$.[134,138–140]

3.3.3.2 Example 1: TEMPO

The breathing of the MIL-53(Al) framework was studied by Sheveleva *et al.* by monitoring the EPR spectrum of TEMPO (2,2,6,6-tetramethyl-1-piperidinyloxyl) molecules introduced in the pores after synthesis and activation.[141] TEMPO is a stable radical with a nitroxide group, in which the unpaired electron ($S = 1/2$) is delocalised over a nitrogen and an oxygen atom. The unpaired electron interacts with a ^{14}N nucleus, which has $I = 1$. The TEMPO molecule is shown in Figure 3.8.

Both the electron Zeeman and the HF interaction are anisotropic. The first-order energy levels are

$$\begin{aligned} E_{(\pm 1/2, \pm 1)} &= \pm\frac{1}{2} g\mu_B B \mp g_n \mu_n B + \frac{1}{2} A \\ E_{(\pm 1/2, 0)} &= \pm\frac{1}{2} g\mu_B B \\ E_{(\pm 1/2, \mp 1)} &= \pm\frac{1}{2} g\mu_B B \pm g_n \mu_n B - \frac{1}{2} A \end{aligned} \tag{3.36}$$

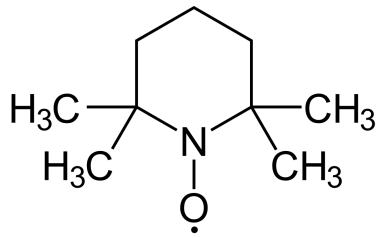

Figure 3.8: Structure of TEMPO.[142]

with g and A defined in Equations 3.34 and 3.33, respectively. The principal axes of these tensors were found to coincide. Considering the selection rules, three allowed EPR transitions are observed for each magnetic field orientation. The powder spectrum reflects the extreme features in the angular dependence of this spectrum.[131]

Figure 3.9 a, shows the published Q-band EPR spectrum of TEMPO molecules immobilized in the MIL-53(Al) framework at 80 K. Spectrum analysis by Shevel-eva *et al.* allowed to determine $g_x = 2.0098$, $g_y = 2.0068$, $g_z = 2.0027$ and $A_x = A_y = 0.65$ mT, $A_z = 3.7$ mT.[141] In the experimental spectrum the g-anisotropy is not completely resolved. This is demonstrated by a spectrum simulation, presented in Figure 3.9 b. The good agreement between experimental and simulated spectrum shows that the spin-*Hamiltonian* parameters have been determined accurately. The different g components in the spectrum are, however, still partly overlapping. If the simulation is made in W-band, the g anisotropy is completely resolved. This is shown in Figure 3.9 c. The g_x, g_y and g_z spectral components are split into three components by the ^{14}N HF interaction.

3.3.3.3 Second-order HF effects

So far only the first-order effect of the HF interaction was considered. If in Equation 3.26 (g and A isotropic) one also takes the terms quadratic in A into account, one finds the following transition fields for the $S = 1/2$, $I = 1/2$ system:

$$\begin{aligned} B(M_I = 1/2) &= \frac{h\nu}{g\mu_B} - \frac{A}{2g\mu_B} - \frac{A^2}{4g\mu_B h\nu} \\ B(M_I = -1/2) &= \frac{h\nu}{g\mu_B} + \frac{A}{2g\mu_B} - \frac{A^2}{4g\mu_B h\nu}. \end{aligned} \tag{3.37}$$

We see that the distance between these two transitions still directly yields the HF coupling A, but the centre of the pattern is shifted downwards from $\frac{h\nu}{g\mu_B}$.

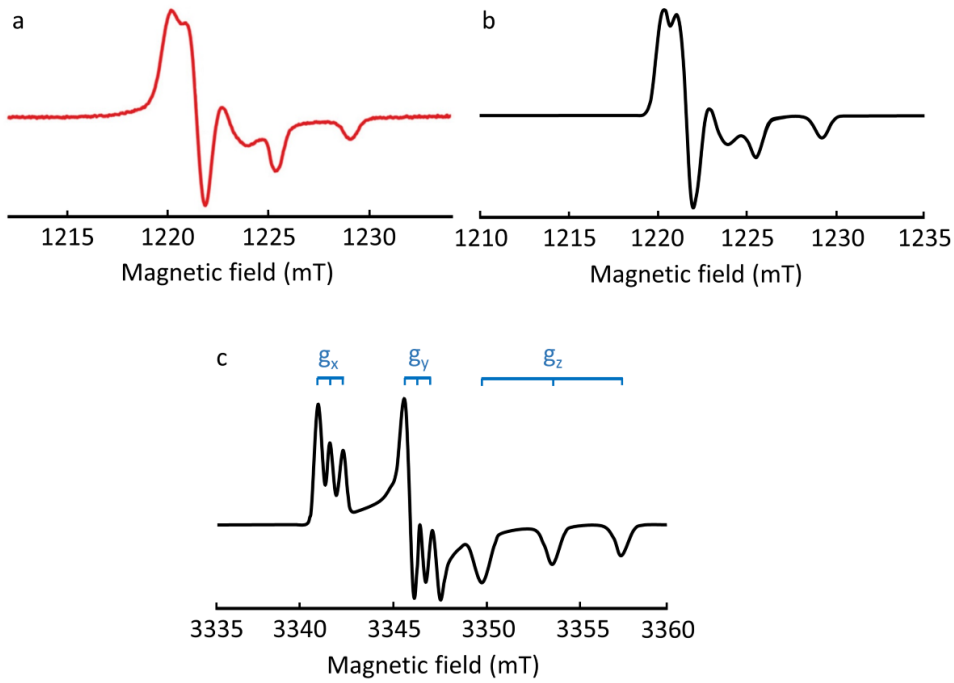

Figure 3.9: a: Experimental Q-band EPR spectrum of TEMPO@MIL-53(Al) at 80 K with $g_x = 2.0098$, $g_y = 2.0068$, $g_z = 2.0027$ and $A_x = A_y = 0.65$ mT, $A_z = 3.7$ mT.[141] b: Simulated Q-band (34.35 GHz) EPR spectrum. c: Simulated W-band (94 GHz) EPR spectrum.

More generally, for spin systems with $S = 1/2$ and arbitrary I one finds

$$B(M_I) = \frac{h\nu}{g\mu_B} - \frac{AM_I}{g\mu_B} - \frac{A^2(I(I+1) - M_I^2)}{2g\mu_B h\nu}. \tag{3.38}$$

Hence, one finds that the second-order correction is the same for the transitions corresponding to $+M_I$ and $-M_I$, but is different for the different $|M_I|$ values.[131,133]

3.3.3.4 Example 2: V(IV)

The majority of the experimental work in this thesis deals with V^{IV} centres, which, as mentioned earlier, have a $3d^1$ electron configuration and $S = 1/2$. The ^{51}V nucleus has $I = 7/2$. There are sixteen possible $|M_S, M_I\rangle$ states. Their energy levels are found by (approximately) diagonalizing the spin-*Hamiltonian* 3.29 and are presented in Figure 3.10, along with the allowed EPR transitions.

A typical experimental X-band powder EPR spectrum of V-doped MIL-53(Al) in the AS state (recorded during this project) is presented in Figure 3.11. The HF

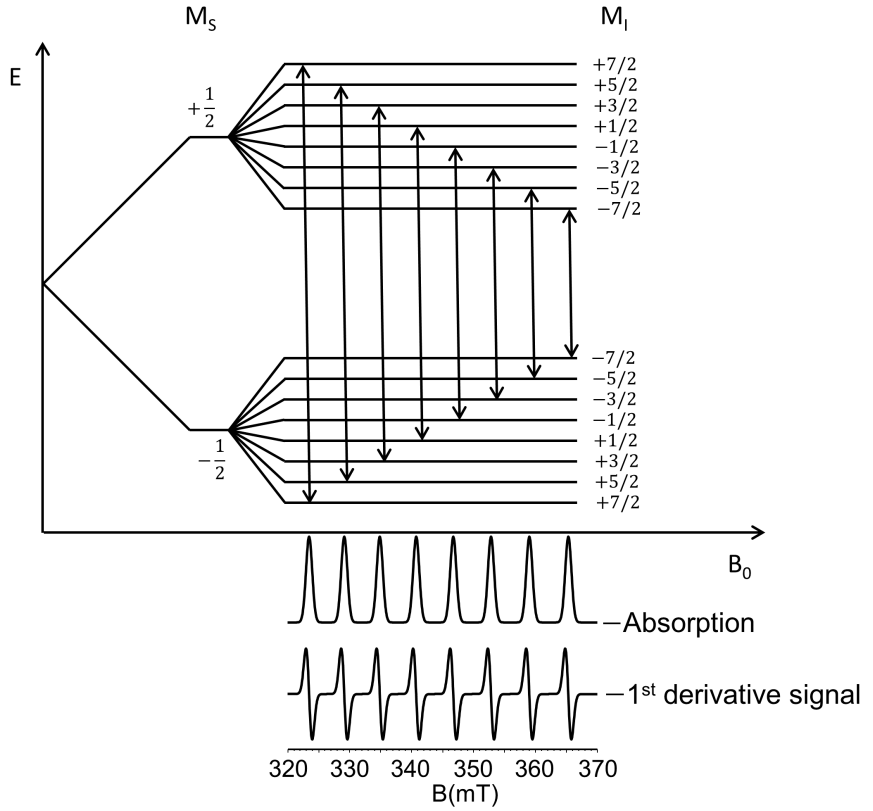

Figure 3.10: Energy levels for a system with $S = 1/2$ and $I = 7/2$ with isotropic g and $A > 0$ and first-order HF interaction approximation taken into account. The arrows represent allowed EPR transitions. The absorption EPR spectrum is represented together with its first derivative.

structure due to the interaction of the unpaired electron with the ^{51}V nucleus is clearly resolved. The red markers indicate two sets of eight resonance lines: the centre has a close-to-axial g tensor with $2 > g_x \approx g_y > g_z$ and a HF tensor with $A_x \approx A_y \approx 165$ MHz and $A_z \approx 500$ MHz, which are typical for the vanadyl molecular ion, V^{IV}=O.

To illustrate the significance of second-order HF effects, Figure 3.12 shows again this spectrum zoomed in on the central region consisting of eight resonance lines. The blue lines indicate the predicted positions when ignoring second-order HF effects (third term in Equation 3.38) and the red lines show the experimental peak positions. All transitions are shifted to lower magnetic field positions with respect to the first-order calculations. The $|M_I| = 1/2$ transitions are shifted the most, while the $|M_I| = 7/2 = I$ are shifted least. As a result, the separation between neighbouring transitions increases with increasing field.

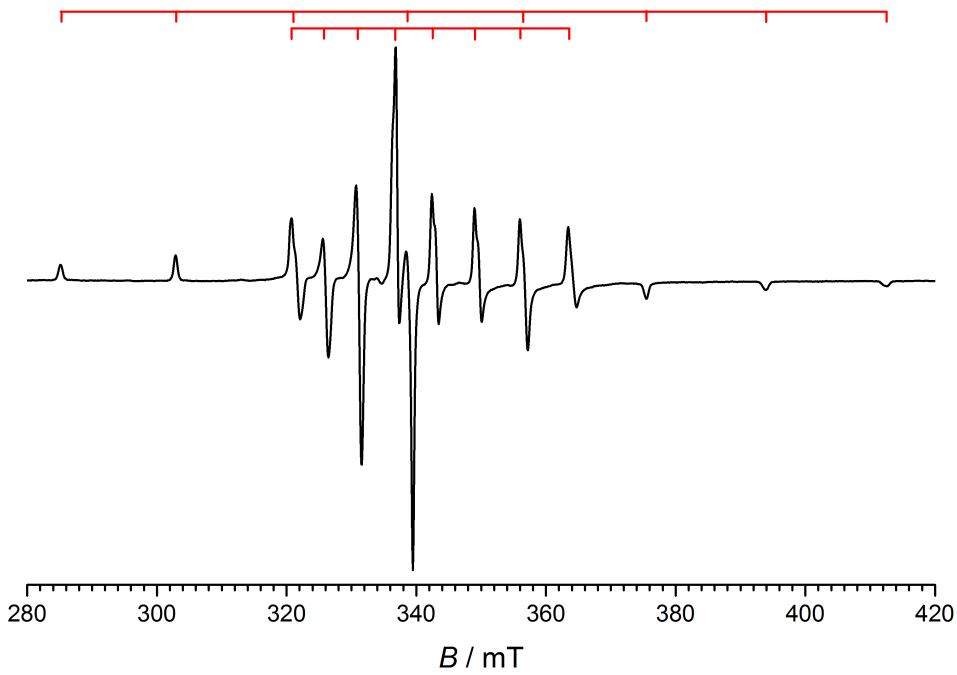

Figure 3.11: Experimental X-band powder EPR spectrum of V-doped MIL-53(Al) in the AS state, $\nu_{MW} = 9.477$ GHz. The red markers indicate the two sets of eight resonance lines corresponding to the "parallel" and "perpendicular" components.

3.3.4 Nuclear quadrupole interaction

Nuclei with $I > 1/2$ can have a non-spherical charge distribution and thus an electric quadrupole moment. The quadrupole moment of nuclei with $I = 1/2$, which have a spherical charge distribution, is zero. The magnitude of the quadrupole moment is a measure of the extent to which the charge distribution deviates from spherical symmetry.

The quadrupole moment shows no interaction with a uniform electric field, but in a non-uniform electric field the quadrupole moment interacts with the electric field gradient. The spin-*Hamiltonian* of this interaction is:

$$\hat{H} = \hat{\vec{I}} \cdot \tilde{Q} \cdot \hat{\vec{I}} \tag{3.39}$$

where $\tilde{Q}$ is the electric quadrupole tensor. The effect of the quadrupole interaction on the nuclear spin levels is analogous to the ZFS of electron spin systems.

It can be calculated that the nuclear quadrupole interaction induces no first-order corrections to the EPR transition fields. Data available in literature indicate that the ^{51}V nuclear quadrupole interaction for vanadyl complexes is very small in

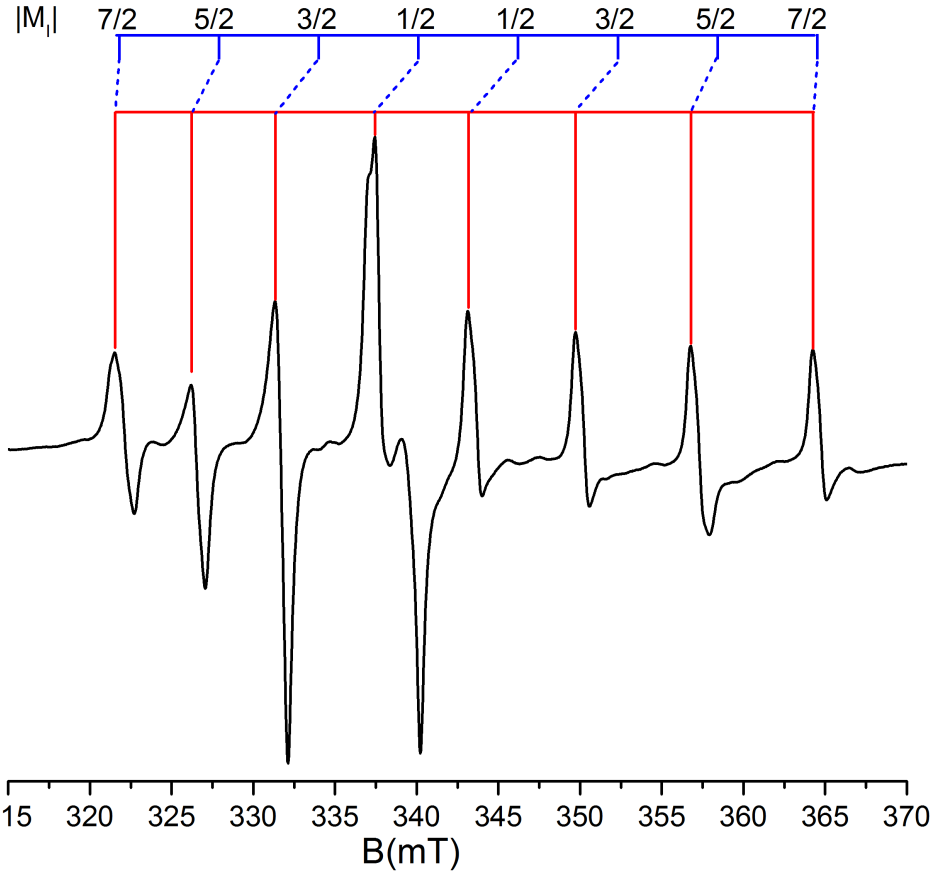

Figure 3.12: Experimental X-band powder EPR spectrum of V-doped MIL-53(Al) in the AS state, $\nu_{MW} = 9.477$ GHz. The blue lines indicate the positions of the resonance peaks predicted by first-order HF interaction. The red lines indicate the experimental peak positions.

comparison with the HF and nuclear Zeeman interactions.[143,144] For this reason, we omitted this interaction in the spectral analyses of these complexes in this work.

3.4 Electron nuclear double resonance (ENDOR)

In the previous sections it was shown how EPR provides symmetry information on paramagnetic centres via the anisotropy revealed in (single crystal and powder) spectra, and chemical information through HF interactions. However, in many practical cases, the unpaired electrons exhibit weak interactions with a large number of nuclear spins, which are not resolved in the EPR spectra. This

limitation can be overcome with the ENDOR technique, which detects NMR transitions via their influence on the EPR spectrum intensity. In this way, ENDOR attains higher resolution than EPR and higher sensitivity than NMR.

If a paramagnetic centre with electron spin S in an external magnetic field interacts with N neighbouring nuclei (with spin I_j, $j = 1, N$), the total number of allowed EPR transitions is:

$$n_{EPR} = 2S\prod_{j=1}^{N}(2I_j + 1) \tag{3.40}$$

taking into account the selection rules $\Delta M_S = \pm 1$ and $\Delta M_I = 0$ for every nucleus. This amount of allowed transitions has a big impact on the shape of the EPR spectrum. In practice only a few strong HF interactions result in resolved splittings in the EPR spectrum, while the others just contribute to the linewidth (inhomogeneous broadening).

The situation is different for the NMR transitions. The selection rules are $\Delta M_S = 0$ and all $\Delta M_{I,k\neq j} = 0$ except for nucleus j, where $\Delta M_{I,j} = \pm 1$. The number of allowed NMR transitions is:

$$n_{NMR} = (2S + 1)\sum_{j=1}^{N}(2I_j). \tag{3.41}$$

The number of NMR transitions thus grows considerably slower with increasing N and ENDOR spectroscopy takes advantage of this.

Figure 3.13 again shows the energy level diagram for an isotropic centre with $S = 1/2$ and $I = 1/2$, along with the lowest order electron Zeeman, HF and nuclear Zeeman energy corrections. The EPR transition microwave frequencies (black arrows) at a fixed field value occur at ν_{e1} and ν_{e2}. NMR transitions at radiofrequencies ν_{n1} and ν_{n2} are shown as blue arrows. In ENDOR experiments, the NMR transitions are detected as an enhancement of the intensity of a partially saturated EPR transition, by creating an additional spin relaxation path. ENDOR spectra are recorded scanning the radiofrequency (RF) while the magnetic field is kept constant at the centre of the saturated EPR line.

To first-order, the NMR transition frequencies are given by

$$\begin{aligned}\nu_{n1} &= \frac{1}{h}(E_{(+1/2,+1/2)} - E_{(+1/2,-1/2)}) = \frac{1}{h}(g_n\mu_n B - \frac{1}{2}A)\\ \nu_{n2} &= \frac{1}{h}(E_{(-1/2,-1/2)} - E_{(-1/2,+1/2)}) = \frac{1}{h}(g_n\mu_n B + \frac{1}{2}A).\end{aligned} \tag{3.42}$$

Here $g_n\mu_n B/h = \nu_n = \nu_L$ is the Larmor frequency of the nucleus for the fixed (static) magnetic field at which the ENDOR spectrum is recorded. It is magnetic field dependent, which allows to identify nuclei by recording how

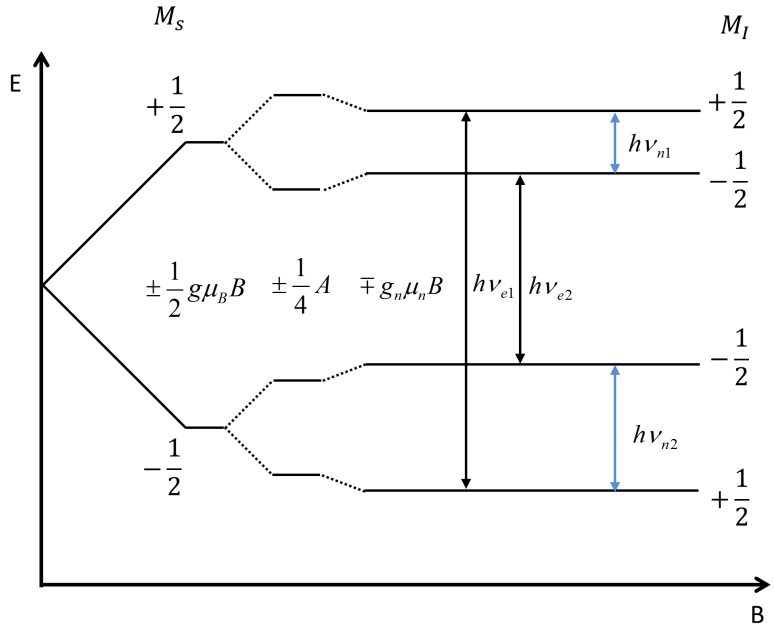

Figure 3.13: Energy level diagram for a system with $S = 1/2$ and $I = 1/2$ considering only first-order energy terms. The EPR transitions following the selection rules $\Delta M_S = \pm 1$ and $\Delta M_I = 0$ are shown with black arrows. Frequencies of microwaves required for these transitions are ν_{e1} and ν_{e2}. The blue lines represent NMR transitions that give rise to ENDOR lines. These transitions follow selection rules $\Delta M_S = 0$ and $\Delta M_I = \pm 1$ with corresponding radiofrequencies ν_{n1} and ν_{n2}.

ENDOR transitions shift when the magnetic field is varied. The ENDOR spectrum analysis further depends on the relative magnitude of the HF and nuclear Zeeman energy terms. If $A < 2h\upsilon_L$ the two ENDOR lines, ν_{n1} and ν_{n2}, are centred at υ_L and separated by A/h. If A and g_n are both positive, the lower frequency line corresponds to the transition in the $M_S = +1/2$ manifold, and both frequencies shift up when raising the static magnetic field. If $A > 2h\upsilon_L$, the two lines are separated by $2\nu_L$ and the sum of their frequencies yields the HF coupling constant (in frequency units). When raising the static magnetic field, the upper line shifts to higher frequencies, whereas the lower shifts downwards.[131,133]

As an example, the low frequency part of the ENDOR spectrum of AS V-doped MIL-53(Al) recorded during this project is presented in Figure 3.14. This spectrum revealed the interaction of the unpaired electron on the V^{IV} ion with two equidistant ^{27}Al nuclei ($I = 5/2$, 100% natural abundance) along the *c*-axis of the framework (Al-OH chains). The Larmor frequency of Al is marked with an arrow. The static magnetic field is set to a position where many (nearly all) molecular orientations contribute to the EPR spectrum (see section 3.4.2). As a result, the ENDOR spectrum reveals the full anisotropy of the (practically axial)

HF interaction. This one spectrum allows to determine the two distinct principal values of the HF tensor: $A_\perp$ and $A_\parallel$.

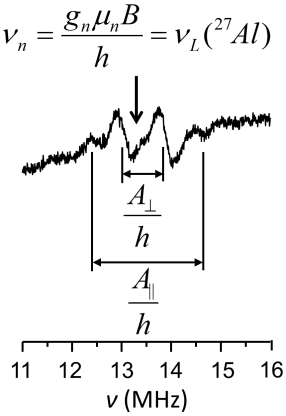

Figure 3.14: Experimental ENDOR spectrum of AS V-doped MIL-53(Al), recorded at 10 K, with $B_{stat} = 1218$ mT. The Larmor frequency of Al is indicated together with $A_\perp$ and $A_\parallel$.

In this example, the HF interaction is dominated by dipolar interaction between the electron and nuclear spins. Since the ^{27}Al nucleus is at a relatively large distance R from the V^{IV} ion on which the electron is centred, the point dipole approximation applies.[134] Allowing also for a (small) HF isotropic contribution, we then find

$$\begin{aligned} A_\parallel &= A_{iso} + 2 g_n \mu_n g_\parallel \mu_B / R^3 \\ A_\perp &= A_{iso} - g_n \mu_n g_\perp \mu_B / R^3. \end{aligned} \tag{3.43}$$

Hence, from $A_\parallel - A_\perp$ we can estimate the distance between the centre of unpaired electron density and the interacting nucleus

$$R = \left(\frac{\mu_0}{4\pi} \mu_B g_n \mu_n \frac{2 g_\parallel + g_\perp}{A_\parallel - A_\perp}\right)^{1/3}. \tag{3.44}$$

It is worth repeating that in practice HF constants are very often determined in frequency or field units. Equation 3.44 can easily be adapted to that. In Chapter 5 we applied Equation 3.44 in analysing the ENDOR spectra of ^{1}H and ^{27}Al nuclei surrounding V^{IV}=O molecular ions, replacing Al-OH in AS MIL-53(Al). For these nuclei the HF interaction was not resolved in the EPR spectra. Their detection with ENDOR was indispensable for demonstrating the success of the doping procedure.[145]

3.4.1 Detecting ENDOR

ENDOR is more sensitive than the direct detection of NMR transitions, because it is observed as a desaturation effect of an EPR transition. ENDOR is the result of a very delicate interplay between electron spin, nuclear spin, and electron-nuclear cross relaxation processes, which restore spin populations to thermal equilibrium after an excitation. These processes and their respective time constants (τ_e, τ_n electron and nuclear spin relaxation times, τ_x, τ_{xx} cross relaxation times) are indicated on Figure 3.15 for a paramagnetic centre with $S = 1/2$ and $I = 1/2$.

Let us concentrate on one of the two allowed EPR transitions of this spin system. Electron spins excited from level 1 to level 4 can relax back to the ground state via three pathways: i) directly with time constant τ_e, ii) following the path $4 \rightarrow 3 \rightarrow 1$ with time constant $\tau_n + \tau_x$, and iii) in the sequence $4 \rightarrow 2 \rightarrow 1$ with time constant $\tau_{xx} + \tau_n$. In practice, only the first pathway is effective, since nuclear spin relaxation times are several orders of magnitude longer than electron spin and cross relaxation times. When at high microwave power the electron spin pumping rate becomes comparable to $1/\tau_e$, the EPR transition starts saturating. Under these conditions, keeping the microwave power fixed, the signal intensity increases if the total relaxation time between levels 4 and 1 decreases, or equivalently, if the total relaxation rate increases. When sweeping the frequency of incident high power radiowaves, the latter happens at the ENDOR resonance frequencies ν_1 and ν_2, where the relaxations times of pathways ii) and iii) are reduced to τ_x and τ_{xx}, respectively. A similar reasoning can be followed to conclude that these two ENDOR transition frequencies can also be detected by saturating the second EPR transition $2 \rightarrow 3$.[132,134]

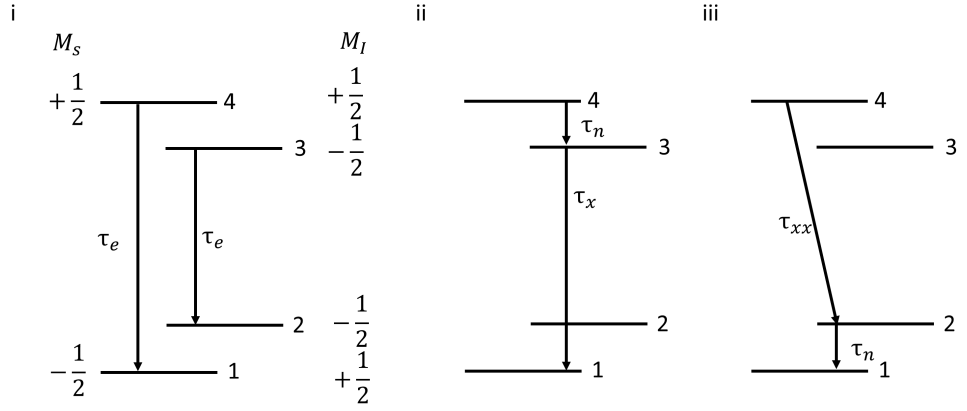

Figure 3.15: Relaxation paths for a system $S = 1/2$ and $I = 1/2$ together with their relaxation times. i: Two allowed EPR transitions with τ_e. ii: In the case where the low field EPR line is saturated and the ENDOR line is observed on the ν_{n1} frequency, relaxation path $4 \rightarrow 3 \rightarrow 1$ is shown. iii: Relaxation path $4 \rightarrow 2 \rightarrow 1$ with time constant $\tau_{xx} + \tau_n$.

3.4.2 Orientation selectivity of ENDOR

In section 3.3.2.1 it was already explained that for anisotropic paramagnetic centres the EPR spectrum depends on the orientation of the crystal with respect to the direction of the external magnetic field, because their molecular reference frame has a fixed relation to the crystallographic axes. Since in the powder EPR spectrum only the extremes of the angular dependence are resolved, the powder EPR spectrum is not orientation dependent.

ENDOR spectra recorded for single crystals can obviously also depend on the magnetic field orientation. Remarkably, orientation dependence of ENDOR spectra can also be recorded on powder samples, because ENDOR spectra are recorded by saturating the EPR spectrum at a fixed magnetic field position. This implies that by choosing a static magnetic field value within the EPR powder spectrum, only those crystal orientations for which an EPR transition is saturated can contribute to the ENDOR spectrum.[137]

This is illustrated in Figure 3.16. On the left side, a simulated powder EPR spectrum (Q-band, 34.00 GHz) of a paramagnetic centre with $S = 1/2$ is shown with $g_\perp = 1.97$ and $g_\parallel = 1.93$. The $g_\perp$ and $g_\parallel$ components are indicated. The simulated field dependence of the ENDOR spectra in the magnetic field range 1225-1265 mT is shown in the middle. The ENDOR spectra are simulated for one hydrogen nucleus ($I = 1/2$) with $A_\perp = -3.1$ MHz and $A_\parallel = 8.6$ MHz. The EPR linewidth is chosen such that this HF interaction is not resolved in the EPR spectrum. If the static magnetic field is set to the $g_\perp$ component, only crystal orientations corresponding to $g_\perp$ will contribute to the ENDOR spectrum. It is convenient to represent the field dependence of the ENDOR spectrum in a colour plot. On the right hand side of the figure this representation is shown. The red to yellow regions are the positive parts of the first derivative (frequency modulated) ENDOR spectra and the blue regions are the parts below zero (green $\approx$ zero).

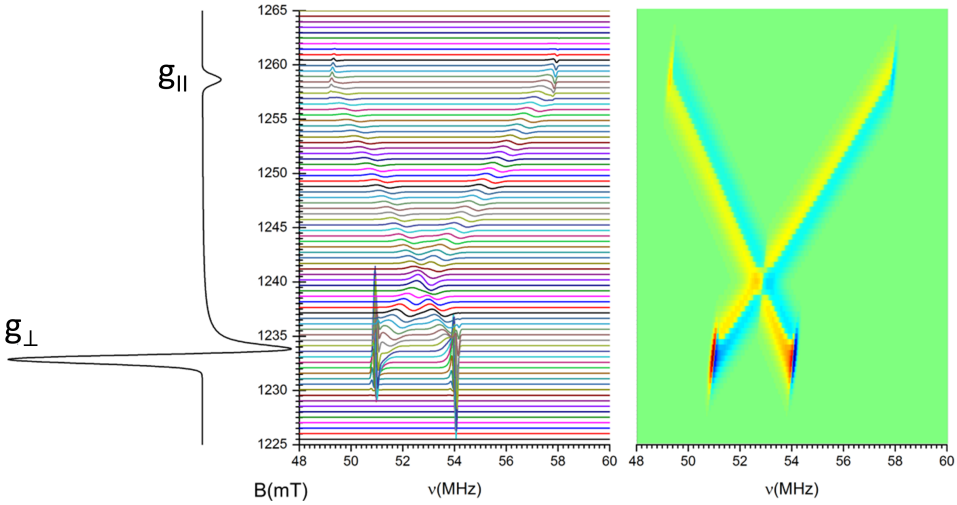

Figure 3.16: Left: Simulation of powder EPR spectrum of an unpaired electron with $g_\perp = 1.97$ and $g_\parallel = 1.93$. Middle: Simulated field dependence of the ENDOR spectra with ^{1}H, $A_\perp = -3.1$ MHz and $A_\parallel = 8.6$ MHz. Right: Colour plot of field dependence ENDOR.

3.5 Experimental detection of the EPR signal

The X and Q-band spectrometers used in the experimental part of this thesis are shown in Figures 3.17 and 3.18. An EPR spectrometer has four main parts: a microwave bridge (marked with light blue rectangle), a microwave cavity, an electromagnet (red) and a console (yellow). Additionally, the magnet power supply (green arrow in X-band setup and green rectangle in Q-band setup) provides current to the magnet. The frequency counter (dark blue) is used for precise microwave frequency measurement. The RF amplifier (purple) forms part of the extension of the setup for ENDOR measurements. The temperature controller (magenta) and the (helium) flow regulator (grey) are used for low temperature measurements (down to 4 K). Low temperature measurements also require pumps (orange), a cryostat and a liquid helium or nitrogen dewar. The X-band spectrometer can be combined with a particular cryostat to measure above RT, up to 373 K (N_2 is used). The high temperature cavity, using N_2 gas for heat transfer and shown in Figure 3.17, allows to go up to 1272 K. It provides a huge range of possibilities. In the Q-band setup the microwave cavity is placed inside the cryostat.

The microwave bridge consists of a microwave source, the detection and the operation system. The microwave source, Figure 3.19 A, is a vacuum tube klystron in old spectrometers, or a solid state source (Gunn diode) in more modern versions. The microwaves are split in two parts, a power arm and a reference arm. The power arm consists of a variable attenuator B, which precisely controls

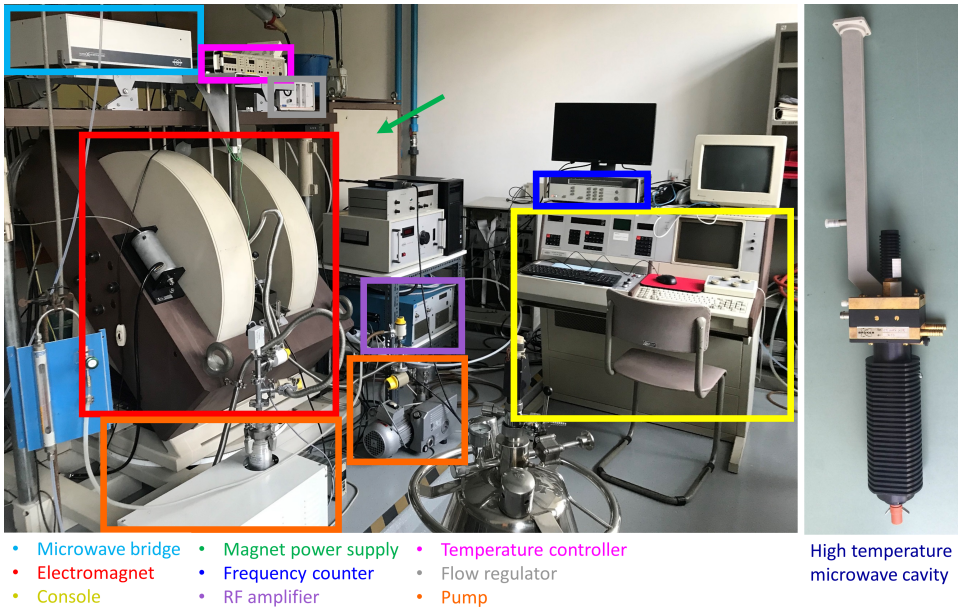

Figure 3.17: X-band EPR setup with high temperature EPR microwave cavity.

the microwave power that gets to the sample. After the attenuator, circulator C directs the microwaves from the source to the sample cavity, D. The detector (E) measures changes in the microwave power reflected back from the cavity through the circulator. In Bruker spectrometers this is a Schottky diode. The diode converts the microwave power to an electrical current. The reference arm consist of an attenuator and a phase shifter, F. It supplies the detector with part of the microwave power from the source (bias). The phase shifter ensures that the microwaves coming from the reference arm are in phase with the reflected microwaves from the cavity. The frequency of the microwaves can slightly shift during the measurements and it is stabilized by the automatic frequency control (AFC). The EPR cavity is a metal rectangular or cylindrical box. Its dimensions are chosen such that its resonance frequency lies in the microwave range of the source. The cavity is placed in between the poles of the electromagnet. The geometry of the cavity is designed so that a standing wave pattern is produced for microwaves at the cavity resonance frequency. This allows a high EM energy density in the cavity. The cavity is characterized by a quality factor Q, defined as

$$Q = \frac{\text{energy stored in cavity}}{\text{energy dissipated per microwave period}} = \frac{\nu_{res}}{\Delta\nu} \tag{3.45}$$

where ν_{res} is the resonant frequency of the cavity and $\Delta\nu$ is the full width at half maximum of the cavity dip. It is a measure of the microwave energy density in the cavity and determines the sensitivity of the system. A standing EM wave

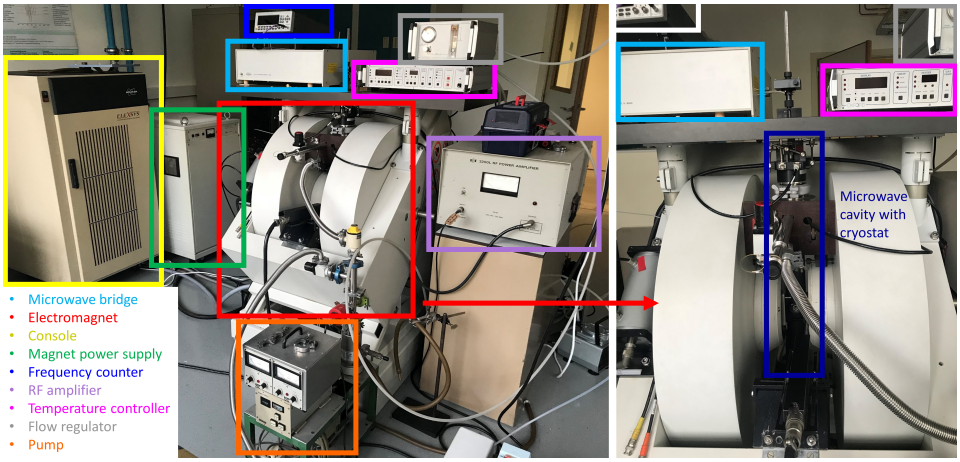

Figure 3.18: Q-band EPR setup.

in the cavity has electric and magnetic field components exactly out of phase. For maximum sensitivity the sample is placed in the node of the microwave electric field to minimize the dielectric losses in the cavity, and in the anti-node of the magnetic field, maximizing the magnetic dipole transition probability. At the resonance frequency of the cavity, the reflected power reaches a minimum. When the sample absorbs microwave energy, cavity losses increase, the resonance frequency slightly changes and the Q factor lowers. This all leads to an increased reflected microwave power: the EPR signal. The cavity makes EPR spectroscopy extremely sensitive but on the other hand it limits the possibility of varying the microwave frequency. That is why in EPR spectroscopy the frequency is kept fixed while the magnetic field is swept.

The electromagnet provides the external magnetic field which is slowly varied in a linear way. The direction of the external magnetic field is perpendicular to the microwave magnetic field in the cavity. Phase sensitive detection is used to improve the sensitivity of the spectrometer and to reduce noise. The amplitude of the external magnetic field is varied sinusoidally at the modulation frequency (1-100 kHz) with a small amplitude ($0.1 - 0.4$ mT in this work) using modulation coils inside the cavity. The output of the detector is proportional to the first derivative of the absorption signal, i.e. the EPR signal. The console consists of electronics for spectrometer control and data acquisition.

The Hall probe used by the console to set the desired magnetic field (by regulating the current through the coils in a feedback system) is not located exactly at the position of the sample. Sometimes the measured and actual magnetic field at the sample position can differ significantly. To overcome that, additional measurements of the magnetic field were done by an external NMR probe at the position as close as possible to the sample. Calibration of the g value was done

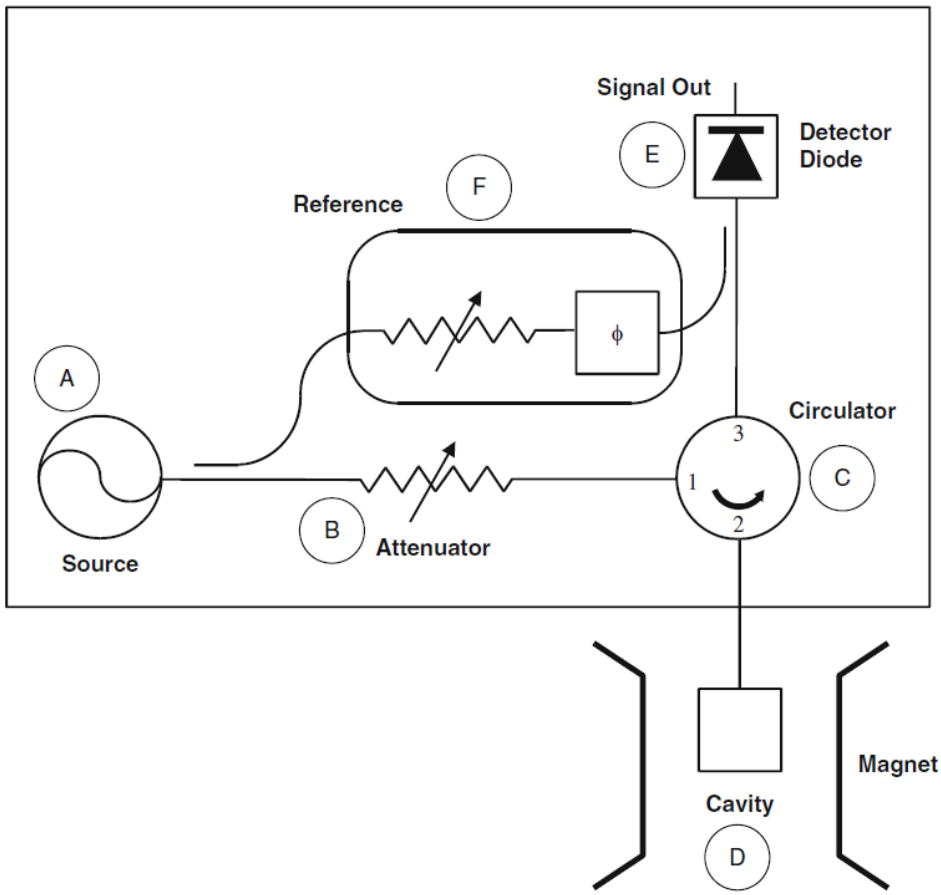

Figure 3.19: Block diagram for a microwave bridge.[146]

by recording the EPR spectrum of a reference sample (DPPH or CO_3^{-3} defect in $CaCO_3$, see Appendix B.1) with a well known $g_{(\perp)}$ value.[137,146,147]

3.6 Literature EPR studies of MIL-53-like MOFs

As already explained in Chapter 2, MOFs are built up of metal centres connected by organic linkers. A variety of metal centres can be employed where transition ions take an important place. MOFs with the topology of MIL-53 show a few exciting features which are still not completely understood, one of them being that some of these structures exhibit breathing. When paramagnetic centres are introduced in these structures, EPR spectroscopy can provide very detailed information on their environment in particular during transformations

of the framework. The paramagnetic centres can either be transition metal ions incorporated in the MOF as metal nodes, or paramagnetic molecules trapped in the pores. Additionally, EPR provides information about the oxidation state of metal centres in a time and cost efficient way.

3.6.1 COMOC-3

The oxidation of V ($V^{III} \rightarrow V^{IV}$) was followed by Liu *et al.* during the calcination of COMOC-3 (V^{IV}=O(NDC)) *in situ*. COMOC-3 AS is almost EPR silent while after calcination COMOC-3 exhibits a very intense broad EPR line with $g = 1.96$. These spectra can be seen in Figure 3.20. $V^{III}Cl_3$ was used as dopant salt. The negligible EPR intensity of the AS structure shows that the major part of vanadium enters the structure in the V^{III} state ($3d^2$ electron configuration). During calcination V^{III} is oxidized to V^{IV}.[100]

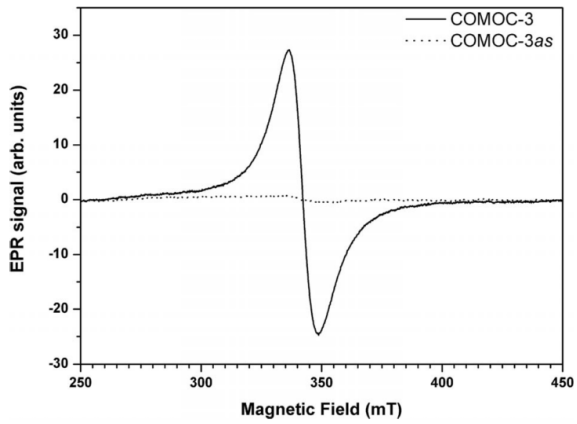

Figure 3.20: EPR spectra of COMOC-3 AS and COMOC-3 after calcination at RT.[100]

3.6.2 MIL-47(V)

Kozachuk *et al.* reported the EPR spectrum of MIL-47(V) before and after calcination. The situation is similar as for COMOC-3. The EPR spectrum of MIL-47(V) AS is very weak and assigned to V^{IV} impurities while the spectrum of MIL-47(V) after calcination exhibits a strong V^{IV} signal with $g = 1.963$.[148] Due to the high concentration of V^{IV} in MIL-47(V), the EPR spectrum consists of one broad line, without resolved HF structure from the ^{51}V nucleus. In the framework of this project, the RT EPR spectrum of MIL-47(V) was recorded in three microwave bands: X, Q and W. In the EPR spectra at higher microwave frequencies (Q and W-band) the g anisotropy gets gradually more resolved, as

seen in Figure 3.21. Spectrum simulations with the same g tensor for all three bands showed that the paramagnetic species have axial symmetry with $g_{\perp} = 1.972$ and $g_{\parallel} = 1.941$.

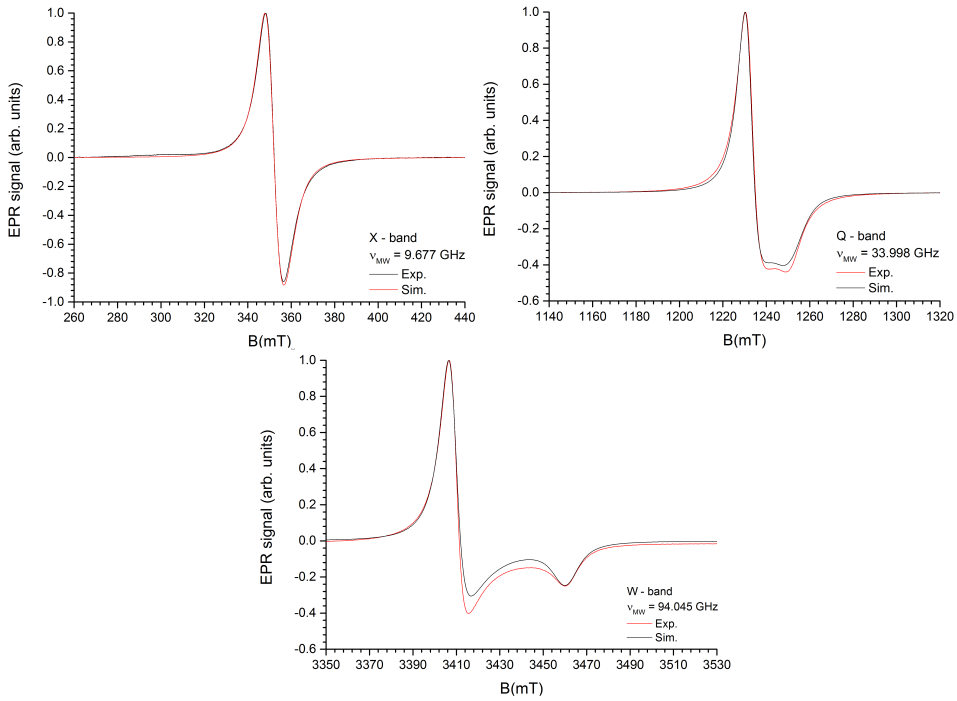

Figure 3.21: RT X, Q and W-band EPR spectra of MIL-47(V) after calcination. Experimental spectra are shown in black and simulated spectra in red. The g anisotropy is partly resolved in Q and W-band.

As already mentioned in Chapter 2, oxidation and reduction reactions are essential steps in redox catalysis. Hence it is important to determine the fraction of V ions in a specific valence state. EPR monitors the V^{IV} fraction, whose EPR intensity is an excellent relative measure of the number of paramagnetic centres. Leus *et al.* monitored the RT EPR signal of MIL-47(V) before and after catalysis and combined this with the results of solid state NMR. It was proven that an important fraction of the V^{IV} ions in the catalyst ($20 - 30\%$) gets oxidized in the first few hours (1-3 h) of catalysis.[6]

A similar study was conducted by the same research group on Ti functionalized NH_2-MIL-47(V). It was shown that at RT the EPR spectrum provides information about the majority of the vanadium centres in the sample, rather than about a minority fraction, e.g. corresponding to defects. In the first 2 h of catalysis, the spectrum intensity decreases by about 20% (Figure 3.22).[99]

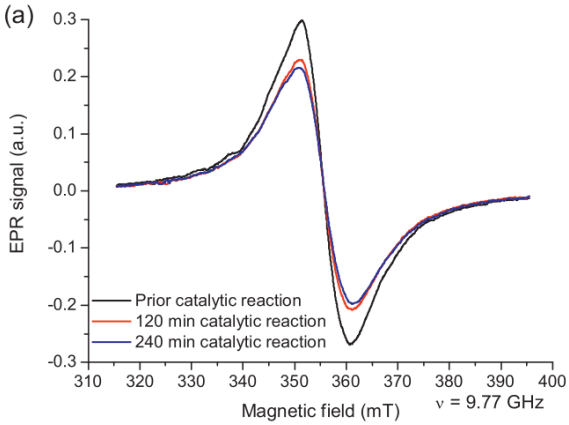

Figure 3.22: X-band EPR spectra of NH_2-MIL-47(V) [Ti] before and after catalysis at RT.[99]

3.6.3 MIL-53

The breathing effect reported for MIL-53 is a complex and still not completely understood phenomenon with many potential applications as discussed in Chapter 2.

The temperature-induced breathing effect was studied by Mendt *et al.* in Cr-doped MIL-53(Al) by means of EPR and ENDOR. Incorporation of Cr^{III} ions in the Al metal nodes was proven via the EPR spectrum of Cr^{III}, displaying a characteristic ZFS (section 3.3.2) that is sensitive to the local symmetry of the $CrO_4(OH)_2$ octahedra. Variable temperature EPR measurements showed a temperature driven phase transition with a pronounced hysteresis.[136] This EPR result is in agreement with a previously published study using neutron diffraction and scattering experiments by Liu *et al.*[59] It was shown that, depending on the thermal history, the LP and NP-d states can coexist at RT. In addition, it was found that even at 8 K a considerable fraction ($\approx$ 20%) of the sample is still in the LP state. This fraction does not undergo the structural transformation to the NP state.[136]

A further study by the same research group of the breathing in Cr-doped MIL-53(Al), this time upon CO_2 adsorption, showed that EPR is very sensitive in distinguishing the LP and NP states of this MOF. Quantification of the LP and NP state fractions proved possible and it was concluded that a small fraction of the LP state remains after the phase transition to the NP state occurred. These results are in agreement with similar XRD and IR experiments. The Cr^{III} EPR probe proved not only to be sensitive to the large structural changes of the MOF (LP $\leftrightarrow$NP) but also to different amounts and configurations of CO_2 molecules trapped in the same structural phase of MIL-53(Al).[149]

Sheveleva *et al.* studied the breathing of MIL-53(Al) by EPR using TEMPO radicals

(section 3.3.3.2) as paramagnetic probes introduced into the pores of the MOF after synthesis and activation. Since the EPR spectrum was very strong, tiny concentrations of TEMPO could be used in this study, about 1 molecule per 1000 unit cells of the framework. In this way, the influence of the guest molecule on the breathing behaviour of the MOF, which may occur at higher concentrations, is avoided. Sheveleva *et al.* showed the possibility of investigating structural dynamics and guest-host interactions of flexible MOFs, which is not feasible using most of the other methods for detecting MOF breathing, like NMR, XRD and TGA.[141,150]

Recently Kozachuk *et al.* studied the impact of vanadium doping on the properties of MIL-53(Al) and in an isostructural MOF with 1,4-naphthalene dicarboxylate as the organic linker. The effective incorporation of vanadium ions was demonstrated by using several characterisation methods (XRD, EPR, NMR spectroscopy, FTIR spectroscopy, CO_2 sorption). In particular, it was shown that the flexibility or rigidity of the MIL-53(Al) framework and the breathing were affected by the doping. Doping concentration, dopant salt (VCl_3 versus $VOSO_4$) and measurement temperature all appeared to exhibit complicated effects on the EPR spectra, leading to a wide variety of distinct paramagnetic V^{IV} centres, characterised by (sometimes only slightly) different g and ^{51}V HF tensors. The conclusion of this study was that in samples with low vanadium concentration, the majority of the dopant ions end up on sites that are not affected by the NP $\rightarrow$ LP transition of the MIL-53(Al) host.[148]

Cao *et al.* investigated the role of MIL-53(Al) for manipulation of the spin dynamics of a spin active fulleropyrrolidine nitroxide radical (1). It was done by following the temperature dependence of the EPR spectra of the nitroxide group (with one unpaired electron) with resolved HF interaction from ^{14}N nuclei ($I = 1$). The EPR spectra revealed that the guest molecule aggregated tightly in the pores of MIL-53(Al). In the MIL-53(Al) framework the molecules (1) have an almost completely restricted motion in comparison with MIL-177, where they are mobile at RT. Therefore, MIL-177 may be a good candidate for quantum information processing and high density data storage.[151]

4

X-Ray Diffraction (XRD)

Besides EPR, XRD was the second technique used in the experimental part of this thesis. The explanation of XRD in this chapter is kept elementary. It is an analytical technique used for unravelling the crystal structure and atomic spacing of a particular material. XRD is based on the constructive interference of X-rays reflected by planes of a crystalline material. All such materials exhibit an XRD pattern that can be considered as its fingerprint. That is why XRD is perfectly suited for characterisation and identification of compounds.

4.1 X-rays

X-rays, discovered by W. C. Röntgen in 1895, are electromagnetic waves with wavelengths in the region of an Ångström (10^{-10} m). Until the 1970s, with the advent of synchrotrons (see below), X-ray tubes were the only source of X-rays. These vacuum tubes contain a heated cathode filament for electron emission and an anode. A high voltage is applied between the cathode and the anode for accelerating the electrons. When the latter collide with the anode, X-rays are produced. The energy, and thus also the wavelength, of the X-rays depends on (besides the voltage) the material of the anode, usually called the target. In crystallography a Cu target is most often used, with $\lambda = 1.5406$ Å. When an electron hits the target, X-rays are created by two different processes: characteristic X-ray emission and Bremsstrahlung. Characteristic X-rays are emitted when the electron has enough energy to knock an orbital electron out of the inner electronic shell of the target material. Then an electron from the outer shell fills the hole in the inner shell, by emitting a photon with energy equivalent to the energy difference between the higher and the lower state. These emitted X-rays have energies characteristic for each target element. The innermost electron

shell is denoted as K, further followed by L, M, ... If the electron fills the hole in the K shell, the transitions are denoted as K_α, K_β, K_γ and so on, depending on the initial state of the electron. Bremsstrahlung is a result of deceleration of the electrons when they collide with the anode. This process produces the continuous part of the X-ray spectrum.[152–154]

4.2 Interaction between X-ray photons and matter

Diffraction is the effect which follows from the interaction between an electromagnetic wave and a periodic lattice with spacings comparable with the wavelength. X-rays interact with matter via various processes, such as: photoelectric effect, Compton scattering or Thomson/Rayleigh scattering. The photoelectric effect is the interaction between X-rays and the electron whereby X-rays are completely absorbed by the electrons and electrons are ejected from a shell. Compton scattering, on the other hand, is inelastic scattering of a photon by (nearly) free electrons which results in a decrease in energy (increase in wavelength) of the photon. Thomson/Rayleigh scattering occurs when photons are completely elastically scattered with no change in energy of both photon and electron/atom.

4.3 Bragg's law

An X-ray beam with wavelength λ is sent to a sample at θ angle with a certain crystal plane with Miller indices (hkl). The reflected beam is a superposition of EM waves reflected from different parallel crystal planes separated by d, the interplanar distance. The interaction of the incident X-rays with the material results in a constructive interference and an intense signal at the detector, when Bragg's law is satisfied:

$$n\lambda = 2dsin\theta \tag{4.1}$$

where n is an integer (Figure 4.1). This implies that waves reflected on consecutive parallel planes are in phase, or, the difference in path length between them is a multiple of the wavelength. The beam reflects at an angle of 2θ with respect to the incident beam.

Possible 2θ angles where constructive interference will happen are determined by the unit cell dimensions while the intensity of the reflected beam will depend on the distribution of the electrons in the unit cell. Both 2θ angles and signal intensity will depend on the types of atoms and the location of the atoms in the unit cell.

A crystal material is characterised by the fact that it can be constructed by repeating a basic structural unit known as the unit cell. In 1845 Auguste Bravais

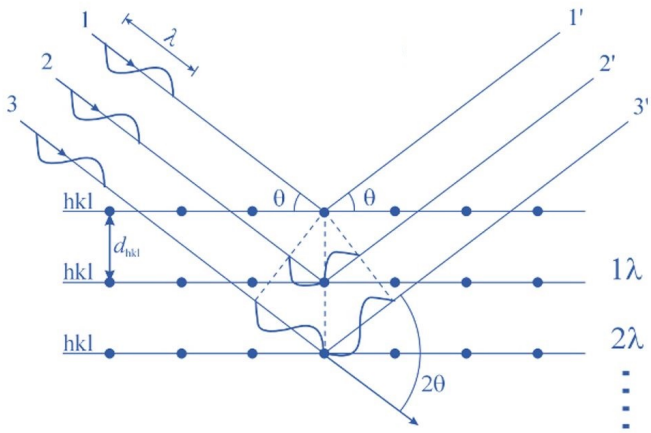

Figure 4.1: Incident and reflected X-ray beams on parallel crystal planes, distance between planes is d.[155]

found out that in a 3D system, there are fourteen types of lattices. A Bravais lattice is an infinite array of discrete points with identical environment. These lattices are characterised by translation symmetry. The crystals are grouped into seven crystal systems according to the symmetry of their unit cell: cubic, hexagonal, tetragonal, trigonal, orthorhombic, monoclinic and triclinic. Additionally four types of unit cells are defined: primitive, volume centred, face centred and side centred. Crystals have series of parallel planes inside the crystal. The orientation and interplanar spacings of these planes are defined by three integers, called Miller indices, (hkl). In the case of a 3D diffraction grating, these three indices, (hkl), become the order of diffraction along the unit cell axes a, b, c.

Powders consist of tiny crystallites in all possible crystal orientations as well as a random distribution of all possible (hkl) planes. In the Bragg-Brentano configuration (used in this work) only crystallites with reflecting planes, (hkl), parallel to the powder sample surface (which has to be smooth) will contribute to the detected intensity.

During the XRD measurements presented in the experimental part of this thesis the sample stage was fixed in a horizontal position (not tilted). The X-ray tube and the detector both moved simultaneously over the angular range θ or both X-ray tube and detector were fixed. This configuration is known as θ-θ measurement.[156–161]

4.4 Synchrotron XRD

Synchrotron radiation emitted from charged particles circulating in synchrotron storage rings is a more intense and versatile source of X-rays than explained in the previous section. One of the two synchrotron facilities visited during this project was the Diamond Light Source in UK. In the Diamond Light Source high resolution *in situ* XRD under vacuum was possible to measure in a broad range of temperature, 80 - 500 K. Additionally, measurement under different atmospheres and pressures are possible. Electrons are generated in an electron gun and fired to a series of three particle accelerators where they are accelerated to nearly the speed of light. After that electrons, depicted in red in Figure 4.2, enter a large storage ring.

Figure 4.2: Schematic representation of Diamond Light Source storage rings.[162] Electrons are represented as red dot, X-ray radiation in cyan. Fun fact: once they enter the storage ring, the electrons are moving so fast that they could travel around the entire world 7.5 times in a single second.

The storage ring is made of 48 straight sections angled together with 48 bending magnets. These magnets are used to guide the electrons around the ring. For production of even more intense X-rays, additional magnets are used which cause the electrons to wiggle. When the path of the electron beam is bent by magnets, the electrons lose energy in the form of an electromagnetic radiation. This pack of energy, depicted in cyan in Figure 4.2, can then be channelled out of the storage ring and into the experimental stations, called beamlines. The beamline consist of the optics hutch, the experimental hutch and a control room. In the optics hutch the X-ray beam is filtered and focused, in the experimental hutch the sample and setup for the measurements are placed.[162]

In situ powder XRD data in vacuum were collected on the I11 powder diffraction beamline at the Diamond Light Source with maximum X-ray flux at 15keV (λ = 0.825086 Å).[163] The experimental hutch is shown in Figure 4.3. The rotational sample holder together with a robotic arm allows automated sample change of up to 200 samples. A precise XYZ table enables the optimal positioning of the

samples in front of the beam pipe.

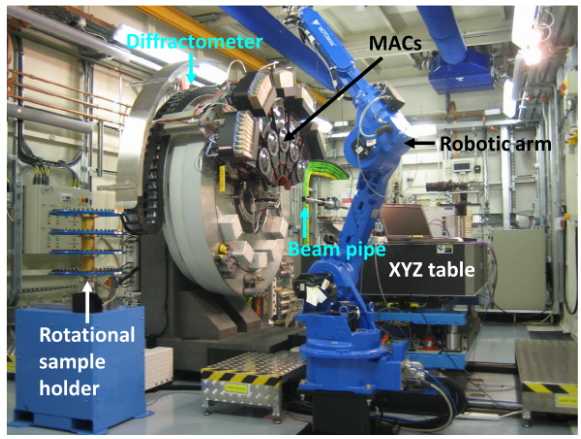

Figure 4.3: The I11 experimental hutch with main elements indicated.

The main and largest element is the diffractometer. It has 3 coaxial high precision rotary stages, θ, 2θ and δ as shown in Figure 4.4. The sample is mounted on the θ circle. It has two types of detectors, multi-analyser crystal (MAC) detectors and position sensitive (PS) detectors. MAC and PS detectors are mounted on the 2θ and δ circle respectively. MAC detectors offer high resolution while PS detectors provide high speed. There are five MAC detectors. Each detector has nine Si(111) analysing crystals and nine detectors giving a total of 45 crystals. The data from a total of 45 detectors are integrated to produce the final pattern.

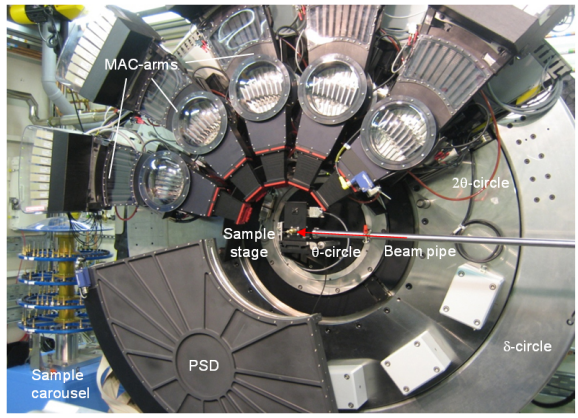

Figure 4.4: Diffractometer with MAC and PS detectors indicated.[164]

A borosilicate glass capillary (Figure 4.5) of 0.5 mm internal diameter was filled with powder to a height of approximately 40 mm, and the capillary was stoppered with glass wool. The capillary was continuously pumped to 10^{-5} mbar with a turbomolecular pump.

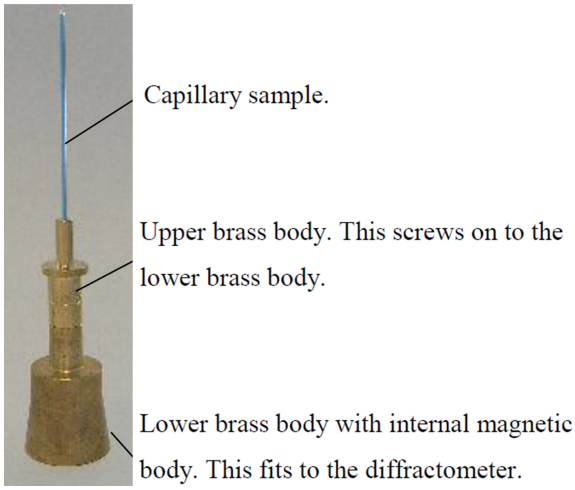

Figure 4.5: Capillary sample tube.[164]

An Oxford Cryostream (80-500 K) system was used for heating the sample from RT to 450 K and cooling back to RT at a heating/cooling rate of 5 K/min. A wide-angle PS detector based on Mythen-2 Si strip modules was used to collect the XRD data. The detector was moved at constant angular speed with 10 s scan time at each temperature and 10 s waiting time in order to let the temperature stabilise.

The data were analysed by Claire A. Murray from Diamond Light Source using Lebail refinements in TOPAS[165] (see Chapter 6). Starting values for the lattice parameters for the V-doped MIL-53(Al) were taken from the literature.[21]

4.5 In-house XRD

In situ powder XRD in air at RT was carried out on a Bruker D8 Discover XRD system equipped with a Cu X-ray source (λ = 1.5406 Å) and a linear X-ray detector (CoCooN research group of Ghent University). The powder sample was spread on a silicon wafer and placed on the sample heating stage. $\theta - \theta$ measurements were carried out in air at atmospheric pressure. The sample was heated from RT to 450 K and cooled back to RT at a heating/cooling rate of 5 K/min. The temperature was measured with a K-type thermocouple. Data were collected in ramping mode with a scanning time of 10 s.

In situ powder XRD in vacuum at RT was carried out on a similar Bruker D8 Discover XRD system. The powder sample was placed in an in-house built reaction chamber and pumped via a manual angle valve with a rotation pump to a pressure of 0.1 mbar. While pumping, the sample was continuously irradiated with X-rays and data was collected via a linear detector.

Part II

Discussion and analysis of research results

5

As-synthesized V-doped MIL-53(Al)

V, where are you now? As already discussed in-depth in Chapter 2 and 3, MIL-47(V) proved to be catalytically active and it became an important MOF in discussions about catalysis. A drawback of MIL-47(V) is its poor stability in aqueous environment. One way to overcome this disadvantage could be doping the well-known and highly stable MIL-53(Al) with V^{IV}-ions. V-doping could lead to significant changes in its breathing behaviour and might have repercussions on its catalytic behaviour as well. In order to understand the properties of the doped MIL-53(Al) framework, it is necessary to determine where and how dopant ions actually are incorporated. The main aim of this part of the research is to establish the effectiveness of the V-doping. Details about the one-pot synthesis/doping procedure are given in Appendix B, section B.5. In this chapter as-synthesized (AS) samples are examined by means of EPR and ENDOR spectroscopy to reveal the nearest environment of the paramagnetic V^{IV} dopant ions in the MIL-53(Al) structure.

The results presented in this chapter are published as:

Multi-frequency (S, X, Q and W-band) EPR and ENDOR Study of Vanadium(IV) Incorporation in the Aluminium Metal-Organic Framework MIL-53

Irena Nevjestić, Hannes Depauw, Karen Leus, Vidmantas Kalendra, Ignacio Caretti, Gunnar Jeschke, Sabine Van Doorslaer, Freddy Callens, Pascal Van Der Voort and Henk Vrielinck

ChemPhysChem, 2015, 16 (14), pp 2968-2973

5.1 Multi-frequency EPR study

In Chapter 3 a characteristic X-band EPR spectrum of vanadyl in V-doped MIL-53(Al) was introduced together with the explanation of the g tensor and resolved ^{51}V HF interaction. In this section it will be shown that multi-frequency EPR, here including both higher and lower frequencies than X-band, is indispensable for accurately determining the g and A tensors for the V=O dopant centres.

The X and Q-band EPR spectra recorded at RT for all samples are summarized in Figure 5.1. The composition of all samples reported in this chapter are listed in Table 5.1. All spectra exhibit the same dominant EPR component with resolved ^{51}V HF structure, with g and A tensors typical of vanadyl molecular ions. This highlights that the synthesis procedure leads to a reproducible production of V^{IV}-centres in the samples, not only with the V^{IV}-containing dopant salt $VOSO_4$, but also when using the V^{III}-salt VCl_3. The well-resolved HF structure and relatively narrow linewidths indicate that the EPR-active (not to be confused with activation of the MOF) fraction of V-ions in the samples is well-dispersed.

Table 5.1: Cation composition and Langmuir surface area (L.S.A.) of the samples reported in this chapter. Columns 2 and 3 report the quantities in the starting mixture for the synthesis, in column 4 the [V]/([V]+[Al]) concentration ratios, as determined by Flame atomic absorption spectroscopy (F-AAS) on activated samples, are shown. Samples *no.* 1-3 were synthesised using VCl_3 and sample *no.* 4 using $VOSO_4$. For further information about synthesis see Appendix B, section B.5 and PhD thesis of Hannes Depauw.[166]

Sample *no.*	**V-salt (mmol)**	**$AlCl_3$ (mmol)**	**Ratio V (mol %)**	**L. S. A.**
1	0.057	5.550	0.98	1482 (m^2/g)
2	0.114	5.491	1.78	1566 (m^2/g)
3	0.286	5.323	2.56	1542 (m^2/g)
4	0.044	3.465	0.97	1403 (m^2/g)

At first glance, the X and Q-band powder EPR patterns in Figure 5.1 appear to be dominated by the contribution of one type of V^{IV}-centres. Nonetheless, it proved impossible to obtain satisfactory simulations (using spin-*Hamiltonian* B.1 from Appendix B, for more information about simulation see further Appendix A) in the two microwave bands based on only one set of g and $A(^{51}V)$ tensors with coincident axes. This is illustrated in Figure 5.2, where simulations are shown with the best-fit parameters extracted from the X-band spectrum, without axes tilting. A considerable mismatch with the Q-band spectrum is evident. When tilting between the g and $A(^{51}V)$ tensor principal axes is introduced, on the other hand, the RT EPR spectra in four frequency bands are convincingly reproduced, as shown in Figure 5.3. The best-fit spin-*Hamiltonian* parameters are summarized in Table 5.2.

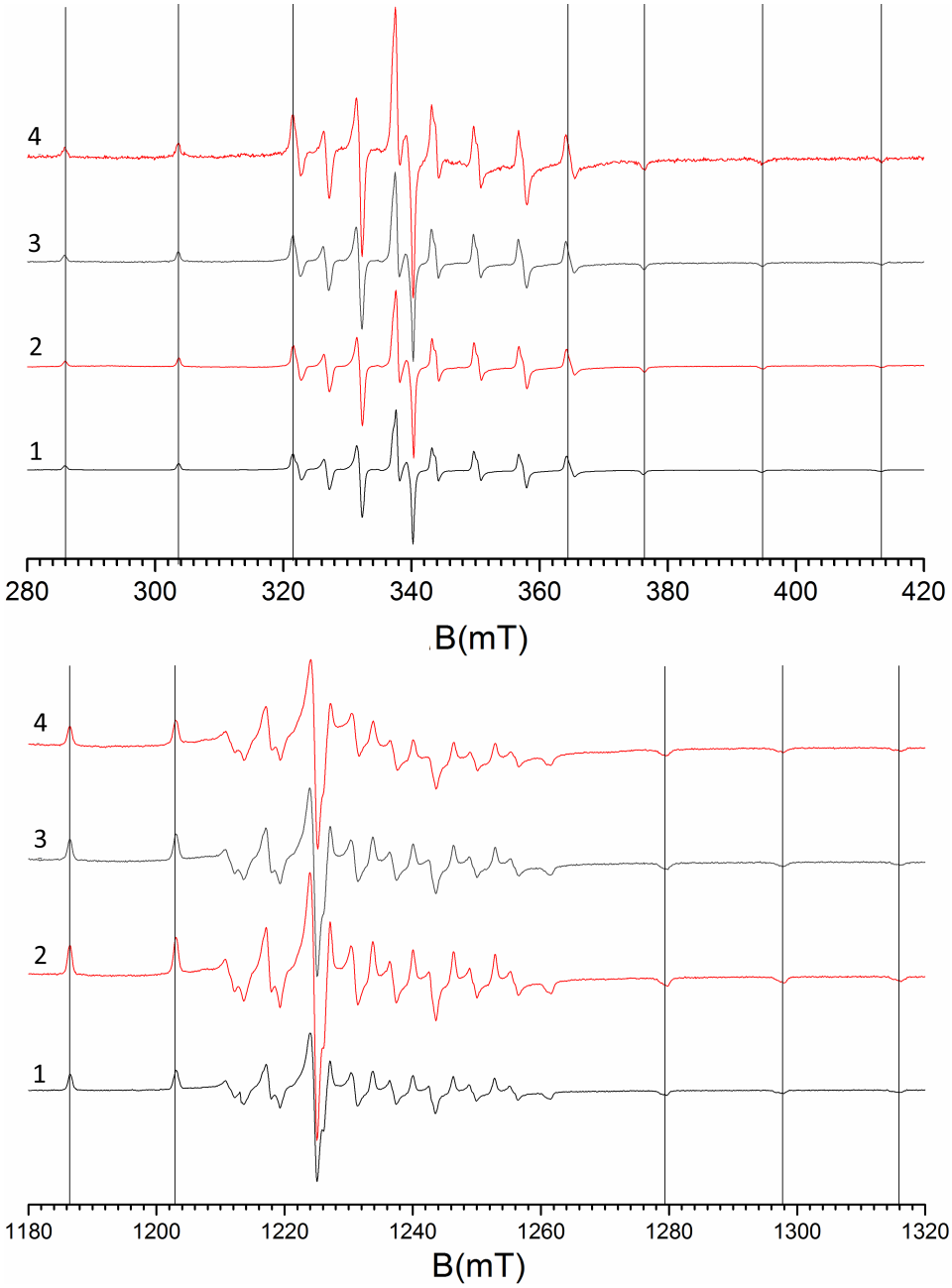

Figure 5.1: X-band (top) and Q-band (bottom) EPR spectra of V-doped MIL-53(Al) AS samples *no*. 1-4 at RT. Guides for the eye indicate specific features in EPR spectra. All samples exhibit the same dominant EPR component with resolved HF structure. Q-band spectra are intensity normalized.

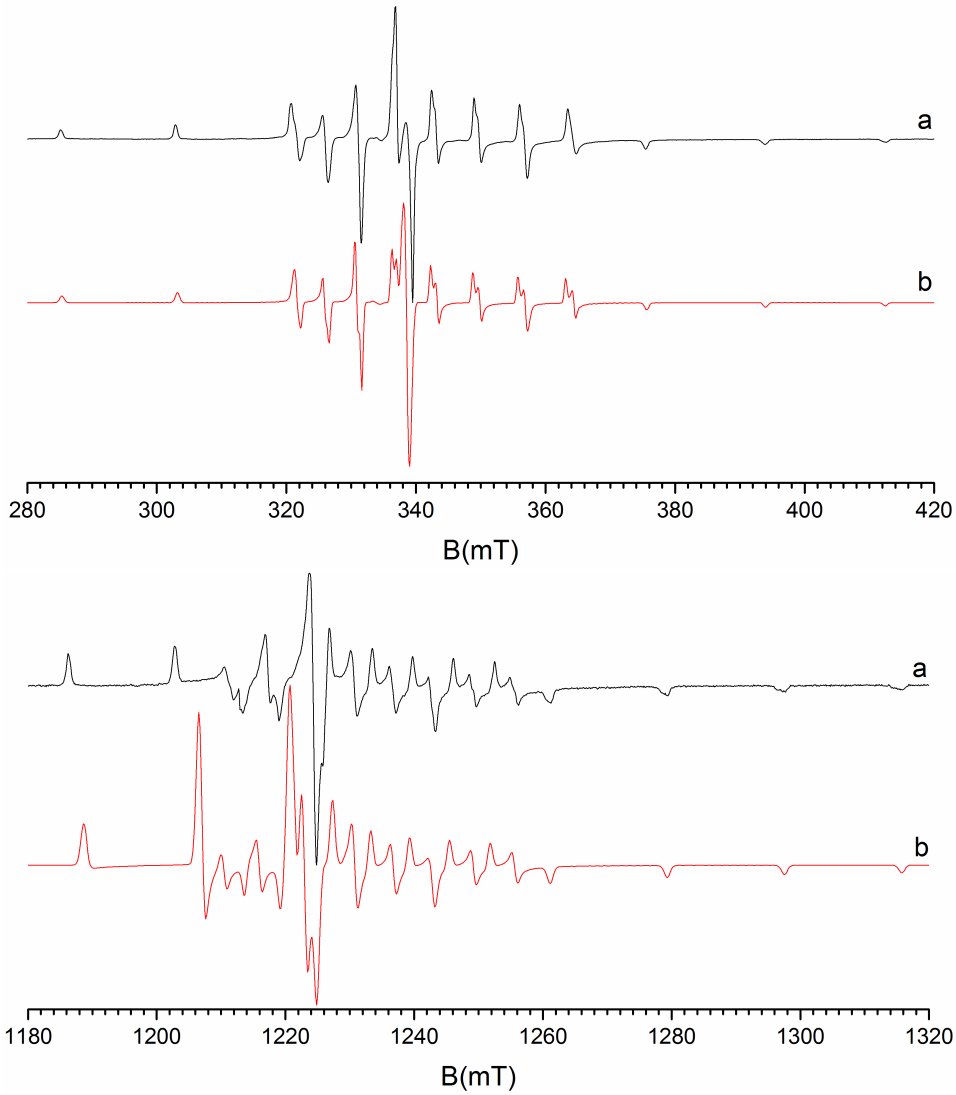

Figure 5.2: Experimental (a) X (top, ν_{MW} = 9.477 GHz) and Q-band EPR spectra (bottom, ν_{MW} = 33.996 GHz) of V-doped MIL-53(Al) AS sample *no*. 1, and spectral simulations (b) using the best-fit g and A tensors with coincident principal axes, as derived from the X-band spectrum. Especially in Q-band, the simulation only shows poor resemblance to the experimental spectrum.

In the insets in Figure 5.3 a zoom-in on the high-field g_z components of the Q and W-band spectra is shown. Especially in W-band, these features are not completely reproduced in the simulations, and give evidence for at least one additional component. In the simulations in the inset, one extra component is introduced which only differs from the main centre by a shift in the g_z value of +0.001,

Table 5.2: Simulation parameter set extracted from multi-frequency EPR spectra at RT: g tensor, $A(^{51}V)$ tensor principal values and directions (in g tensor principal axes as reference frame). The Euler angles[167] of the A tensor with respect to the g tensor (tilting angles) are $\alpha = 0\pm2°$, $\beta = 12\pm2°$, $\gamma = 8\pm2°$. The other errors are estimated as $\Delta g = \pm0.0010$, $\Delta A = \pm2$ MHz.

g	**x**	**y**	**z**
1.9725	1	0	0
1.9669	0	1	0
1.9391	0	0	1
A [MHz]	**x**	**y**	**z**
163	0.9686	-0.1361	0.2079
165	0.1392	0.9903	0
492 (497 for LT)	-0.2059	0.0289	0.9781

and roughly doubling the linewidth. Although these simulations reproduce the spectra very well, it cannot be excluded that, rather than just two, a range of slightly different V^{IV} centres is responsible for this effect.

The principal g and $A(^{51}V)$ values in Table 5.2 are, within the experimental error, in agreement with those previously reported by Kozachuk *et al.*[148] for the dominant V^{IV}-related centre in VCl_3-doped MIL-53(Al) AS (labelled II^{ort}). Obviously the tilting angles between the g and $A(^{51}V)$ tensors, resolved in our multi-frequency measurements, represent the most significant difference with these literature results. The presence of slightly different variants of this V^{IV}-centre was also not resolved previously. The Q-band EPR spectrum at 10 K (Figure 5.4) indicates only very small changes in the spin-*Hamiltonian* parameters upon cooling.

A simulation with the parameters in Table 5.2 indeed leads to a very small mismatch. By slightly increasing the principal z component of $A(^{51}V)$ (to 497 MHz) this may, however, be solved. Also at 10 K the V^{IV}-centres in both the VCl_3- and the $VOSO_4$-doped MIL-53(Al) clearly have a rhombic g tensor and the principal axes of the g and $A(^{51}V)$ tensors do not coincide, the tilting angles being, within the experimental error, the same as at RT. This is not in agreement with the results of Kozachuk *et al.*[148] who reported axial g and $A(^{51}V)$ tensors for the dominant V^{IV}-centre at low temperature.

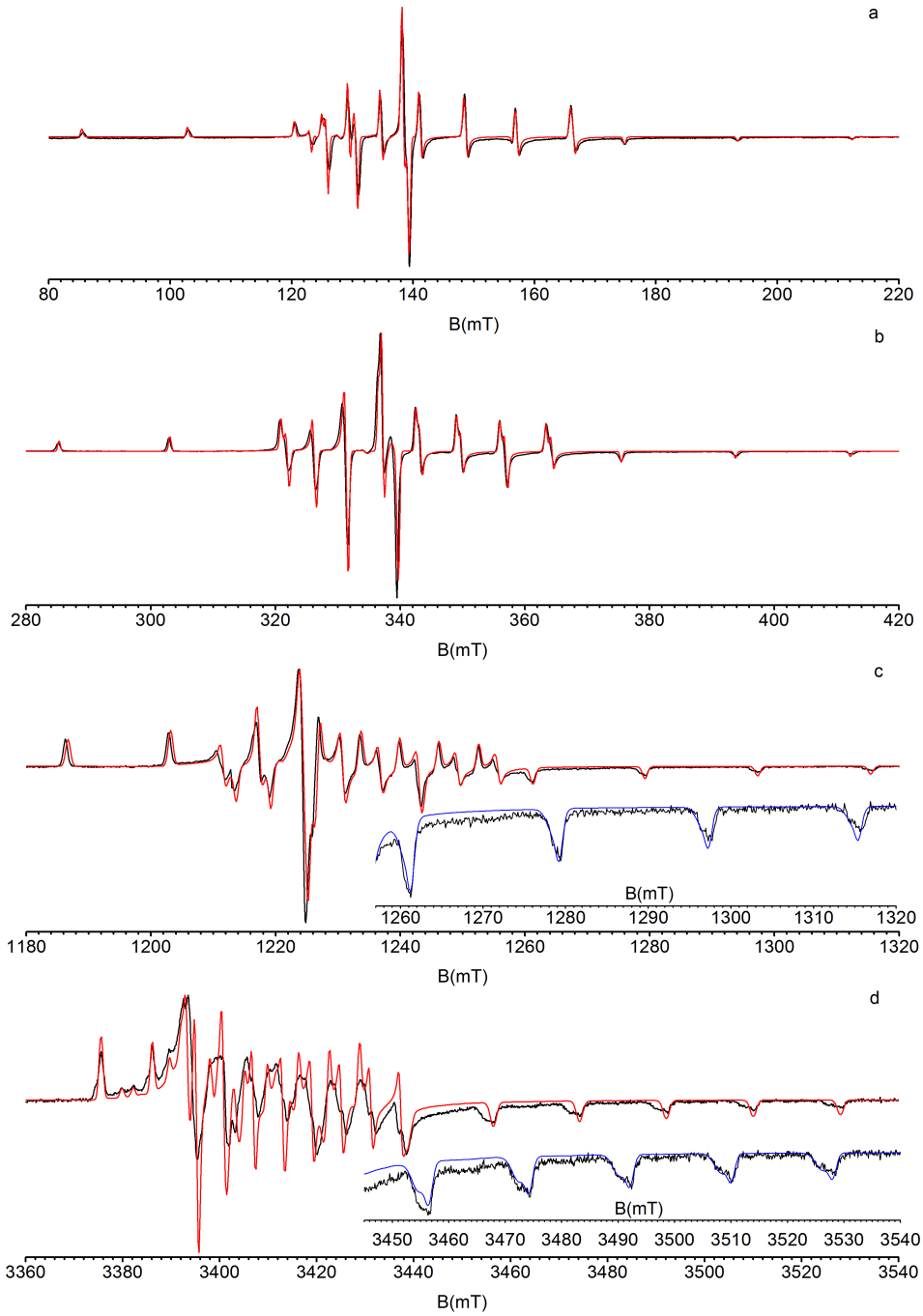

Figure 5.3: Multi-frequency (S (a, ν_{MW} = 4.055 GHz), X (b, ν_{MW} = 9.477 GHz), Q (c, ν_{MW} = 33.996 GHz) and W-band (d, ν_{MW} = 94.053 GHz)) EPR spectra of V-doped MIL-53(Al) AS samples *no*. 2 (S-band) and 1 (X, Q and W-band). Experimental (black) and simulated (red) spectra with parameters from Table 5.2 are shown. The insets in the Q and W-band spectra show a zoom-in on the high-field g_z components where the simulation (blue) is made with one extra component.

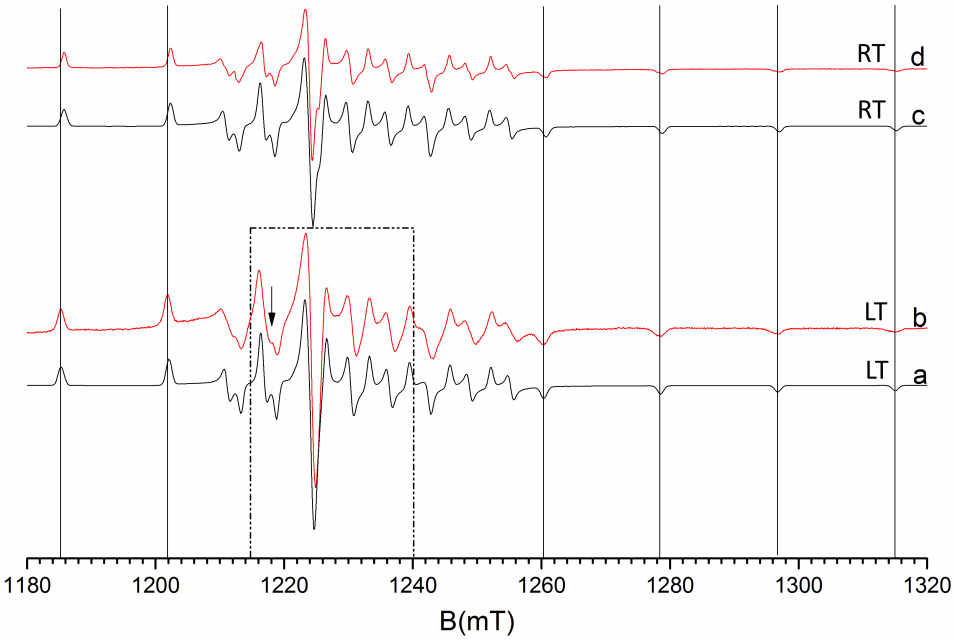

Figure 5.4: EPR Q-band spectra of V-doped MIL-53(Al) AS sample *no.* 1 at RT (d - experimental spectrum, c - simulated spectrum) and 10 K (b - experimental spectrum, a - simulated spectrum). Guides for the eye indicate small shifts in particular EPR features. The simulation parameters are shown in Table 5.2. The arrow marks the field where the ENDOR spectra in Figure 5.5 were recorded (B = 1218 mT). The dashed rectangle indicates the range where the ENDOR spectra in Figure 5.6 were recorded.

5.2 ENDOR study of V^{IV} incorporation in the MIL-53(Al)

The occurrence of one dominant V^{IV}=O centre in the sample is a strong indication for an ordered introduction of V in the framework, very probably by incorporation on the Al sites. Observation of the HF interaction with framework nuclei in the V^{IV}=O EPR spectrum, however, is the ultimate proof. Since these are buried in the EPR linewidth, ENDOR experiments were made to resolve them.

Figure 5.5 shows the ENDOR spectrum recorded at 10 K and B = 1218 mT (marked with an arrow in Figure 5.4). Transitions are observed close to the Larmor frequencies of ^{27}Al ($I = 5/2$, $g_n = 1.4566$) and ^{1}H ($I = 1/2$, $g_n = 5.58569$), along with broad resonance lines in the 60-100 MHz range.

The ^{1}H region exhibits a very rich structure that is explored in detail by recording the field dependence of the ENDOR spectrum (Figure 5.6a, for explanation on the representation, see Chapter 3, section 3.4.2) in the range marked with the dotted box in Figure 5.4. This 2D spectrum is successfully simulated (Figure 5.6b) considering HF interactions with the nearest proton (hydroxyl) and 4 sets of 4 (approximately) equivalent protons on the BDC linkers of the V^{IV}-ion. The HF simulation parameters are given in Table 5.3. Initial values for these parameters were determined by calculating the anisotropy for each ^{1}H nucleus in the point-dipole approximation (see Chapter 3), using crystallographic data for the undistorted MIL-53(Al) structure (Figure 5.6c) and adding a small isotropic HF value for each interaction. These start parameters were further optimized by fitting the experimental ENDOR field dependence, keeping all principal directions fixed and assuming axial A tensors for all BDC protons.

The spectra in the ^{27}Al range exhibit a lower signal-to-noise ratio than in the ^{1}H-range, but could still be recorded at several magnetic field positions, as shown in Figure 5.7. These spectra can be explained assuming an axial HF tensor ($A_{\parallel}$(^{27}Al)=

Table 5.3: Parameters used for the simulation of the ENDOR spectra in the ^{1}H range. Principal values of the HF interaction of the ^{51}V nucleus with the nearest proton (hydroxyl) and with 4 sets of 4 (approximately) equivalent protons on the 4 BDC linkers. For each set of four nuclei, only one set of polar angles (θ,ϕ) for the principal A_z direction is shown: the others are found at (-ϕ,θ), (180°-ϕ,180°-θ) and (180°+ϕ,180°-θ).

	OH	**$H_{1(1-4)}$**	**$H_{2(1-4)}$**	**$H_{3(1-4)}$**	**$H_{4(1-4)}$**
$\mathbf{A_x}$ [MHz]	-3.1	-1.3	-0.6	-0.2	-0.1
$\mathbf{A_y}$ [MHz]	-3.4	-1.3	-0.6	-0.2	-0.1
$\mathbf{A_z}$ [MHz]	8.6	2.4	0.7	0.6	0.4
$\boldsymbol{\phi}$ [deg]	0	53	53	53	53
$\boldsymbol{\theta}$ [deg]	37	100	45	95	60

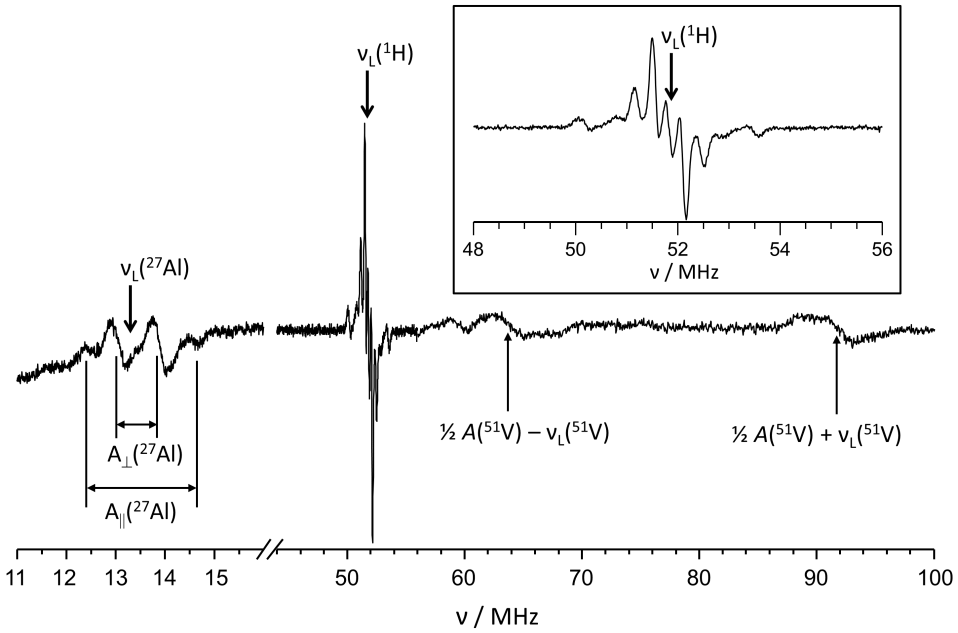

Figure 5.5: ENDOR of MIL-53(Al) AS sample *no*. 1 recorded at B = 1218 mT. The ENDOR transitions from interaction with ^{51}V, ^{27}Al and ^{1}H nuclei are shown. Larmor frequencies (ν_L) are indicated. The spectrum zoomed-in on the region close to the ^{1}H Larmor frequency is shown as an inset.

2.30 MHz; $A_\perp(^{27}\text{Al})$= 0.75 MHz), as shown in Figure 5.5 (see also Chapter 3, section 3.4). In the point-dipole approximation, from the anisotropy in $A(^{27}\text{Al})$, a V-Al distance of 3.4 Å is calculated, which corresponds very well to the Al-Al distance in the MIL-53(Al) lattice (3.3 Å). No quadrupole splitting was resolved in these transitions.

Of course, the experimental uncertainty and the applied approximation do not exclude that either the V ion or the neighbouring Al ion (or both) are not perfectly at regular MIL-53(Al) lattice positions. Considering that the V=O bond is longer than the pristine Al-OH bond, it seems obvious that the oxygen atom will move towards the V-Al axis, thereby lowering the symmetry. A possible small displacement of the V ion could further contribute to this effect. This implies that the g and A tensor axes are tilted away (slightly) from their orthorhombic counterparts, most probably leading to triclinic symmetry (as all axes are non-coincident). As soon as symmetry becomes lower than orthorhombic, the g and A tensor axes no longer need to be coincident, in agreement with our observations.

The two broad resonance lines in Figure 5.5 at 64 and 92 MHz, are assigned to the ^{51}V HF interaction. The sum of these frequencies (156 MHz) corresponds reasonably well with the $A_x(^{51}\text{V}) \approx A_y(^{51}\text{V})$ value determined from the EPR

spectra (see Table 5.2) and the distance between the transitions (≈30 MHz) roughly corresponds with twice the ^{51}V Larmor frequency (27.3 MHz at 1218 mT). In view of the low intensity and resolution in this spectral range, a more detailed analysis of these transitions, which would also include nuclear quadrupole interaction, was not attempted.

The g and $A(^{51}V)$ tensors, and the ENDOR results are thus compatible with a V^{IV}=O molecular ion replacing a regular Al^{III}-OH unit in the MIL-53(Al) framework, which does not even require charge compensation. The ENDOR spectra do not provide evidence for the presence of V^{IV}-centres with clearly different environments in the samples. The high-frequency EPR spectra do reveal several (at least two) types of V-centres, but the difference between them appears to be very subtle and due to variations in the further environment or irregularities in the MOF structure. Possible origins include the proximity to the surface of the MIL-53(Al) microcrystals, the (random occupation of the pores by) remaining linker molecules in the MIL-53(Al) AS framework, or perhaps even inhomogeneity in the V-dopant concentration.

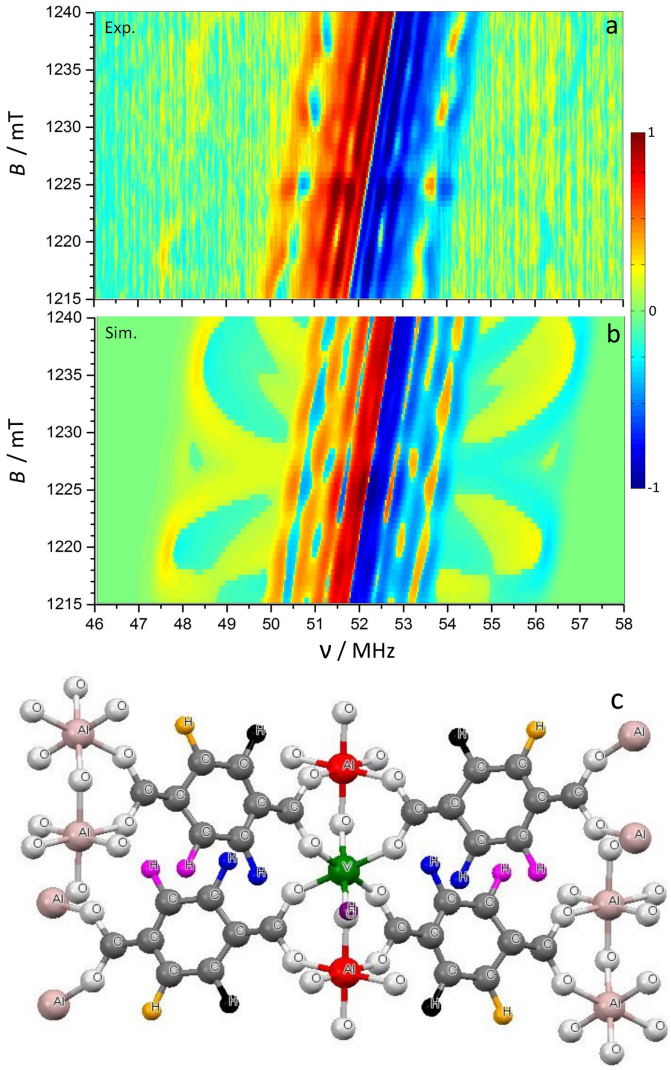

Figure 5.6: Field dependence of ENDOR spectra (normalized signal heights in colour scale) near the ^{1}H Larmor frequency of MIL-53(Al) AS sample *no*. 1. Experimental (a) and simulated spectra (b) are shown. Parameters used for simulation are shown in Table 5.3. c - Nearest environment of a V^{IV}-ion (green) at a regular Al-site in MIL-53(Al) AS. The nuclei to which ENDOR transitions have been assigned are marked in colour: the nearest two aluminium nuclei (red), hydroxyl proton (purple) and 4 sets of (approximately) equivalent protons on the 4 BDC linkers (blue, black, magenta, yellow, in order of increasing distance to the central V^{IV}-ion). The Mercury Software was used for crystal structure visualisation[168]

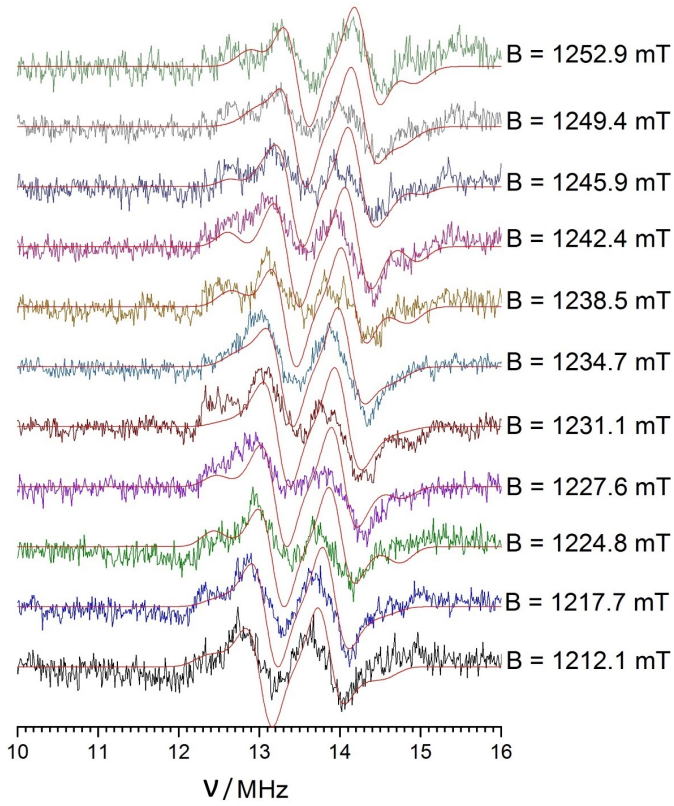

Figure 5.7: Field dependence of Q-band ENDOR spectra near the Larmor frequency of ^{27}Al for V-doped MIL-53(Al), sample *no*. 1. Magnetic fields are indicated and simulations using $A_{||}(^{27}\text{Al})$= 2.30 MHz; $A_{\perp}(^{27}\text{Al})$= 0.75 MHz are shown in red.

5.3 Conclusions

A series of V-doped MIL-53(Al) AS samples with low V concentration was synthesised and characterised with EPR and ENDOR. The AS samples exhibit an EPR spectrum dominated by the same low-symmetry V^{IV}-related component. In Chapters 6 and 7 a similar V^{IV}=O EPR spectrum will be used for monitoring transitions of the host MOF and for observing interactions between framework and guest molecules. Even though VCl_3 is used as dopant salt, V^{IV}=O doping of the (Al-OH)BDC MOF is observed meaning that partial oxidation of the dopant occurred during the synthesis procedure. This will be studied in-depth in Chapter 7.

A detailed analysis of the ligand ENDOR spectra proves that the observed V^{IV}-ions occupy regular Al-sites (V^{IV}=O substituting for A^{III}-OH) in MIL-53(Al). The well-resolved HF structure and relatively narrow linewidths in the EPR spectra indicate that the EPR-observable V^{IV}-centres are well dispersed in the framework. Thus, the synthesis and doping method presents a reproducible and reliable base for studying the properties of MIL-53(Al) after activation both for breathing and catalysis.

6

Temperature-Induced Breathing in Activated V-Doped MIL-53(Al)

It is too hot, can you breathe? Activated MIL-53(Al) is characterised by a distinct reversible structural transition between a hydrated NP and a LP state, resulting in expansion (NP $\rightarrow$ LP) or contraction (LP $\leftarrow$ NP) of this 3D porous framework. In this chapter we examine whether EPR-active V^{IV}=O molecular ions, incorporated in the Al metal nodes, can be used as local probes to detect these breathing transitions. Since the NP $\rightarrow$ LP transition is reported to occur in the range $300 - 450$ K, we studied the temperature dependence of the EPR spectrum while *in situ* heating the sample in a high-temperature EPR cavity. XRD is a well-established method for distinguishing the NP and LP states of MIL-53. Hence, in order to validate the EPR results, we recorded similar temperature dependences of the XRD patterns of the samples.

After activation (see Appendix B, section B.5), the EPR spectrum of V^{IV}=O in MIL-53(Al) has undergone important changes with respect to the AS state spectrum. Moreover, the RT EPR spectrum of activated samples was found to depend on the history of the sample and on the atmosphere in which it is recorded. Careful study of these phenomena led to the following conclusions: i) all X-band EPR spectra of activated samples are composed of two clearly different contributions that can be separated by thermal treatment, and ii) O_2 should be avoided when recording the spectra.

In agreement with the EPR results, the powder XRD patterns of activated V-doped MIL-53(Al), measured at RT in air to check the crystallinity of the sample, reveal a not *a priori* predictable ratio of NP and LP state fractions. Moreover, the XRD

pattern of the LP state proved very reproducible, whereas for the NP fraction the XRD 2θ peak positions seemed to vary somewhat from sample to sample. For most samples the XRD pattern of the NP fraction was close to that reported by Loiseau *et al.*,[21] who specified that in this state the framework is hydrated. In this chapter, it is shown with *in situ* XRD that when heating the NP, the framework undergoes a continuous change of lattice parameters before the transition to the LP state occurs. At the end of this chapter, the former changes are correlated with the hydration state of NP MIL-53(Al) and the existence of hydrated (NP-h) and dehydrated (NP-d) states. Until then, we only make the distinction between the NP and the LP state in this chapter.

The results presented here are mostly based on publication:

> ***In Situ* Electron Paramagnetic Resonance and X-ray Diffraction Monitoring of Temperature-Induced Breathing and Related Structural Transformations in Activated V-Doped MIL-53(Al)**
>
> Irena Nevjestić, Hannes Depauw, Karen Leus, Geert Rampelberg, Claire A. Murray, Christophe Detavernier, Pascal Van Der Voort, Freddy Callens, and Henk Vrielinck
>
> The Journal Of Physical Chemistry C, 2016, 120 (31), pp 17400-17407

6.1 Two V^{IV}=O States in Activated V-Doped MIL-53(Al)

The top two traces in Figure 6.1 show the powder EPR spectra of activated 1.5% V-doped MIL-53(Al) in two situations: (a) where the majority of the powder sample is in the NP state and (b) with a predominance of the LP state. Situation (a) was obtained by immersing a tube containing the powder in air overnight in liquid N_2. For the other extreme (b), the sample was heated to 445 K under vacuum (10^{-2} mbar) during 4 h.

In order to exclude possible influences of the temperature and atmosphere, both EPR spectra were recorded at RT and 1 mbar, thus by continuously pumping the sample tube. The third spectrum in Figure 6.1 (trace c) is that of the AS powder. All three spectra exhibit the typical characteristics for vanadyl molecular ions (see section 3.3.3.4). They have a close-to-axial g tensor with $2 > g_x \approx g_y > g_z$ and a ^{51}V HF tensor with $A_x \approx A_y \approx 165$ MHz $< A_z \approx 500$ MHz. In spite of these similarities, the three spectra can be clearly distinguished. In the spectra of AS and LP, peaks appear at approximately the same field positions. The difference between them seems to be mainly resulting from a change in linewidth. Spectrum (a) is more substantially different: in comparison with the other two spectra,

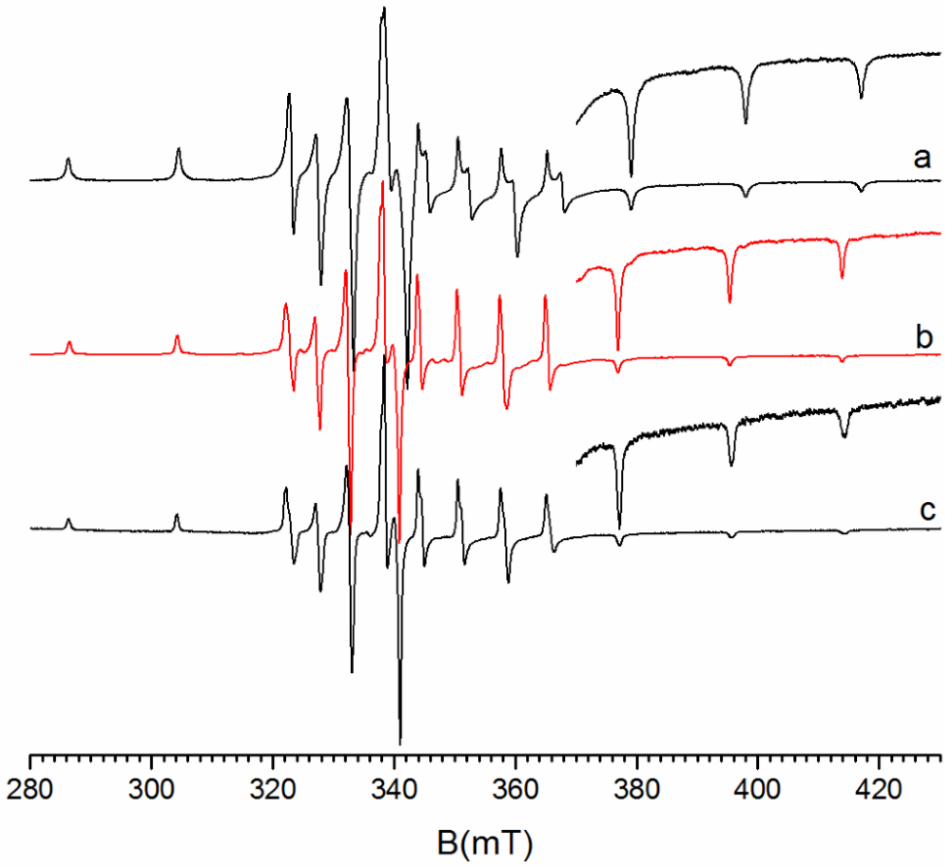

Figure 6.1: Powder EPR spectra of activated 1.5% V-doped MIL-53(Al) in vacuum at RT: (a) NP state, (b) LP state, and (c) AS state. The insets show a magnification of the high-field part of the spectra.

resonance peaks appear at clearly different positions. In addition, in the central part of the spectrum corresponding with the NP state, more resolved features appear than in the corresponding parts of the spectra for LP and AS. This points to a larger deviation from axial symmetry for the V^{IV}=O sites in the NP state, in comparison with the LP and AS states. This observation seems well correlated with the differences in the local environment (symmetry) at the Al-OH nodes in MIL-53(Al) in these three states, as shown in Table 6.1. Indeed, the AlO_4 'planes' (approximately perpendicular to the Al-OH chains) in the NP state deviate more substantially from a square planar arrangement than for the other two states. In a square planar arrangement distances to the four oxygen atoms should be equal and angles between bonds should be 90°. One might thus suspect that the V^{IV}=O ions can be used as paramagnetic probes for observing the NP to LP transitions. This is further explored in the following subsections by *in situ* heating EPR and

XRD experiments.

Table 6.1: Structural parameters of AlO_6 complexes in AS, NP and LP states.[21] The Mercury software was used for crystal-structure visualisation.[168]

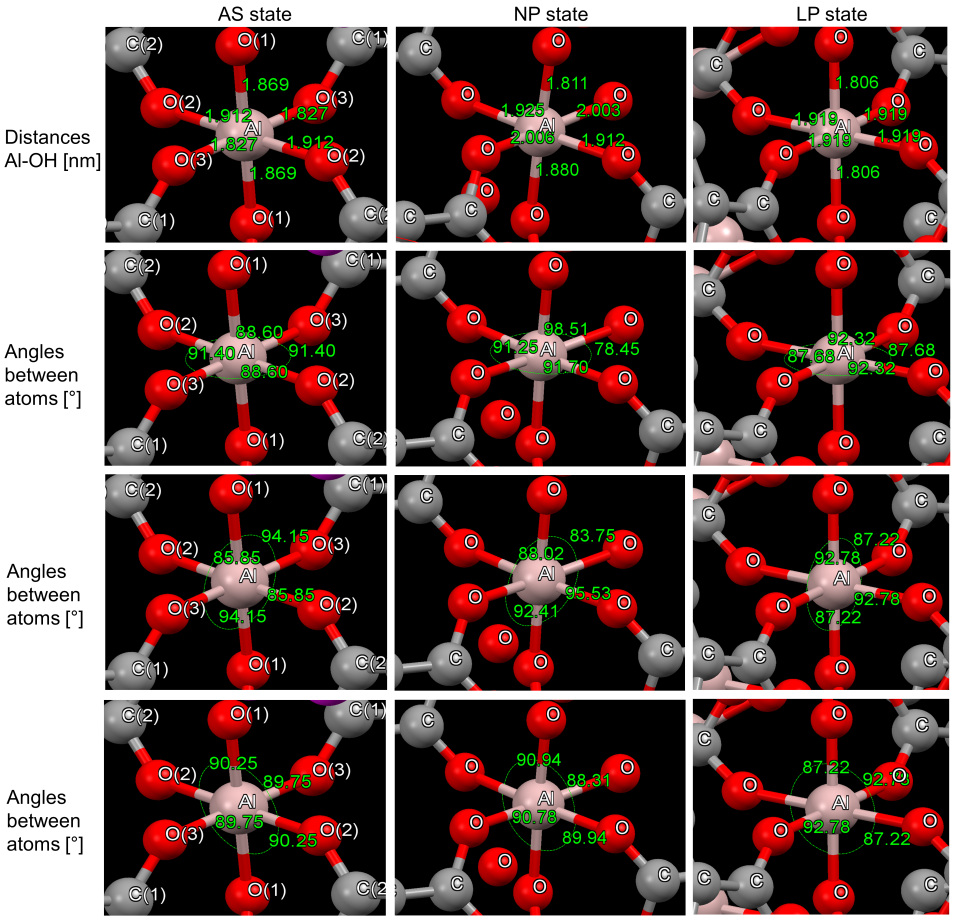

By heating the samples, Kozachuk *et al.*[148] succeeded in isolating one of the spectral components, which they labelled *II*. Judging on the shape of the spectrum and supported by simulations in Figure 6.2 with parameters from Table 6.2, we may conclude that this component corresponds with the spectrum we associate with the LP state (all spectral features are reproduced, indicated in top spectrum with green lines). No spectra of the isolated second component were reported by Kozachuk *et al.* They interpreted the spectra for samples containing a mixture of the two states as arising from an additional component with axial spin-*Hamiltonian* parameters, labelled *b*.

Simulations suggest that spectra from samples containing a mixture of NP and LP

Table 6.2: Parameters from Kozachuk *et al.*[148] for EPR spectra simulations.

	II	*b*
$\mathbf{g_x}$	1.969	1.965
$\mathbf{g_y}$	1.969	1.965
$\mathbf{g_z}$	1.940	1.932
$\mathbf{A_x}$ [MHz]	164.9	173.6
$\mathbf{A_y}$ [MHz]	164.9	173.6
$\mathbf{A_z}$ [MHz]	493.8	505.8

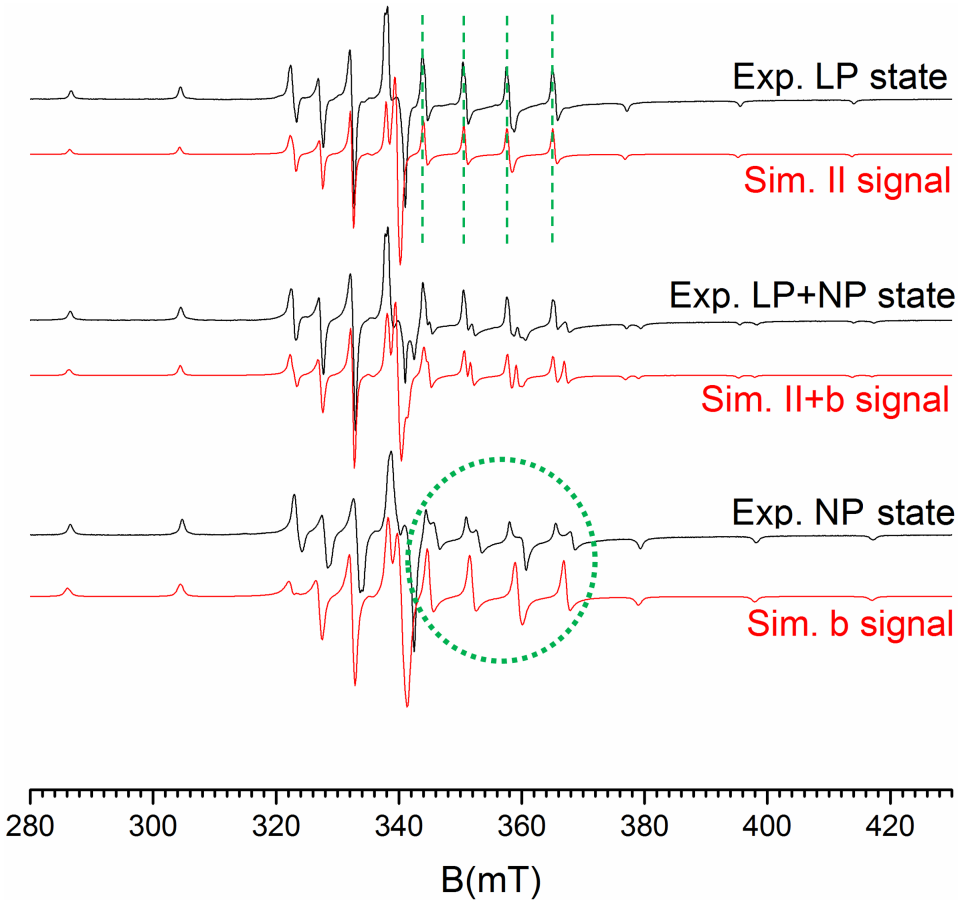

Figure 6.2: Powder EPR spectra of activated 1.5% V-doped MIL-53(Al) associated with the LP state (top), a mixture of the NP and LP state (middle) and the NP state (bottom)(black: experimental). Simulations (red) of signal *II*, *II*+*b* and *b* from Kozachuk *et al.*[148]

V-doped MIL-53(Al) can indeed be (mis)interpreted in this way. The isolated EPR component associated with the NP state, however, does not match this second axial component *b* at all (not all spectral features are reproduced, indicated in

bottom spectrum with green circle). This EPR spectrum thus appears to be due to a centre with lower than axial symmetry.

Obtaining reliable spin-*Hamiltonian* parameters involves recording EPR spectra in several microwave bands as already shown in Chapter 5 for V^{IV}=O in AS MIL-53(Al). In particular, this holds true for the spectra corresponding to the NP and LP states: a multi-frequency analysis of these spectra will be presented in Chapter 7. However, for now, these two spectra are sufficiently different to distinguish them, even without such detailed spin-*Hamiltonian* analysis.

6.2 Transformation between NP and LP States in Vacuum

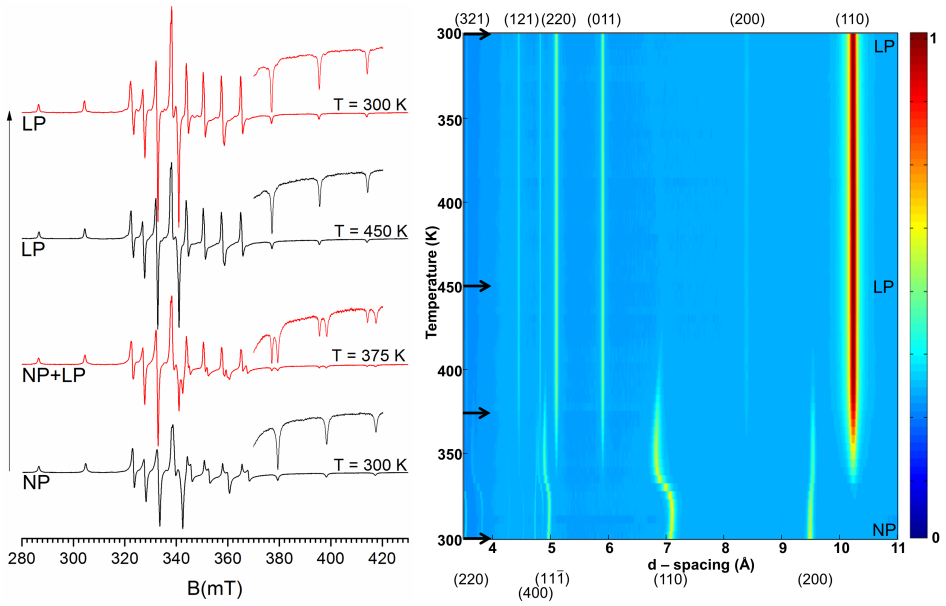

Figure 6.3: Left: Powder EPR spectra of activated 1.5% V-doped MIL-53(Al) in vacuum recorded at four temperatures. The complete T-dependent EPR experiment is reported in Figure 6.4. Insets show a magnification of the high-field part of the spectra. The arrow indicates start and end EPR spectrum together with associated states. Right: Temperature dependence of synchrotron XRD patterns of activated 1.5% V-doped MIL-53(Al) in vacuum, λ = 0.825086 Å. This experiment was performed at the Diamond Light Source facility. 2θ is converted to d-spacing in Å via Bragg's law (Chapter 4). Miller indices for all high-intensity peaks are indicated, both for the NP and LP states of MIL-53(Al). The sample was at RT in the NP state, after the heating experiment the XRD pattern of the LP state of MIL-53(Al) is observed. The arrows indicate temperatures where EPR spectra presented on the left were recorded.

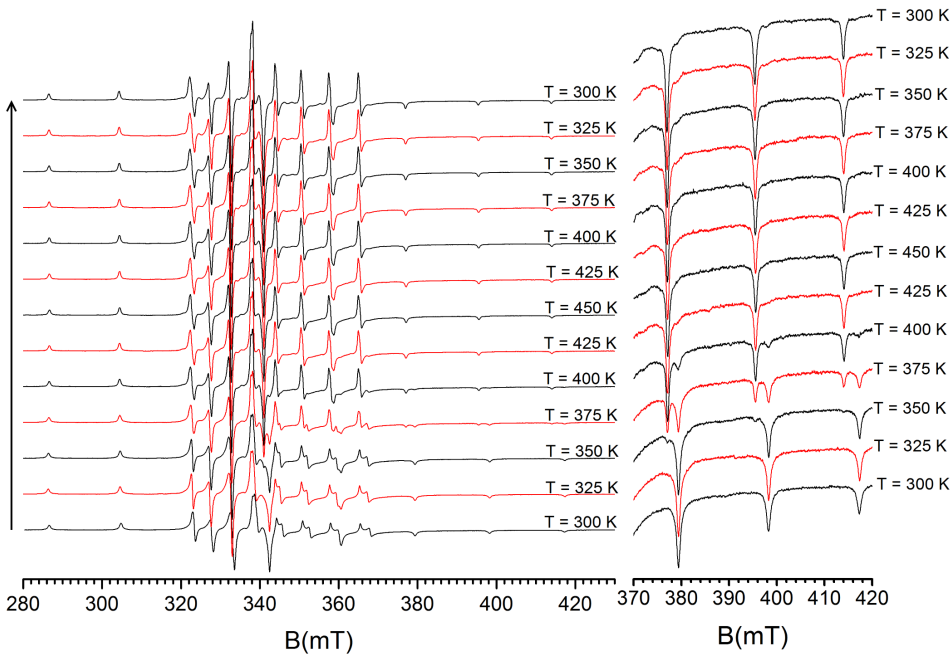

Figure 6.4: Powder EPR spectra for the T-experiment of activated 1.5% V-doped MIL-53(Al) in vacuum. Insets show a magnification of the high-field part of the spectra. The first spectrum recorded in the experiment is shown as the bottom trace, and the temperature is indicated at the right hand side. The arrow indicates start and end EPR spectrum.

The correlation between the two types of V^{IV}=O EPR spectra and the two states of activated MIL-53(Al) is further explored by recording EPR spectra at low pressure during *in situ* heating in a high-temperature EPR resonator (see Appendix B, section B.1 for experimental details). For starting the temperature experiment, the sample was brought in the NP state as described above in section 6.1. In Figure 6.3, the left bottom trace is assigned to the NP state. The EPR spectra were recorded while continuously pumping the quartz sample tube to 0.01 mbar. The temperature was raised from RT (300 K) to 450 K and back to RT, in steps of 25 K, after keeping the sample for 0.5 h at each temperature in order to ensure stabilisation. In Figure 6.3, right, the results of *in situ* T-dependent synchrotron XRD experiments on the same sample in vacuum (continuous pumping) are shown. In these experiments XRD patterns were monitored every 60 s while continuously ramping up (and afterward down) the temperature. The experiment was completed in 1 h. In view of the considerable difference in heating speed, sample mass, and sample tube dimensions, all influencing the heat transfer, a perfect correspondence between the T-axes of the two experiments is not expected. The similarities between the results in Figure 6.3 are, nonetheless, obvious:

1. In the early stages of the heating experiment the EPR spectrum remains (practically) unaltered and the XRD pattern is that of the NP state.

2. There is a transition T-range where EPR spectra of the two V^{IV}=O states are simultaneously present, and also the XRD patterns contain contributions of two states: the LP state and a NP or very closely related state.

3. From 400 K onwards (when raising the temperature), only the V^{IV}=O EPR spectrum associated with the LP state is further observed. The EPR spectrum remains basically unaltered when slowly bringing the temperature back to RT. Meanwhile, the XRD pattern of the LP state of MIL-53(Al) is observed.

Detailed analysis of the XRD patterns shows that the LP state appears at 344 K and the NP state disappears at 424 K. The bulk of the transition occurs between 350 and 400 K, which is in agreement with reported values for MIL-53(Al).[59,136] In addition to this essentially identical information that can be extracted from both experiments, the XRD T-experiment reveals an effect that is not obvious in the X-band EPR spectra. Between 320 and 350 K, the diffraction peaks (110), (11$\bar{1}$), and (220) of NP MIL-53(Al) exhibit a clear shift to smaller d-spacings (higher 2θ values, Bragg's Law), while the NP peaks (200) and (400) shift to slightly larger d-spacings (lower 2θ values). This points to a gradual change in the lattice parameters, resulting in a decrease of the unit cell volume, confirmed by Lebail refinements on the experimental data. In Figures 6.5 and 6.6 unit cell volume together with lattice parameters of the NP state are shown as a function of temperature. It can be see that the trend in unit cell volume is governed by the trend in lattice parameter *b*. Table 6.3 compares crystallographic data for the NP state obtained from Lebail refinement at 298 K and 419 K and data reported by Loiseau *et al*.[21] for the stable state at RT and ambient atmosphere conditions, which they label MIL-53 LT. For the LP state none of the diffraction peaks exhibits similarly clear temperature dependence.

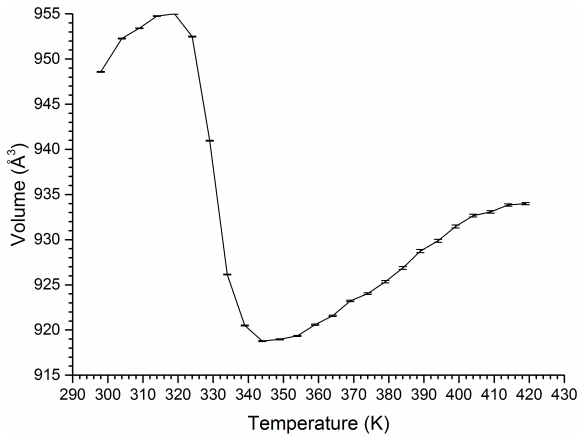

Figure 6.5: Unit cell volume of the NP state as a function of temperature during the heating experiment. Error bars represent 1σ.

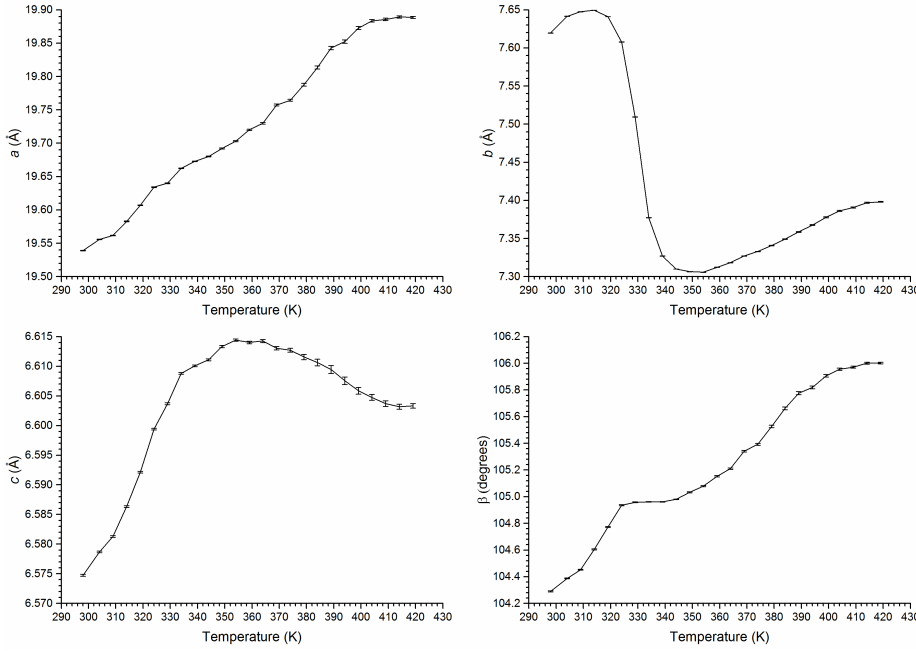

Figure 6.6: Lattice parameters of the NP state as a function of temperature during the heating experiment obtained from Lebail refinements. Error bars represent 1σ.

Table 6.3: Crystallographic data of the NP state at 298 K at 419 K in vacuum determined from Lebail refinements of synchrotron powder diffraction data compared to reported results for MIL-53 LT from Loiseau *et al*.[21] LT corresponds to 'low temperature' state which is assigned as NP state in this work.

	MIL-53 LT	MIL-53 NP state	
Space Group	Cc	Cc	Cc
Crystal System	Monoclinic	Monoclinic	Monoclinic
a/Å	19.513(2)	19.5392(6)	19.8889 (14)
b/ Å	7.612(1)	7.61970(11)	7.3982(7)
c/ Å	6.576(1)	6.57475(17)	6.6033 (4)
$\beta/^\circ$	104.24(1)	104.2890(4)	106.002(6)
Volume/ Å^3	946.74	948.57(4)	933.98(13)
Diffractometer		I11/Diamond Light Source	
Wavelength (Å)		0.825870(10)	
Temperature (K)		298	419

6.3 Transformation between NP and LP States in Air

A similar *in situ* T-experiment of EPR and XRD measurements was performed while keeping the sample in contact with air at ambient pressure and humidity. The results are summarized in Figure 6.7. In the first half of the experiment (RT $\rightarrow$ 450 K) the results are nearly identical to those with the sample in vacuum. The linewidth of the EPR spectrum associated with the LP state is, however, slightly larger than when the sample is kept in vacuum. This change in linewidth is most apparent in the centre of the spectrum, which exhibits slightly higher resolution when it is recorded in vacuum. In the XRD patterns, the shift of the NP state (110), (11$\bar{1}$), and (220) peaks to lower d-spacings, observed in the vacuum experiment, is nicely reproduced. The XRD T-experiment for undoped MIL-53(Al) showed similar gradual change to smaller d-spacings, Figure 6.9, pointing to the fact that this effect is not induced by vanadium doping.

Also in the second half of the experiment (450 K $\rightarrow$ RT) the XRD experiments in air and in vacuum exhibit no important differences, except that under air conditions, close to RT, part of the sample returns to the NP state most probably as a result of uptake of water from the air. The NP state XRD pattern obtained is the same as in the starting conditions of the experiment. However, the EPR spectra reveal an interesting additional feature. From about 375 K downward, the linewidth of the EPR spectra gets broader as temperature lowers, while the spectrum (peak positions) remains that associated with the LP state. This broadening cannot be related to changes in the MIL-53(Al) lattice parameters since no evidence for such changes is found in the XRD patterns. When the air atmosphere is removed by pumping, the narrow-line EPR spectrum as obtained in the vacuum experiment is recovered. Finally, in the top EPR spectrum of Figure 6.7, left, no clear evidence of the NP state is seen, in contrast with the XRD result. In view of the differences in geometry between the experiments, one may expect that longer exposures to air are necessary in the EPR experiments in comparison with XRD. When monitoring the EPR spectrum at RT for a longer time after ending the T-experiment, the NP component clearly grows in. This experiment is shown in Figure 6.10.

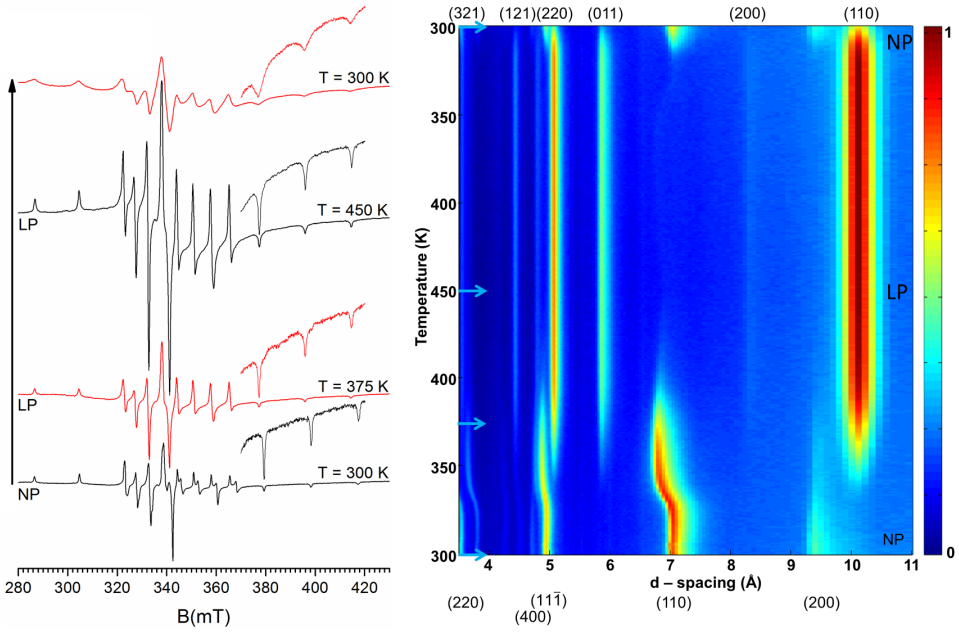

Figure 6.7: Left: Powder EPR spectra of activated 1.5% V-doped MIL-53(Al) in air recorded at four temperatures. The complete T-dependent EPR experiment is reported in Figure 6.8. Insets show a magnification of the high-field part of the spectra. The arrow indicates start and end EPR spectrum together with associated states. Right: Temperature dependence of XRD patterns of activated 1.5% V-doped MIL-53(Al) in air, λ = 1.54056 Å. This experiment was performed at Ghent University, in a setup of the research group CoCooN. 2θ is converted to d-spacing in Å via Bragg's law. Miller indices for all high-intensity peaks are indicated for both the NP and LP states of MIL-53(Al). The sample was at RT in the NP state; at approximately 425 K full transition to the LP state occurred. Cooling down the sample to RT, the XRD pattern of the NP state of MIL-53(Al) starts appearing again. The arrows indicate temperatures where EPR spectra presented on the left were recorded.

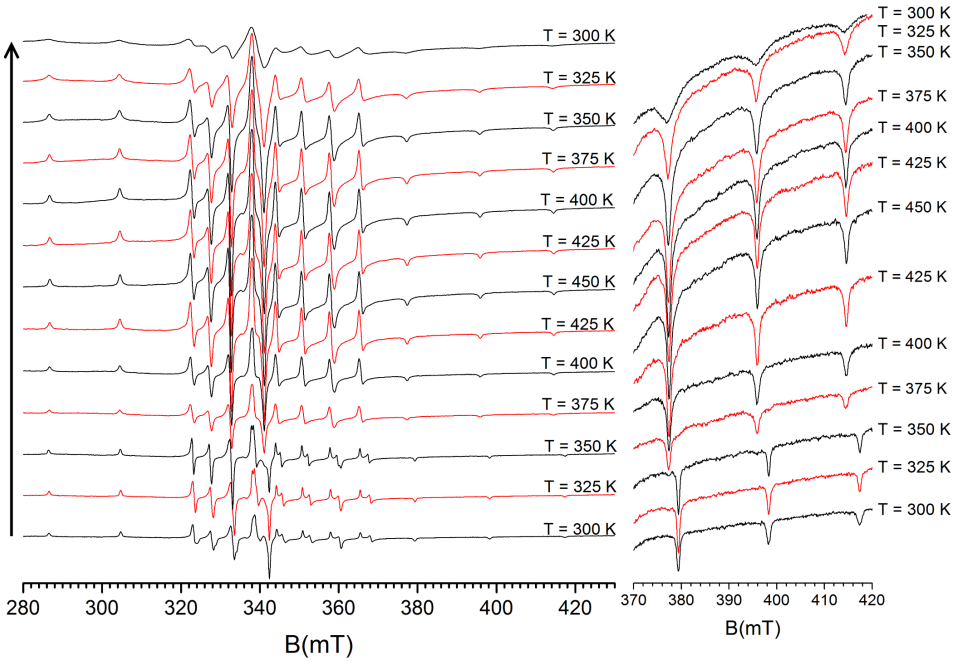

Figure 6.8: Powder EPR spectra for the T-experiment of activated 1.5% V-doped MIL-53(Al) in air. Insets show a magnification of the high-field part of the spectra. The first spectrum recorded in the experiment is shown as the bottom trace and is associated with the NP state. The temperature is indicated at the right hand side. The arrow indicates start and end EPR spectrum.

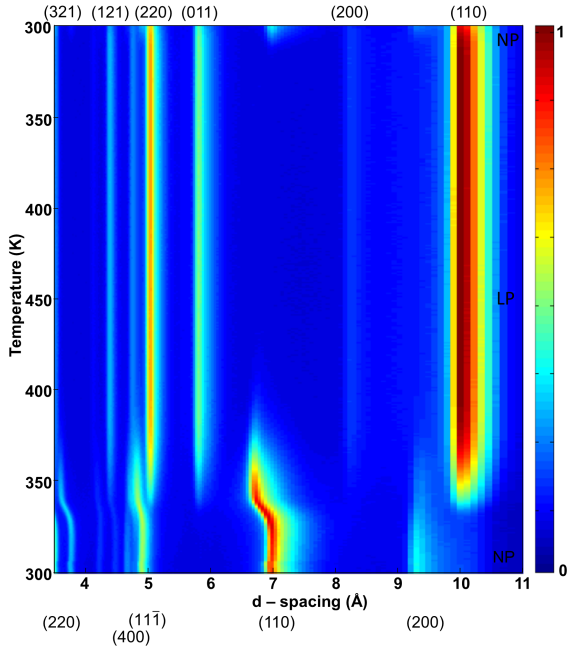

Figure 6.9: Temperature dependence of XRD patterns of undoped MIL-53(Al) in air, λ = 1.54056 Å. This experiment was performed at Ghent University, in a setup of the research group CoCooN. 2θ is converted to d-spacing in Å via Bragg's law. Miller indices for all high-intensity peaks are indicated for both the NP and LP state of MIL-53(Al). The sample was at RT in the NP state, at approximately 425 K full transition to the LP state occurred. Cooling down the sample to RT, the XRD pattern of the NP state of MIL-53(Al) starts appearing again.

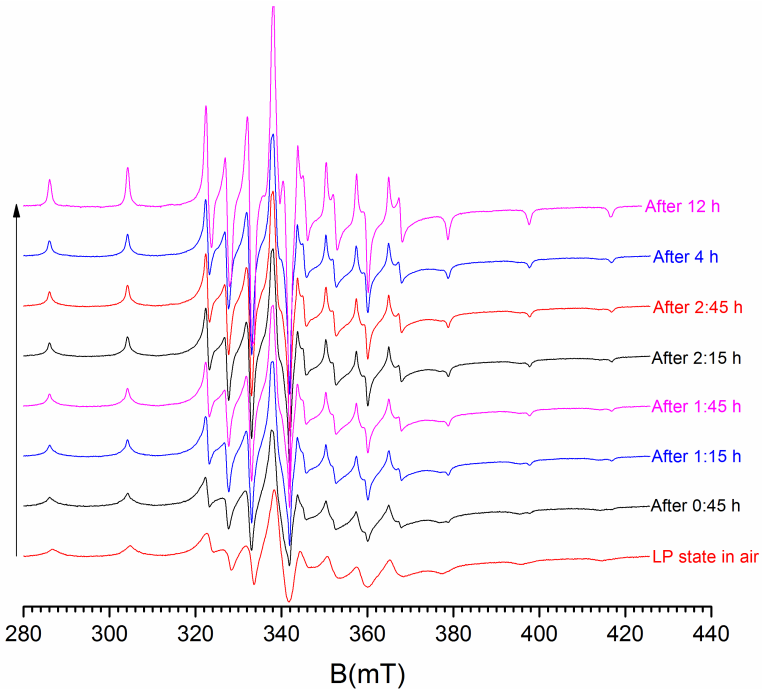

Figure 6.10: Monitoring RT EPR spectra of activated 1.5% V-doped MIL-53(Al) after T-experiment in air. The bottom spectrum is associated with the LP state and the top spectrum is associated with the NP state. It is visible that the NP component grows in after 45 minutes. The arrow indicates start and end EPR spectrum.

6.4 Discussion and identification of the intermediate NP state

We have shown that the breathing effect in V-doped MIL-53(Al), induced by varying the temperature above RT, can be monitored by *in situ* EPR spectroscopy. This yields complementary information to the XRD analysis. The EPR spectra reflect the local environment of the V^{IV}=O molecular ion. Apparently, the EPR spectrum of paramagnetic V^{IV}=O complexes substituting for Al-OH follows the global, reversible LP to NP transitions of the activated MIL-53(Al) crystals. In a first approximation, one may expect this to correspond to the geometry of the distorted (HO-V=O)O_4 octahedron, which apparently follows that of the (OH-Al-OH)O_4 octahedra in the activated MIL-53(Al), rather than remaining fixed in itself, as in the case of the fully V=O substituted rigid lattice MIL-47(V). The hypothesis that X-band EPR probes the environment of the V^{IV}=O nodes very locally is confirmed by the absence of clear changes in the NP EPR spectra in the heating part of the T-experiments under vacuum and air conditions. XRD demonstrates that the host lattice may undergo global structural changes, corresponding to shifts in the d-spacing in the order of a few percent (in the region from approximately 320 to 350 K) without notable influence on the NP X-band EPR spectrum of the V^{IV}=O dopant molecular ions. A Lebail refinement of the XRD peak positions shows that these changes mainly correspond with an expansion of the *a* parameter and a contraction of *b*, together leading to a slight decrease of the unit cell volume. A metastable intermediate NP state is reached before the transition to the LP state occurs.

Because such strong changes in the lattice parameters are absent for the LP state, they are very probably related to how H_2O is bound to the NP framework. The involvement of H_2O was further investigated via TGA. Figure 6.11 shows that the V-doped MIL-53(Al) sample exhibits a weight loss of slightly more than 6% in the $310 - 350$ K range, where the strong changes in the NP lattice parameters were observed with XRD. On the other hand, between 350 and 450 K the sample loses less than 1% weight, while XRD reveals that in this range the transition from the intermediate metastable NP state to LP takes place. Our TGA results agree with those for pure MIL-53(Al),[21] but there the dehydration of the MIL-53(Al) structure was associated with the hydrated NP to LP transition. Our combined XRD and TGA results reveal a more detailed picture of the temperature-induced framework changes of (V-doped) MIL-53(Al), starting from RT and ambient atmosphere conditions. Upon heating, the hydrated NP state (NP-h) first dehydrates in a continuous way, leading to a gradual change in lattice parameters, and the structure is (practically) completely dehydrated before the transition to the LP state occurs. Hence, the metastable intermediate NP state may be identified as

the dehydrated NP (NP-d) state of MIL-53(Al). TGA measurement on this NP-d state (red curve in Figure 6.11, for experimental details see Appendix B, section B.2) showed no weight loss in the same temperature region.

Finally, cooling the sample down from 450 K to RT, the situations in air and in vacuum are not completely the same. In vacuum the sample stays in the LP state since water cannot reenter the pores to contract them. In air a fraction of the sample contracts to the NP-h state close to RT within a couple of minutes. The broadening of the EPR spectrum observed when the sample is cooled down in air, will be further investigated in Chapter 8.

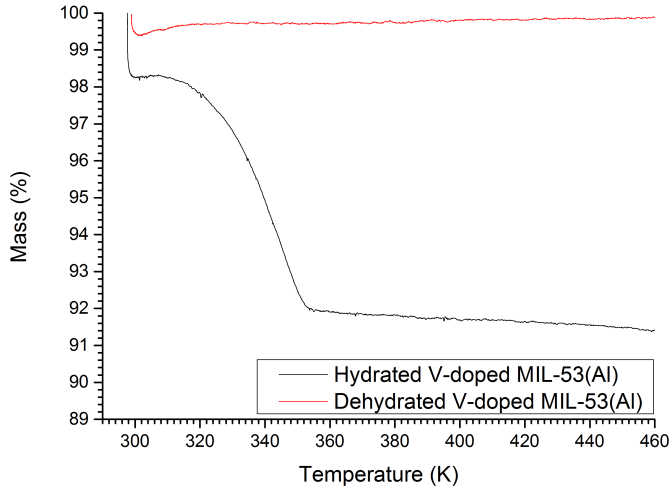

Figure 6.11: TGA measurements of NP-h and NP-d activated V-doped MIL-53(Al) in air.

In situ XRD studies of MIL-47(V^{III}) and various MIL-53(M) variants (M = Al, Ga, Cr, Fe, Sc)[51–53,169] have revealed either stepwise or continuous changes in the diffraction patterns when following NP to LP transitions. In the cases of MIL-47(V^{III}),[67] MIL-53(Fe),[169] and MIL-53(Sc),[53] the NP-h to LP transition happens via a dehydrated (assigned as closed or very narrow pore) and an intermediate state where half of the pores are completely open and half are completely closed. In MIL-53(Ga)[52] a contraction of the pores is observed before the NP-h to LP transition occurs and has been associated with a NP-d state. Neimark *et al.*[170] reported slight shifts of the XRD peaks during CO_2 sorption in MIL-53(Cr), which have also been associated with changes in the configuration of the guest molecules. The particular continuous change in lattice parameters to a metastable intermediate NP state observed here for MIL-53(Al) has so far, to the best of our knowledge, not been reported. Considering the observations for other MIL-53 frameworks, the identification of the intermediate metastable NP state for MIL-53(Al) as NP-d appears obvious. However, two inconsistencies with earlier results delayed this conclusion.

First, Liu *et al*.[59] had shown that under vacuum conditions, the NP-h MIL-53(Al) framework dehydrates. In our *in situ* powder XRD measurements in vacuum (collected at the I11 beamline of the Diamond Light Source) this was clearly not the case: the sample was in the NP-h state at RT at the start of the measurements, even though the sample capillary was pumped to 10^{-5} mbar before ramping up the temperature, and further continuously pumped during *in situ* heating. Both the continuous dehydration and the transition to the LP state occurred in (almost) the same temperature ranges as for the experiments in air. After cooling back to RT, the sample remained in the LP state, indicating that the capillary was indeed evacuated in this experiment. In order to prevent pumping the sample out of the capillary, it was stoppered with glass wool (for experimental details see Chapter 4, section 4.4). The most plausible explanation for these contradictory results is that this glass wool prevented the dehydration of the framework at the beginning of the experiment.

A second problem in the identification was the mismatch of our experimental XRD pattern of the intermediate metastable NP state with simulations using the lattice parameters for the NP-d state reported by Liu *et al*.[59] Figure 6.12 shows our experimental and simulated XRD patterns of the intermediate NP state and simulated XRD patterns using reported lattice parameters (see Table 6.4) of the NP-d state in MIL-53(Al) (neutron powder diffraction, Liu *et al*.[59]) and the NP-d state in MIL-53(Al) (XRD (not refined), Volkringer *et al*.[52]). The discrepancy between experiment and the patterns calculated with the reported parameters for NP-d is very clear. The TGA experiment is, however, very clear: the change in the lattice parameters observed when heating the sample to 350 K is correlated with the dehydration of the framework. One possible reason for the mismatch with literature lattice parameters for the NP-d state are differences in experimental conditions. While in our experiments the NP-d state is obtained at elevated temperature (from 350 K onwards), Liu *et al*.[59] and Volkringer *et al*.[52] obtained the NP-d state at RT and at low pressure. Since the MIL-53 framework is highly flexible both temperature and pressure could have an effect on the unit cell dimensions.

Table 6.4: Available lattice parameters for the NP-d state in MIL-53(Al) compared with results from this study for V-doped MIL-53(Al). *data were not refined.

	a (Å)	**b (Å)**	**c (Å)**	**β (°)**	**Space group**
MIL-53(Al/V) **NP-d** (350 K)	19.8889(14)	7.3982(7)	6.6033(4)	106.002(6)	Monoclinic Cc
MIL-53(Al) **NP-d**[59] (295 K)	20.756(1)	7.055(2)	6.6087(5)	113.580(6)	Monoclinic C2/c
MIL-53(Al)* **NP-d**[52] (333 K)	20.49	7.37	6.58	112.4	Monoclinic C2/c

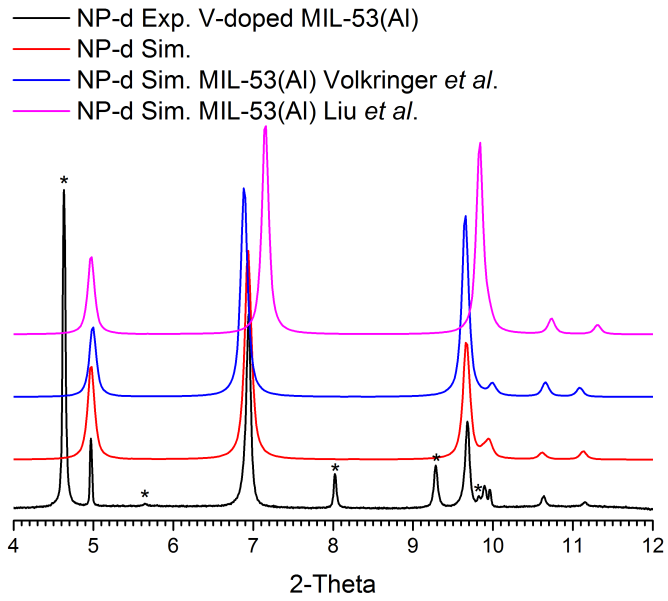

Figure 6.12: Experimental and simulated XRD pattern of the NP-d state from the heating cycle in vacuum, black (λ = 0.825086 Å). Asterisks indicate peaks from the LP state. Simulated XRD patterns from reported lattice parameters by Liu *et al.*[59] and Volkringer *et al.*[52] for MIL-53(Al). Lattice parameters are presented in Table 6.4.

6.5 Conclusions

Combining X-band EPR and XRD experiments during *in situ* heating, we demonstrated that the EPR spectrum of V^{IV}=O dopant centres allows to follow the framework state transformations of MIL-53(Al). The XRD experiments demonstrated that when starting the heating experiment from RT and ambient air conditions, the NP-h framework first dehydrates (to NP-d) and only then makes the transition to the LP state. In the following chapter the EPR spectra of V^{IV}=O in the NP-h, NP-d and LP states are studied in more detail and a complete spin-*Hamiltonian* analysis is carried out.

7

Distinguishing the three states of V-doped MIL-53(Al)

Are you afraid of water? XRD and EPR were combined to study the structural transformations induced by temperature, pressure and air humidity of the breathing MIL-53(Al), doped with paramagnetic V^{IV} ions, after activation. Using XRD, the transition from the NP-h to the NP-d state is probed by heating in ambient air, by reducing the air pressure (pumping) at RT and by reducing the air humidity at RT and ambient pressure (dessication). Moreover, the reversibility of these transformations is tested. Some of these results were combined with Fourier-transform infrared spectroscopy. This study unveiled the conditions for bringing MIL-53(Al) exclusively in one state.

As an extension of Chapter 6, we show here that the EPR spectra of V^{IV}=O molecules, replacing Al^{III}-OH in activated MIL-53(Al), in the three mentioned states are clearly distinguishable. Multi-frequency (9.5-275 GHz) EPR experiments allowed a consistent spin-*Hamiltonian* analysis for V^{IV}=O in NP-h, NP-d and LP MIL-53(Al).

The results presented in this chapter are published as:

Sensing the framework state and guest molecules in MIL-53(Al) via the electron paramagnetic resonance spectrum of V^{IV} dopant ions

Irena Nevjestić, Hannes Depauw, Peter Gast, Pieter Tack, Davy Deduytsche, Karen Leus, Melissa Van Landeghem, Etienne Goovaerts, Laszlo Vincze, Christophe Detavernier, Pascal Van Der Voort, Freddy Callens, Henk Vrielinck

Physical Chemistry Chemical Physics, 2017, 19 (36), pp 24545-24554

7.1 Conditions for dehydration monitored with XRD and FTIR

In Chapter 6 it was demonstrated with *in situ* XRD that the transition of activated MIL-53(Al) doped with V from the NP-h to the LP state happens via the NP-d state, when heating (from RT) in ambient air or in vacuum. By heating, a gradual change in the lattice parameters occurs in the 320-350 K range, after which NP-h MIL-53(Al) reaches a NP-d state with a decreased unit cell volume compared to the NP-h state.

This intriguing continuous dehydration was further investigated with *in situ* XRD, changing also other conditions than T. The reversibility of the hydration/dehydration of V-doped MIL-53(Al) in air was tested by recording XRD patterns in the temperature range from RT up to 350 K (where the gradual change occurs) and back (Figure 7.1 a). At RT the sample is in the NP-h state and by heating in air a gradual transformation to the NP-d state is observed. Cooling the sample down demonstrates a gradual and completely reversible return to the NP-h state. The changes in the framework lattice parameters observed during dehydration and hydration are very similar. Some traces of the LP state are also present when the NP-d state is induced, in particular peaks at approximately 5.8 Å and 10 Å. The intensity of these peaks drops during cooling but they do not vanish completely at RT indicating that part of the framework needs more time to hydrate back to the NP-h state.

Liu *et al*.[59] previously reported a NP-d state for MIL-53(Al), obtained by exposing the MOF to high vacuum. Inspired by this, we also followed the MIL-53(Al) state by *in situ* XRD while reducing the air pressure. The results of these experiments are summarized in Figure 7.1 b. At the start, the sample was in the NP-h state at ambient conditions. After switching on the pump (bottom yellow line) the continuous shift of the diffraction peak near 7Å indicates that MIL-53(Al) is dehydrating quite quickly. The total shift in d-spacing observed in this process (0.33±0.03 Å) is similar to that observed in the *in situ* heating experiment (0.20±0.07 Å), even though these two experiments are not completely equivalent due to the temperature, and possibly also pressure dependence of the lattice parameters. When the NP-d state is obtained 1 bar of dry N_2 was directly applied to the sample. Almost no change in lattice parameters is observed. After that, N_2 was removed from the sample compartment. When the sample was re-exposed to ambient air, the XRD pattern slowly (within 60 min) returned to that of the NP-h state. The experiments presented here were performed on MIL-53(Al) samples doped with V, but we checked via experiments on undoped MIL-53(Al) that the results do not depend on the small fraction of V^{III}-OH or V^{IV}=O ions replacing Al-OH in the structure.

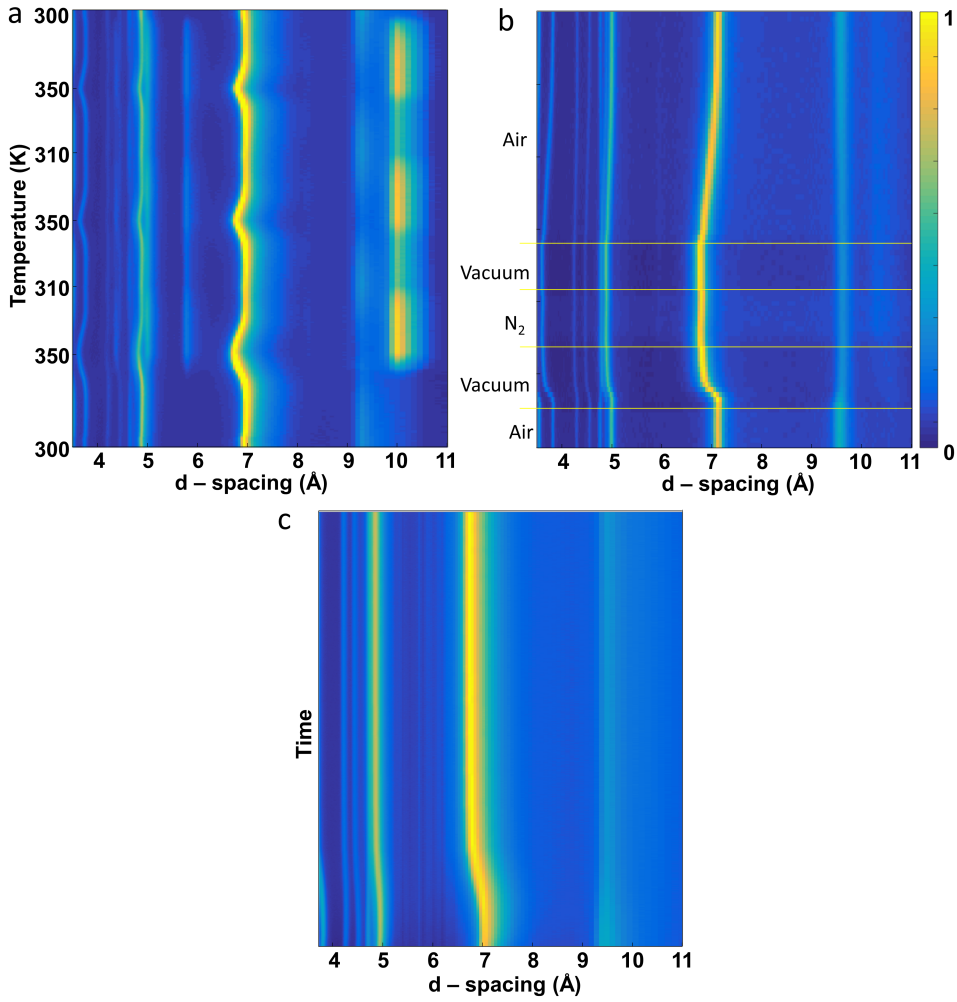

Figure 7.1: XRD patterns of V-doped MIL-53(Al) powder, λ = 1.54056 Å. 2θ is converted to d-spacing in Å via Bragg's law. a - Temperature dependence from RT up to 350 K and back to 310 K, three cycles in air. One cycle 310 K - 350 K - 310 K took 16 min. b - RT XRD measurements. The sample was in the NP-h state, the bottom yellow line indicates the moment when the pump was switched on and the sample started dehydrating for 25 min. The second yellow line indicates when N_2 was applied to the sample. 20 min later, N_2 was evacuated (for 12 min) and the sample was left in air until the NP-h state was obtained again. c - RT XRD measurements done on V-doped MIL-53(Al) in a closed sample compartment (at the start atmospheric (humid) air was inside) with silica gel. The reduction in d-spacing around d = 7 Å, characteristic for the dehydration of the structure, is confirmed.

In view of the hydration/dehydration process another experiment was performed. V-doped MIL-53(Al) powder in the NP-h state was placed in the sample compartment together with 2 cups of 2 mL silica gel and the compartment was

closed off. XRD patterns were followed as a function of time (Figure 7.1 c) during 3 hours after closing the sample compartment, after which the XRD pattern did not notably change any further. The total shift of the XRD peaks was smaller than the shift obtained by heating or by pumping which is probably because the silica gel did not have the capacity to adsorb all water originally present in the framework and the sample chamber.

Additional to the above described experiments, the temperature cycle experiments were repeated in different atmospheres, in particular N_2 and He gas. In the in-house XRD setup (see Chapter 4), the sample compartment is closed off and pumped before N_2 or He gas is added. As a result at the start of the heating experiment the sample was already in the NP-d state. Only the NP-d to LP transition was observed in the temperature rise, and when cooling down, the sample stayed in the LP state.

The dehydration of the NP-h state by desiccation that was followed on a V-doped MIL-53(Al) powder with *in situ* XRD (Figure 7.1 c), was recorded also with attenuated total reflection (ATR) FTIR spectroscopy. These experiments were performed and analysed by Engineering Physics student Alexander Hoffman in the framework of his master thesis 'Experimental and computational vibrational spectroscopy of metal-organic frameworks'.[171]

In the ATR setup the IR light is totally internally reflected on one side of a diamond crystal and the studied sample (powder) is brought in contact with this side (pressed onto it with a lever (anvil)). This system is placed in a sample compartment that can either be evacuated or brought under a controlled atmosphere at (near) ambient pressure (~1 bar). Like in the XRD experiment, silica gel was placed into the sample compartment together with the MIL-53(Al) powder and the sample compartment was closed off. At the beginning of the measurements the sample was in ambient atmospheric conditions. Gradually the air humidity in the sample compartment was decreased due to the adsorption of water on the silica gel. Mid-IR spectra were recorded during several hours and the results are presented in Figure 7.2.

The spectra are presented only from 400-1200 cm^{-1} because at higher frequencies the contribution of the absorption bands related to CO_2 and H_2O from the air in the sample compartment overlap with the bands related to the MIL-53(Al) framework. The first spectrum was taken immediately after the sample compartment was closed, with the MIL-53(Al) in the NP-h state (black spectrum). A gradual transition from the NP-h to the NP-d state (red spectrum) is visible mainly by the changes in the peaks at 985 and 1125 cm^{-1}. The intensity of the peak at 985 cm^{-1} increases while intensity of the peak at 1125 cm^{-1} decreases with dehydration. Three hours after closing the sample compartment, hardly any further changes in the IR spectra were observed. Since the 1125 cm^{-1} had (almost)

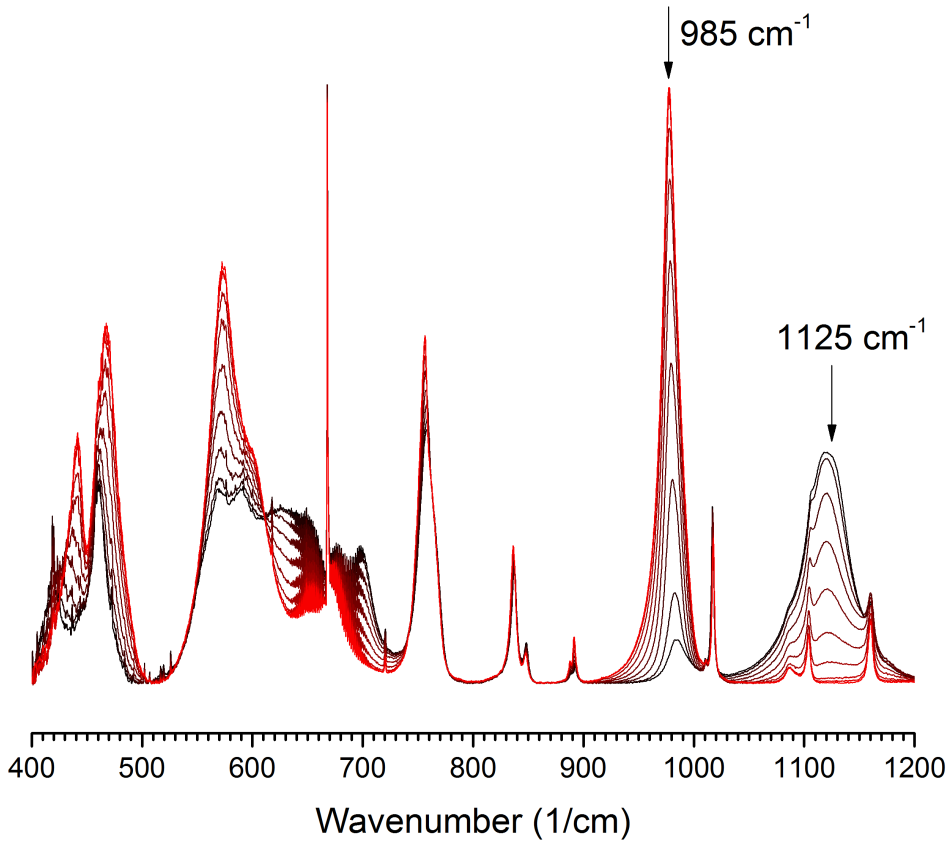

Figure 7.2: Dehydration process of MIL-53(Al) by silica gel monitored by *in situ* ATR IR (spectra as recorded). At the beginning of the measurements the sample was in the NP-h state (black spectrum). After several hours the MIL-53(Al) framework got dehydrated (red spectrum). The arrows indicate the peaks that are characteristics for the (de)hydration.

completely disappeared, the dehydration was very probably close to complete in this experiment. By examining the IR spectra at higher frequencies (3000-4000 cm^{-1}), it was concluded that at the end of the experiment the water vapour concentration in the sample compartment was still significant. The situation was thus similar as in the XRD measurements where the structure was (partially) dehydrated by the silica gel.

From these experiments we can draw a few important conclusions concerning the conditions for obtaining a particular MIL-53(Al) state in activated MIL-53(Al). When MIL-53(Al) is exposed to humid (ambient) air for sufficiently long time (hours, at least) it will be in the NP-h state. The NP-d state can be reached following three methods. Heating in air to ~350 K will induce the NP-d state, however, when the dehydration is completed, the transition to the LP state sets in soon. The NP-d state can also be obtained by reducing the pressure to a couple

of mbar. In this case, care has to be taken that geometric factors do not delay or slow down the dehydration, like in the synchrotron experiments at the Diamond Light Source. The third method is desiccating the sample's atmosphere at ambient pressure. Care has to be taken that dehydration may only be partial, depending on the effectiveness of the dehydration process.

Knowing how to obtain the three distinct states of activated MIL-53(Al) at RT, the effect of the framework hydration on the EPR spectra of the V^{IV}=O probes was studied in detail and a spin-*Hamiltonian* analysis on NP-h, NP-d and LP V^{IV}=O EPR spectra was carried out.

7.2 Three distinct states monitored with EPR

Figure 7.3 shows powder EPR spectra of the LP, NP-d and NP-h state recorded in X-band at RT. Samples were activated by solvent extraction. The LP state was obtained after heating the sample to 450 K and cooling back to RT under vacuum. The NP-d state was obtained at RT, evacuating the sample tube by continuous pumping for two hours. The NP-h state was realised by immersing a sample tube containing powder in liquid N_2 for 12 h and warming up to RT, short time before the EPR measurements to assure that most of the pores are contracted to the NP-h state. In order to exclude influences of pressure for all three states 1 bar of dry N_2 was introduced in the sample tube during measurements. For further experimental details we refer to Appendix B, section B.1.

The ^{51}V HF structure is well-resolved and the EPR linewidths are narrow, which indicates that the V^{IV}=O ions are well-dispersed in the framework for these samples with low V concentration. As already noted in Chapter 6, the EPR spectra reflect the larger deviation from axial symmetry for V^{IV}=O in the NP states, as compared to the LP state, resulting in a larger number of spectral features in the former states. The differences in the V^{IV}=O X-band EPR spectra between the two NP states are more subtle, but still clearly visible. In particular, the linewidth for NP-h is considerably larger than for NP-d, whereas the total spectral range of the latter is slightly larger. The differences between these two states become clearer at higher microwave frequencies, as will be discussed in detail in section 7.4. Details of the samples used in this chapter are summarized in Table 7.1.

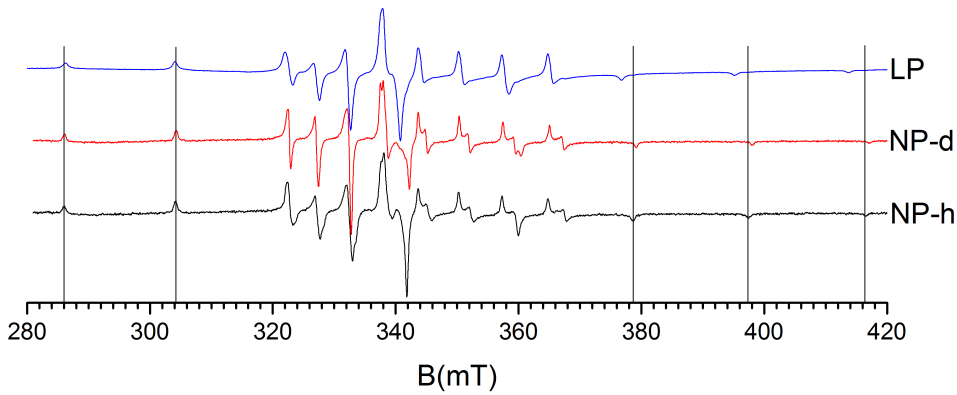

Figure 7.3: Experimental X-band powder EPR spectra of activated V-doped MIL-53(Al) in the LP (sample 1), NP-d (sample 6) and NP-h (sample 6) states recorded in N_2 at RT, ν_{MW} = 9.510 GHz. The vertical lines serve as a guide for the eye, to highlight changes in the position of the first two and last three lines in the z-component (smallest principal g and largest principal A) HF pattern of the vanadyl spectrum. The intensities of the spectra are normalized to the same height. The EPR spectra of the NP-h and LP states agree very well with the spectra presented in Figure 6.1, recorded in vacuum, but have a slightly larger linewidth.

Table 7.1: Composition and Langmuir surface area of the samples reported in this chapter. Columns 2 and 3 report the concentrations in the starting mixture for the synthesis, in the column 4 the [V]/([V]+[Al]) concentration ratios are shown. For further information about synthesis see Appendix B, section B.5 and PhD thesis of Hannes Depauw.[166]

Sample *no.*	V-salt (mmol)	Al-salt (mmol)	V (mol %)	Langmuir S. A.
1	0.0814	8.2173	1.47	1527 (m^2/g)
2	0.2797	5.3172	2.56	1542 (m^2/g)
3	0.1118	5.4867	1.48	1494 (m^2/g)
4	0.0559	5.3172	0.55	1520 (m^2/g)
5	0.0559	5.5422	0.57	1488 (m^2/g)
6	0.1118	5.4867	1.65	1536 (m^2/g)
7	0.2797	5.3172	4.71	1462 (m^2/g)

7.3 Oxidation state of vanadium in V-doped MIL-53

Even though a V^{III} dopant salt was used for the synthesis, V-doped MIL-53(Al) AS already exhibits a clear V^{IV}=O related EPR signal in samples with low vanadium concentration (0.5-5 % V). This implies that part of the V^{III} ions were oxidized to V^{IV} during the synthesis.[145] In order to obtain a more quantitative insight in the V-dopant oxidation state distribution in MIL-53(Al) and its evolution throughout the activation processes, XANES experiments were performed and correlated with V^{IV}=O EPR intensity measurements. In Figure 7.4 a and b, the XANES spectra are

shown for samples 5, 6 and 7 in the AS state, after activation by solvent extraction, and after calcination. For experimental details about the XANES experiments we refer to Appendix B. In K-edge XANES spectroscopy on vanadium oxides, the main edge energy position (μ_x=0.5) is linearly correlated to the oxidation state of vanadium in the oxide. A correlation curve of the oxidation state as a function of the main edge energy position was made using four reference compounds with increasing vanadium oxidation state: V_2O_3, VO_2, V_6O_{13} and V_2O_5. This curve was then employed to determine the average oxidation state of the V dopant in MIL-53(Al). The obtained average oxidation states are listed in Table 7.2. On the other hand, the pre-edge peak gives information on the local symmetry at the vanadium site: the peak is absent for sites with inversion symmetry. For AS samples the pre-edge peak has very low intensity (Figure 7.4 a), while it grows considerably upon activation by solvent extraction, and even further when samples are calcined. In Figure 7.4 d and e the incorporation sites for V^{III}-OH and V^{IV}=O in MIL-53(Al) are compared. The former site is (close to) inversion symmetric, whereas the latter clearly lacks inversion symmetry in the first coordination shell, since along the *c*-axis V^{IV} has one O and one OH ligand. Hence, the pre-edge peak intensity may here be considered as a measure for the dopant fraction present as V^{IV}=O. The integrated pre-edge peak intensities are also listed in Table 7.2.

Figure 7.4 c shows RT EPR spectra of samples 5, 6 and 7, again in AS and both activated states. For reliable EPR intensity determination, the activated samples were brought to the LP state by heating under vacuum to 450 K for 1h, and then cooled down under vacuum to RT. EPR spectra were recorded at RT. The EPR intensities were evaluated by double integration of the simulated spectra (V^{IV}=O in AS and LP MIL-53(Al)) in order to avoid interfering effects of background signals. The results are presented in Table 7.2. We observe that activation by solvent extraction already strongly increases the total intensity of the V^{IV} EPR spectrum. Activation mainly aims at removing unreacted linker molecules from the structure (clearing the pores) and not at oxidizing the dopant. In all three samples investigated, after calcination, which according to the XANES analysis brings (nearly) all vandium in oxidation state IV: the intensity of the signal grows by at least a factor of three. The limited number of samples studied here suggests that the fraction of dopant directly incorporated as V^{IV}=O during synthesis decreases with increasing dopant concentration. Although a larger concentration series should be studied to obtain conclusive results, the trend observed here is consistent with earlier results for MIL-47(V)[148] and related V-MOFs (COMOC-3,[100] NH_2-MIL-47[87]), where AS samples exhibit only a very small EPR signal, that grows about two orders of magnitude in intensity after calcination.

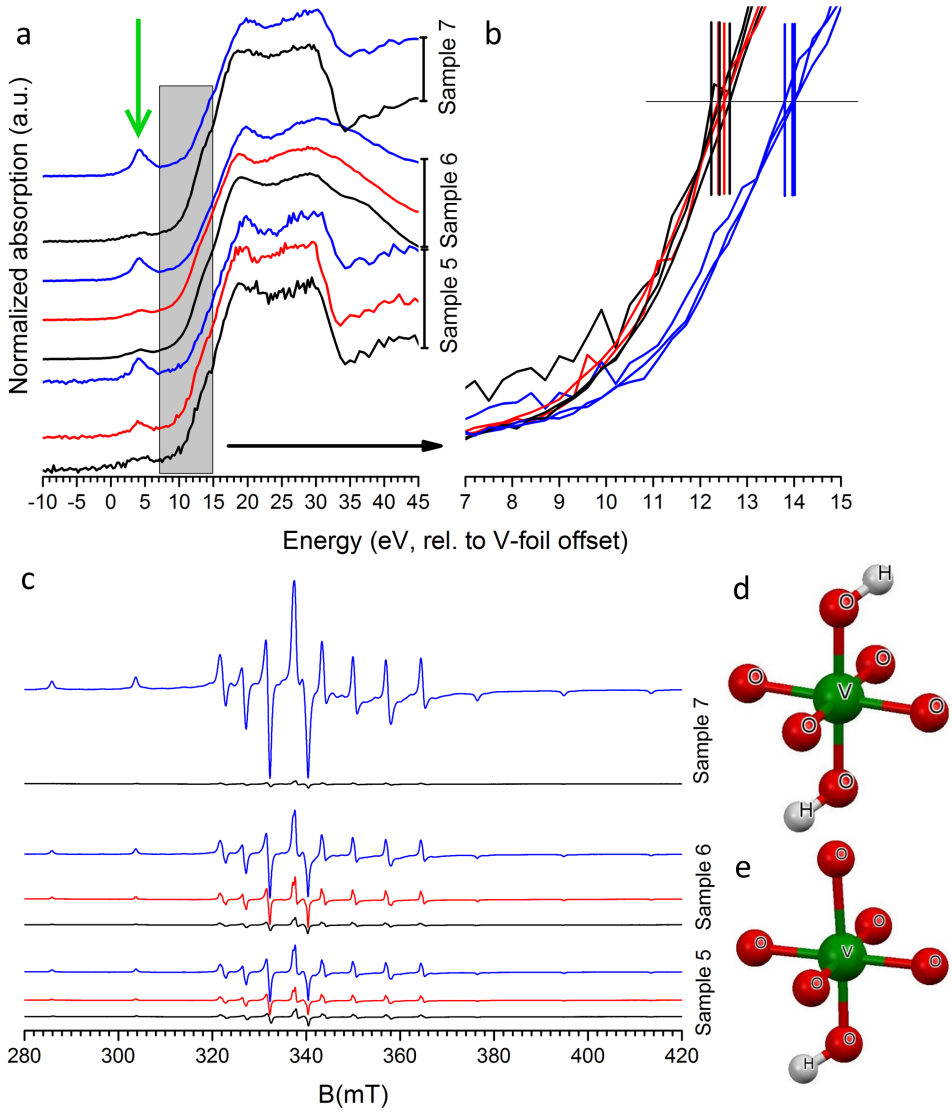

Figure 7.4: a: XANES spectra of V-doped MIL-53(Al) sample 5, 6 and 7 in AS (black), activated by the solvent extraction method (red) and activated by calcination (blue). The spectra are intensity normalized. The grey region is the zoomed region shown in Figure 7.4 b. The green arrow indicates the pre-edge peak. b: Horizontal and vertical lines represent the main edge energy position (μ_x=0.5) that is linearly correlated to the V oxidation state of each sample. c: RT X-band EPR spectra in vacuum of V-doped MIL-53(Al) sample 5, 6 and 7 in AS (black), activated by the solvent extraction method (red) and activated by calcination (blue). The spectra are normalized to the mass and simulated with the parameters from Table 7.3 (see section 7.4). The simulated spectrum is double integrated to obtain the EPR intensities listed in Table 7.2. d and e: Representation of inversion symmetry and lack of it in V-doped MIL-53(Al) (Mercury software used for visualisation[168]).

Table 7.2: Average oxidation states and pre-edge peak intensity of V-doped MIL-53(Al) determined from XANES measurements for sample 5, 6 and 7 in AS, activated by the solvent extraction method and activated by calcination compared to results of V^{IV} ions in the V-doped MIL-53(Al) framework obtained by double integration of EPR spectra. The error on the oxidation state is ± 0.4 and $\pm 10\%$ on the EPR intensities.

	Oxidation state	**EPR intensity**	**Pre-edge peak intensity**
Sample 5 (0.57 V%)			
AS	3.4	90	0
Extraction	3.5	146	0.5
Calcination	4.1	322	0.8
Sample 6 (1.65 V%)			
AS	3.4	77	0.35
Extraction	3.5	221	0.5
Calcination	4.2	536	0.61
Sample 7 (4.71 V%)			
AS	3.4	33	0.5
Calcination	4.2	1240	0.77

7.4 Spin-Hamiltonian analysis of V^{IV} in three states of MIL-53(Al)

LP state

As already discussed in Chapter 5, a detailed and accurate spin-*Hamiltonian* analysis of the EPR spectra for V^{IV} in V-doped MIL-53(Al) requires a multi-frequency EPR approach. RT EPR spectra of V-doped LP MIL-53(Al) were recorded in X, Q and W-band. W-band measurements were performed at the University of Antwerp. Figure 7.5 shows experimental spectra together with simulations. Using a single set of spin-*Hamiltonian* parameters (Table 7.3) all spectral features are convincingly reproduced by the simulations for all three bands. The resulting g and $A(^{51}V)$ tensors have non-coincident principal directions. They are very close to those presented for the AS state in Chapter 5, which could be expected considering the similarities in crystal structure between the AS and LP states of MIL-53(Al) (refer to Table 6.1 in Chapter 6). The main differences are found for the γ Euler angle and the linewidth (typically a 2-3 times smaller linewidth was found for the LP than for the AS state).

NP-d state

The RT EPR spectrum of V-doped MIL-53(Al) in the NP-d state was recorded in X, Q and J-band. The J-band measurements were kindly provided by Dr. P.

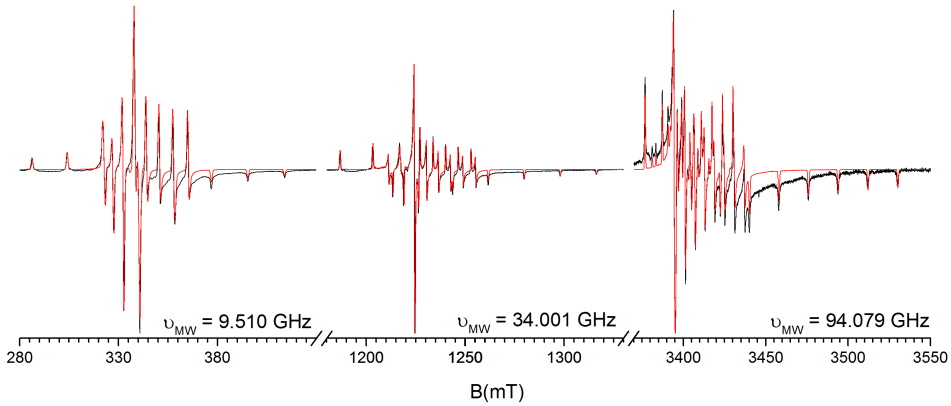

Figure 7.5: EPR spectra of activated V-doped MIL-53(Al) in the LP state at RT in X (sample 1), Q (sample 3) and W-band (sample 2) in 1 bar N_2. The experimental spectra are shown in black and the simulated spectra with parameters in Table 7.3 are in red. The spectra are normalized to the same maximum signal height.

Table 7.3: Simulation parameter set extracted from multi-frequency EPR spectra at RT of activated V-doped MIL-53(Al) in the LP and AS state: g, $A(^{51}V)$ tensor principal values and the Euler angles of the A tensor with respect to the g tensor (tilting angles). The errors are estimated as $\Delta g = \pm 0.0001$, $\Delta A = \pm 1.0$ MHz and $\Delta\alpha, \Delta\beta, \Delta\gamma = \pm 2^\circ$ for the LP state. Parameters for AS are reproduced from Chapter 5, with errors $\Delta g = \pm 0.0010$, $\Delta A = \pm 2.0$ MHz and $\Delta\alpha, \Delta\beta, \Delta\gamma = \pm 2^\circ$.

	x	y	z	α	β	γ
LP state						
g	1.9724	1.9675	1.9387	0°	11°	0°
A(MHz)	165.6	164.3	495.5			
AS state						
g	1.9725	1.9669	1.9391	0°	12°	8°
A(MHz)	163.0	165.0	492.0			

Gast from Leiden University. Figure 7.6 shows experimental spectra together with simulations. Like for LP, simulations using a single set of spin-*Hamiltonian* parameters (Table 7.4) reproduce the X and Q-band spectra perfectly. The J-band spectrum is also reproduced for the major part, but at low fields an additional spectral component with substructure occurs. Because of its high g value (≈ 1.978) it seems practically excluded that this feature is related to the V^{IV}=O complex observed in X and Q-band. Very probably it is due to a paramagnetic centre with low concentration and rather isotropic spin-*Hamiltonian*, whose spectrum remains buried under the strong V^{IV}=O spectrum at the lower microwave frequencies. In comparison with those for AS and LP, the g and A tensors for V^{IV}=O in NP-d MIL-53(Al) are considerably more rhombic. This is already revealed in the X-band

Table 7.4: Simulation parameter set extracted from multi-frequency EPR spectra at RT of activated V-doped MIL-53(Al) in the NP-d state: g, $A(^{51}V)$ tensor principal values and the Euler angles of the A tensor with respect to the g tensor (tilting angles). The errors are estimated as $\Delta g = \pm 0.0001$, $\Delta A = \pm 1.0$ MHz and $\Delta\alpha, \Delta\beta, \Delta\gamma = \pm 2°$.

	x	y	z	α	β	γ
NP-d state						
g	1.9719	1.9634	1.9292	0°	14°	8°
A(MHz)	165.9	173.0	505.7			

spectrum and is also expected when comparing crystallographic data for NP and LP MIL-53(Al).

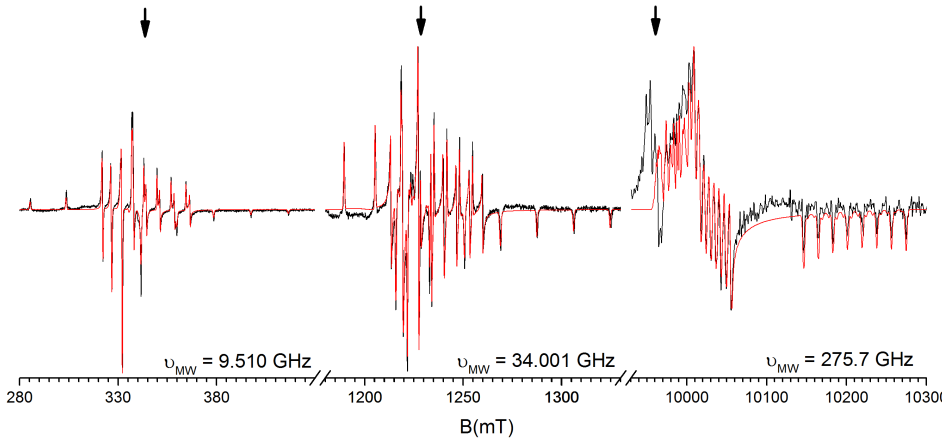

Figure 7.6: EPR spectra of activated V-doped MIL-53(Al) in the NP-d state in X, Q and J-band in vacuum. X and Q-band spectra were recorded at RT while the J-band spectrum was recorded at 325 K. Experimental spectra are shown in black and simulated spectra with parameters from Table 7.4 in red. Spectra are normalized to the same maximum signal height. Sample 4 was used for all frequencies. Arrows indicate the position where the signal with $g = 1.978$ would be in all three bands.

NP-h state

For the NP-h state it appeared impossible to simulate spectra simultaneously matching the experiments in X, Q, W and J-band with only one set of spin-*Hamiltonian* parameters. In particular in the Q-band spectrum the best fit simulations failed to reproduce three peaks, marked with red arrows in Figure 7.7. In the W and J-band spectra, the g_x - g_y region was not sufficiently resolved to allow conclusive fitting. In J-band again an extra spectral component occurred around 9950 mT ($g \approx 1.978$), further complicating the analysis of the V^{IV}=O spectrum. All these characteristics indicate that at least two (slightly) different

V^{IV}=O centres contribute to the EPR spectrum for NP-h MIL-53(Al).

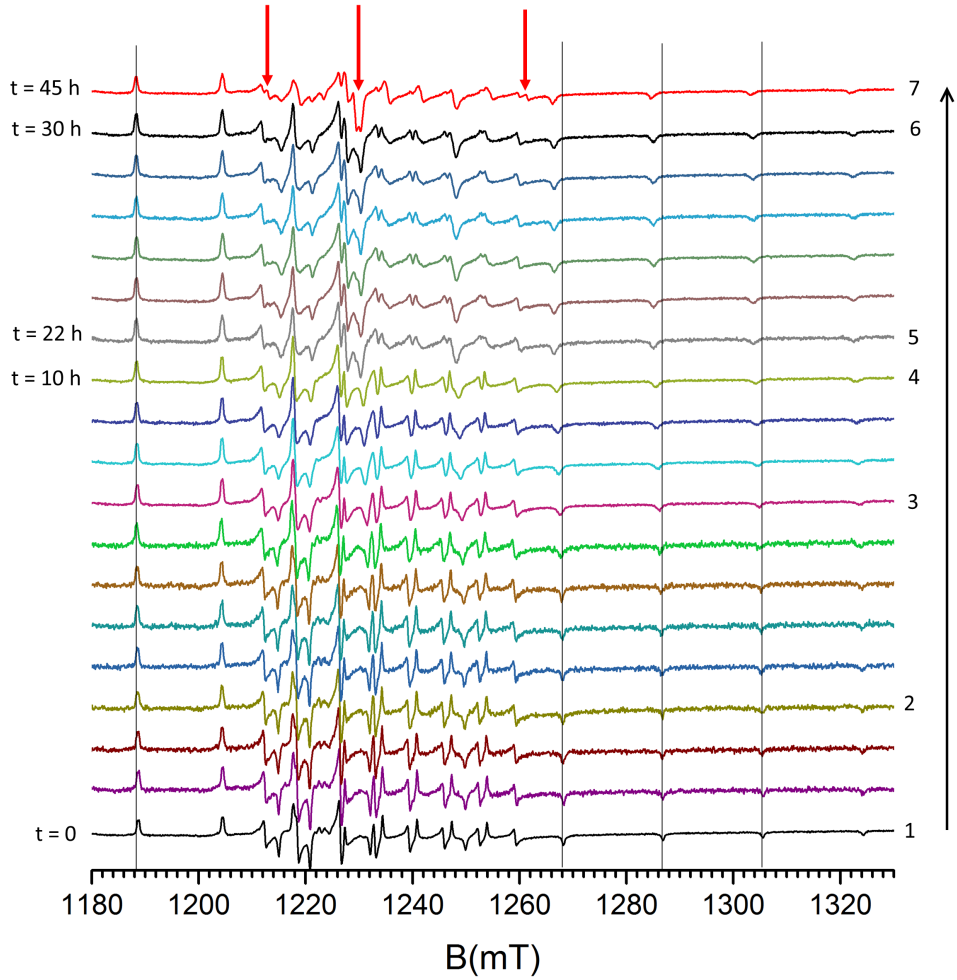

Figure 7.7: The hydration process of V-doped MIL-53(Al) was monitored with *in situ* Q-band EPR at RT (sample 4). At t = 0 the sample was in the NP-d (spectrum 1) state and still sealed with Parafilm. After this measurement the seal was broken and the sample started to hydrate. The spectrum recorded after 45 h (spectrum 7) is considered to correspond to the NP-h state. The red arrows indicate three peaks in the NP-h spectrum that were not reproduced by simulations with only one component. The black arrow indicates start and end EPR spectrum.

For the AS state at higher microwave frequencies (W-band) it became obvious that a second V^{IV}=O component (second set of spin-*Hamiltonian* parameters) was needed for a complete reproduction of the spectra (Chapter 5). This approach was also tested here for the NP-h state. As XRD revealed a gradual change from NP-d to NP-h when exposing a sample dried in vacuum conditions to ambient (humid)

Table 7.5: Simulation parameters extracted from EPR spectra 1-6 presented in Figure 7.7. g, $A(^{51}V)$ tensor principal values and the Euler angles of the A tensor with respect to the g tensor (tilting angles) are given. The errors are estimated as $\Delta g = \pm 0.0001$, $\Delta A = \pm 1.0$ MHz and $\Delta\alpha, \Delta\beta, \Delta\gamma = \pm 2^\circ$.

Spectrum	g_x	g_y	g_z	A_x	A_y	A_z	α	β	γ
1	1.9719	1.9634	1.9292	165.9	173.0	505.7	0	13.7	8.0
2	1.9721	1.9635	1.9292	166.6	174.0	506.7	0	13.5	8.0
3	1.9722	1.9634	1.9301	166.2	174.3	506.1	0	13.2	8.0
4	1.9724	1.9632	1.9312	165.5	174.7	506.0	0	12.7	8.0
5	1.9720	1.9623	1.9316	165.7	174.8	507.4	0	12.0	8.0
6	1.9719	1.9622	1.9317	165.6	174.8	507.1	0	12.1	8.0

air, we followed the hydration of NP-d *in situ* with Q-band EPR (measurements monitoring spectra as a function of exposure time to air) (Figure 7.7).

The sample was originally in the NP-d state in a sealed sample tube (spectrum 1). After recording spectrum 1 the seal was broken and EPR spectra were recorded over a period of 45 h, during which water from the air started occupying the pores (gradually) leading to the NP-h state (spectrum 7). A gradual change of the EPR spectrum occurred in the first hours of air exposure. These spectra could be convincingly reproduced by single V^{IV}=O centre simulations with gradually changing g and A tensors (Table 7.5). The EPR spectrum recorded after 30 h exposure to air (spectrum 6) was taken as a first component of the finally obtained NP-h spectrum, since the latter still clearly exhibited one dominant component with only a small contribution of a second component. A second component was then found by subtracting the first component from the finally obtained NP-h EPR spectrum and initial guesses for its spin-*Hamiltonian* parameters were obtained by fitting the Q-band difference spectrum. Finally, by fitting the EPR spectra for the NP-h state in all four microwave bands simultaneously, satisfactory agreement with experiment was obtained (Figure 7.8 and Figure 7.9). The resulting spin-*Hamiltonian* parameters for the two components are listed in Table 7.6. Since these parameter sets are only slightly different, it is perfectly understandable that the two components are not resolved in X-band. Even though the simulated spectra now reproduce (almost) all resolved spectral features in the four bands (except for the extra component in J-band), the calculated two component spectra are not as convincingly matching the experiment as the one component simulations for LP and NP-d. The analysis presented here by no means excludes that more than two distinct V-dopant sites are present in the NP-h state of MIL-53(Al), or that a (quasi) continuous range of different environments for V^{IV}=O exists in this state. A summary of all experimental and simulated spectra in the four states is given in Figure 7.10.

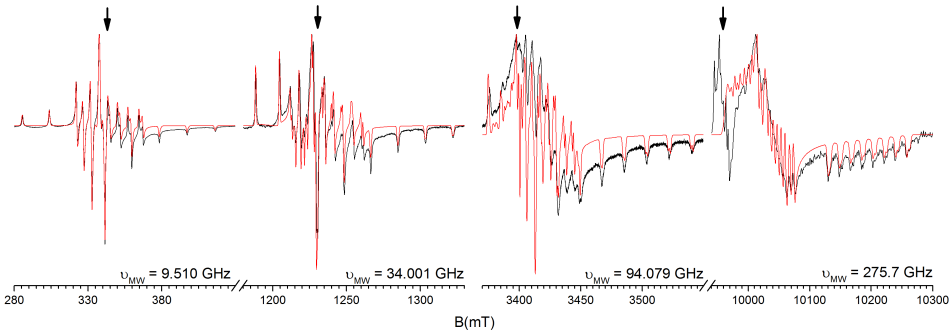

Figure 7.8: EPR spectra of activated V-doped MIL-53(Al) in the NP-h state at RT in X (sample 1), Q (sample 1), W (sample 2) in air and J-band (sample 4) in N_2 atmosphere. Experimental spectra are shown in black and simulated spectra with parameters from Table 7.6 in red. Spectra are normalized to the same maximum signal height. The arrows indicate the positions where the signal with $g = 1.978$ would occur in all four bands.

Table 7.6: Simulation parameter set extracted from multi-frequency EPR spectra at RT of activated V-doped MIL-53(Al) in the NP-h state: g, $A(^{51}V)$ tensor principal values and the Euler angles of the A tensor with respect to the g tensor (tilting angles). The errors are estimated as $\Delta g = \pm 0.0010$, $\Delta A = \pm 1.0$ MHz and $\Delta\alpha, \Delta\beta, \Delta\gamma = \pm 2°$.

	x	y	z	α	β	γ
NP-h state						
Component 1						
g	1.9720	1.9620	1.9320	0°	14°	8°
A(MHz)	164.9	174.2	506.4			
Component 2						
g	1.9710	1.9590	1.9320	0°	14°	8°
A(MHz)	162.5	170.9	504.1			

The fact that the V^{IV}=O EPR spectrum follows the phase transition of the MIL-53(Al) MOF serves as a strong indication for substitutional incorporation of V at Al sites. A superhyperfine interaction observed in the EPR spectra for the LP and NP-d states and the ENDOR spectra recorded for the NP-h state serve as additional, explicit evidence.

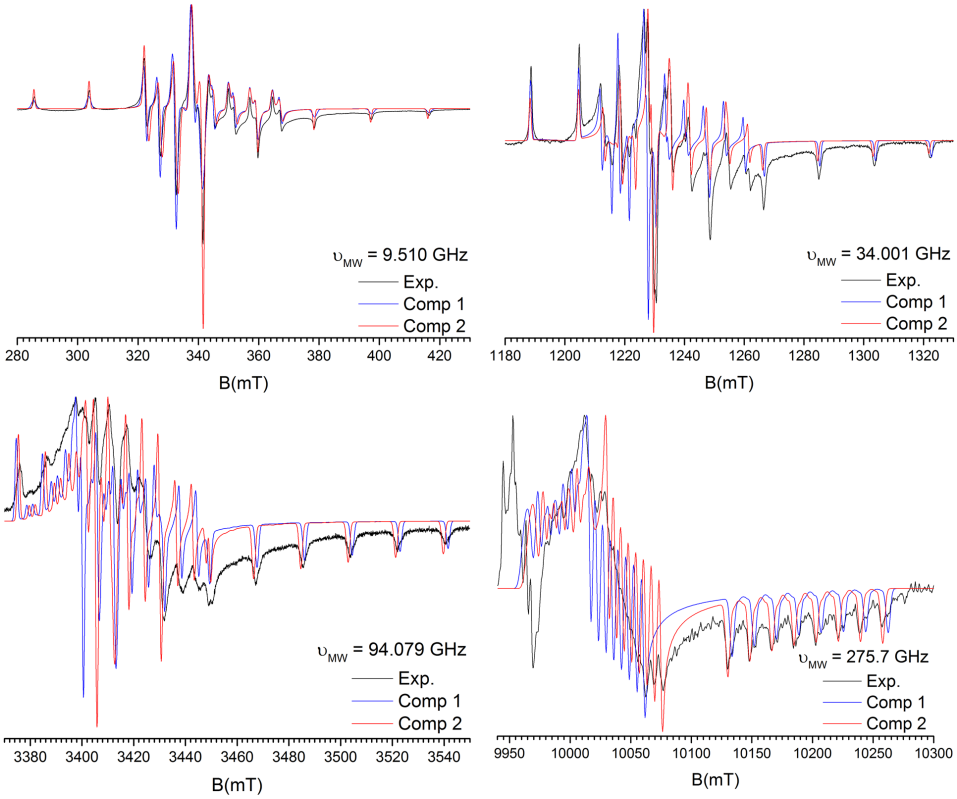

Figure 7.9: Multi-frequency (X, Q, W and J-band) powder EPR spectra of activated V-doped MIL-53(Al) in the NP-h state at RT in air, J-band in N_2 atmosphere. The experimental spectra are shown in black and the simulation of the two components separately with the parameters from Table 7.6 are shown in blue and red. Spectra are normalized to the same maximum signal height.

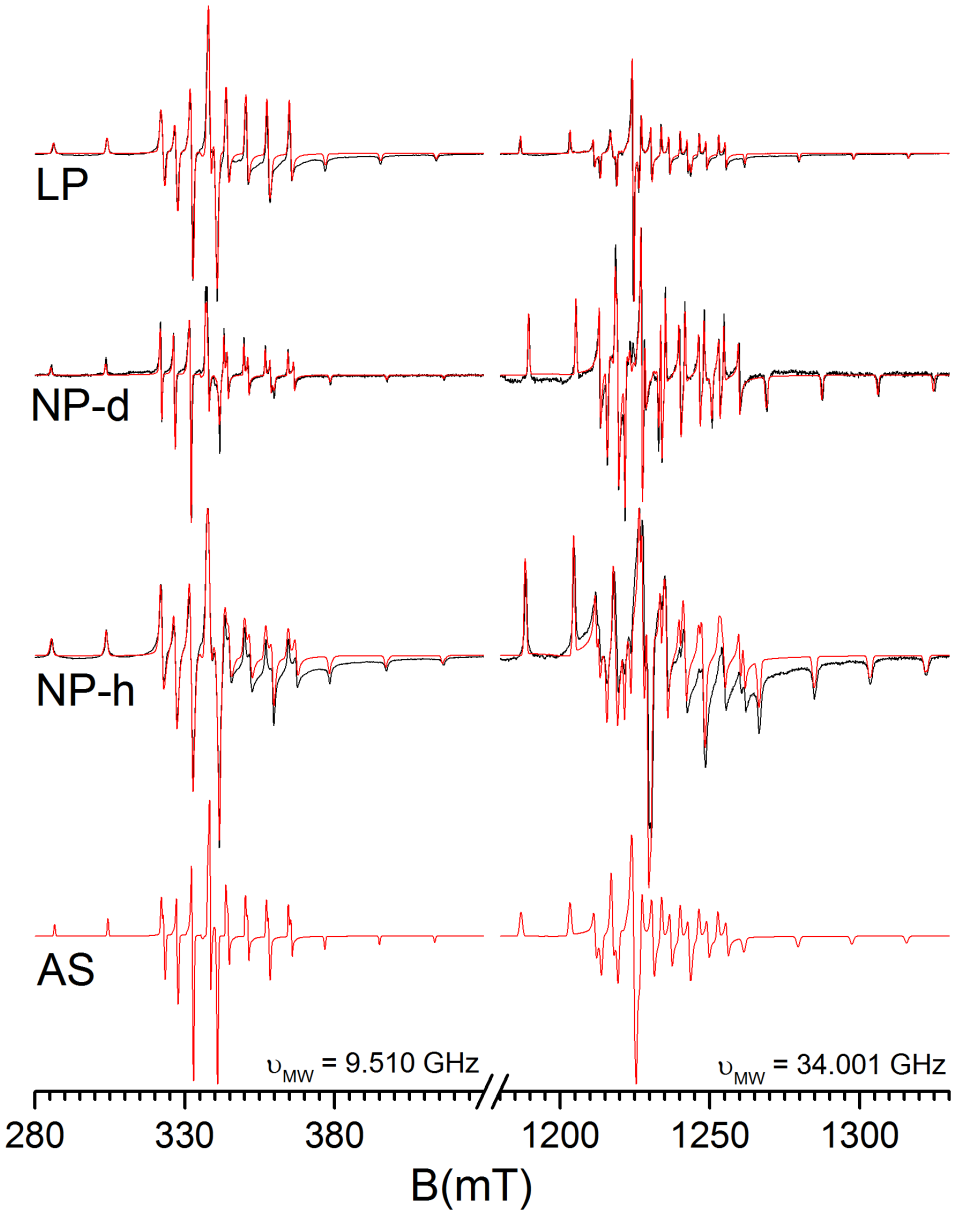
LP
NP-d
NP-h
AS
υMW = 9.510 GHz
υMW = 34.001 GHz
280
330
380
1200
1250
1300
B(mT)

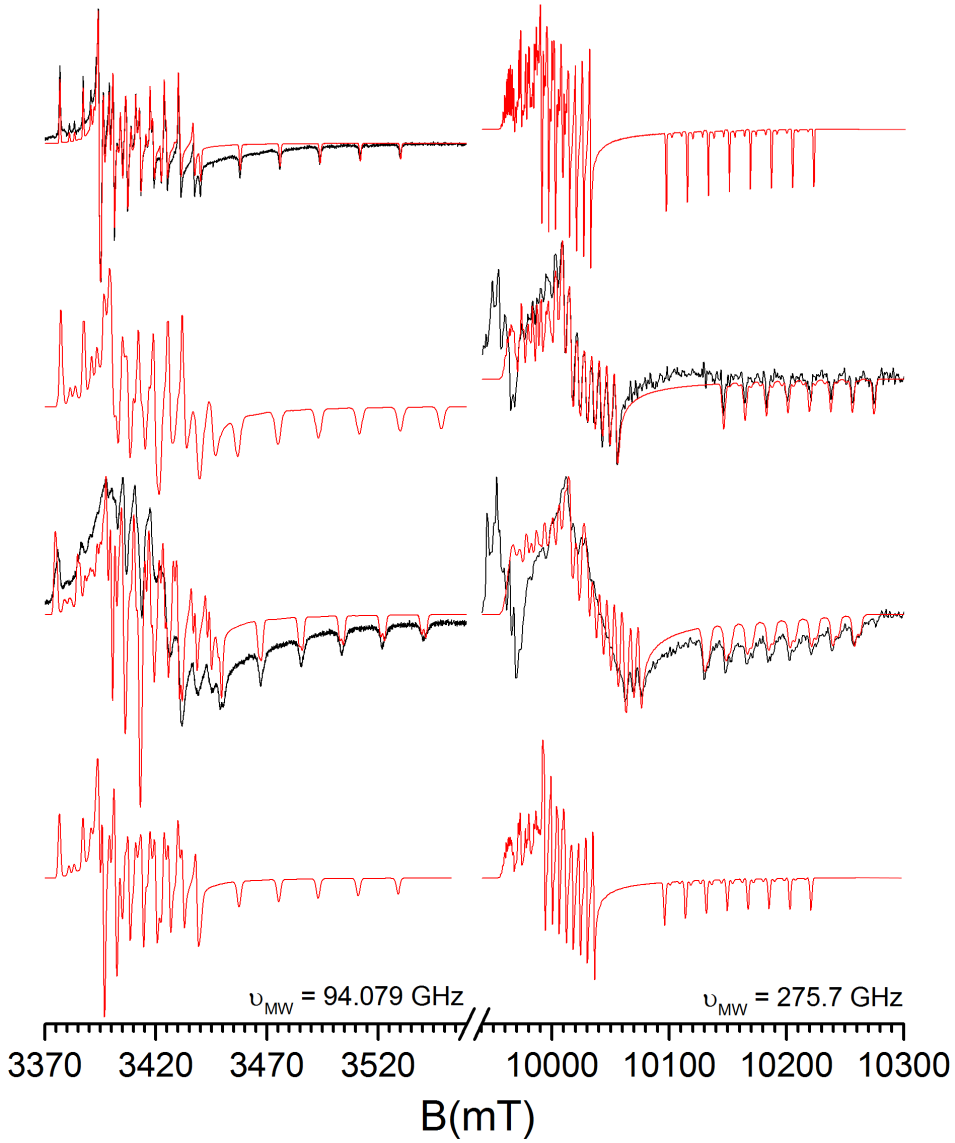

Figure 7.10: Powder EPR spectra of V-doped MIL-53(Al) in the LP, NP-d, NP-h and AS state. The experimental and simulated spectra are shown in black and red, respectively. The simulations were done with the parameters from Table 7.3 for the LP state, Table 7.4 for the NP-d and Table 7.6 for the NP-h state. The parameters for the AS state were taken from Chapter 5 for comparison. The spectra are normalized to the same maximum signal height. The EPR spectra of activated V-doped MIL-53(Al) in the LP state were recorded at RT in N_2 atmosphere. The EPR spectra of activated V-doped MIL-53(Al) in the NP-d state were recorded in vacuum. X and Q-band spectra were recorded at RT while the J-band spectrum is recorded at 325 K. EPR spectra of activated V-doped MIL-53(Al) in the NP-h state were recorded at RT in air, the J-band spectrum in N_2 atmosphere.

Superhyperfine interaction

When recording X and Q-band EPR spectra of V^{IV}=O in LP and NP-d MIL-53(Al) with low modulation field amplitudes, an additional splitting is observed in the first two peaks of the EPR spectra (Figure 7.11). These spectra were simulated with the spin-*Hamiltonian* parameters for the LP and NP-d states reported in Table 7.3 and Table 7.4 and including a HF interaction with the nearest hydroxyl proton to the V ion, using the same A tensor as for the AS state ($A_x = -3.1$ MHz, $A_y = -3.4$ MHz, $A_z = 8.6$ MHz, $\theta = 37°$, $\phi = 0°$, see Table 5.3). The experimental and simulated spectra are in good agreement, leading to the conclusion that this splitting can be attributed to the HF interaction with the proton in the OH group of one of the Al^{III} ions neighbouring the V^{IV}=O centre along the metal chains. Thus, the hydroxyl proton in the activated V-doped MIL-53(Al) matrix is in a similar position as in the AS state.

ENDOR of V-doped MIL-53(Al) in the NP-h state

Figure 7.12 shows Q-band ENDOR spectra of V^{IV}=O in the NP-h state of MIL-53(Al), recorded at 10K. ENDOR transitions are observed close to the Larmor frequencies of ^{27}Al and ^{1}H. In the ^{1}H region (Figure 7.12 a) a very rich structure is observed that is explored in detail by recording the field dependence of the ENDOR spectrum in the range indicated in the inset. The 2D spectrum shows similarities with already presented ENDOR results on V-doped MIL-53(Al) in Chapter 5. In the case of the NP-h state, interaction with the nearest hydroxyl proton is not visible from the ENDOR spectra. The spectrum in the ^{27}Al range was also recorded for several magnetic field positions, as shown in the Figure 7.12 b. These spectra can be explained assuming an axial HF tensor similar to the one reported in Chapter 5. Due to the low signal-to-noise ratio a more detailed analysis of the ENDOR spectra was not attempted.

These findings explicitly confirm that in all MIL-53(Al) states V^{IV}=O replaces Al^{III}-OH at regular node positions.

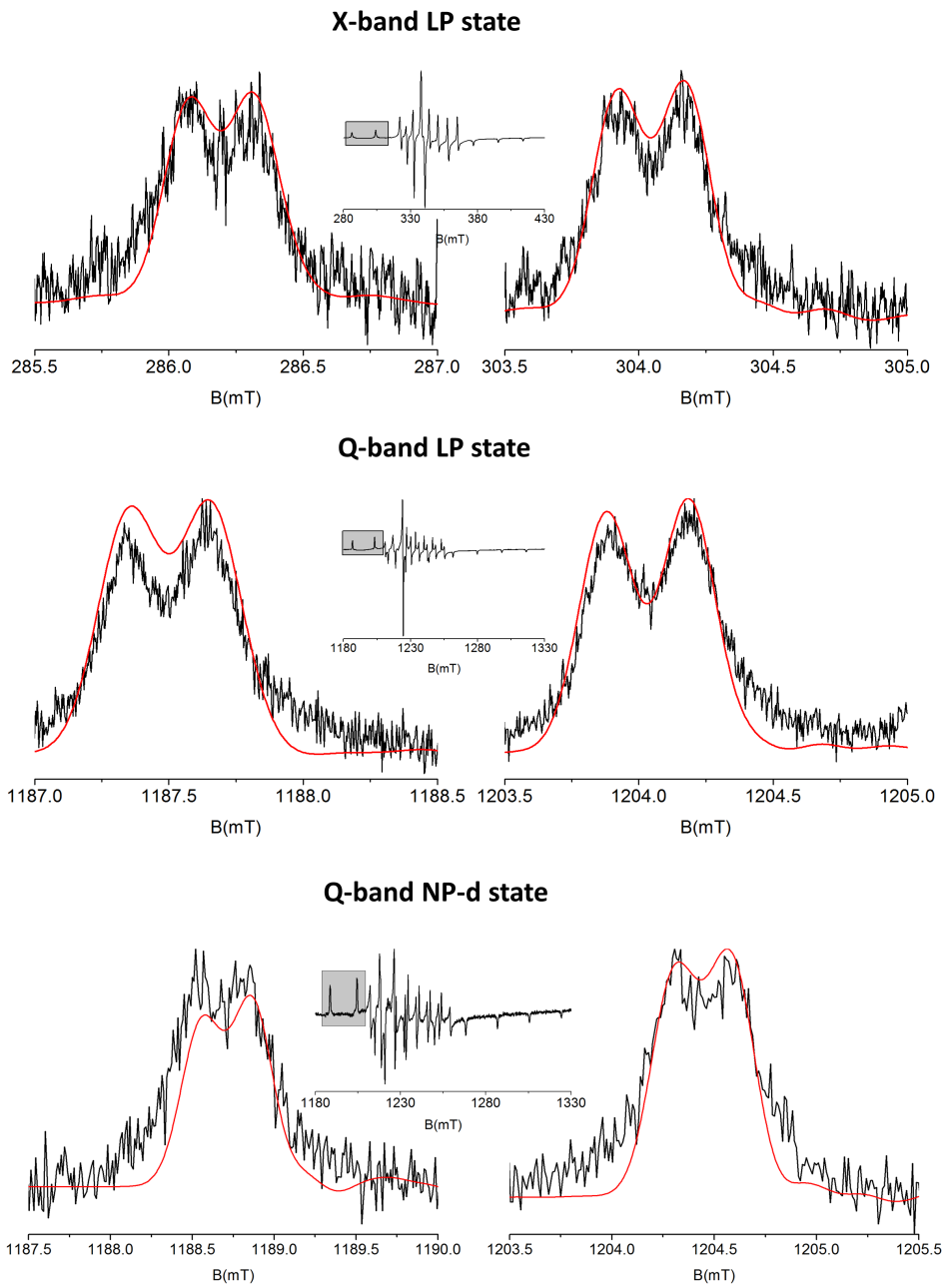

Figure 7.11: RT EPR spectra (zoomed regions, first and second peak of the EPR spectrum) of V-doped MIL-53(Al) sample 5 in the LP state in X (top) and Q-band (middle) and NP-d state in Q-band (bottom) in vacuum. Insets show the complete EPR spectrum in X and Q-band indicating the zoomed region. Experimental (black) and simulated (red) spectra are shown. Simulations were made with the parameters for the LP (Table 7.3) and NP-d state (Table 7.4) including the interaction with the nearest hydroxyl proton in the V-doped MIL-53(Al) framework from Chapter 5. The spectra were recorded with 0.05 mT modulation amplitude.

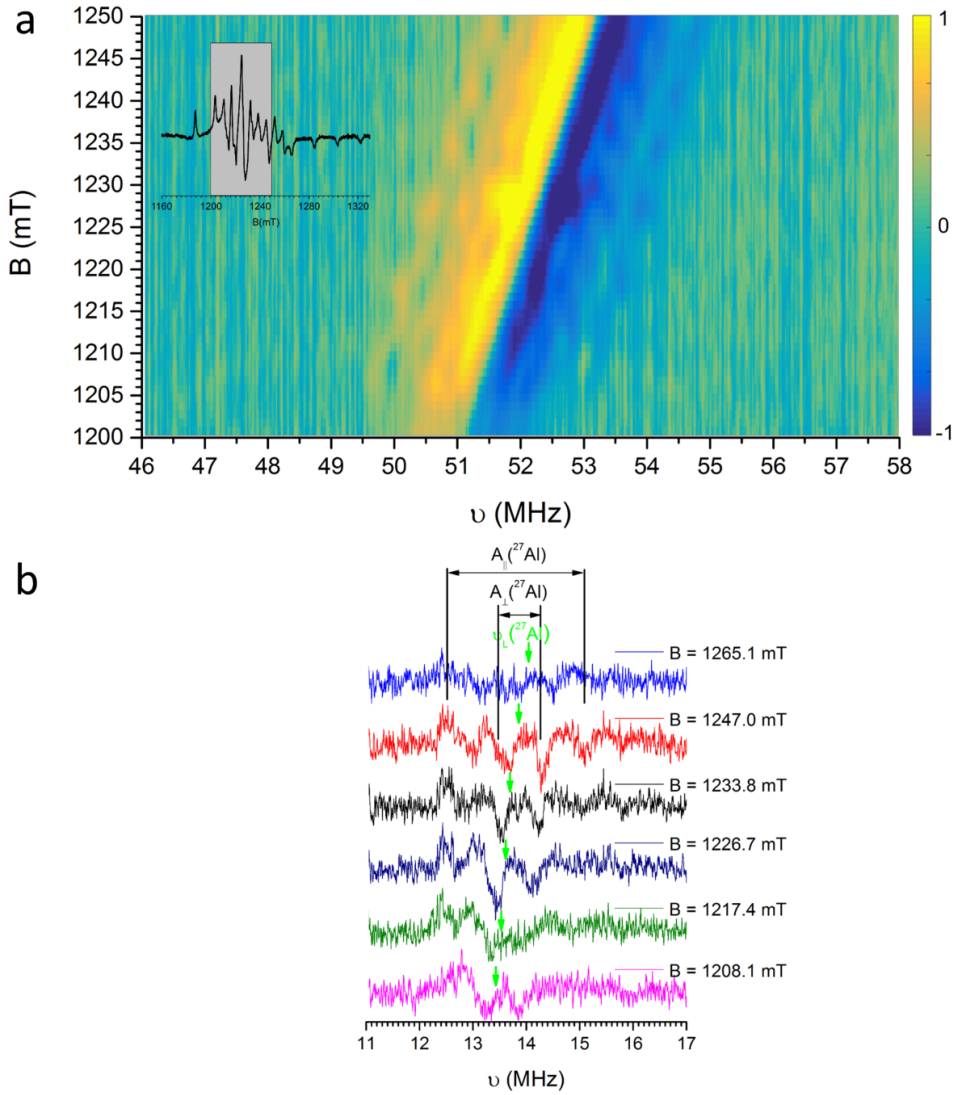

Figure 7.12: a: Experimental field dependence of ENDOR spectra (normalized signal heights in colour scale) near the ^{1}H Larmor frequency of activated V-doped MIL-53(Al) sample 1 at 10 K (ENDOR ν_{MW} = 34.007 GHz, EPR ν_{MW} = 34.000 GHz). The inset shows the EPR spectrum at 10K and the grey region where the field dependent ENDOR spectra were recorded. b: ENDOR spectra near the ^{27}Al Larmor frequency at 10 K. The green arrows indicate the ^{27}Al Larmor frequency for every field, $A_{\parallel}$ and $A_{\perp}$ are also shown.

7.5 Conclusions

A combined XANES and X-band EPR intensity analysis revealed that, when doping MIL-53(Al) with the VCl_3 salt, only a minority of the V-dopant incorporated in the metal nodes is in the +IV state after synthesis (AS state). The V^{IV} fraction increases considerably upon solvent extraction and is close to 1 after calcination.

XRD experiments, complemented with FTIR, showed that the NP-h phase, obtained after activation by storing the sample at RT and ambient atmospheric conditions, is relatively easily dehydrated by pumping, without production of the LP state. The latter state is obtained by heating to 450K, starting from either the NP-h or the NP-d state.

A consistent spin-*Hamiltonian* analysis was obtained for the multi-frequency V^{IV}=O EPR spectra in the three separate states. For the LP and NP-d states the EPR spectra were convincingly reproduced with only one set of spin-*Hamiltonian* parameters, indicating that all V-dopant sites in these empty-pore frameworks are equivalent. A single component analysis appeared impossible for the NP-h state. Apparently the presence of H_2O in the pores produces (at least two) different environments for the V^{IV}=O paramagnetic centres, which is reflected in slightly different EPR spectra. Interestingly, a similar situation was encountered for the AS state, where the pores are (randomly) occupied by solvent and/or unreacted linker molecules.

8

O_2 sensing with MOFs

Too much oxygen makes me dizzy! By following the EPR spectra of V-doped MIL-53(Al) as a function of oxygen pressure, the (exchange) interaction between V^{IV}=O and O_2 molecules was investigated. It was shown that the spectra of the distinct states of V-doped MIL-53(Al) are differently affected. This led to information about the accessibility of oxygen in the MOF framework and the linewidth of the V^{IV}=O EPR spectrum could be correlated with the oxygen pressure in the range from a few mbar up to 1 bar. The sensitivity of the EPR spectrum to oxygen was also tested for the COMOC-2(V) - DUT-5(Al) concentration series. The observed features may lead to interesting applications in paramagnetic gas sensing.

8.1 Sensitivity of the V-doped MIL-53(Al) spectra to O_2 molecules

As already noted in Chapter 6, when cooling V-doped MIL-53(Al) in air after heating, an interesting property of the EPR spectrum is observed. From approximately 375 K down to RT the EPR spectrum broadens as the temperature lowers. At the same time the peak positions do not change and the EPR spectrum can still be associated with the LP state. This effect is not related to changes in the lattice parameters since no evidence for this is found in the XRD patterns. When the air is removed by evacuating the sample tube, the narrow-line spectrum reappears. This property is explored further in this chapter.

In Figure 8.1 the RT EPR spectra are shown of a sample with the MIL-53(Al) lattice dominantly in the LP state, as a function of air pressure. Increasing the pressure clearly increases the linewidth of the component associated with the LP state. Meanwhile the NP-h component, present as a trace, hardly undergoes any

broadening. In Figure 8.1 it is also demonstrated that the EPR spectra for both the LP and NP-h state experience virtually no change by exposure to N_2. We checked that humid and dry air both lead to a strong broadening of the LP spectral component, whereas dry or humid N_2 does not. The line broadening should thus mainly be due to an exchange interaction between the V^{IV}=O and (paramagnetic) O_2 molecules.

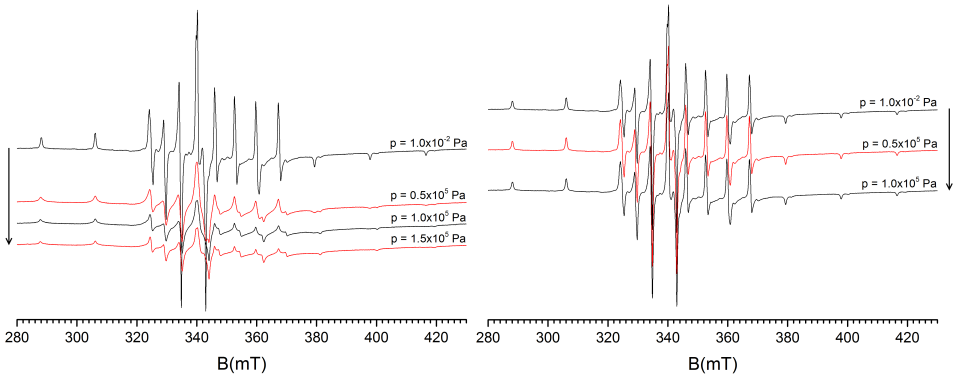

Figure 8.1: Left: RT EPR spectra of activated V-doped MIL-53(Al) after heating, dominantly in the LP state, as a function of air pressure. Right: RT EPR spectra of activated V-doped MIL-53(Al) in the LP state, as a function of N_2 pressure. The arrows indicate start and end EPR spectrum.

From these results it can be concluded that in air, O_2 can closely approach the V^{IV}=O ion when the MOF is in the LP state. This is in agreement with results published by Salles *et al.*[172] stating that the LP state is easily accessible for guest molecules.

EPR spectra of V-doped MIL-53(Al) in the LP state were also recorded as a function of (pure) oxygen pressure in order to study this phenomenon in more detail. Powder sample was heated to induce the LP state and cooled down to RT under vacuum. O_2 gas was allowed into the sample tube in steps of approximately 10 mbar and the results of X-band EPR measurements are presented in Figure 8.2.

Since the EPR spectrum of V-doped MIL-53(Al) extends over a wide field range (160 mT), we zoomed in on its central part. Two effects are clearly observed: the height of the EPR signal drops with increasing oxygen pressure, already from 5 mbar, and at the same time the spectrum broadens. With the spin-*Hamiltonian* parameters for V^{IV}=O in LP MIL-53 accurately known (Table 7.3), fittings (assuming an isotropic Lorentzian linewidth) have been used to accurately determine the linewidth and amplitude, as shown in Figure 8.3.

From these findings this system seems to possess promising features for gas sensing, i.e., a narrow EPR linewidth in the absence of oxygen and a large linear increase of the linewidth with oxygen pressure. Also the signal amplitude (Δa

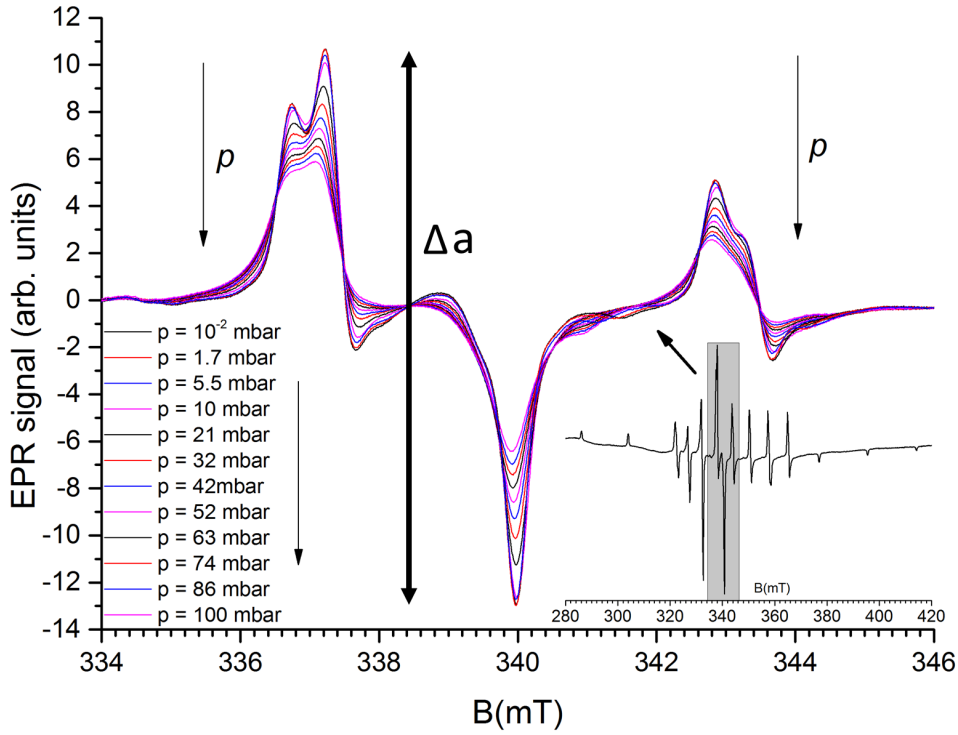

Figure 8.2: RT X-band EPR spectra (zoomed region) of activated V-doped MIL-53(Al) sample 4 in the LP state as a function of O_2 pressure at RT. The inset shows the complete EPR spectrum. The arrows indicate the decrease in peak amplitude with increasing O_2 pressure p.

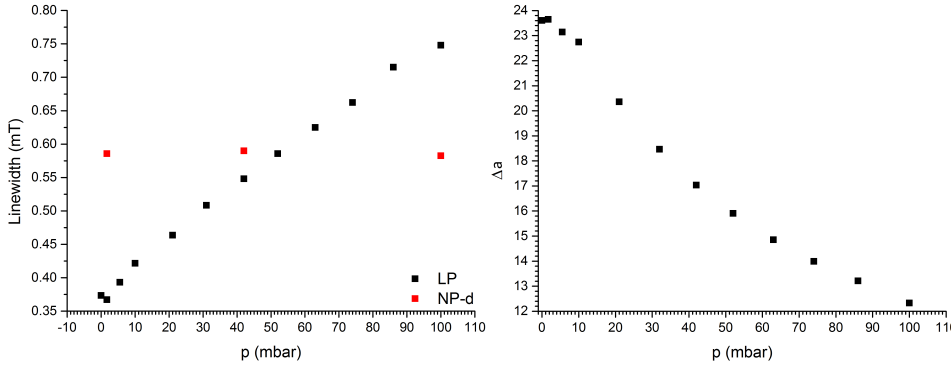

Figure 8.3: Left: Linewidth of the EPR spectra shown in Figures 8.2 and 8.4 as a function of O_2 pressure. The linewidths (full width at half maximum) are obtained from simulations with the parameters from Table 7.3 for the LP and Table 7.4 for the NP-d state (Chapter 7). Right: Amplitude Δa measured between two EPR extrema (337 mT and 340 mT) of the LP state as a function of O_2 pressure.

in Figure 8.2) is monotonously dependent on the O_2 pressure in a wide range. It seems both parameters can be used to sense oxygen pressure, but the linewidth evaluation is clearly to be preferred since it is independent of sample quantity and instrument parameters. The sensitivity threshold of this system to O_2 pressure, estimated at 5 mbar, is comparable with the EPR sensitivity of some commercially available charcoals for EPR oximetry. Paramagnetically concentrated metallic-organic crystals, like lithium phthalocyanine (LiPc) and lithium naphthalocyanine (LiNc), which exhibit an intense and very narrow single line EPR spectrum, exhibit a considerably higher sensitivity to oxygen pressure, reported down to 1.33 mbar. The latter systems have been shown to be very suitable for *in vivo* medical O_2 sensing.

Contrary to the LP state, the spectra of the NP-h state do not show a similar effect. Salles *et al.*[172] reported that the NP-h state presents a mixture of hydrophobic and hydrophilic regions as a result of the (nearly) close packing of phenyl rings in the structure, making it less accessible for guest molecules. This may mean that the O_2 molecules cannot enter the pores at all or cannot come close enough to the paramagnetic V^{IV}=O to produce a measurable broadening.

Also the NP-d state exhibits no or only subtle changes in the V^{IV}=O EPR spectrum for O_2 pressures up to 1 bar (Figure 8.4). Efforts were made in trying to estimate number of paramagnetic centres in EPR spectra recorded in vacuum and 1 bar of oxygen pressure by simulating EPR spectra (using parameters for NP-d state, Chapter 7, Table 7.4) and double integration of simulated spectra. It was concluded that the difference in total intensity (and linewidth) between the spectra is within the error on the measurements and calculations.

Although the results for the NP-h and NP-d states were not *a priori* expected, they seem to be in line with the observations of Mishra *et al.*[173] stating that O_2 can only enter NP MIL-53(Al) at pressures considerably higher than 1 bar. Even if O_2 cannot enter the framework in NP-h and NP-d MIL-53(Al), we might still expect an effect of the paramagnetic gas on the V^{IV}=O centres at the interfaces of the crystals. However, the results in Figure 8.4 seem to indicate that the contribution of V^{IV}=O centres in such a location to the total EPR spectrum is negligible. Further research will be necessary to understand all details of the interaction between O_2 and paramagnetic dopant ions in the MIL-53 framework.

In the past few decades, various EPR active materials have been considered for measuring O_2 pressure or concentration, in particular in biomedical samples like blood and tissue. Most of these exhibit a simple spectrum consisting of one or a few narrow lines. Examples of these are the water soluble nitroxide spin probes (three-lines spectra) and titryl radicals (TAM, one narrow line). Also particle-based (particulate) EPR probes, like coals, chars, carbon black, and the metallic-organic paramagnetic crystallites LiPc and LiNc have been studied. LiPc was

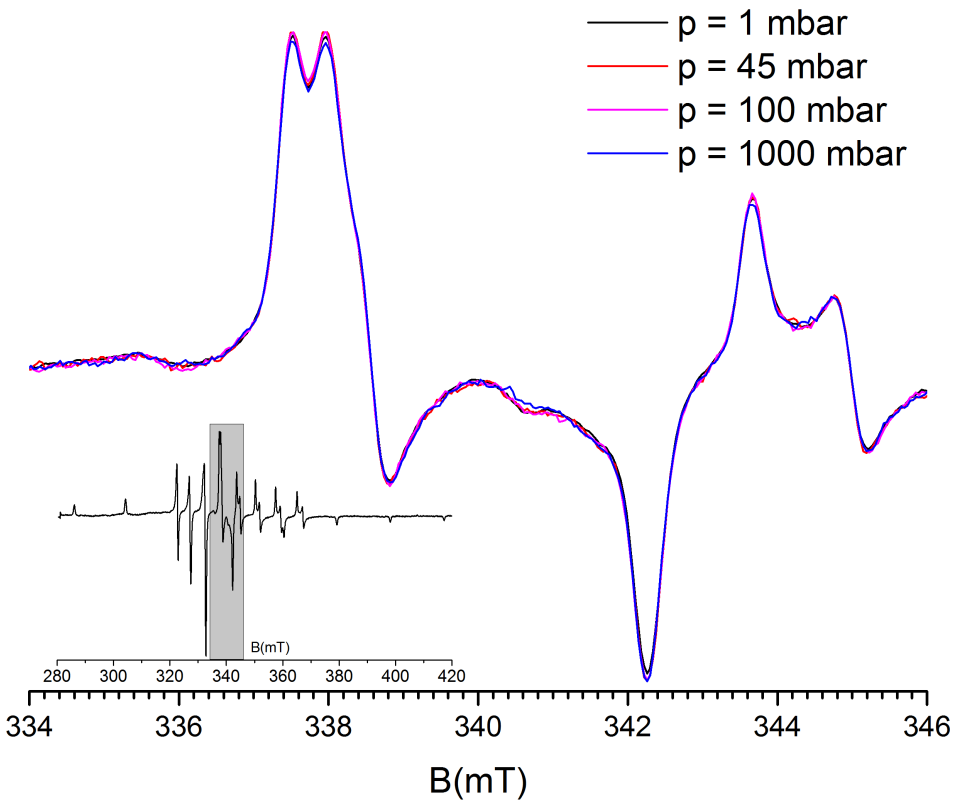

Figure 8.4: RT X-band EPR spectra (zoomed region) of activated V-doped MIL-53(Al) sample 4 in the NP-d state as a function of O_2 pressure at RT. The inset shows the complete EPR spectrum.

the first synthetic particulate spin probe widely used in both *in vitro* and *in vivo* biological applications.[174] The linear dependence of its EPR linewidth on O_2 pressure was shown to be independent of the surrounding medium and LiPc is physicochemically very stable. Their application was convincingly demonstrated in *in vivo* measurements of the oxygen pressure in the heart, brain and kidneys of rats. The experimental range tested was up to 211 mbar and the results were reported to be accurate down to 1.33 mbar.[175] LiPc however still has a few drawbacks, among which the saturation of its EPR spectrum at lower power, the nonlinear relation between linewidth and oxygen pressure in the low O_2 pressure ranges and lack of long-term stability in tissues. In comparison with LiPc, the lithium naphthalocyanine (LiNc) synthetic spin probe has higher spin density, a broader range of linear response to oxygen pressure and better power saturation properties. The synthesis of this material in pure form is, however, difficult and it showed limited stability and responsiveness in tissue.[174] Thus, although very good spin probes for EPR oximetry have been developed there is still room for

improvement.

Regarding the application of V-doped MIL-53(Al) as a pressure sensor, it should first be noted that the absence of broadening in the NP-d and NP-h states limits the scope of V-doped MIL-53(Al) to dry gas environments. In the presence of H_2O (gas or liquid phase) MIL-53(Al) will adopt the NP-h state which is not sensitive to O_2 exposure. V-doping in a rigid diamagnetic MIL-53-like structure, e.g. in DUT-4 or DUT-5, may present a system that does not have this problem. A second important disadvantage of the V-doped MOF systems is their complicated and very broad EPR spectrum. As a result, large amounts of sensor material are required for recording the spectrum with sufficient signal to noise ratio. Moreover, a complicated fitting procedure is required for correct evaluation of the EPR linewidth. In order to make paramagnetically doped MIL-53-like MOFs truly suitable for O_2 sensing, one should thus find a paramagnetic probe ion that can be incorporated in the framework - a metal ion or functional group on a linker - that exhibits a very simple EPR spectrum, preferably consisting of only one line. If *in vivo* applications are envisaged, the biocompatibility should also be considered.

8.2 Influence of O_2 on COMOC-2(V) and DUT-5(Al) structures

The MOFs COMOC-2(V)[73] and DUT-5(Al)[74] are isoreticular structures of MIL-47(V) and MIL-53(Al), respectively. As mentioned earlier, contrary to MIL-47(V) and MIL-53(Al) respectively, COMOC-2(V) does exhibit breathing whereas DUT-5(Al) is a rigid structure. A concentration series of V-doped DUT-5(Al) was synthesised in order to investigate the breathing behaviour of this mixed-metal MOF series, and also to investigate the O_2 sensitivity of the EPR spectrum of V in DUT-5(Al). Samples were synthesised by direct solvothermal synthesis and Table 8.1 presents the composition and Langmuir surface area of the samples reported in this section.

The RT X-band EPR spectra of samples *no.* 6-9, were recorded under vacuum conditions (p = 1 mbar) and are presented in Figure 8.5. The spectrum of the fully V-concentrated COMOC-2(V) (Sample *no.* 9) exhibits a broad EPR line at $g \approx 1.964$, lacking HF structure. This is consistent with the situation for other concentrated V-MOFs like MIL-47(V) where strong interactions occur between the V^{IV} ions in the (V=O)-(V=O) chains in the framework.

In the mixed Al-V samples, the intensity of the broad line decreases and a component with resolved HF structure gradually grows in as the V concentration decreases. The narrow-lines component is barely visible in the spectrum of sample *no.* 8, but quite clear in the spectra of samples *no.* 6 and 7. A detailed spin-*Hamiltonian* analysis of this component is expected to imply measurements in

Table 8.1: Composition and Langmuir surface area of mixed-metal DUT-5 and pure COMOC-2(V) samples reported in this chapter. The experimental molar ratio of vanadium and aluminium in all samples are determined with Inductively coupled plasma mass spectrometry (ICP) analysis. Prior to the analysis, the samples are destructed under acid conditions and diluted to fit the detection range of the equipment. Metal salts used for synthesis were $VOSO_4$ and $Al(NO_3)$. For further information about synthesis see Appendix B, section B.5 and PhD thesis of Hannes Depauw.[166]

Sample no.	V(x)	Al(1-x)	Langmuir S. A.
1	0.01	0.99	2147 (m^2/g)
2	0.03	0.97	2203 (m^2/g)
3	0.07	0.93	1965 (m^2/g)
4	0.09	0.91	1648 (m^2/g)
5	0.23	0.77	1339 (m^2/g)
6	0.46	0.54	1238 (m^2/g)
7	0.66	0.34	1264 (m^2/g)
8	0.81	0.19	1280 (m^2/g)
9 COMOC-2(V)	1	0	958 (m^2/g)

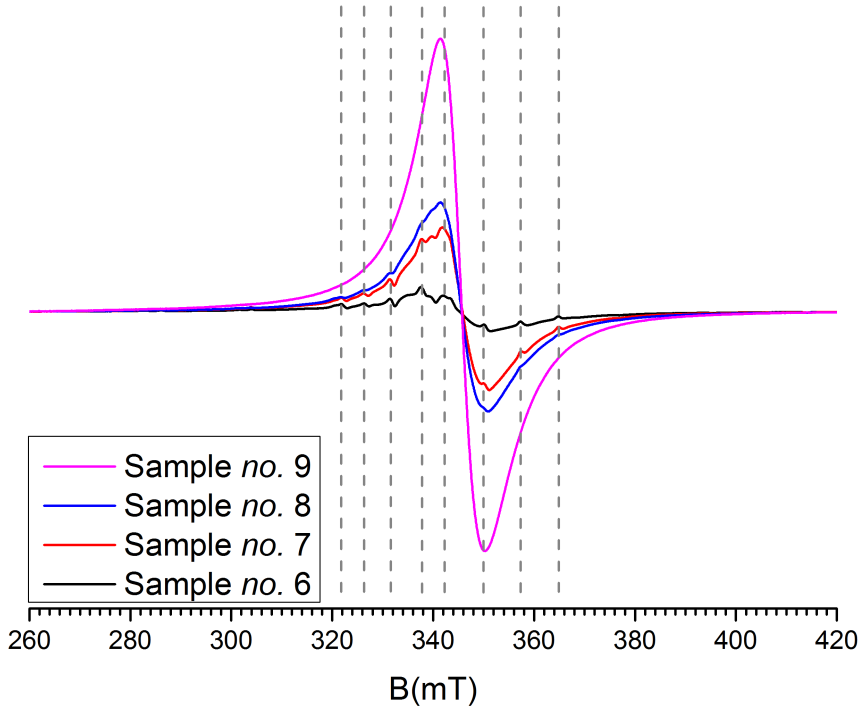

Figure 8.5: The RT powder X-band (ν_{MW} = 9.510 GHz) EPR spectra of the mixed-metal DUT-5 samples *no.* 6-8 and COMOC-2 sample *no.* 9 in vacuum (Table 8.1). The vertical lines are meant to guide the eye and indicate specific EPR features.

several microwave frequency bands, as already illustrated in Chapters 5 and 7, but due to time limitation this was not done here.

The identification then had to be based on comparison of the EPR spectra of samples *no.* 3-6 with spectra of V-doped MIL-53(Al) in the LP state, as shown in Figure 8.6. The spectra of the two types of V-doped Al-MOFs are very similar. The positions of the spectral lines (grey dashed lines) in the patterns of samples *no.* 3-6 practically coincide with the corresponding features in the spectrum of the V-doped MIL-53(Al) in the LP state. In the EPR spectrum of sample *no.* 5 the linewidth appears somewhat larger while in the EPR spectrum of sample *no.* 6 the broad line underneath the narrow-lines component is still pronounced.

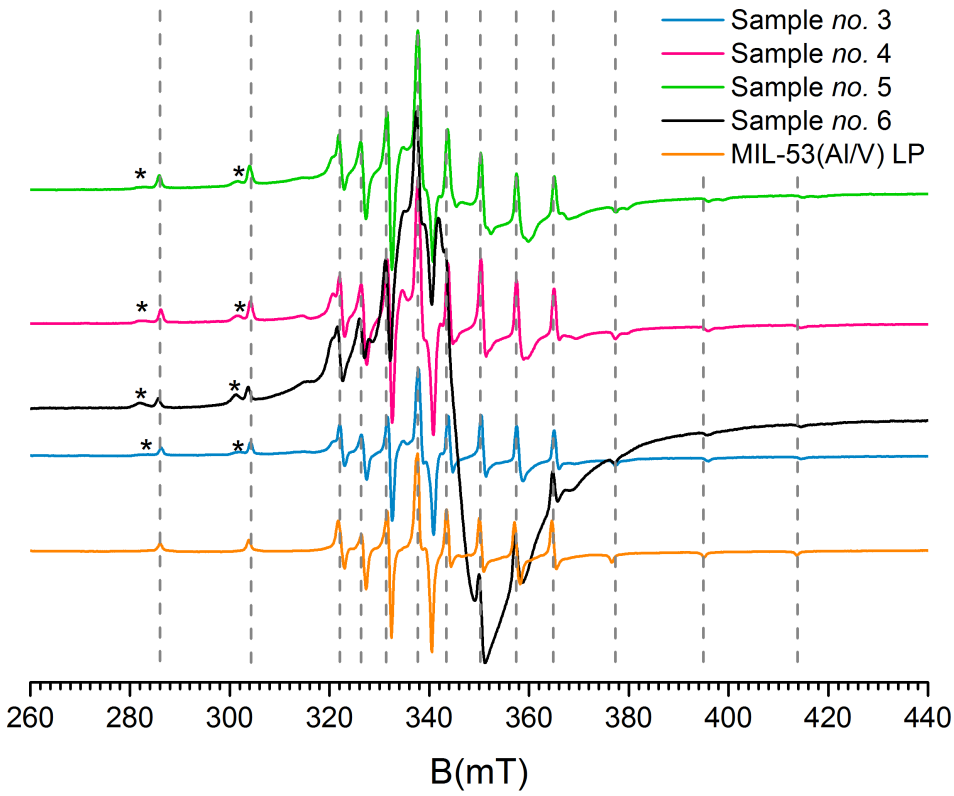

Figure 8.6: The RT powder X-band (ν_{MW} = 9.510 GHz) EPR spectra of the samples *no.* 3-6 and V-doped MIL-53(Al) in the LP state (1 V%), in vacuum. The asterisks indicate features of an extra V^{IV} related component. The vertical lines are meant to guide the eye and indicate features that correspond with the EPR spectrum of V-doped MIL-53(Al) in the LP state.

For all samples the specific 'LP-like' component strongly broadens when the sample is exposed to air (Figure 8.7). This feature is again attributed to the interaction between O_2, entering the framework in the open LP state, and V^{IV}

substituting for Al framework ions. In addition to the broad resonance line of V^{IV} in COMOC-2(V) and the narrow-line O_2 sensitive component, very probably related with V^{IV} diluted in DUT-5, the EPR spectrum of samples *no.* 3-6 contains at least one extra V^{IV} related spectrum (indicated with * in Figure 8.6), whose origin is at this moment still not completely clear. Efforts were made to try and identify this component starting from the idea that the dopant salt, $VOSO_4$, could produce a similar vanadyl signal. For that purpose an additional sample was made where $VOSO_4$ was diluted in DUT-5(Al) by mixing 1% of $VOSO_4$ and 99% of DUT-5(Al) and stirring for 10 min in the the reaction vessel, which was temperature controlled by an oil bath. In these conditions we do not expect that V^{IV} ions substitute Al in the metal nodes, but rather that they would be dispersed in the pores.

The EPR spectra of this sample were also taken in air and in vacuum and are shown in the last graph in Figure 8.7. The EPR spectrum of $VOSO_4$ dispersed in DUT-5(Al) has a resolved HF structure but a larger linewidth than the signal that we assign to V^{IV} incorporated in the metal sites of DUT-5(Al). The effect of O_2 on the EPR spectrum is visible, but qualitatively different from that for V^{IV} incorporated in the metal nodes of MIL-53(Al) and DUT-5(Al). A few peak positions are shifted due to the contact of the MOF with O_2 but the linewidth itself has hardly changed.

In Figure 8.8 the EPR spectrum of $VOSO_4$ dispersed in DUT-5(Al) in vacuum is compared with the EPR spectra of samples *no.* 1-3. In the EPR spectra of samples *no.* 1 and 2 the * component is more pronounced in comparison with the EPR spectra of the other samples. Sample *no.* 3 is taken as a representative of samples *no.* 3-9 where both the 'LP-like' and the * component are present. Furthermore, the EPR spectrum of sample *no.* 3 was scaled up to emphasise the * component.

In the low field range the positions of a few resonance lines of $VOSO_4$@DUT-5 correspond reasonably well with the positions of the * component in samples *no.* 1-3 even though this agreement is not perfect. However, on the high field side, the positions of the resonance peaks of $VOSO_4$@DUT-5 do not correspond with the EPR spectra of samples *no.* 1-3. This can be clearly seen from the insets in Figure 8.8.

The * component thus exhibits a similar line broadening with O_2 pressure as $VOSO_4$ dispersed in the pores of DUT-5(Al). In view of their significantly different EPR spectra, these V^{IV}=O centres are clearly not the same. CO_2 sorption experiments correlated with *in situ* XRD[176] showed that there are two types of LP states in mixed COMOC-2 - DUT-5 crystals. A first type is accessible to CO_2 and first transforms to a NP state upon CO_2 exposure at low pressure, and at higher pressure it transforms to a LP state different from the original state. A second fraction does not change state, which was attributed to blocking of the

pores. The observation of two types of V^{IV}=O centres may have a similar origin. Further thorough experiments and simulations are necessary to characterize the * component precisely.

Nonetheless, the EPR results strongly indicate that the synthesis of mixed (Al,V) BPDC MOFs was successful. Additionally, the COMOC-2 - DUT-5 series showed a similar interaction of V^{IV}=O with paramagnetic O_2 molecules as in the V-doped MIL-53(Al) framework in the LP state.

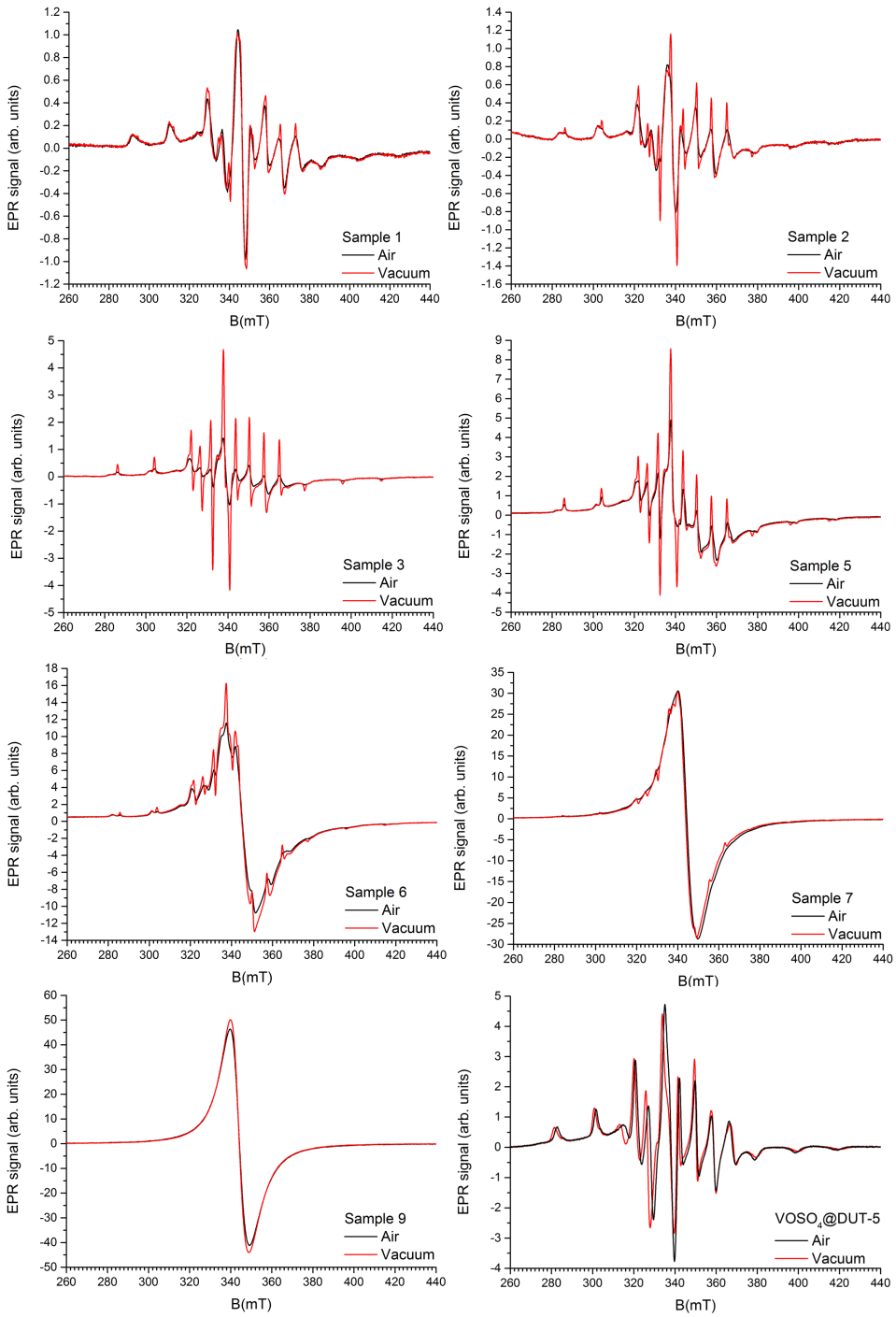

Figure 8.7: The RT X-band EPR spectra of samples *no.* 1-3, 5-7, sample *no.* 9 and $VOSO_4$ dispersed in DUT-5(Al) recorded in air (black) and under vacuum conditions (p = 1 mbar) (red).

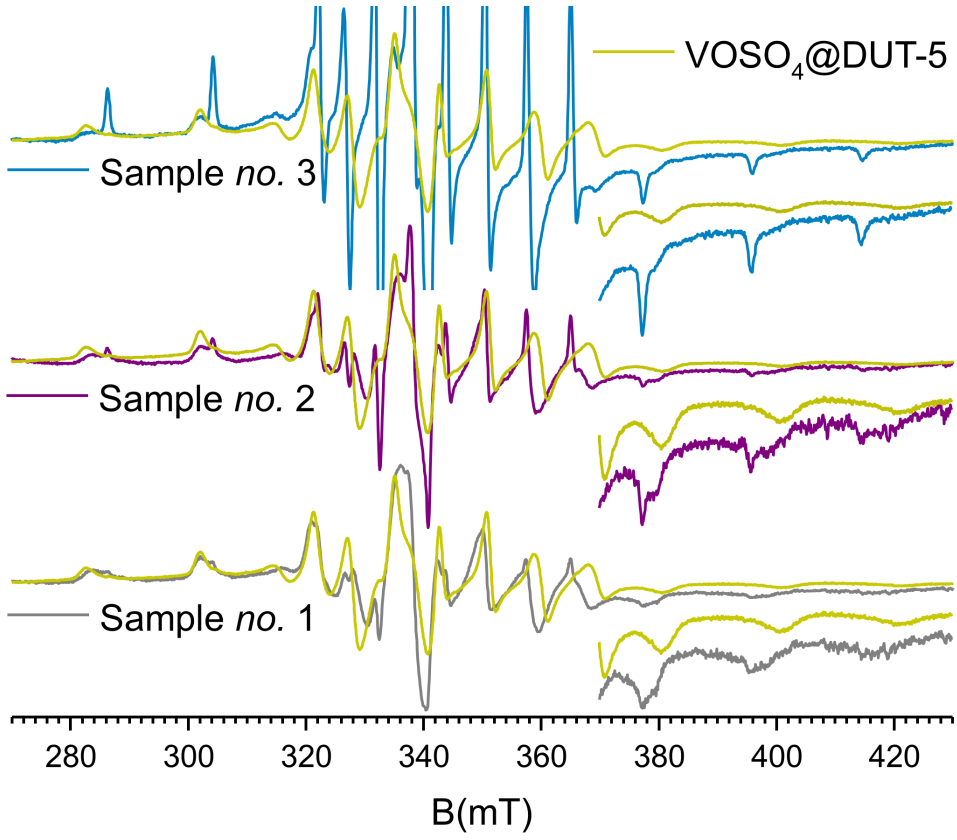

Figure 8.8: The RT powder X-band EPR spectra ($\nu_{MW} = 9.510$ GHz) of samples *no.* 1-3 and $VOSO_4$ dispersed in DUT-5(Al) (yellow), in vacuum.

8.3 Conclusions

The Lorentzian EPR linewidth of V^{IV} in the metal nodes of LP MIL-53(Al) strongly increases with O_2 pressure, suggesting that this system can be used for sensing oxygen with a sensitivity of $\approx$ 5 mbar. The EPR spectrum of V^{IV} in NP-h and NP-d MIL-53(Al) does not exhibit such broadening, most probably because in the probed pressure range O_2 cannot enter the framework in these states.

The EPR spectrum of V-doped DUT-5(Al) revealed the presence of two types of V^{IV} centres. The component with an EPR spectrum very similar to that of V-doped LP MIL-53(Al) and also strongly broadening when exposing the framework to O_2, is assigned to V^{IV} incorporated in the metal sites of DUT-5(Al). The origin of the second component is not completely clear. It exhibits a similar response to oxygen exposure as the EPR spectrum of $VOSO_4$ (the dopant salt) dispersed in the pores of DUT-5(Al), but these two EPR spectra themselves are markedly different.

9 Catalysis

Vanadium, do you want to participate? One of the motivations for the research presented in this thesis, besides the study of the breathing effect, was gaining deeper insight into the catalytic activity of this kind of MOFs. As already mentioned, MIL-47(V) has been reported as a highly selective catalyst in the oxidation of cyclohexene. One drawback of this material is its limited stability in aqueous environment. An *a priori* attractive solution for this problem is to incorporate catalytically active ions in the more stable MIL-53(Al) framework. It could be expected that such a mixed-metal MOF is a more efficient and selective catalyst. Mixed-metal MIL-53(Al^{III}/V^{IV}), however, showed an unexpectedly low catalytic activity. Possible implications for catalysis of the results reported in the previous chapters will be discussed here.

9.1 Oxidation of cyclohexene

The selective oxidation of cyclohexene is primary interesting as a benchmark reaction for testing the catalytic performance. However, in industrial applications the oxidation of cyclohexene is interesting for the production of adipic acid. Adipic acid is one of the most produced commodity chemicals worldwide. It is mainly used for the production of polyester and polyurethane resins, in the production of polyvinyl chloride (PVC) and as an additive in cosmetics, fertilizers, insecticides, paper, waxes and many more.[177] The oxidation of cyclohexene is shown in Figure 9.1a. The catalytic test reactions with V-doped MIL-53(Al) were performed by Hannes Depauw. In this study, the reaction was carried out with tert-butyl hydroperoxide (TBHP) (70 wt% TBHP in decane) as oxidant, 60 mL of chloroform (anhydrous) as solvent and 5 mL of cyclohexene. The internal standard for the gas chromatography analysis used was 1,2,4-trichlorobenzene

(6.2 mL). The molar ratio cyclohexene/oxidant was 1/2. All the catalytic tests were performed at a temperature of 323 K and with an Ar-containing balloon on top of the condenser. Blank tests were performed without catalyst and no cyclohexene conversion was observed.[5]

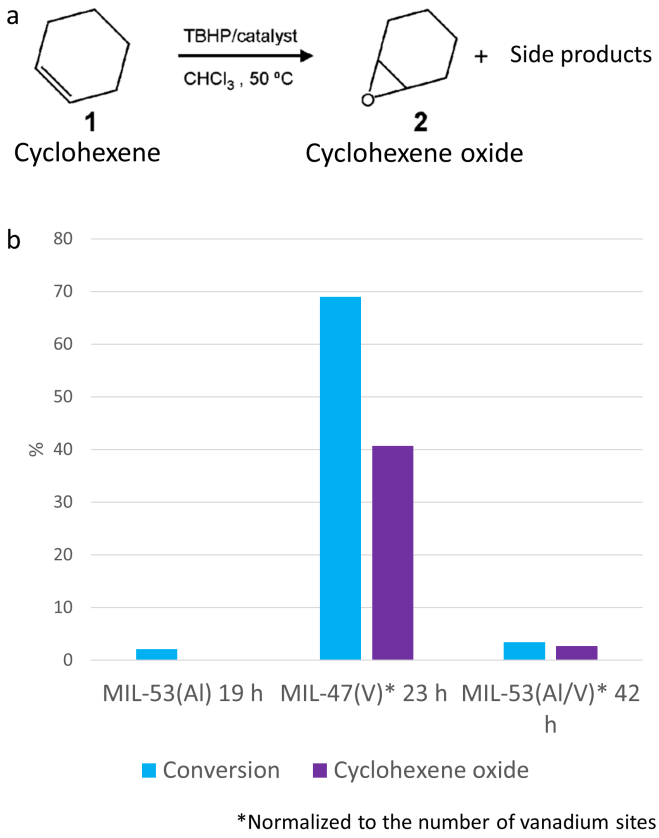

Figure 9.1: a: Oxidation of cyclohexene.[5] b: Oxidation of cyclohexene using MIL-53(Al), after 19 hours, using MIL-47(V), after 23 h and using V-doped MIL-53(Al) (10% vanadium loading), after 42 h. Conversion is normalized to the number of vanadium sites in the sample.

The conversion of MIL-47(V) was as expected, around 70% with 40% of cyclohexene oxide after 23 hours. The studied V-doped MIL-53(Al) framework with 10% vanadium is considerably less catalytically active with a really small conversion of around 3.4% even after a doubled reaction time, a result similar to that for blank MIL-53(Al). In the two tests, using either MIL-47(V) or V-doped MIL53(Al) as catalyst, the same amount of vanadium active sites were present implying that for the experiments with V-doped MIL-53(Al) about 10 times more catalyst was used. The activity is lower than expected, even if in the V-doped MIL-53(Al) catalyst only V-centres at metal sites on the outer surface of the crystals would

be accessible.

9.2 Discussion

If we consider the results reported in this thesis, a few conclusions can be drawn. In aqueous (and probably in any other liquid) environment the MOF is expected to be in the NP state (NP-h or another solvated state). Since V-doped MIL-53(Al) in the LP state is shown to be sensitive to oxygen molecules, O_2 molecules can, most probably, enter the LP state framework. A similar experiment was carried out with V-doped MIL-53(Al) in the NP-h state. The EPR spectra of V-doped MIL-53(Al) in the NP-h state in vacuum and in air do not differ much, leading to the conclusion that even O_2 molecules cannot enter the framework. Thus, in the liquid phase oxidation of cyclohexene most probably only vanadium at boundary metal sites of the MOF is accessible and only surface catalysis can be relevant. A solution for this could be the use of certain mixed DUT-5(Al)-COMOC-2(V) structures as catalysts, since these structures do not show breathing triggered by temperature or H_2O molecules. Further experiments are needed for a complete understanding of the behaviour of mixed-metal (Al,V)BPDC MOFs.

From the O_2 exposure EPR experiments on V-doped MIL-53(Al) in the NP-d and NP-h states, we concluded that at maximum a few percent of the V ions can be reached. In fact, the spectral changes were too small to quantify the fraction of accessible V centres, situated at border sites. This may provide a mechanistic explanation for the observed reduced activity in V-doped MIL-53(Al). The fundamental reason would then be the solution-induced inaccessible NP-state of the flexible MIL-53(Al) framework in contrast with the rigid open MIL-47 structure. It might even be that the fraction of boundary V ions is even lower than expected geometrically. A recent article on an 'egg yolk' structure in V-doped MIL-53(Cr), published by Hannes Depauw *et al.* within the framework of this project, reports a mixed-metal MOF with a core of MIL-53(Cr/V) and a shell of MIL-53(Cr).[58] If a similar dopant distribution would occur in MIL-53(Al/V), this would further lower the measured catalytic activity. Supporting this hypothesis more quantitatively presents a real challenge for future research.

Other factors could play a role as well. DFT calculations indicate that the V=O bond in MIL-47(V) is weaker than in MIL-53(Al). This might lead to easier bond breaking and an increased catalytical activity of the V site in MIL-47(V). Kozachuk *et al.* concluded from the *g* tensor analysis of MIL-47(V) that this complex exhibits characteristics closer to that of VO_6 distorted octahedra, than to V=O vanadyl complexes, which seems to be in agreement with the DFT results.[148] XANES experiments on MIL-47(V), on the contrary, indicate that the VO_6 complexes clearly lack inversion symmetry. This can be seen in Figure 9.2. The pre-edge

peak (indicated by the green arrow) which gives information on the vanadium site symmetry (see Chapter 7), has very low intensity for AS MIL-47(V), while it grows considerably upon activation by calcination. Further experiments will be needed to bring more definite conclusions.

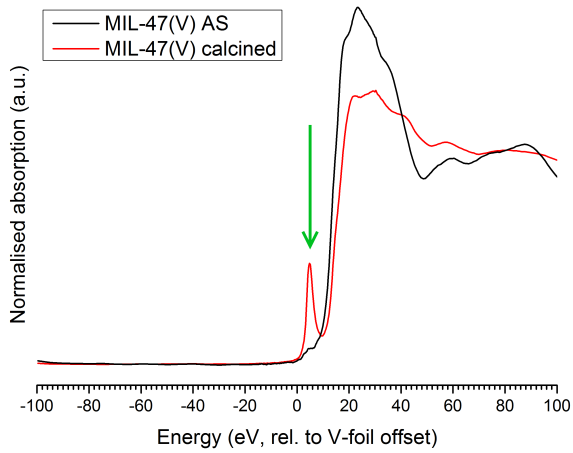

Figure 9.2: XANES spectra of MIL-47(V) in AS state (black) and MIL-47(V) activated by calcination (red). The spectra are intensity normalized.

10

Conclusions

Metal-organic frameworks (MOFs) represent a novel class of materials with a broad range of (possible) applications. In this thesis a thorough characterisation of a selection of MOFs was done using several experimental methods, EPR and XRD being the most important ones. Within this project a successful collaboration has been established between the EMR and COMOC research groups of Ghent University with the main aim of gaining further insight into the breathing mechanism and the catalytic activity of MOFs. This fruitful research resulted in six publications in prestigious peer-reviewed international journals.

The focus of our research was mainly on V-doped MIL-53(Al) but the obtained knowledge appeared to be advantageous when studying a DUT-5(Al)-COMOC-2(V) concentration series and likely so for other MOFs in future research. EPR and ENDOR spectroscopy thus proved to be useful techniques in MOF studies in general. These techniques gave direct insight how vanadium dopant ions are incorporated and dispersed in the framework. A detailed spin-*Hamiltonian* analysis of the EPR spectra in five frequency bands revealed accurate g and A tensors including information about relative tilting angles between them. Since the absolute orientation of the g and A tensors with respect to the molecular frame cannot be assessed from powder EPR spectra, support from density functional theory calculations will be necessary for extracting further details about the V-complex structures.

Furthermore, the EPR spectra appear excellent probes to discriminate between or monitor V^{IV}=O centres in the different states of V-doped MIL-53(Al). Due to the low V loading in the used samples this would point to the fact that EPR and ENDOR can follow both the local and global environment of the MOF where a local V^{IV}=O paramagnetic probe also provides information about the global MOF structure. The use of other experimental techniques provides results complementary to EPR and ENDOR. The advantages of a combined *in situ* XRD and EPR

study were convincingly demonstrated. It was shown that the transformation from the NP-h to the LP state happens via the NP-d state. The transition from the NP-h to the NP-d state goes gradually resulting in a continuous change in lattice parameters. This continuous change seems not compatible with abrupt changes in the crystal symmetry/space group. The transition from the NP-h to the NP-d state of V-doped MIL-53(Al) was investigated in different ambient conditions: during heating, changing air pressure and air humidity at RT. The transition was shown to be reversible.

XANES and EPR intensity measurements have provided consistent information on the oxidation state of the V dopant in MIL-53(Al). Even though $V^{III}Cl_3$ is used as a dopant salt, a small fraction of the dopant is already present in the V^{IV} state immediately after synthesis. Activation by both solvent extraction and calcination increases the V^{IV} fraction, but calcination makes the III→IV valence state transition (practically) complete. Here, EPR provided more accurate results at much lower cost than XANES even though EPR could only detect one of the valence states (V^{IV}).

The spin-*Hamiltonian* analysis of the V^{IV}=O centres in the four states of V-doped MIL-53(Al) revealed that in the 'empty' frameworks, NP-d and LP, all V^{IV}=O centres are equivalent (within experimental uncertainty). In the NP-h and AS state two or more slightly different environments for V^{IV}=O in the metal nodes exist. This is most probably the result of random or not completely ordered pore occupation by guest (BDC, H_2O) molecules. The spin-*Hamiltonian* parameters of the LP and AS states are strikingly close which can be explained by a similar wide pore crystal structure.

The EPR spectrum of activated V-doped MIL-53(Al) in the LP state is found to be sensitive to O_2 pressure. EPR showed that exchange interaction between paramagnetic V^{IV}=O centres and O_2 molecules causes broadening of the LP EPR spectrum. This feature opens perspectives for applications in oxygen sensing, with a sensitivity of a few mbar. Contrary to that, the EPR spectrum of activated V-doped MIL-53(Al) in NP-h and NP-d states did not show similar effect. For fundamental understanding a few questions remain unanswered, one of them being why this effect is less pronounced in the MIL-47(V) case and where exactly the O_2 molecules are in the framework/how close to the V^{IV}=O centres the O_2 molecules can approach.

A concentration series of mixed-metal COMOC-2(V) - DUT-5(Al) structures revealed similarities with V-doped MIL-53(Al) and MIL-47(V). So far it appears that the EPR spectra of these samples consist of three different EPR components. One component is very similar to the broad MIL-47(V) EPR spectrum. The second EPR component resembles the EPR spectrum of V-doped MIL-53(Al) in the LP state and strongly broadens in contact with paramagnetic O_2 molecules.

The origin of the third component is still not completely clear. Contrary to the situation with MIL-47(V) and MIL-53(Al), COMOC-2(V) exhibits breathing while the DUT-5(Al) structure is rigid. The breathing effect can be triggered only by changing the pressure and not by heating. Further experiments involving recording EPR at elevated pressures are necessary to gain more insight into this effect.

MIL-47(V) was reported in literature as a good catalyst in the oxidation of cyclohexene but it showed poor stability in contact with water. Solution for this problem could be doping the highly stable MIL-53(Al) structure with catalytically active V^{IV} ions. Surprisingly, V-doped MIL-53(Al) showed considerably lower catalytic activity than expected. A few reasons for that can be derived from the knowledge obtained via the experimental work in this thesis. A first reason could be the fact that MIL-53(Al) in liquid environment is in the NP state which is non accessible to guest molecules. Concentration of vanadium sites on the boundaries, i.e. the ones that could play a role in catalysis, is shown to be lower than geometrically expected. This points to the 'egg yolk' structure where vanadium would preferentially incorporate in the MIL-53(Al/V) core. Furthermore, from the DFT calculations the V^{IV}=O bond in MIL-47(V) appears to be weaker than in the V-doped MIL-53(Al) framework. Contrary to the literature results, XANES experiments on the MIL-47(V) suggested that the VO_6 complex lacks inversion symmetry. Additional experimental work is needed to bring more insight into this problem.

A

Simulations of EPR spectra

In order to extract spin-*Hamiltonian* parameters, g and A tensors, from experimental spectra simulations and fittings of the EPR spectrum are necessary. This analysis usually starts by estimating certain parameters directly from the experimental spectrum, followed by a limited optimisation of the parameters by visual inspection of the agreement between the experimental spectrum and simulations. The parameters obtained in this way serve as initial values for least squares error fitting of the spectra. The simulations of powder EPR spectra were performed using the Easyspin toolbox for Matlab,[167] based on diagonalisation of the appropriate spin-*Hamiltonian* for the paramagnetic centre in question (see Equation B.1).

Input parameters for the simulation are information about spin system (electron spin S, nuclear spin I and identity of the nucleus), the spin-*Hamiltonian* parameters (three principal values of the g and A tensors and three Euler angles describing the tilting between the g and A principal axes) and line broadening parameters.

Figures A.1-A.15 demonstrate the influence of the g and A tensors and the tilting between their principal axes: the complexity of the simulation (number of non-zero input parameters) is gradually increased and the simulated spectrum gradually approaches the experimental. In the optimisation process, the most important is that all spectral features from the experimental spectrum are reproduced by the simulations. Furthermore, all peak positions (maxima, minima, zero crossings) are expected to be as accurate as possible. This can be obtained through least-squares error fitting on selected resonance field positions. Ultimately, the linewidth and relative intensities of peaks should be reproduced by a least-squares error fitting on the complete spectra. This gives a very strong argument that simulations (and determined spin-*Hamiltonian* parameters) completely describe the paramagnetic centre in question, but it only works

well for spectra for one type of paramagnetic centres with a single set of spin-*Hamiltonian* parameters (or for at most a few types, with well-resolved, well separated spectra).

The errors on the spin-*Hamiltonian* parameters are determined by varying the values from the best-fit values and observing the effect on the squared error. Evidently, the lower bound for errors is determined by the resolution with which spectra have been recorded.

Q-band (34 GHz) simulations of paramagnetic centre with isotropic *g* tensor.

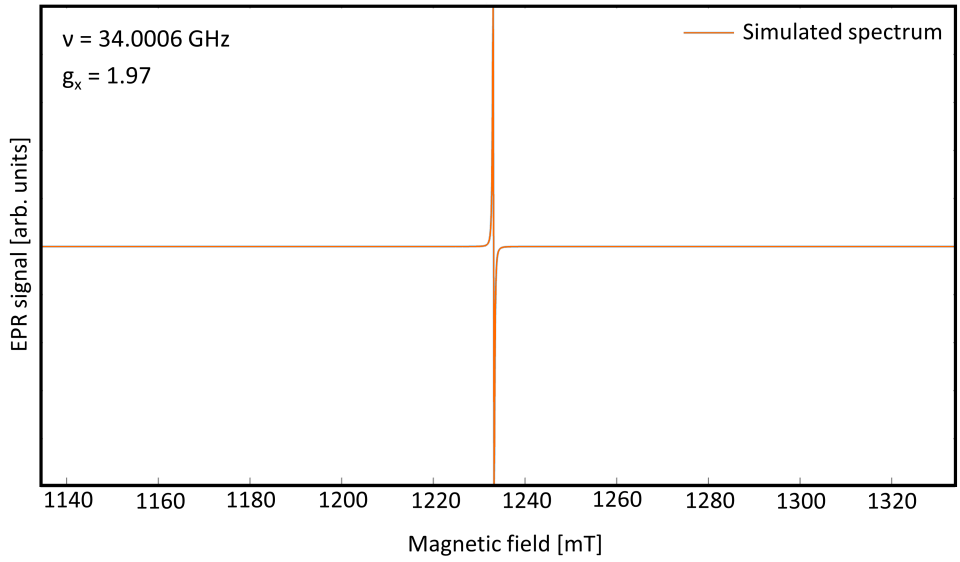

Figure A.1

Q-band (34 GHz) simulations of paramagnetic centre with axial *g* tensor.

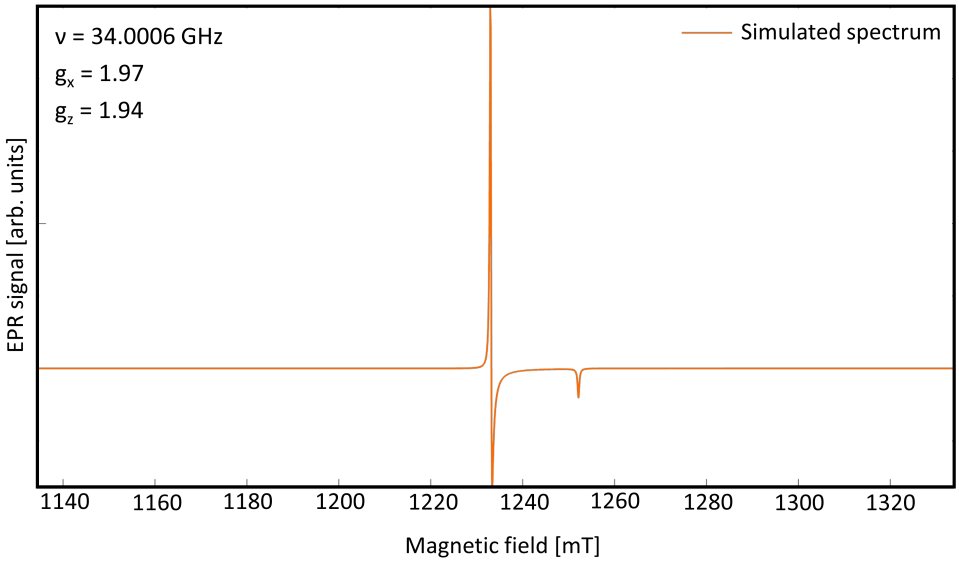

Figure A.2

Q-band (34 GHz) simulations of paramagnetic centre with orthorhombic *g* tensor.

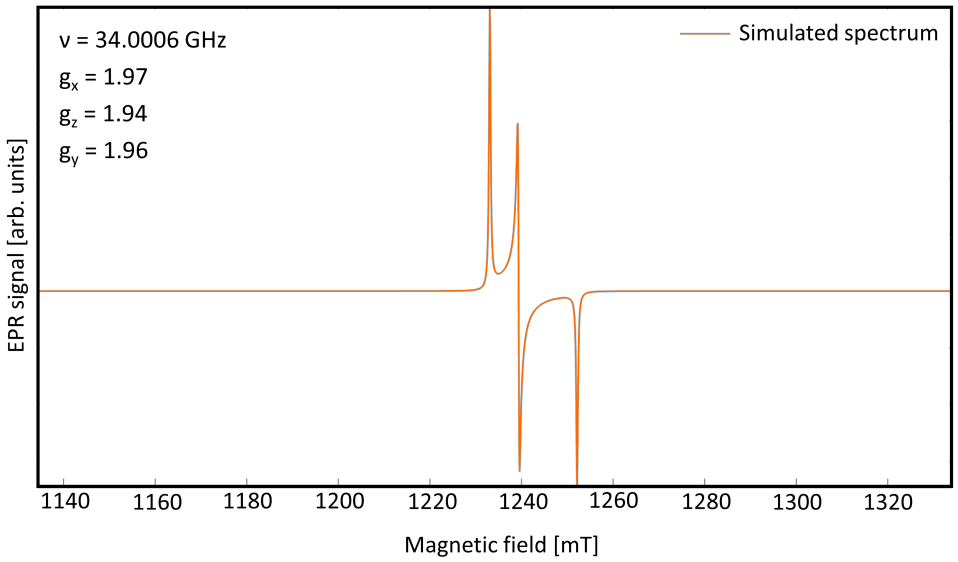

Figure A.3

Q-band (34 GHz) simulations of paramagnetic centre with orthorhombic *g* tensor and isotropic ^{51}V hyperfine tensor (*A*).

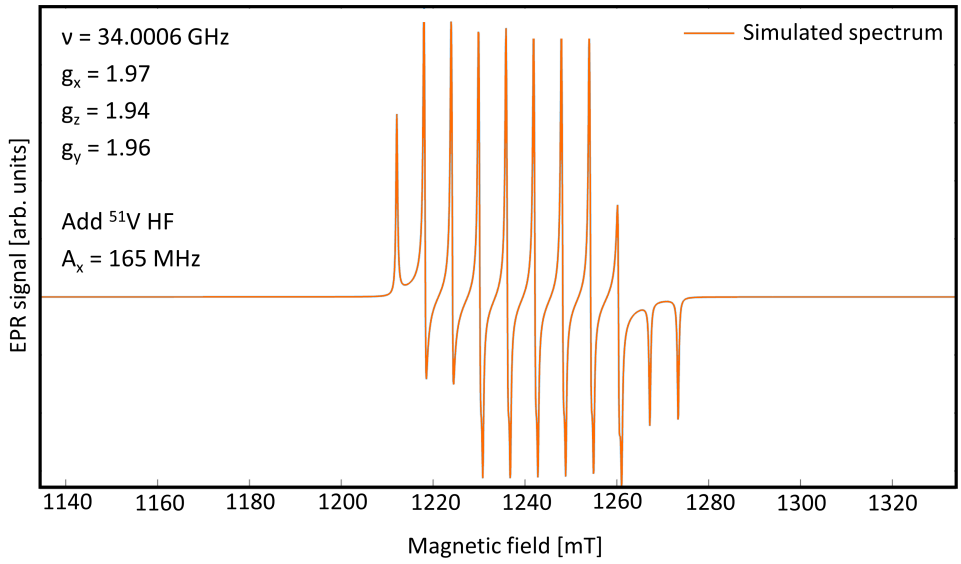

Figure A.4

Q-band (34 GHz) simulations of paramagnetic centre with orthorhombic *g* tensor and axial ^{51}V hyperfine tensor (*A*).

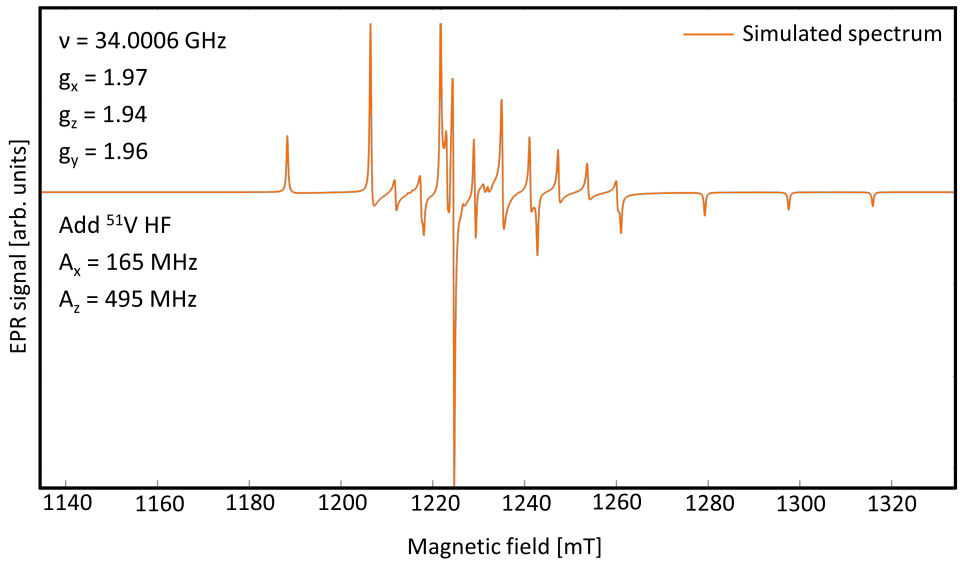

Figure A.5

Q-band (34 GHz) simulations of paramagnetic centre with orthorhombic *g* tensor and axial ^{51}V hyperfine tensor (*A*).

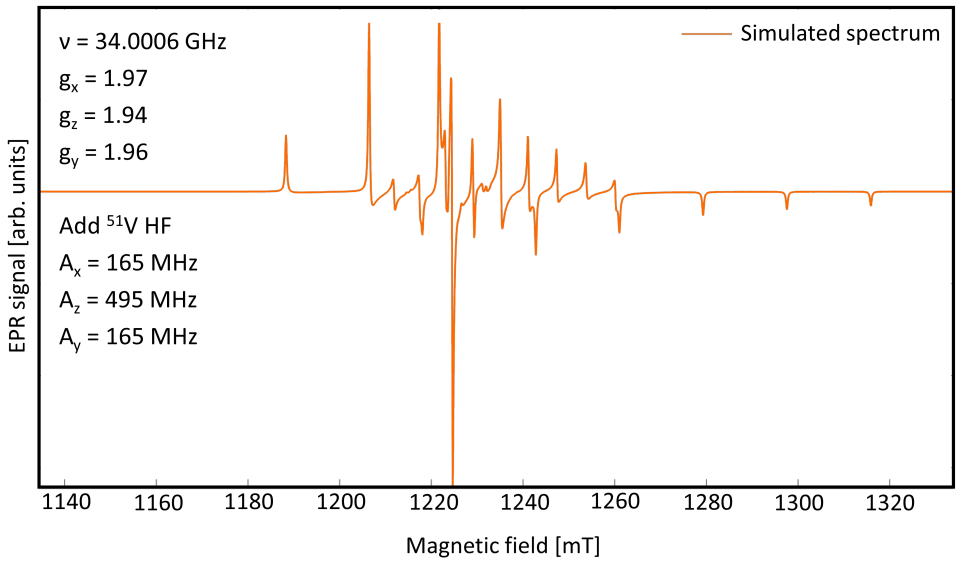

Figure A.6

Comparison of simulated and experimental spectra (V-doped MIL-53(Al) in LP state). Some resemblance is obvious but it is still far from good agreement. Main problem is that not all spectra features are reproduced by simulations.

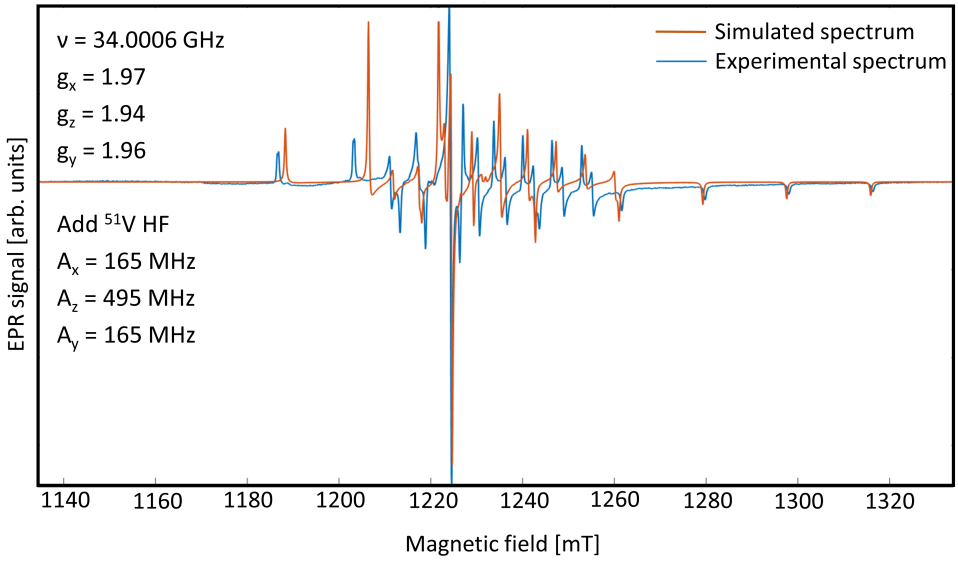

Figure A.7

If additional parameter is introduced, tilting angle between *g* and *A* tensor β, improvement is visible.

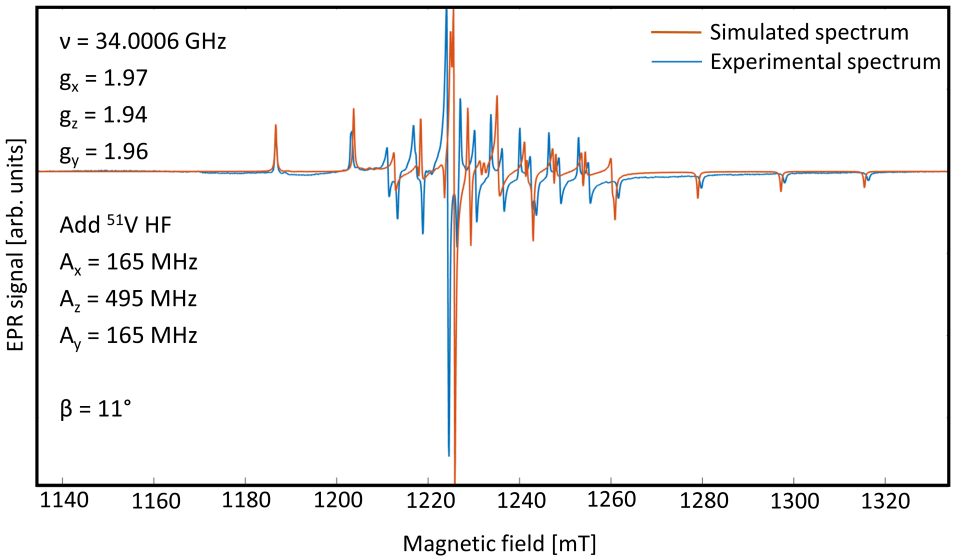

Figure A.8

Optimisation of spin-*Hamiltonian* parameters, g_x.

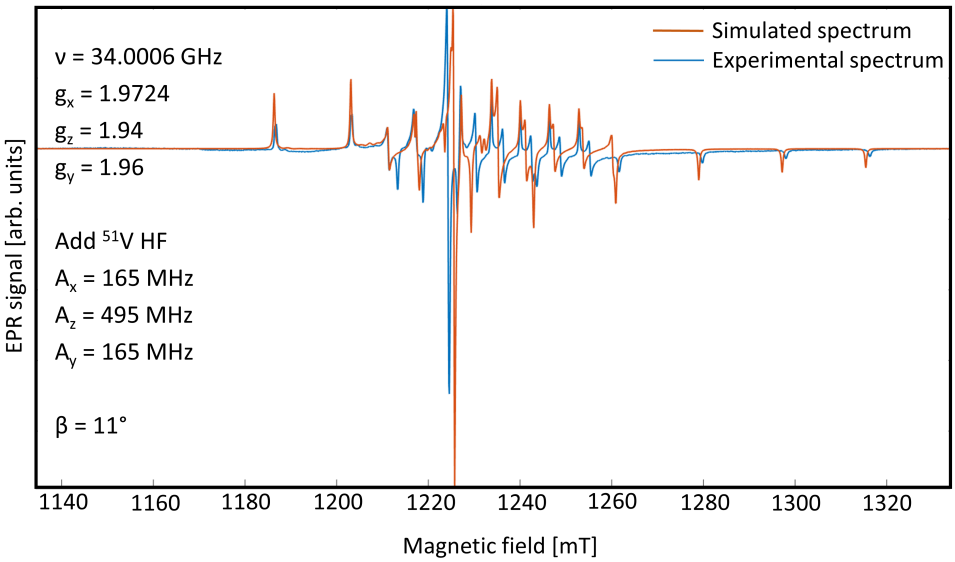

Figure A.9

Optimisation of spin-*Hamiltonian* parameters, g_z.

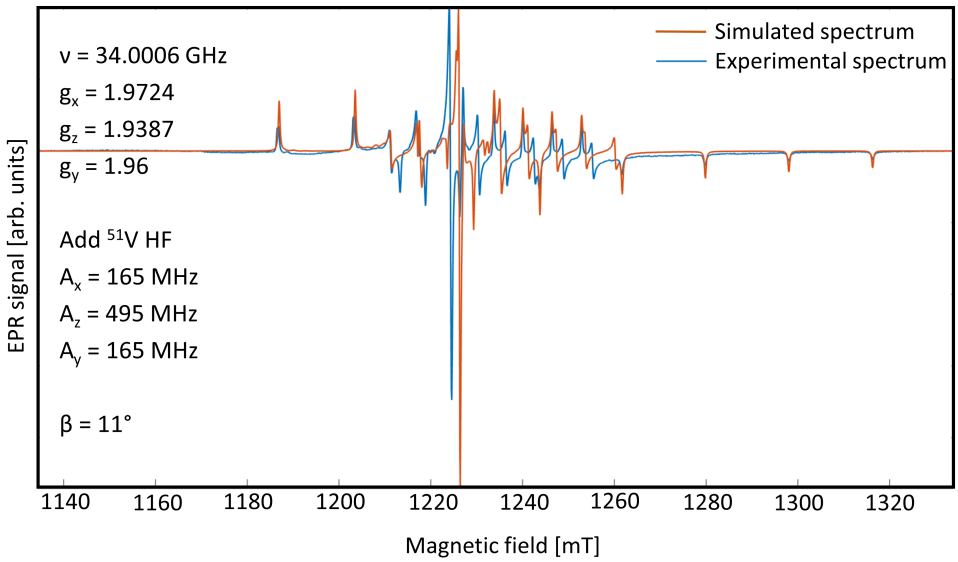

Figure A.10

Optimisation of spin-*Hamiltonian* parameters, g_y.

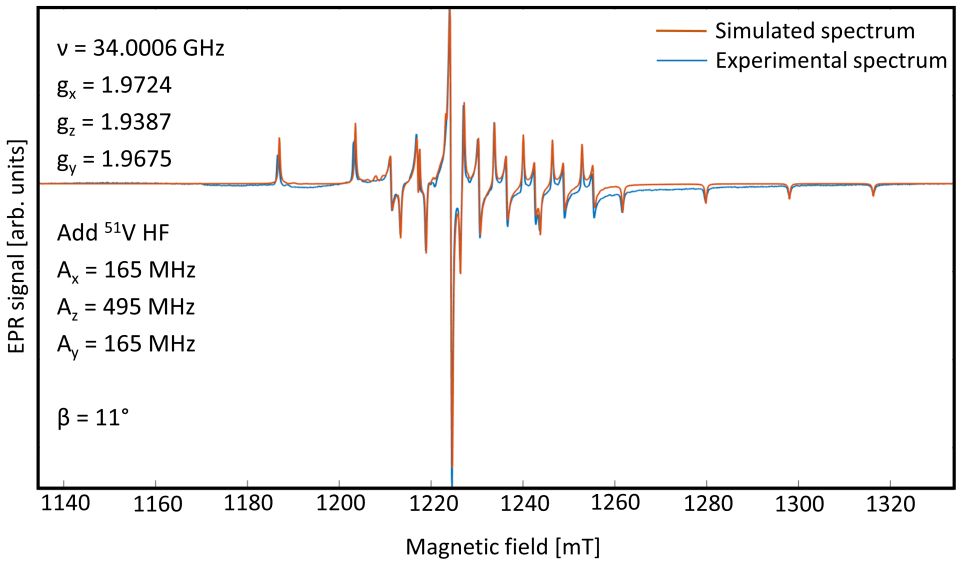

Figure A.11

Optimisation of spin-*Hamiltonian* parameters, A_x.

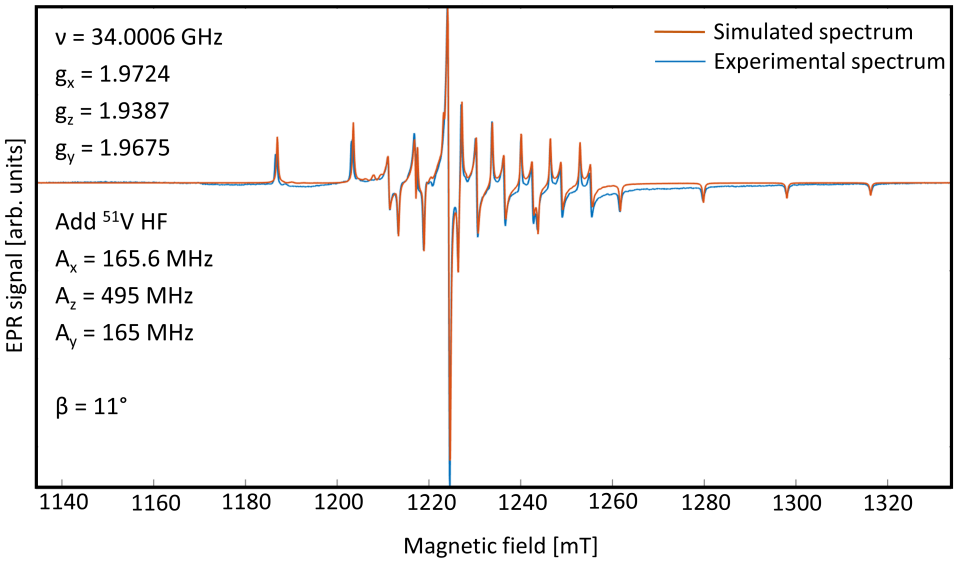

Figure A.12

Optimisation of spin-*Hamiltonian* parameters, A_z.

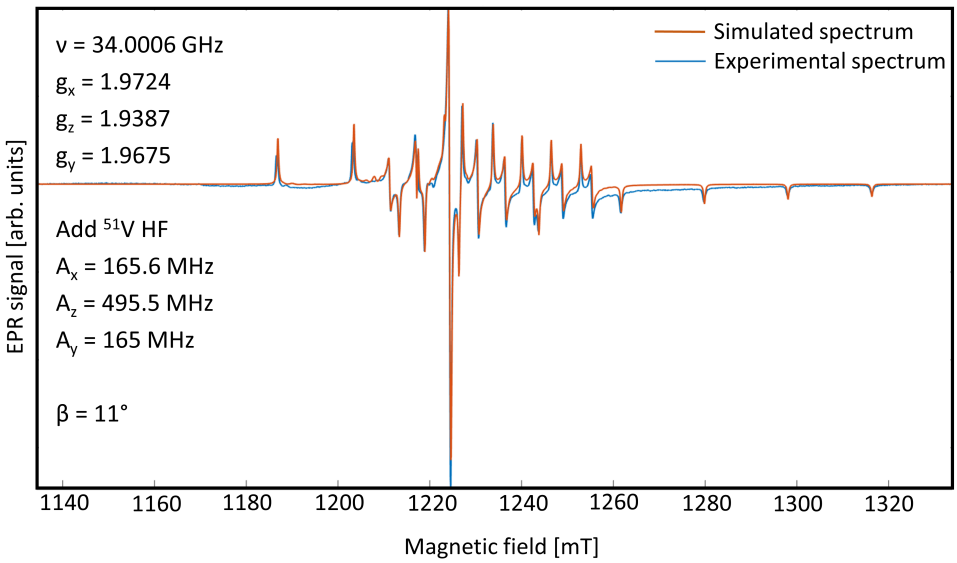

Figure A.13

Optimisation of spin-*Hamiltonian* parameters, A_y.

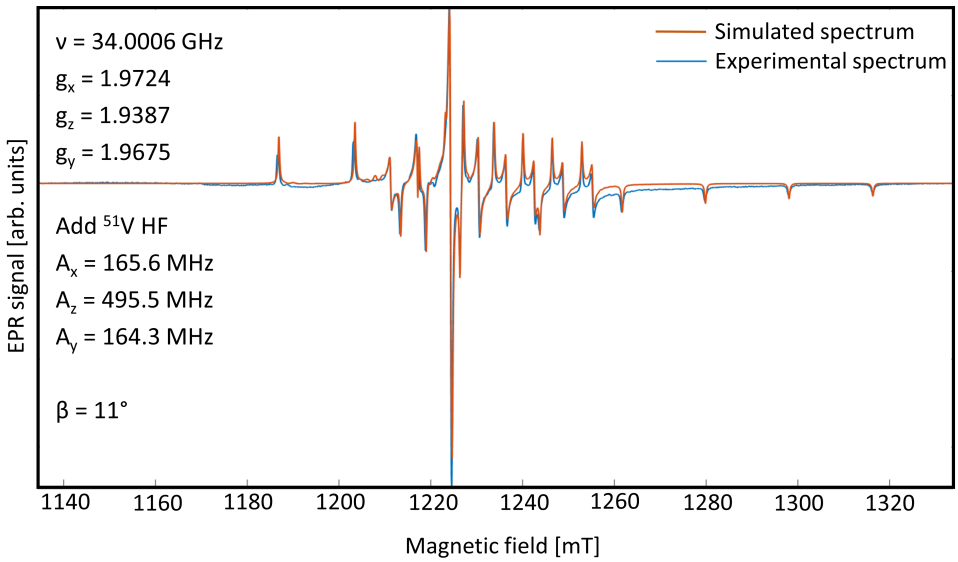

Figure A.14

Optimisation of spin-*Hamiltonian* parameters, *б*.

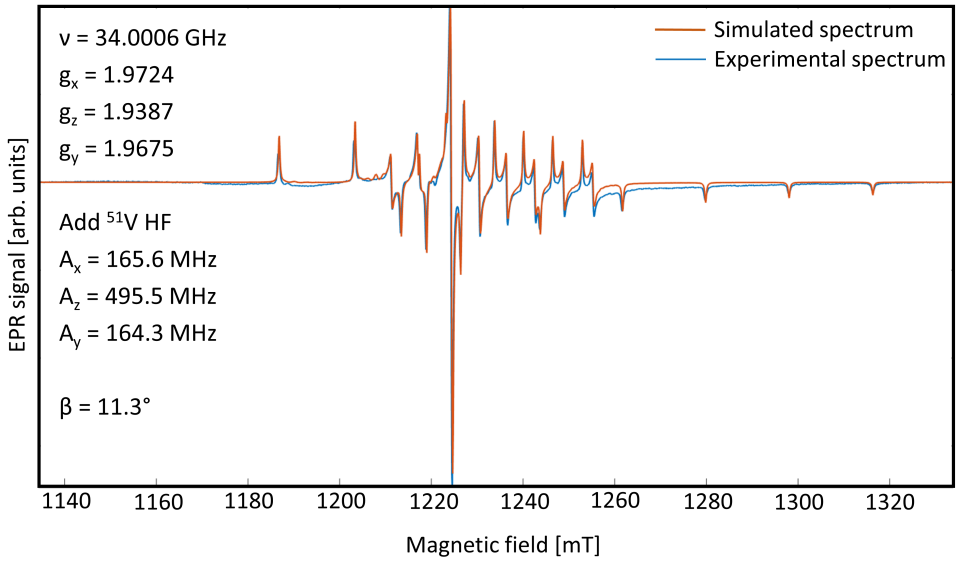

Figure A.15

B

Experimental Details

B.1 EPR and ENDOR

All EPR and ENDOR measurements presented in this thesis were recorded in CW mode. X and Q-band equipment was available at Ghent University.

The X-band setup is a Bruker ESP300E spectrometer equipped with an ER 4102ST standard cavity or ER 4114HT high temperature cavity (presented in Figure 3.17), a HP5350 B frequency counter and a Bruker ER 035M Gaussmeter. Alternatively a Varian E-line spectrometer equipped with a HP 5342A microwave frequency counter and the same high temperature cavity and Gaussmeter was used. The magnetic fields were calibrated using the spectrum of diphenyl picryl hydrazyl (DPPH, $g = 2.0036$). Q-band EPR and ENDOR spectra were recorded using a Bruker ElexSys E500 spectrometer equipped with a CF910 He-flow cryostat (2-300 K, Oxford Instruments), a Pendulum CNT-90XL frequency counter and a Bruker ER035 M Gaussmeter. The magnetic fields were calibrated against the $g_\perp$ component of the CO_3^{3-} radical in irradiated $CaCO_3$ powder ($g_\perp = 2.0031$).[178]

S-band EPR spectra were obtained with an in-house built spectrometer at ETH Zürich.[179] For the W-band measurements a Bruker ElexSys E680 setup (University of Antwerp), equipped with a liquid He flow cryostat (Oxford Instruments) was used (100 kHz modulation frequency, 90 μW microwave power). J-band EPR spectra were taken on a spectrometer developed at the Huygens Laboratory of Leiden University.[180] The applied microwave power was in the μW range, a modulation amplitude of 1.2 mT and 1.7 kHz modulation frequency was used. RT S, X and Q-band EPR spectra were recorded at approximately 5 mW microwave power (avoiding saturation) and 100 kHz modulation with exception of 10 KHz on the Varian setup. For low temperature measurements at X and Q-band, both modulation frequency and microwave power needed to be reduced (3 kHz and 5 μW).

Simulations of EPR spectra were performed using the Easyspin toolbox for Matlab[167] by diagonalisation of the appropriate spin-*Hamiltonian* for the paramagnetic centre in question:

$$\hat{H} = \mu_B \vec{B} \cdot \tilde{g} \cdot \hat{\vec{S}} + \hat{\vec{S}} \cdot \tilde{A} \cdot \hat{\vec{I}} - g_n \mu_n \vec{B} \cdot \hat{\vec{I}}. \tag{B.1}$$

For the simulation of the spectra of V-doped MIL-53(Al) in the AS state, version 4.5.4 was used. Spectra of V-doped MIL-53(Al) in the NP-d, NP-h and LP states were simulated using the updated version 5.1.8 with another convention for the Euler angles.[167] However, for easy comparison, all Euler angles have been converted to the Easyspin 4.5.4 convention.

For *in situ* X-band EPR heating experiments using the Bruker ER 4114HT cavity the powder samples were placed in one-end closed (under no circumstances sealed) quartz capillaries (3 mm inner diameter), which were during the EPR experiments either evacuated by continuous pumping (0.01 mbar with a rotary pump or 10^{-4} mbar with a turbomolecular pump) or in contact with air at ambient conditions. The sample temperature was controlled by a continuous flow of heated N_2 over the bottom part of these tubes, which were centred in the EPR cavity. Since there was no direct contact between the heating gas and the sample, EPR spectra were recorded 20-30 min after a stable temperature in the heating gas was reached. The X-band EPR spectrum of V^{IV} in the LP state was recorded at RT after heating up to 450 K. The sample was then cooled down to RT in vacuum and 1 bar of N_2 gas was introduced into the sample tube at RT.

Q and W-band EPR spectra of the LP state were also recorded at RT. The samples were placed in one-end closed capillaries, heated in a N_2 glove box at 400 K for 2h and sealed with Parafilm (Q-band tube) and wax (W-band tube). The spectra were then recorded under He gas flow to avoid oxygen and air humidity.

The spectra of the NP-d state were recorded in X-band at RT on a powder in a one-end closed quartz capillary, evacuated by continuous pumping for 2 hours. The powder in a Q-band sample tube was evacuated in a glove box and sealed with Parafilm. The spectra were again recorded under He gas flow. For the J-band measurements the quartz sample tubes were closed at one end. The microwave cavity and waveguide assembly were placed into a bath cryostat that was flushed two times with nitrogen gas to reduce contributions of molecular oxygen.[181] Spectra were recorded at 325 K and 6×10^{-3} mbar vacuum.

The X, Q and W-band NP-h state EPR spectra were recorded in air, the J-band spectra in N_2 atmosphere. In order to bring the MOF in this state a one-end closed sample tube containing powder in air was immersed in liquid nitrogen for 12 h, and warmed up to RT a short time before the measurements.

X-band EPR spectra as a function of O_2 pressure were recorded after a heating

step described above to induce the LP state. The sample was cooled down to RT in vacuum and compressed O_2 from a gas cylinder was directly connected to the sample tube and introduced in steps of approximately 10 mbar. An EPR spectrum was recorded after each step. The linewidth of the EPR spectra was determined by simulations with the parameters reported for the LP state (see Table 7.3 in Chapter 7) and fitting the linewidth (full width at half maximum) with Lorentzian isotropic broadening using the Easyspin toolbox for Matlab.[167]

B.2 TGA

TGA data were collected on a Netzsch STA-409CD thermal analyser in a temperature range of 300-460 K under air atmosphere at a heating rate of 2 K/min. At the start of the experiment, V-doped MIL-53(Al) was at RT and has been exposed to (humid) air for a considerable time. For the measurements on the NP-d state the sample was kept under vacuum (10^{-4} bar) for 48 h prior to the measurements to ensure all water was removed from the structure.

B.3 XANES

XANES was performed at the ESRF (European Synchrotron Radiation Facility, Grenoble, France), beamline BM26A-DUBBLE (Dutch-Belgian Beamline). This 0.4 T bending magnet beamline utilizes a Si(111) monochromator, rendering an X-ray beam flux of approximately $1x10^{10}$ photons/s and an energy resolution $\Delta E/E$ of $1.7x10^{-4}$ at 9.689 keV.[182] Measurements were performed in a He-filled cryostat (Oxford Instruments) at 80 K. The samples were prepared and analysed as pressed pellets, containing a mixture of MOF and cellulose as a binding agent, providing a theoretical absorption of two absorption lengths for 5515 eV X-ray photons. XANES scans were performed over the V K-edge (E_0: 5465 eV) with steps of 0.3 eV over the pre-edge peak and edge regions. Multiple scans were performed to obtain better data quality. XANES data were normalized and processed using the UGent Athena software package by Pieter Tack from the Department of Inorganic and Physical Chemistry of Ghent University. A pseudo-Voigt function was fitted to the pre-edge peak, corresponding to the $1s - 3d$ electron transition, after subtracting an error function corresponding to the rising edge.

B.4 FTIR

There are three methods to obtain a vibrational absorption spectrum of the sample by FTIR spectrometry: transmission spectroscopy, diffuse reflectance

spectroscopy and attenuated total reflection (ATR). In the first two methods the use of matrix material is required, KBr for the mid-IR range or PE for the far-IR range, in combination with high pressures necessary for forming the pellets. It was found that both the matrix material and the pressure does influence the behaviour of the MIL-53(Al) framework. To avoid using KBr or PE and pressing pellets ATR IR spectroscopy proved to be useful. In the ATR setup, a diamond crystal is used which is transparent in both the mid and far-IR range. An additional advance is that no sample preparation is required and the powder is placed directly on the diamond crystal. The IR spectrum can be measured in atmosphere conditions but also under vacuum. For the ATR measurements, a Bruker Vertex 80v spectrometer was used with silicon carbide rod (Gobar) source, a beam splitter made of KBr and a wide-range DLaTGS detector.

B.5 Synthesis and material characterisation

All samples reported in this thesis were synthesised in the Centre for Ordered Materials, Organometallics and Catalysis (COMOC) at the Department of Inorganic and Physical Chemistry of Ghent University, by Hannes Depauw. The vanadium doping concentrations in the samples are kept low to avoid contributions from broad EPR backgrounds. For concentration series samples with different loadings are used. For some experiments a number of samples of similar loadings were synthesised and used because a large number of measurements had to be performed.

B.5.1 MIL-47(V)

MIL-47 was synthesized according to a synthesis route described in literature.[66] Typically, 1.37 g VCl_3 and 0.36 g H_2BDC were mixed together with 15.7 mL of deionised water. The resulting mixture was transferred into a Teflon-lined stainless autoclave for 4 days at 475 K. The AS MIL- 47 was filtered, washed with acetone, and calcined for 21 h and 30 min at 575 K to remove free H_2BDC from the pores.

B.5.2 V-doped MIL-53(Al)

The synthesis of V-doped MIL-53(Al) was performed under autogenous pressure for 72 h at 473 K in a 23 ml Teflon-lined steel autoclave by using a mixture of VCl_3 and $AlCl_3$, H_2BDC and deionized water. In general 0.232 g (1.4 mmol) of H_2BDC was used. The AS powders were white coloured and stable in air. After filtration, powders were washed several times with deionized water and dried

under vacuum at RT. Of each sample, a part was activated for further material characterisation. A solvent extraction method[56] was used for activation instead of calcination, during which the unreacted linker and metal salts were removed. This procedure consists of three steps. First, the solid was heated at 423 K with DMF in a Teflon-lined autoclave for 24 h (Figure B.1 for MIL-53(Cr)). Secondly, the solid was treated at 393 K in methanol for 72 h. Finally, the powder was dried at 473 K for 2 h under vacuum for a complete activation. A few samples with $VOSO_4$ as dopant salt were synthesized and activated following the same procedure. Some samples were also activated by calcination. For the calcination procedure, 0.2 gram of AS sample was spread over the surface of a ceramic plate. All samples were heated in a muffle furnace at 573 K for 72 h under air. After this heating step the samples were collected and stored under dry argon atmosphere.

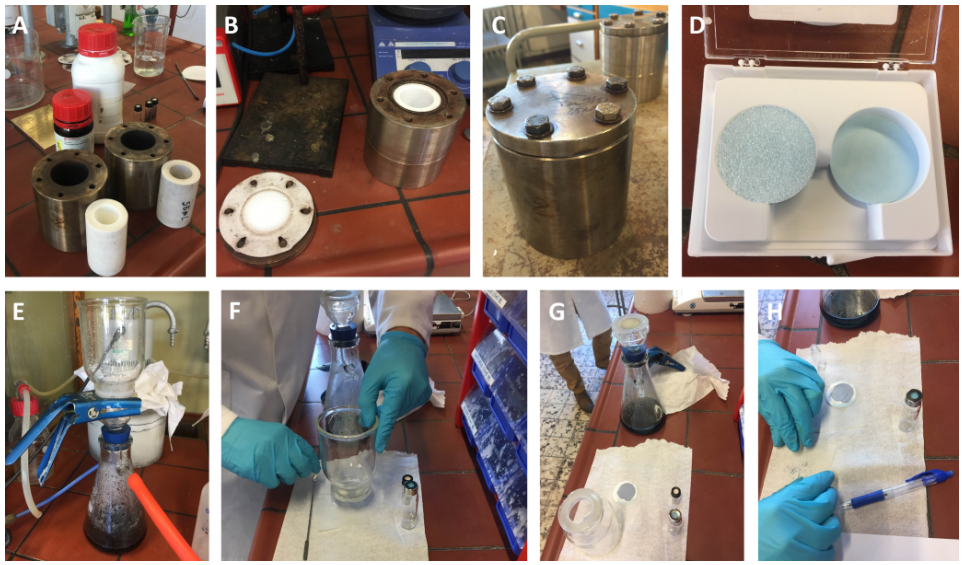

Figure B.1: Synthesis procedure of MIL-53(Cr). A, B and C - Teflon liners with stainless steel autoclaves. D - Filtration paper. E - Filtration setup. F, G and H - Extraction of the powder from filtration setup.

Powder XRD patterns were recorded on AS and activated samples using a Thermo Scientific ARL X'TRA diffractometer, operated at 40 kV, 30 mA using Cu-Kα radiation (λ =1.5406 Å). N_2 sorption measurements on activated samples were performed by using a Belsorp-mini II setup (Bell Japan, Inc.). A Varian FS-220 F-AAS (Flame Atomic Absorption Spectroscopy) with a nitrous oxide-acetylene flame was used to determine the V/Al atomic concentration ratios in the samples after activation together with a Perkin Elmer Elan DRC 6000 ICP-MS (inductively coupled mass spectroscopy) to determine the vanadium content and a Varian Vista MPX ICP-OES (inductively coupled plasma optical emission spectroscopy) to measure the Al content. To avoid interference with ClO^- anions, during the

analysis of vanadium, methane was added as a reaction gas. Before the analysis, the MOF powders were destroyed in an acidic medium.

B.5.3 COMOC-2(V) - DUT-5(Al)

The synthesis of COMOC-2(V) was performed by the recipe developed previously by Liu *at al.* (COMOC group).[73] In brief, an amount of 0.5 g of $VOSO_4 \cdot H_2O$, 1.02 g of H_2BPDC and 70 mL of DMF were transferred into a 100 mL round-bottom flask equipped with a magnetic stirrer. The reaction vessel was sealed, slowly heated to 420 K under stirring and kept at this temperature for 16 h. Afterwards, the yellow-green powder was collected over a membrane filter and washed thoroughly with DMF, methanol and acetone to remove unreacted starting materials. In a final step the material was dried under vacuum for 2 h at 395 K.

DUT-5(Al) was synthesized and activated according to a previously reported procedure by Senkovska *et al*.[74] In a typical synthesis 0.26 g of H_2BPDC, 0.52 g of $Al(NO_3 \cdot 9H_2O)$, and 30 mL of DMF were mixed in a 50 mL round-bottom flask equipped with a magnetic stirrer. The flask was sealed, slowly heated to 420 K under stirring, and kept at this temperature for 16h. The white powder was filtered and washed with DMF, methanol and acetone. All solvents were removed by a drying step at 395 K under vacuum for 2 hours.

The mixed-metal MOFs COMOC-2 V(x)-Al(1-x) were all synthesized via a direct one-pot synthesis. A mixture of organic H_2BPDC linker, different ratios of metal salts $VOSO_4 \cdot H_2O / Al(NO_3)_3 \cdot 9H_2O$ and DMF were added in a 50 mL round-bottom flask equipped with a magnetic stirring bar. The reaction mixture was slowly heated to 420 K and kept at this temperature for 16 hours. Subsequently the created crystalline material was filtered at synthesis temperature and washed with DMF, methanol and acetone. All compounds were in a final step dried at 395 K for 2 hours. This synthesis was published in the framework of this project by Depauw *et al*.[176]

Bibliography

[1] J.-R. Li, R. J. Kuppler, and H.-C. Zhou, "Selective gas adsorption and separation in metal-organic frameworks," *Chemical Society Reviews*, vol. 38, no. 5, pp. 1477–1504, 2009.

[2] M. I. Nandasiri, S. R. Jambovane, B. P. McGrail, H. T. Schaef, and S. K. Nune, "Adsorption, separation, and catalytic properties of densified metal-organic frameworks," *Coordination Chemistry Reviews*, vol. 311, pp. 38–52, 2016.

[3] M. P. Suh, H. J. Park, T. K. Prasad, and D.-W. Lim, "Hydrogen storage in metal-organic frameworks," *Chemical Reviews*, vol. 112, no. 2, pp. 782–835, 2012.

[4] X. Lin, N. R. Champness, and M. Schröder, *Hydrogen, Methane and Carbon Dioxide Adsorption in Metal-Organic Framework Materials*, pp. 35–76. Berlin, Heidelberg: Springer Berlin Heidelberg, 2010.

[5] K. Leus, I. Muylaert, M. Vandichel, G. B. Marin, M. Waroquier, V. Van Speybroeck, and P. Van Der Voort, "The remarkable catalytic activity of the saturated metal organic framework V-MIL-47 in the cyclohexene oxidation," *Chemical Communications*, vol. 46, no. 28, pp. 5085–5087, 2010.

[6] K. Leus, M. Vandichel, Y.-Y. Liu, I. Muylaert, J. Musschoot, S. Pyl, H. Vrielinck, F. Callens, G. B. Marin, C. Detavernier, P. V. Wiper, Y. Z. Khimyak, M. Waroquier, V. V. Speybroeck, and P. V. D. Voort, "The coordinatively saturated vanadium MIL-47 as a low leaching heterogeneous catalyst in the oxidation of cyclohexene," *Journal of Catalysis*, vol. 285, no. 1, pp. 196–207, 2012.

[7] A. Dhakshinamoorthy, A. M. Asiri, and H. García, "Metal-organic framework (MOF) compounds: Photocatalysts for redox reactions and solar fuel production," *Angewandte Chemie International Edition*, vol. 55, no. 18, pp. 5414–5445, 2016.

[8] J. Lee, O. K. Farha, J. Roberts, K. A. Scheidt, S. T. Nguyen, and J. T. Hupp, "Metal-organic framework materials as catalysts," *Chemical Society Reviews*, vol. 38, no. 5, pp. 1450–1459, 2009.

[9] Z. Hu, B. J. Deibert, and J. Li, "Luminescent metal-organic frameworks for chemical sensing and explosive detection," *Chemical Society Reviews*, vol. 43, no. 16, pp. 5815–5840, 2014.

[10] L. E. Kreno, K. Leong, O. K. Farha, M. Allendorf, R. P. Van Duyne, and J. T. Hupp, "Metal-organic framework materials as chemical sensors," *Chemical Reviews*, vol. 112, no. 2, pp. 1105–1125, 2012.

[11] J. Della Rocca, D. Liu, and W. Lin, "Nanoscale metal-organic frameworks for biomedical imaging and drug delivery," *Accounts of Chemical Research*, vol. 44, no. 10, pp. 957–968, 2011.

[12] O. M. Yaghi and H. Li, "Hydrothermal synthesis of a metal-organic framework containing large rectangular channels," *Journal of the American Chemical Society*, vol. 117, no. 41, pp. 10401–10402, 1995.

[13] H. Li, M. Eddaoudi, M. O'Keeffe, and O. M. Yaghi, "Design and synthesis of an exceptionally stable and highly porous metal-organic framework," *Nature*, vol. 402, no. 6759, pp. 276–279, 1999.

[14] O. M. Yaghi, H. Li, C. Davis, D. Richardson, and T. L. Groy, "Synthetic strategies, structure patterns, and emerging properties in the chemistry of modular porous solids," *Accounts of Chemical Research*, vol. 31, no. 8, pp. 474–484, 1998.

[15] C. J. Kepert and M. J. Rosseinsky, "Zeolite-like crystal structure of an empty microporous molecular framework," *Chemical Communications*, pp. 375–376, 1999.

[16] G. Férey, "Hybrid porous solids: past, present, future," *Chemical Society Reviews*, vol. 37, no. 1, pp. 191–214, 2008.

[17] H.-C. Zhou, J. R. Long, and O. M. Yaghi, "Introduction to metal-organic frameworks," *Chemical Reviews*, vol. 112, no. 2, pp. 673–674, 2012.

[18] H. Furukawa, N. Ko, Y. B. Go, N. Aratani, S. B. Choi, E. Choi, A. O. Yazaydin, R. Q. Snurr, M. O'Keeffe, J. Kim, and O. M. Yaghi, "Ultrahigh porosity in metal-organic frameworks," *Science*, vol. 329, no. 5990, pp. 424–428, 2010.

[19] W. J. Thomas and B. Crittenden, "3 - Fundamentals of adsorption equilibria," in *Adsorption Technology & Design* (W. J. Thomas and B. Crittenden, eds.), pp. 31 – 65, Oxford: Butterworth-Heinemann, 1998.

[20] J. W. ed. Ferdi Schüth, Kenneth S. W. Sing, *Handbook of Porous Solids*. Wiley-VCH Verlag GmbH, 2002.

[21] T. Loiseau, C. Serre, C. Huguenard, G. Fink, F. Taulelle, M. Henry, T. Bataille, and G. Férey, "A rationale for the large breathing of the porous aluminum terephthalate (MIL-53) upon hydration," *Chemistry-A European Journal*, vol. 10, no. 6, pp. 1373–1382, 2004.

[22] S. S.-Y. Chui, S. M.-F. Lo, J. P. H. Charmant, A. G. Orpen, and I. D. Williams, "A chemically functionalizable nanoporous material $[Cu_3(TMA)_2(H_2O)_3]_n$," *Science*, vol. 283, no. 5405, pp. 1148–1150, 1999.

[23] D. Saha, Z. Bao, F. Jia, and S. Deng, "Adsorption of CO_2, CH_4, N_2O, and N_2 on MOF-5, MOF-177, and Zeolite 5A," *Environmental Science & Technology*, vol. 44, no. 5, pp. 1820–1826, 2010.

[24] N. T. Phan, K. K. Le, and T. D. Phan, "MOF-5 as an efficient heterogeneous catalyst for Friedel-Crafts alkylation reactions," *Applied Catalysis A: General*, vol. 382, no. 2, pp. 246 – 253, 2010.

[25] `http://www.chemtube3d.com/`. August 30, 2017.

[26] I. E. Ertas, M. Gulcan, A. Bulut, M. Yurderi, and M. Zahmakiran, "Metal-organic framework (MIL-101) stabilized ruthenium nanoparticles: Highly efficient catalytic material in the phenol hydrogenation," *Microporous and Mesoporous Materials*, vol. 226, pp. 94 – 103, 2016.

[27] K. S. Park, Z. Ni, A. P. Côté, J. Y. Choi, R. Huang, F. J. Uribe-Romo, H. K. Chae, M. O'Keeffe, and O. M. Yaghi, "Exceptional chemical and thermal stability of zeolitic imidazolate frameworks," *Proceedings of the National Academy of Sciences*, vol. 103, no. 27, pp. 10186–10191, 2006.

[28] B. Chen, Z. Yang, Y. Zhu, and Y. Xia, "Zeolitic imidazolate framework materials: recent progress in synthesis and applications," *Journal of Materials Chemistry A*, vol. 2, pp. 16811–16831, 2014.

[29] E. Jang, E. Kim, H. Kim, T. Lee, H.-J. Yeom, Y.-W. Kim, and J. Choi, "Formation of ZIF-8 membranes inside porous supports for improving both their H_2/CO_2 separation performance and thermal/mechanical stability," *Journal of Membrane Science*, vol. 540, pp. 430 – 439, 2017.

[30] A. Huang, Q. Liu, N. Wang, and J. Caro, "Highly hydrogen permselective ZIF-8 membranes supported on polydopamine functionalized macroporous stainless-steel-nets," *Journal of Materials Chemistry A*, vol. 2, pp. 8246–8251, 2014.

[31] Y. Zhu, Q. Liu, J. Caro, and A. Huang, "Highly hydrogen-permselective zeolitic imidazolate framework ZIF-8 membranes prepared on coarse and macroporous tubes through repeated synthesis," *Separation and Purification Technology*, vol. 146, pp. 68 – 74, 2015.

[32] G. Lu and J. T. Hupp, "Metal-organic frameworks as sensors: A ZIF-8 based Fabry-Pérot device as a selective sensor for chemical vapors and gases," *Journal of the American Chemical Society*, vol. 132, no. 23, pp. 7832–7833, 2010.

[33] Y. Li and R. T. Yang, "Hydrogen storage in metal-organic frameworks by bridged hydrogen spillover," *Journal of the American Chemical Society*, vol. 128, no. 25, pp. 8136–8137, 2006.

[34] B. Panella and M. Hirscher, "Hydrogen physisorption in metal-organic porous crystals," *Advanced Materials*, vol. 17, no. 5, pp. 538–541, 2005.

[35] J. L. C. Rowsell and O. M. Yaghi, "Strategies for hydrogen storage in metal-organic frameworks," *Angewandte Chemie International Edition*, vol. 44, no. 30, pp. 4670–4679, 2005.

[36] A. Dhakshinamoorthy, M. Alvaro, and H. Garcia, "HKUST-1 catalyzed room temperature hydrogenation of acetophenone by silanes," *Catalysis Communications*, vol. 97, pp. 74 – 78, 2017.

[37] A. Nagaraj and D. Amarajothi, "$Cu_3(BTC)_2$ as a viable heterogeneous solid catalyst for Friedel-Crafts alkylation of indoles with nitroalkenes," *Journal of Colloid and Interface Science*, vol. 494, pp. 282 – 289, 2017.

[38] G. Férey, C. Mellot-Draznieks, C. Serre, F. Millange, J. Dutour, S. Surblé, and I. Margiolaki, "A chromium terephthalate-based solid with unusually large pore volumes and surface area," *Science*, vol. 309, no. 5743, pp. 2040–2042, 2005.

[39] S. Biswas, S. Couck, M. Grzywa, J. F. M. Denayer, D. Volkmer, and P. Van Der Voort, "Vanadium analogues of nonfunctionalized and amino-functionalized MOFs with MIL-101 topology synthesis, characterization, and gas sorption properties," *European Journal of Inorganic Chemistry*, vol. 2012, no. 15, pp. 2481–2486, 2012.

[40] K. M. L. Taylor-Pashow, J. D. Rocca, Z. Xie, S. Tran, and W. Lin, "Postsynthetic modifications of iron-carboxylate nanoscale metal-organic frameworks for imaging and drug delivery," *Journal of the American Chemical Society*, vol. 131, no. 40, pp. 14261–14263, 2009.

[41] P. Serra-Crespo, E. V. Ramos-Fernandez, J. Gascon, and F. Kapteijn, "Synthesis and characterization of an amino functionalized MIL-101(Al): Separation and catalytic properties," *Chemistry of Materials*, vol. 23, no. 10, pp. 2565–2572, 2011.

[42] A. Henschel, K. Gedrich, R. Kraehnert, and S. Kaskel, "Catalytic properties of MIL-101," *Chemical Communications*, pp. 4192–4194, 2008.

[43] S. Bhattacharjee, C. Chen, and W.-S. Ahn, "Chromium terephthalate metal-organic framework MIL-101: synthesis, functionalization, and applications for adsorption and catalysis," *RSC Advances*, vol. 4, pp. 52500–52525, 2014.

[44] L. Bromberg, Y. Diao, H. Wu, S. A. Speakman, and T. A. Hatton, "Chromium(III) terephthalate metal organic framework (MIL-101): HF-free synthesis, structure, polyoxometalate composites, and catalytic properties," *Chemistry of Materials*, vol. 24, no. 9, pp. 1664–1675, 2012.

[45] K. Leng, Y. Sun, X. Li, S. Sun, and W. Xu, "Rapid synthesis of metal-organic frameworks MIL-101(Cr) without the addition of solvent and hydrofluoric acid," *Crystal Growth & Design*, vol. 16, no. 3, pp. 1168–1171, 2016.

[46] J. H. Cavka, S. Jakobsen, U. Olsbye, N. Guillou, C. Lamberti, S. Bordiga, and K. P. Lillerud, "A new zirconium inorganic building brick forming metal organic frameworks with exceptional stability," *Journal of the American Chemical Society*, vol. 130, no. 42, pp. 13850–13851, 2008.

[47] M. Taddei, "When defects turn into virtues: The curious case of zirconium-based metal-organic frameworks," *Coordination Chemistry Reviews*, vol. 343, pp. 1 – 24, 2017.

[48] R. Kitaura, K. Seki, G. Akiyama, and S. Kitagawa, "Porous coordination-polymer crystals with gated channels specific for supercritical gases," *Angewandte Chemie International Edition*, vol. 42, no. 4, pp. 428–431, 2003.

[49] S. Kitagawa and M. Kondo, "Functional micropore chemistry of crystalline metal complex-assembled compounds," *Bulletin of the Chemical Society of Japan*, vol. 71, no. 8, pp. 1739–1753, 1998.

[50] G. Alberti, S. Murcia-Mascarós, and R. Vivani, "Pillared derivatives of γ-zirconium phosphate containing nonrigid alkyl chain pillars," *Journal of the American Chemical Society*, vol. 120, no. 36, pp. 9291–9295, 1998.

[51] C. Serre, F. Millange, C. Thouvenot, M. Noguès, G. Marsolier, D. Louër, and G. Férey, "Very large breathing effect in the first nanoporous chromium(III)-based solids: MIL-53 or $Cr^{III}(OH)\{O_2C\text{-}C_6H_4\text{-}CO_2\}\{HO_2C\text{-}C_6H_4\text{-}CO_2H\}_xH_2O_y$," *Journal of the American Chemical Society*, vol. 124, no. 45, pp. 13519–13526, 2002.

[52] C. Volkringer, T. Loiseau, N. Guillou, G. Férey, E. Elkaim, and A. Vimont, "XRD and IR structural investigations of a particular breathing effect in the MOF-type gallium terephthalate MIL-53(Ga)," *Dalton Transactions*, no. 12, pp. 2241–2249, 2009.

[53] J. P. S. Mowat, V. R. Seymour, J. M. Griffin, S. P. Thompson, A. M. Z. Slawin, D. Fairen-Jimenez, T. Duren, S. E. Ashbrook, and P. A. Wright, "A novel structural form of MIL-53 observed for the scandium analogue and its response to temperature variation and CO_2 adsorption," *Dalton Transactions*, vol. 41, no. 14, pp. 3937–3941, 2012.

[54] F. Millange, N. Guillou, R. I. Walton, J.-M. Greneche, I. Margiolaki, and G. Férey, "Effect of the nature of the metal on the breathing steps in MOFs with dynamic frameworks," *Chemical Communications*, no. 39, pp. 4732–4734, 2008.

[55] G. Férey, "Structural flexibility in crystallized matter: from history to applications," *Dalton Transactions*, vol. 45, pp. 4073–4089, 2016.

[56] P. Rallapalli, D. Patil, K. P. Prasanth, R. S. Somani, R. V. Jasra, and H. C. Bajaj, "An alternative activation method for the enhancement of methane storage capacity of nanoporous aluminium terephthalate, MIL-53(Al)," *Journal of Porous Materials*, vol. 17, no. 5, pp. 523–528, 2010.

[57] S. Bourrelly, P. L. Llewellyn, C. Serre, F. Millange, T. Loiseau, and G. Férey, "Different adsorption behaviors of methane and carbon dioxide in the isotypic nanoporous metal terephthalates MIL-53 and MIL-47," *Journal of the American Chemical Society*, vol. 127, no. 39, pp. 13519–13521, 2005.

[58] H. Depauw, I. Nevjestić, J. De Winne, G. Wang, K. Haustraete, K. Leus, A. A. Verberckmoes, C. Detavernier, F. Callens, E. De Canck, H. M. Vrielinck, and P. Van Der Voort, "Microwave induced "egg yolk" structure in Cr/V-MIL-53," *Chemical Communications*, vol. 53, pp. 8478–8481, 2017.

[59] Y. Liu, J.-H. Her, A. Dailly, A. J. Ramirez-Cuesta, D. A. Neumann, and C. M. Brown, "Reversible structural transition in MIL-53 with large temperature hysteresis," *Journal of the American Chemical Society*, vol. 130, no. 35, pp. 11813–11818, 2008.

[60] I. Nevjestić, H. Depauw, K. Leus, G. Rampelberg, C. A. Murray, C. Detavernier, P. Van Der Voort, F. Callens, and H. Vrielinck, "*In Situ* electron paramagnetic resonance and X-ray diffraction monitoring of temperature-induced breathing and related structural transformations in activated V-doped MIL-53(Al)," *The Journal of Physical Chemistry C*, vol. 120, no. 31, pp. 17400–17407, 2016.

[61] F.-X. Coudert, M. Jeffroy, A. H. Fuchs, A. Boutin, and C. Mellot-Draznieks, "Thermodynamics of guest-induced structural transitions in hybrid organic-inorganic frameworks," *Journal of the American Chemical Society*, vol. 130, no. 43, pp. 14294–14302, 2008.

[62] J. K. Dewhurst, S. Sharma, and L. Nordstrom, "The spacegroup manual, version 1.2.1," *http://elk.sourceforge.net/spacegroup.pdf*.

[63] C. Serre, F. Millange, S. Surblé, and G. Férey, "A route to the synthesis of trivalent transition-metal porous carboxylates with trimeric secondary building units," *Angewandte Chemie International Edition*, vol. 43, no. 46, pp. 6285–6289, 2004.

[64] C. Mellot-Draznieks, C. Serre, S. Surblé, N. Audebrand, and G. Férey, "Very large swelling in hybrid frameworks: a combined computational and powder diffraction study," *Journal of the American Chemical Society*, vol. 127, no. 46, pp. 16273–16278, 2005.

[65] C. Serre, C. Mellot-Draznieks, S. Surblé, N. Audebrand, Y. Filinchuk, and G. Férey, "Role of solvent-host interactions that lead to very large swelling of hybrid frameworks," *Science*, vol. 315, no. 5820, pp. 1828–1831, 2007.

[66] K. Barthelet, J. Marrot, D. Riou, and G. Férey, "A breathing hybrid organic-inorganic solid with very large pores and high magnetic characteristics," *Angewandte Chemie International Edition*, vol. 41, no. 2, pp. 281–284, 2002.

[67] H. Leclerc, T. Devic, S. Devautour-Vinot, P. Bazin, N. Audebrand, G. Férey, M. Daturi, A. Vimont, and G. Clet, "Influence of the oxidation state of the metal center on the flexibility and adsorption properties of a porous metal organic framework: MIL-47(V)," *Journal of Physical Chemistry C*, vol. 115, no. 40, pp. 19828–19840, 2011.

[68] P. G. Yot, Q. Ma, J. Haines, Q. Yang, A. Ghoufi, T. Devic, C. Serre, V. Dmitriev, G. Férey, C. Zhong, and G. Maurin, "Large breathing of the MOF MIL-47(V^{IV}) under mechanical pressure: a joint experimental-modelling exploration," *Chemical Science*, vol. 3, pp. 1100–1104, 2012.

[69] M. Kondo, T. Yoshitomi, H. Matsuzaka, S. Kitagawa, and K. Seki, "Three-dimensional framework with channeling cavities for small molecules: {[M_2(4, 4-bpy)$_3$(NO_3)$_4$]·xH_2O}$_n$ (M = Co, Ni, Zn)," *Angewandte Chemie International Edition in English*, vol. 36, no. 16, pp. 1725–1727, 1997.

[70] `https://www.degruyter.com/downloadpdf/j/pac.2015.87.issue-9-10/pac-2014-1117/pac-2014-1117.pdf`. January 23, 2018.

[71] P. Van Der Voort, K. Leus, Y.-Y. Liu, M. Vandichel, V. Van Speybroeck, M. Waroquier, and S. Biswas, "Vanadium metal-organic frameworks: structures and applications," *New Journal of Chemistry*, vol. 38, pp. 1853–1867, 2014.

[72] A. Lieb, H. Leclerc, T. Devic, C. Serre, I. Margiolaki, F. Mahjoubi, J. S. Lee, A. Vimont, M. Daturi, and J.-S. Chang, "MIL-100(V) a mesoporous vanadium metal organic framework with accessible metal sites," *Microporous and Mesoporous Materials*, vol. 157, pp. 18 – 23, 2012.

[73] Y.-Y. Liu, S. Couck, M. Vandichel, M. Grzywa, K. Leus, S. Biswas, D. Volkmer, J. Gascon, F. Kapteijn, J. F. M. Denayer, M. Waroquier, V. Van Speybroeck, and P. Van Der Voort, "New V^{IV}-based metal-organic framework having

framework flexibility and high CO_2 adsorption capacity," *Inorganic Chemistry*, vol. 52, no. 1, pp. 113–120, 2013.

[74] I. Senkovska, F. Hoffmann, M. Froeba, J. Getzschmann, W. Boehlmann, and S. Kaskel, "New highly porous aluminium based metal-organic frameworks: Al(OH)(ndc)(ndc=2,6-naphthalene dicarboxylate) and Al(OH)(bpdc) (bpdc=4,4-biphenyl dicarboxylate)," *Microporous and Mesoporous Materials*, vol. 122, no. 1-3, pp. 93–98, 2009.

[75] A. Lieb, H. Leclerc, T. Devic, C. Serre, I. Margiolaki, F. Mahjoubi, J. S. Lee, A. Vimont, M. Daturi, and J.-S. Chang, "MIL-100(V) a mesoporous vanadium metal organic framework with accessible metal sites," *Microporous and Mesoporous Materials*, vol. 157, pp. 18 – 23, 2012.

[76] P. L. Llewellyn, S. Bourrelly, C. Serre, Y. Filinchuk, and G. Férey, "How hydration drastically improves adsorption selectivity for CO_2 over CH_4 in the flexible chromium terephthalate MIL-53," *Angewandte Chemie International Edition*, vol. 45, no. 46, pp. 7751–7754, 2006.

[77] N. Guillou, S. Bourrelly, P. L. Llewellyn, R. I. Walton, and F. Millange, "Location of CO_2 during its uptake by the flexible porous metal-organic framework MIL-53(Fe): a high resolution powder x-ray diffraction study," *CrystEngComm*, vol. 17, pp. 422–429, 2015.

[78] N. L. Rosi, J. Eckert, M. Eddaoudi, D. T. Vodak, J. Kim, M. O'Keeffe, and O. M. Yaghi, "Hydrogen storage in microporous metal-organic frameworks," *Science*, vol. 300, no. 5622, pp. 1127–1129, 2003.

[79] A. Schoedel, Z. Ji, and O. M. Yaghi, "The role of metal-organic frameworks in a carbon-neutral energy cycle," *Nature Energy*, vol. 1, p. 16034, 2016.

[80] L. Wang and R. T. Yang, "New sorbents for hydrogen storage by hydrogen spillover - a review," *Energy and Environmental Science*, vol. 1, pp. 268–279, 2008.

[81] J. L. C. Rowsell and O. M. Yaghi, "Effects of functionalization, catenation, and variation of the metal oxide and organic linking units on the low-pressure hydrogen adsorption properties of metal-organic frameworks," *Journal of the American Chemical Society*, vol. 128, no. 4, pp. 1304–1315, 2006.

[82] Y. He, W. Zhou, G. Qian, and B. Chen, "Methane storage in metal-organic frameworks," *Chemical Society Reviews*, vol. 43, pp. 5657–5678, 2014.

[83] T. A. Makal, J.-R. Li, W. Lu, and H.-C. Zhou, "Methane storage in advanced porous materials," *Chemical Society Reviews*, vol. 41, pp. 7761–7779, 2012.

[84] B. Li, H.-M. Wen, Y. Cui, W. Zhou, G. Qian, and B. Chen, "Emerging multifunctional metal-organic framework materials," *Advanced Materials*, vol. 28, no. 40, pp. 8819–8860, 2016.

[85] Y. Peng, V. Krungleviciute, I. Eryazici, J. T. Hupp, O. K. Farha, and T. Yildirim, "Methane storage in metal-organic frameworks: Current records, surprise findings, and challenges," *Journal of the American Chemical Society*, vol. 135, no. 32, pp. 11887–11894, 2013.

[86] G. Férey, "Yes, we can!," *European Journal of Inorganic Chemistry*, vol. 2016, no. 27, pp. 4275–4277, 2016.

[87] K. Leus, S. Couck, M. Vandichel, G. Vanhaelewyn, Y.-Y. Liu, G. B. Marin, I. V. Driessche, D. Depla, M. Waroquier, V. V. Speybroeck, J. F. M. Denayer, and P. V. D. Voort, "Synthesis, characterization and sorption properties of NH_2-MIL-47," *Physical Chemistry Chemical Physics*, vol. 14, no. 44, pp. 15562–15570, 2012.

[88] L. J. Murray, M. Dinca, J. Yano, S. Chavan, S. Bordiga, C. M. Brown, and J. R. Long, "Highly-selective and reversible O_2 binding in Cr_3(1,3,5-benzenetricarboxylate)$_2$," *Journal of the American Chemical Society*, vol. 132, no. 23, pp. 7856–7857, 2010.

[89] E. D. Bloch, L. J. Murray, W. L. Queen, S. Chavan, S. N. Maximoff, J. P. Bigi, R. Krishna, V. K. Peterson, F. Grandjean, G. J. Long, B. Smit, S. Bordiga, C. M. Brown, and J. R. Long, "Selective binding of O_2 over N_2 in a redox-active metal-organic framework with open iron(II) coordination sites," *Journal of the American Chemical Society*, vol. 133, no. 37, pp. 14814–14822, 2011.

[90] S. Couck, J. F. M. Denayer, G. V. Baron, T. Rémy, J. Gascon, and F. Kapteijn, "An amine-functionalized MIL-53 metal-organic framework with large separation power for CO_2 and CH_4," *Journal of the American Chemical Society*, vol. 131, no. 18, pp. 6326–6327, 2009.

[91] P. Tundo, P. Anastas, D. Black, J. Breen, T. Collins, S. Memoli, J. Miyamoto, M. Polyakoff, and W. Tumas, "Synthetic pathways and processes in green chemistry. Introductory overview," *Pure and Applied Chemistry*, vol. 72, no. 7, pp. 1207–1228, 2000.

[92] I. Chorkendorff and J. W. Niemantsverdriet, *Introduction to Catalysis*, pp. 1–21. Wiley-VCH Verlag GmbH Co. KGaA, 2005.

[93] M. Fujita, Y. J. Kwon, S. Washizu, and K. Ogura, "Preparation, clathration ability, and catalysis of a two-dimensional square network material composed of cadmium(II) and 4,4'-bipyridine," *Journal of the American Chemical Society*, vol. 116, no. 3, pp. 1151–1152, 1994.

[94] F. X. Llabres i Xamena, A. Abad, A. Corma, and H. Garcia, "MOFs as catalysts: Activity, reusability and shape-selectivity of a Pd-containing MOF," *Journal of Catalysis*, vol. 250, no. 2, pp. 294–298, 2007.

[95] L. Alaerts, E. Seguin, H. Poelman, F. Thibault-Starzyk, P. A. Jacobs, and D. E. De Vos, "Probing the lewis acidity and catalytic activity of the metal-organic framework $[Cu_3(BTC)_2]$(BTC = benzene-1,3,5-tricarboxylate)," *Chemistry - A European Journal*, vol. 12, no. 28, pp. 7353–7363, 2006.

[96] I. Muylaert and P. Van Der Voort, "Supported vanadium oxide in heterogeneous catalysis: elucidating the structure-activity relationship with spectroscopy," *Physical Chemistry Chemical Physics*, vol. 11, pp. 2826–2832, 2009.

[97] A. Phan, A. U. Czaja, F. Gandara, C. B. Knobler, and O. M. Yaghi, "Metal-organic frameworks of vanadium as catalysts for conversion of methane to acetic acid," *Inorganic Chemistry*, vol. 50, no. 16, pp. 7388–7390, 2011.

[98] M. Vandichel, S. Biswas, K. Leus, J. Paier, J. Sauer, T. Verstraelen, P. Van der Voort, M. Waroquier, and V. Van Speybroeck, "Catalytic performance of vanadium MIL-47 and linker-substituted variants in the oxidation of cyclohexene: A combined theoretical and experimental approach," *ChemPlusChem*, vol. 79, no. 8, pp. 1183–1197, 2014.

[99] K. Leus, G. Vanhaelewyn, T. Bogaerts, Y.-Y. Liu, D. Esquivel, F. Callens, G. B. Marin, V. Van Speybroeck, H. Vrielinck, and P. Van Der Voort, "Ti-functionalized NH_2-MIL-47: An effective and stable epoxidation catalyst," *Catalysis Today*, vol. 208, pp. 97–105, 2013.

[100] Y.-Y. Liu, K. Leus, M. Grzywa, D. Weinberger, K. Strubbe, H. Vrielinck, R. Van Deun, D. Volkmer, V. Van Speybroeck, and P. Van Der Voort, "Synthesis, structural characterization, and catalytic performance of a vanadium-based metal-organic framework (COMOC-3)," *European Journal of Inorganic Chemistry*, vol. 2012, no. 16, pp. 2819–2827, 2012.

[101] S. Bhattacharjee, C. Chen, and W.-S. Ahn, "Chromium terephthalate metal-organic framework MIL-101: synthesis, functionalization, and applications for adsorption and catalysis," *RSC Advances*, vol. 4, pp. 52500–52525, 2014.

[102] A. H. Chughtai, N. Ahmad, H. A. Younus, A. Laypkov, and F. Verpoort, "Metal-organic frameworks: versatile heterogeneous catalysts for efficient catalytic organic transformations," *Chemical Society Reviews*, vol. 44, pp. 6804–6849, 2015.

[103] L. Zhu, X.-Q. Liu, H.-L. Jiang, and L.-B. Sun, "Metal-organic frameworks for heterogeneous basic catalysis," *Chemical Reviews*, vol. 117, no. 12, pp. 8129–8176, 2017.

[104] D. J. Wales, J. Grand, V. P. Ting, R. D. Burke, K. J. Edler, C. R. Bowen, S. Mintova, and A. D. Burrows, "Gas sensing using porous materials for automotive applications," *Chemical Society Reviews*, vol. 44, pp. 4290–4321, 2015.

[105] A. Lan, K. Li, H. Wu, D. Olson, T. Emge, W. Ki, M. Hong, and J. Li, "A luminescent microporous metal-organic framework for the fast and reversible detection of high explosives," *Angewandte Chemie International Edition*, vol. 48, no. 13, pp. 2334–2338, 2009.

[106] W. Ma, Q. Jiang, P. Yu, L. Yang, and L. Mao, "Zeolitic imidazolate framework-based electrochemical biosensor for *in vivo* electrochemical measurements," *Analytical Chemistry*, vol. 85, no. 15, pp. 7550–7557, 2013.

[107] S. Liu, Z. Xiang, Z. Hu, X. Zheng, and D. Cao, "Zeolitic imidazolate framework-8 as a luminescent material for the sensing of metal ions and small molecules," *Journal of Materials Chemistry*, vol. 21, pp. 6649–6653, 2011.

[108] Y. Yu, J.-P. Ma, and Y.-B. Dong, "Luminescent humidity sensors based on porous Ln^{3+}-MOFs," *CrystEngComm*, vol. 14, pp. 7157–7160, 2012.

[109] C.-C. Wang, C.-C. Yang, W.-C. Chung, G.-H. Lee, M.-L. Ho, Y.-C. Yu, M.-W. Chung, H.-S. Sheu, C.-H. Shih, K.-Y. Cheng, P.-J. Chang, and P.-T. Chou, "A new coordination polymer exhibiting unique 2D hydrogen-bonded $(H_2O)_{16}$ ring formation and water-dependent luminescence properties," *Chemistry A European Journal*, vol. 17, no. 33, pp. 9232–9241, 2011.

[110] I. Ellern, A. Venkatasubramanian, J. H. Lee, P. Hesketh, V. Stavila, A. Robinson, and M. Allendorf, "HKUST-1 coated piezoresistive microcantilever array for volatile organic compound sensing," *IET Micro Nano Letters*, vol. 8, no. 11, pp. 766–769, 2013.

[111] M. Höckel, K. Schlenger, B. Aral, M. Mitze, U. Schäffer, and P. Vaupel, "Association between tumor hypoxia and malignant progression in advanced cancer of the uterine cervix," *Cancer Research*, vol. 56, no. 19, pp. 4509–4515, 1996.

[112] R.-B. Lin, S.-Y. Liu, J.-W. Ye, X.-Y. Li, and J.-P. Zhang, "Photoluminescent metal-organic frameworks for gas sensing," *Advanced Science*, vol. 3, no. 7, pp. 1500434–1500454, 2016.

[113] R. Xu, Y. Wang, X. Duan, K. Lu, D. Micheroni, A. Hu, and W. Lin, "Nanoscale metal-organic frameworks for ratiometric oxygen sensing in live cells," *Journal of the American Chemical Society*, vol. 138, no. 7, pp. 2158–2161, 2016.

[114] X.-L. Qi, S.-Y. Liu, R.-B. Lin, P.-Q. Liao, J.-W. Ye, Z. Lai, Y. Guan, X.-N. Cheng, J.-P. Zhang, and X.-M. Chen, "Phosphorescence doping in a flexible

ultramicroporous framework for high and tunable oxygen sensing efficiency," *Chemical Communications*, vol. 49, pp. 6864–6866, 2013.

[115] P. Horcajada, R. Gref, T. Baati, P. K. Allan, G. Maurin, P. Couvreur, G. Férey, R. E. Morris, and C. Serre, "Metal-organic frameworks in biomedicine," *Chemical Reviews*, vol. 112, no. 2, pp. 1232–1268, 2012.

[116] C. He, D. Liu, and W. Lin, "Nanomedicine applications of hybrid nanomaterials built from metal-ligand coordination bonds: Nanoscale metal-organic frameworks and nanoscale coordination polymers," *Chemical Reviews*, vol. 115, no. 19, pp. 11079–11108, 2015.

[117] Y. Chen, V. Lykourinou, C. Vetromile, T. Hoang, L.-J. Ming, R. W. Larsen, and S. Ma, "How can proteins enter the interior of a MOF? Investigation of cytochrome c translocation into a MOF consisting of mesoporous cages with microporous windows," *Journal of the American Chemical Society*, vol. 134, no. 32, pp. 13188–13191, 2012.

[118] P. Horcajada, T. Chalati, C. Serre, B. Gillet, C. Sebrie, T. Baati, J. F. Eubank, D. Heurtaux, P. Clayette, C. Kreuz, J.-S. Chang, Y. K. Hwang, V. Marsaud, P.-N. Bories, L. Cynober, S. Gil, G. Férey, P. Couvreur, and R. Gref, "Porous metal-organic-framework nanoscale carriers as a potential platform for drug delivery and imaging," *Nature Materials*, vol. 9, no. 2, pp. 172–178, 2010.

[119] P. Horcajada, C. Serre, M. Vallet-Regí, M. Sebban, F. Taulelle, and G. Férey, "Metal-organic frameworks as efficient materials for drug delivery," *Angewandte Chemie International Edition*, vol. 45, no. 36, pp. 5974–5978, 2006.

[120] P. Horcajada, C. Serre, G. Maurin, N. A. Ramsahye, F. Balas, M. Vallet-Regí, M. Sebban, F. Taulelle, and G. Férey, "Flexible porous metal-organic frameworks for a controlled drug delivery," *Journal of the American Chemical Society*, vol. 130, no. 21, pp. 6774–6780, 2008.

[121] W. J. Rieter, K. M. Pott, K. M. L. Taylor, and W. Lin, "Nanoscale coordination polymers for platinum-based anticancer drug delivery," *Journal of the American Chemical Society*, vol. 130, no. 35, pp. 11584–11585, 2008.

[122] M. R. Lohe, K. Gedrich, T. Freudenberg, E. Kockrick, T. Dellmann, and S. Kaskel, "Heating and separation using nanomagnet-functionalized metal-organic frameworks," *Chemical Communications*, vol. 47, pp. 3075–3077, 2011.

[123] C. Wang, X. Liu, N. Keser Demir, J. P. Chen, and K. Li, "Applications of water stable metal-organic frameworks," *Chemical Society Reviews*, vol. 45, pp. 5107–5134, 2016.

[124] C.-Y. Sun, C. Qin, X.-L. Wang, G.-S. Yang, K.-Z. Shao, Y.-Q. Lan, Z.-M. Su, P. Huang, C.-G. Wang, and E.-B. Wang, "Zeolitic imidazolate framework-8 as efficient pH-sensitive drug delivery vehicle," *Dalton Transactions*, vol. 41, pp. 6906–6909, 2012.

[125] I. B. Vasconcelos, T. G. d. Silva, G. C. G. Militao, T. A. Soares, N. M. Rodrigues, M. O. Rodrigues, N. B. d. Costa, R. O. Freire, and S. A. Junior, "Cytotoxicity and slow release of the anti-cancer drug doxorubicin from ZIF-8," *RSC Advances*, vol. 2, pp. 9437–9442, 2012.

[126] L. He, T. Wang, J. An, X. Li, L. Zhang, L. Li, G. Li, X. Wu, Z. Su, and C. Wang, "Carbon nanodots@zeolitic imidazolate framework-8 nanoparticles for simultaneous pH-responsive drug delivery and fluorescence imaging," *CrystEngComm*, vol. 16, pp. 3259–3263, 2014.

[127] `https://www.britannica.com/science/Zeeman-effect`. July 04, 2017.

[128] `https://en.wikipedia.org/wiki/Stern%E2%80%93Gerlach_experiment`. July 04, 2017.

[129] `https://www.aps.org/programs/outreach/history/historicsites/rabi.cfm`. July 04, 2017.

[130] `https://chem.libretexts.org/Core/Physical_and_Theoretical_Chemistry/Spectroscopy/Magnetic_Resonance_Spectroscopies/Electron_Paramagnetic_Resonance/EPR%3A_Theory#Historical_Development_of_EPR`. July 04, 2017.

[131] N. M. Atherton, *Principles of electron spin resonance*. New York : Ellis Horwood : PTR Prentice Hall, 1993.

[132] J. A. Weil, J. R. Bolton, and J. E. Wertz, *Electron paramagnetic resonance: Elementary theory and applications*. Wiley-interscience, New York, 1994.

[133] F. Mabbs and D. Collison, *Electron Paramagnetic Resonance of d Transition Metal Compounds*. Elsevier Science, 1992.

[134] J.-M. Spaeth, J. R. Niklas, and R. H. Bartram, *Structural Analysis of Point Defects in Solids*. Springer-Verlag Berlin Heidelberg, 1992.

[135] A. Abragam and B. Bleaney, *Electron Paramagnetic Resonance of Transition Ions*. Oxford University Press, 1970.

[136] M. Mendt, B. Jee, N. Stock, T. Ahnfeldt, M. Hartmann, D. Himsl, and A. Pöppl, "Structural phase transitions and thermal hysteresis in the metal-organic framework compound MIL-53 as studied by electron spin resonance spectroscopy," *Journal of Physical Chemistry C*, vol. 114, no. 45, pp. 19443–19451, 2010.

[137] H. Vrielinck, *Magnetic resonance analysis of Rh complexes in AgCl and NaCl*. PhD thesis, Ghent University, 2002.

[138] J. R. Pilbrow, *Transition Ion Electron Paramagnetic Resonance*. Clarendon Oress, Oxford, 1990.

[139] S. K. Misra, ed., *Multifrequency Electron Paramagnetic Resonance: Theory and Applications*. Wiley-VCH Verlag GmbH and Co. KGaA, 2011.

[140] J. W. Orton, *Electron Paramagnetic Resonance*. Pitman Press, 1968.

[141] A. M. Sheveleva, D. I. Kolokolov, A. A. Gabrienko, A. G. Stepanov, S. A. Gromilov, I. K. Shundrina, R. Z. Sagdeev, M. V. Fedin, and E. G. Bagryanskaya, "Structural dynamics in a "breathing" metal-organic framework studied by electron paramagnetic resonance of nitroxide spin probes," *Journal of Physical Chemistry Letters*, vol. 5, no. 1, pp. 20–24, 2014.

[142] https://en.wikipedia.org/wiki/TEMPO. July 04, 2017.

[143] T. S. Smith, R. LoBrutto, and V. L. Pecoraro, "Paramagnetic spectroscopy of vanadyl complexes and its applications to biological systems," *Coordination Chemistry Reviews*, vol. 228, no. 1, pp. 1 – 18, 2002.

[144] C. V. Grant, W. Cope, J. A. Ball, G. G. Maresch, B. J. Gaffney, W. Fink, and R. D. Britt, "Electronic structure of the aqueous vanadyl ion probed by 9 and 94 GHz EPR and pulsed ENDOR spectroscopies and density functional theory calculations," *The Journal of Physical Chemistry B*, vol. 103, no. 48, pp. 10627–10631, 1999.

[145] I. Nevjestić, H. Depauw, K. Leus, V. Kalendra, I. Caretti, G. Jeschke, S. Van Doorslaer, F. Callens, P. Van Der Voort, and H. Vrielinck, "Multi-frequency (S, X, Q and W-band) EPR and ENDOR study of vanadium(IV) incorporation in the aluminium metal-organic framework MIL-53," *ChemPhysChem*, vol. 16, no. 14, pp. 2968–2973, 2015.

[146] G. Eaton, S. Eaton, D. Barr, and R. Weber, *Quantitative EPR*. Springer-Verlag Wien, 2010.

[147] H. D. Cooman, *A combined EMR and DFT study of iradiation-induced defects in sucrose and clucose 1-phosphate*. PhD thesis, Ghent University, 2009.

[148] O. Kozachuk, M. Meilikhov, K. Yusenko, A. Schneemann, B. Jee, A. V. Kuttatheyil, M. Bertmer, C. Sternemann, A. Pöppl, and R. A. Fischer, "A solid-solution approach to mixed-metal metal-organic frameworks - detailed characterization of local structures, defects and breathing behaviour of Al/V frameworks," *European Journal of Inorganic Chemistry*, vol. 2013, no. 26, pp. 4546–4557, 2013.

[149] M. Mendt, B. Jee, D. Himsl, L. Moschkowitz, T. Ahnfeldt, N. Stock, M. Hartmann, and A. Pöppl, "A continuous-wave electron paramagnetic resonance study of carbon dioxide adsorption on the metal-organic framework MIL-53," *Applied Magnetic Resonance*, vol. 45, no. 3, pp. 269–285, 2014.

[150] A. S. Poryvaev, A. M. Sheveleva, D. I. Kolokolov, A. G. Stepanov, E. G. Bagryanskaya, and M. V. Fedin, "Mobility and reactivity of 4-substituted TEMPO derivatives in metal-organic framework MIL-53(Al)," *The Journal of Physical Chemistry C*, vol. 120, no. 19, pp. 10698–10704, 2016.

[151] J. Cao, Y. Feng, S. Zhou, X. Sun, T. Wang, C. Wang, and H. Li, "Spatial aromatic fences of metal-organic frameworks for manipulating the electron spin of a fulleropyrrolidine nitroxide radical," *Dalton Transactions*, vol. 45, pp. 11272–11276, 2016.

[152] `https://en.wikipedia.org/wiki/Characteristic_X-ray`. July 04, 2017.

[153] `https://en.wikipedia.org/wiki/Bremsstrahlung`. July 04, 2017.

[154] `https://en.wikipedia.org/wiki/X-ray`. July 04, 2017.

[155] `https://publish.illinois.edu/x-raycrystallography/2014/12/18/introduction/`. July 04, 2017.

[156] `http://www.ing.unitn.it/~luttero/phd/C1_crystallography.pdf`. July 04, 2017.

[157] `https://old.vscht.cz/clab/RTG/dokumenty/thermo/xrd/Introduction%20to%20powder%20diffraction.pdf`. July 04, 2017.

[158] `https://dasher.wustl.edu/bio5325/reading/vanholde-xray-98.pdf`. July 04, 2017.

[159] J. Als-Nielsen and D. McMorrow, *X-rays and their interaction with matter*, pp. 1–28. John Wiley and Sons, Inc., 2011.

[160] J. Als-Nielsen and D. McMorrow, *Sources*, pp. 29–67. John Wiley and Sons, Inc., 2011.

[161] J. Als-Nielsen and D. McMorrow, *Kinematical scattering I: non-crystalline materials*, pp. 113–146. John Wiley and Sons, Inc., 2011.

[162] `http://www.diamond.ac.uk/Home/About/How-Diamond-Works.html`. July 04, 2017.

[163] S. P. Thompson, J. E. Parker, J. Potter, T. P. Hill, A. Birt, T. M. Cobb, F. Yuan, and C. C. Tang, "Beamline I11 at Diamond: A new instrument for high resolution powder diffraction," *Review of Scientific Instruments*, vol. 80, no. 7, p. 075107, 2009.

[164] http://www.diamond.ac.uk/Beamlines/Engineering-and-Environment/I11/layout/specs/detectors.html. July 04, 2017.

[165] G. Bruker AXS, Karlsruhe, "Bruker AXS (2008): TOPAS V4: General profile and structure analysis software for powder diffraction data. - user's manual," *http://algol.fis.uc.pt/jap/TOPAS%204-2%20Users%20Manual.pdf*.

[166] H. Depauw, *Investigation of the doping effect in bimetallic metal-organic frameworks to tune their structural flexibility*. PhD thesis, Ghent University, 2018.

[167] S. Stoll and A. Schweiger, "Easyspin, a comprehensive software package for spectral simulation and analysis in EPR," *Journal of Magnetic Resonance*, vol. 178, no. 1, pp. 42–55, 2006.

[168] C. F. Macrae, I. J. Bruno, J. A. Chisholm, P. R. Edgington, P. McCabe, E. Pidcock, L. Rodriguez-Monge, R. Taylor, J. van de Streek, and P. A. Wood, "Mercury CSD 2.0 - new features for the visualization and investigation of crystal structures," *Journal of Applied Crystallography*, vol. 41, no. 2, pp. 466–470, 2008.

[169] P. L. Llewellyn, P. Horcajada, G. Maurin, T. Devic, N. Rosenbach, S. Bourrelly, C. Serre, D. Vincent, S. Loera-Serna, Y. Filinchuk, and G. Férey, "Complex adsorption of short linear alkanes in the flexible metal-organic-framework MIL-53(Fe)," *Journal of the American Chemical Society*, vol. 131, no. 36, pp. 13002–13008, 2009.

[170] A. V. Neimark, F.-X. Coudert, C. Triguero, A. Boutin, A. H. Fuchs, I. Beurroies, and R. Denoyel, "Structural transitions in MIL-53 (Cr): View from outside and inside," *Langmuir*, vol. 27, no. 8, pp. 4734–4741, 2011.

[171] A. Hoffman, "Experimental and computational vibrational spectroscopy of metal-organic frameworks," Master's thesis, Ghent University, 2017.

[172] F. Salles, S. Bourrelly, H. Jobic, T. Devic, V. Guillerm, P. Llewellyn, C. Serre, G. Férey, and G. Maurin, "Molecular insight into the adsorption and diffusion of water in the versatile hydrophilic/hydrophobic flexible MIL-53(Cr) MOF," *Journal of Physical Chemistry C*, vol. 115, no. 21, pp. 10764–10776, 2011.

[173] P. Mishra, S. Edubilli, H. P. Uppara, B. Mandal, and S. Gumma, "Effect of adsorbent history on adsorption characteristics of MIL-53(Al) metal organic framework," *Langmuir*, vol. 29, no. 39, pp. 12162–12167, 2013.

[174] R. Ahmad and P. Kuppusamy, "Theory, instrumentation, and applications of electron paramagnetic resonance oximetry," *Chemical Reviews*, vol. 110, no. 5, pp. 3212–3236, 2010.

[175] K. J. Liu, P. Gast, M. Moussavi, S. W. Norby, N. Vahidi, T. Walczak, M. Wu, and H. M. Swartz, "Lithium phthalocyanine: a probe for electron paramagnetic resonance oximetry in viable biological systems," *Proceedings of the National Academy of Sciences*, vol. 90, no. 12, pp. 5438–5442, 1993.

[176] H. Depauw, I. Nevjestić, G. Wang, K. Leus, F. Callens, E. De Canck, K. De Buysser, H. M. Vrielinck, and P. Van Der Voort, "Discovery of a novel, large pore phase in a bimetallic Al/V metal-organic framework," *Journal of Materials Chemistry A*, pp. 24580–24584, 2017.

[177] S. Van de Vyver and Y. Roman-Leshkov, "Emerging catalytic processes for the production of adipic acid," *Catalysis Science and Technology*, vol. 3, pp. 1465–1479, 2013.

[178] R. A. Serway and S. A. Marshall, "Electron spin resonance absorption spectra of CO_3^- and CO_3^{3-} molecule-ions in irradiated single-crystal calcite," *The Journal of Chemical Physics*, vol. 46, no. 5, pp. 1949–1952, 1967.

[179] M. Willer, J. Forrer, J. Keller, S. Van Doorslaer, A. Schweiger, R. Schuhmann, and T. Weiland, "S-band (2-4 GHz) pulse electron paramagnetic resonance spectrometer: Construction, probe head design, and performance," *Review of Scientific Instruments*, vol. 71, no. 7, pp. 2807–2817, 2000.

[180] H. Blok, J. A. J. M. Disselhorst, S. B. Orlinskii, and J. Schmidt, "A continuous-wave and pulsed electron spin resonance spectrometer operating at 275 GHz," *Journal of Magnetic Resonance*, vol. 166, no. 1, pp. 92–99, 2004.

[181] M. Tinkham and M. W. P. Strandberg, "Theory of the fine structure of the molecular oxygen ground state," *Physical Review*, vol. 97, no. 4, pp. 937–951, 1955.

[182] S. Nikitenko, A. M. Beale, A. M. J. van der Eerden, S. D. M. Jacques, O. Leynaud, M. G. O'Brien, D. Detollenaere, R. Kaptein, B. M. Weckhuysen, and W. Bras, "Implementation of a combined SAXS/WAXS/QEXAFS set-up for time-resolved *in situ* experiments," *Journal of Synchrotron Radiation*, vol. 15, no. 6, pp. 632–640, 2008.

List of Publications

B.6 Articles in Peer-Reviewed Journals

- *Elucidating the vibrational fingerprint of the flexible metal-organic framework MIL-53(Al) using a combined experimental/computational approach*, Alexander E. J. Hoffman, Louis Vanduyfhuys, Irena Nevjestić, Jelle Wieme, Sven M. J. Rogge, Hannes Depauw, Pascal Van Der Voort, Henk Vrielinck, and Veronique Van Speybroeck, *The Journal of Physical Chemistry C*, 2018, DOI: 10.1021/acs.jpcc.7b11031.

- *Sensing the framework state and guest molecules in MIL-53(Al) via the electron paramagnetic resonance spectrum of V^{IV} dopant ions*, Irena Nevjestić, Hannes Depauw, Peter Gast, Pieter Tack, Davy Deduytsche, Karen Leus, Melissa Van Landegheme, Etienne Goovaerts, Laszlo Vincze, Christophe Detavernier, Pascal Van Der Voort, Freddy Callens, Henk Vrielinck, *Physical Chemistry Chemical Physics*, 2017, 19 (36), 24545-24554.

- *Discovery of a novel, large pore phase in a bimetallic Al/V metal-organic framework*, Hannes Depauw, Irena Nevjestić, Guangbo Wang, Karen Leus, Freddy Callens, Els De Canck, Klaartje De Buysser, Henk Vrielinck, Pascal Van Der Voort, *Journal of Materials Chemistry A*, 2017, 5, 24580-24584.

- *Microwave induced 'egg yolk' structure in Cr/V-MIL-53*, Hannes Depauw, Irena Nevjestić, Jonatan De Winne, Guangbo Wang, Katrien Haustraete, Karen Leus, An Verberckmoes, Christophe Detavernier, Freddy Callens, Els De Canck, Henk Vrielinck, Pascal Van Der Voort, *Chemical Communications*, 2017, 53 (60), 8478-8481.

- *In situ electron paramagnetic resonance and X-ray diffraction monitoring of temperature-induced breathing and related structural transformations in activated V-doped MIL-53(Al)*, Irena Nevjestić, Hannes Depauw, Karen Leus, Geert Rampelberg, Claire A. Murray, Christophe Detavernier, Pascal Van Der Voort, Freddy Callens, Henk Vrielinck, *The Journal of Physical Chemistry C*, 2016, 120(31), 17400-17407.

- *Multi-frequency (S, X, Q and W-band) EPR and ENDOR study of vanadium(IV) incorporation in the aluminium metal-organic framework MIL-53*, Irena Nevjestić, Hannes Depauw, Karen Leus, Vidmantas Kalendra, Ignacio Caretti, Gunnar Jeschke, Sabine Van Doorslaer, Freddy Callens, Pascal Van Der Voort, Henk Vrielinck, *ChemPhysChem*, 2015, 16(14), 2968-2973.

B.7 International Conference Contributions

- *Sensing the environment of V^{4+} dopant ions in a metal organic framework with EPR spectroscopy and X-ray diffraction*, Nevjestić, I., Depauw, H., Leus, K., Van Der Voort, P., Vrielinck, H., Callens, F., *The 50th Annual International Meeting of the ESR Spectroscopy Group of the Royal Society of Chemistry*, poster presentation, Oxford, UK, 2017.

- *Temperature-induced breathing effect of V-doped MIL-53(Al) monitored in situ by electron paramagnetic resonance and X-ray diffraction*, Nevjestić, I., Depauw, H., Leus, K., Van Der Voort, P., Callens, F., Vrielinck, H., *The 5th International conference on Metal-Organic Frameworks and Open Framework Compounds (MOF 2016)*, oral presentation, Long Beach, CA, USA, 2016.

- *Tailoring the breathing effect of a flexible MOF, COMOC-2 by a mixed-metal approach*, Depauw, H., Nevjestić, I., Leus, K., Wang, G., Callens, F., Vrielinck, H., Van Der Voort, P., *The 5th International conference on Metal-Organic Frameworks and Open Framework Compounds (MOF 2016)*, oral presentation, Long Beach, CA, USA, 2016.

- *V^{IV} ions as paramagnetic probe for monitoring the structural flexibility of V-doped MIL-53(Al)*, Nevjestić, I., Depauw, H., Leus, K., Van Der Voort, P., Callens, F., Vrielinck, H., *EFEPR, Xth conference*, poster presentation, Torino, Italy, 2016.

- *Breathing effect in activated V-doped Al-MOF studied with EPR*, Nevjestić, I., Depauw, H., Leus, K., Callens, F., Van Der Voort, P., Vrielinck, H., *European Federation of EPR groups on Advanced EPR, 7th Summer school*, poster presentation, Berlin, Germany, 2015.

- *Studying the effectiveness of V-incorporation in the Al-metal-organic framework MIL-53 with electron-nuclear double resonance spectroscopy*, Nevjestić, I., Depauw, H., Leus, K., Kalendra, V., Caretti, I., Jeschke, G., Van Doorslaer, S., Callens, F., Van Der Voort, P., Vrielinck, H., *The 12th Europhysical conference on Defects in Insulating Materials (Eurodim 2014)*, poster presentation, Canterbury, UK, 2014.

- *Studying the environment of vanadyl complexes in the Al-Metal-Organic framework MIL-53 by a multi-frequency EPR and ENDOR approach*, Nevjestić, I., Depauw, H., Leus, K., Kalendra, V., Caretti, I., Jeschke, G., Van Doorslaer, S., Callens, F., Van Der Voort, P., Vrielinck, H., *EFEPR, IXth conference*, poster presentation, Marseille, France, 2014.

B.8 Regional Conference Contributions and Others

- *Regulating the breathing effect of a flexible biphenyl MOF, by a mixed-metal approach*, Depauw, H., Nevjestić, I., Leus, K., Callens, F., Vrielinck, H., Van Der Voort, P., *1st Symposium Chemical Research in Flanders (CRF 2016)*, oral presentation, Blankenberge, Belgium, 2016.
- *Breathing effect in V-doped metal organic framework MIL-53(Al) studied by electron paramagnetic resonance (EPR)*, Nevjestić, I., Depauw, H., Leus, K., Van Der Voort, P., Callens, F., Vrielinck, H., *The General scientific meeting of the Belgian Physical Society (BPS)*, poster presentation, Gent, Belgium, 2016.
- *Breathing effect in the V-doped metal organic framework MIL-53(Al) monitored in situ by electron paramagnetic resonance and X-ray diffraction*, Nevjestić, I., Depauw, H., Leus, K., Van Der Voort, P., Callens, F., Vrielinck, H., *Benelux EPR Society*, poster presentation, Liège, Belgium, 24th Meeting, 2016.
- *Breathing of V-doped MIL-53(Al) monitored in situ by electron paramagnetic resonance and X-ray diffraction*, Nevjestić, I., Depauw, H., *The Doctoraatssymposium Faculteit Wetenschappen Universiteit Gent*, oral presentation, Gent, Belgium, 2016.
- *EPR and ENDOR study of a V-doped Al-metal organic framework*, Nevjestić, I., Depauw, H., Leus, K., Kalendra, V., Caretti, I., Jeschke, G., Van Doorslaer, S., Callens, F., Van Der Voort, P., Vrielinck, H., *Benelux EPR Society*, 23rd Meeting, oral presentation, Gent, Belgium, 2015.
- *Confirming vanadium dopant incorporation in an Al-Metal-Organic framework MIL-53 by EPR and ENDOR spectroscopy*, Nevjestić, I., Depauw, H., Leus, K., Kalendra, V., Caretti, I., Jeschke, G., Van Doorslaer, S., Callens, F., Van Der Voort, P., Vrielinck, H., *Young Belgian Magnetic Resonance Scientist*, poster presentation, Spa, Belgium, 2014.
- *Characterizing vanadium dopant sites in an Al-metal-organic framework by electron magnetic resonance spectroscopy*, Nevjestić, I., Depauw, H., Leus, K., Callens, F., Van Der Voort, P., Vrielinck, H., *The 8th Belgian Crystallography symposium (BCS-8)*, poster presentation, Brussels, Belgium, 2014.

- *Resolving the relative tilting of hyperfine and g tensors for vanadyl complexes in the Al-metal-organic framework MIL-53 by a multi-frequency (S, X, Q, and W-band) EPR approach*, Nevjestić, I., Depauw, H., Leus, K., Kalendra, V., Caretti Giangaspro, I., Jeschke, G., Van Doorslaer, S., Callens, F., Van Der Voort, P., Vrielinck, H., *Benelux EPR Society, 22nd Meeting*, poster presentation, Maastricht, The Netherlands, 2014.